Title
Ultraviolet Light Emitting Diodes Grown on Sapphire and Silicon Carbide Substrates

Permalink
https://escholarship.org/uc/item/6qc728t1

Author
Zollner, Christian J

Publication Date
2022

Peer reviewed|Thesis/dissertation

UNIVERSITY OF CALIFORNIA

Santa Barbara

Ultraviolet Light Emitting Diodes Grown on Sapphire and Silicon Carbide Substrates

A dissertation submitted in partial satisfaction of the
requirements for the degree
Doctor of Philosophy in Materials

by

Christian J. Zollner

Committee in charge:
Professor Shuji Nakamura, Chair
Professor James S. Speck
Professor Steven P. DenBaars
Professor Umesh K. Mishra

March 2022

The dissertation of Christian J. Zollner is approved.

Shuji Nakamura

James Speck

Steven DenBaars

Umesh Mishra

January 2022

Ultraviolet Light Emitting Diodes Grown on Sapphire and Silicon Carbide Substrates

ACKNOWLEDGEMENTS

Prof. Nakamura, it has been such an inspiration to work with and learn from you, and thank you for your enduring support of my ideas—you always encouraged me to try new things, take risks, and find opportunity in challenges. My PhD committee has been incredibly encouraging and supportive throughout my time at UCSB. The world-class MOCVD and LED facilities you have built here at UCSB made all of this work possible. Prof. Speck, thank you for your support and teaching me everything I know about x-ray diffraction and materials characterization, and for the many long discussions in your office on everything from film stress, to semiconductor physics, to Strade Bianche. Prof. DenBaars, thank you for your advice on career-related and MOCVD-related questions, and for giving me the opportunity to participate in strategic conversations about the long term goals and overall shape of the UV Project, including the decision to switch MOCVD reactors. Prof. Mishra, it was a privilege to learn device physics from you, thank you for your career advice, and for always taking time to thoroughly answer my questions, especially about p-type AlGaN.

It has been an absolute pleasure and privilege to work on a PhD project which was so thoroughly a team endeavor from start to finish. It was a wonderful opportunity to work with and learn from the talented scientists who made up the UV Team. Humberto, Burhan, and Abdullah, you showed me by example how to be a good scientist and trained me on all the techniques I needed to conduct this research. Your work on establishing a strong foundation of AlN, AlGaN, and UV LED growth and processing formed the basis of all of the work in this dissertation. Michael and Yifan, it has been so great to work with you two on bringing our UV LED project to where it is now, and I cannot wait to see the incredible things you will do next. Mike, thank you for being a voice of reason when things got chaotic, a voice of support when the project was in hard times, and a friend and mentor these past 5 years. H. Foronda, B. SaifAddin, A. Almogbel, M. Iza, Y. Yao, M. Wang, F. Wu, and many others made significant contributions to the work presented in this dissertation. I would also like to thank Tal Margalith and Stacia Keller for their mentorship, advice, encouragement, insightful conversations, and encyclopedic knowledge of the GaN material system and the growth and fabrication of GaN based devices.

I would also like to acknowledge the support of all my friends from New York and California, my housemates at the Mill House, my SSLEEC colleagues past and present, and my loving family without whom none of this would have been possible. Your support throughout my PhD and especially in these past two years of COVID lockdowns has been incredible.

This dissertation is dedicated to my parents. Mom and Dad, you were the first ones who nurtured my interest in understanding the natural world, which eventually became a passion for math and science. Mom, you taught me how to look at everything in the world with a sense of curiosity, always to see the beauty of the natural world, and to see the bright side when things got difficult. Dad, you taught me to listen and learn from others, to communicate with honesty and clarity, to say what you mean and mean what you say.

VITA OF CHRISTIAN J. ZOLLNER

January 2022
cjzollner@gmail.com

Education and Teaching

2012-2016 Cornell University Ithaca, NY

- Bachelor of Science in Applied and Engineering Physics, honors track
- Coursework in electrical engineering, materials science, computer science, mathematics
- Minor in German
- Tutored engineering students in differential equations and linear algebra

2016-2022 University of California Santa Barbara Santa Barbara, CA

- PhD in Materials Science, focus: Electronic Materials.
- Coursework in electrical engineering and physics
- Teaching assistant for Mat. 209B: *High Resolution X-ray Diffraction for Thin-Film Characterization* (W2019, W2020, S2021), teaching labs for PhD students, writing & grading problem sets and exams and office hours

Research Experience

2016-2022 University of California Santa Barbara PhD Advisor: Shuji Nakamura

- PhD (Jan. 2022): *MOCVD Growth of Ultraviolet LEDs on sapphire and SiC substrates*
- Improved MOCVD AlN material quality by reducing dislocation density from 8×10^{8} cm^{-2} to 2×10^{8} cm^{-2}, improved n-$Al_{0.65}Ga_{0.35}N$ conductivity from 50 mΩ-cm to 7 mΩ-cm, and deep-UV LED efficiency from 2% to 10%
- Expertise in AlGaN MOCVD on foreign substrates and x-ray diffraction crystal quality analysis, materials characterization and deep-UV LED device design, fabrication, packaging, and testing
- Worked closely with staff on customization and modifications of high-T, low-pressure MOCVD reactor using trial-and-error and first-principles, with feedback from characterization data and UV LED results
- Trained over 20 PhD students in x-ray diffraction of epitaxial films, trained five PhD students in atomic force microscopy, photoluminescence, and LED device fabrication and characterization; tool manager for wire bonder and wafer polisher including training, troubleshooting, repair, and communication with vendors
- LED Packaging and Testing Lab co-manager, independently repaired and developed SOP for low-temperature optical characterization instrument including determining which parts were needed, purchasing from vendors and installing
- Contributed to strategic decision making in UV-LED project, including epitaxy and device design, selection of substrate, and acquisition of a new MOCVD system built for high-temperature, low-pressure AlN growth
- Over 2,000 hours cleanroom experience in AlGaN processing, incl. flip-chip wafer bonding and substrate removal

- Conceived and implemented a locally hosted Wiki for tracking methods and data within the research group

2014-2016 Cornell University

- 300 hours fabrication experience in Cornell Nanoscale Science/Technology Facility, MBE sample preparation
- PPMS magnetic and transport studies of microscale oxide thin films and heterostructures
- Helped repair and align a 4-circle XRD, including manually aligning beam, motors

Summer 2015 UCSB

- Improved solid-state synthesis yield of $Nd_2Ir_2O_7$ from 10% to 91%; measured possible emergent quantum effects

2012-2013 New Mexico State University, Las Cruces, NM

- Ellipsometry/Raman spectroscopy studies of $MgAl_2O_4$ spinel; research conducted at: NMSU; Sandia National Lab, CINT User Facility, Albuquerque, NM; NREL, Golden CO (Raman); J.A. Woollam Company, Lincoln, NE.

Honors, Awards, and Memberships

UC Santa Barbara

1. NSF Graduate Research Fellow
2. SSLEEC Outstanding Graduate Student Research Achievement Award (2017, 2019, 2021)
3. UCSB College of Engineering Regent's in Materials Fellow
4. Member: IEEE (Student and Young Professional), IEEE Photonics, DPG (German Physical Society), and IUVA

Cornell University

1. College of Engineering Dean's List 2013-2015
2. APS Minority Scholar
3. LSAMP Member
4. Support from J. A. Woollam Foundation

Leadership and Outreach Experience

Family Ultimate Science Exploration (FUSE) – UCSB, 80 hours
Volunteered as an instructor in physics talks, demonstrations, and hands-on labs for over 400 8th graders and families, targeted at increasing family engagement and discussion in science.

The Power of Light – UCSB, 20 hours
Led lab tours, held televised and print news interviews, and gave invited seminar talks to communicate the impact of our UV LED research on disinfection technologies during the COVID-19 pandemic. Helped establish personal connections with private donors, disinfection companies, and others interested in supporting our UV research at SSLEEC.

College Mentors for Kids – Cornell, 40 hours
Mentored local 2nd-3rd graders at weekly one-on-one and group activities to spark interest in science and introduce students to a college environment, encouraging future academic success.

Publications

1. Y. Yao, **C. J. Zollner**, M. Wang, M. Iza, J. S. Speck, S. P. DenBaars, S. Nakamura. *Design of hole injection superlattice layers for UV-C LEDs grown on sapphire substrates.* (accepted)
2. **C. J. Zollner**, J. S. Speck, S. P. DenBaars, S. Nakamura. *Germicidal ultraviolet LEDs: a review of applications and semiconductor technologies*. Semicond. Sci. Technol. **36** 123001 (2021). https://doi.org/10.1088/1361-6641/ac27e7
3. A. S. Almogbel, **C. J. Zollner**, B. K. SaifAddin, M. Iza, J. Wang, Y. Yao, M. Wang, H. Foronda, I. Prozheev, F. Tuomisto, A. Albadri, S. Nakamura, S. P. DenBaars, J. S. Speck. *Growth of highly conductive Al-rich AlGaN:Si with low group-III vacancy concentration*. AIP Advances 11, 095119 (2021). https://doi.org/10.1063/5.0066652
4. **C. J. Zollner**, Y. Yao, M. Wang, F. Wu, M. Iza, J. S. Speck, S. P. DenBaars, S. Nakamura. *Highly Conductive n-$Al_{0.65}Ga_{0.35}N$ Grown by MOCVD Using Low V/III Ratio.* Crystals 2021 11(8), 1006 https://doi.org/10.3390/cryst11081006
5. M. E. A. Samsudin, Y. Yusuf, N. Zainal, A. S. A. Bakar, **C. Zollner**, M. Iza, S. P. DenBaars. *Effect of nucleation layer thickness on reducing dislocation density in AlN layer for AlGaN-based UVC LED*. Microelectronics International (2021). DOI 10.1108/MI-02-2021-0012.
6. **C. J. Zollner**, A. Almogbel, Y. Yao, M. Wang, M. Iza, S. P. DenBaars, J. S. Speck, S. Nakamura. *Superlattice hole injection layers for GUV LEDs grown on SiC.* Opt. Mat. Exp. 10(9) 2171-2180 (2020). https://doi.org/10.1364/OME.398146
7. B. K. SaifAddin, A. S. Almogbel, **C. J. Zollner**, F. Wu, B. Bonef, M. Iza, S. Nakamura, S. P. DenBaars, J. S. Speck. *AlGaN Deep-Ultraviolet Light-Emitting Diodes Grown on SiC Substrates.* ACS Photonics 7(3), 554-561 (2020) https://dx.doi.org/10.1021/acsphotonics.9b00600
8. **C. J. Zollner**, A. Almogbel, B. K. SaifAddin, Y. Yao, F. Wu, M. Iza, S. P. DenBaars, J. S. Speck, S. Nakamura. *Reduced dislocation density and residual tension in AlN grown on SiC by MOCVD*. Appl. Phys. Lett. 115, 161101 (2019) https://doi.org/10.1063/1.5123623
9. P. B. Meisenheimer, R. Steinhardt, S. Zhuang, S. H. Sung, M. E. Nowakowski, S. Novakov, B. Prasad, **C. Zollner**, Z. Wang, N. M. Dawley, A. H. Hunter, S. Manipatruni, D. Nikonov, I. Young, L.Q. Chen, J. Bokor, R. Ramesh, R. Hovden, J.-M. Hu, D. G. Schlom, J. T. Heron, *Engineering new limits to magnetostriction through metastability in iron-gallium alloys.* Nature communications **12** 1-8 (2021). https://doi.org/10.1038/s41467-021-22793-x

10. B. K. SaifAddin, M. Iza, H. Foronda, A. Almogbel, **C. J. Zollner**, F. Wu, A. Alyamani, A. Albadri, S. Nakamura, S. P. DenBaars, J. S. Speck. *Impact of roughening density on the light extraction efficiency of thin-film flip-chip ultraviolet LEDs grown on SiC.* Op. Ex. **27** 16 (2019) https://doi.org/10.1364/OE.27.0A1074
11. B. K. SaifAddin, A. Almogbel, **C. J. Zollner**, H. Foronda, A. Alyamani, A. Albadri, M. Iza, S. Nakamura, S. P. DenBaars, J. S. Speck. *Fabrication Technology for high light-extraction ultraviolet thin-film flip-chip (UV TFFC) LEDs grown on SiC.* Semicond. Sci. Technol. **34** (2019) 035007; https://doi.org/10.1088/1361-6641/aaf58f
12. B. SaifAddin, **C. J. Zollner**, A. Almogbel, H. Foronda, F. Wu, et al. *Developments in AlGaN and UV-C LEDs grown on SiC*. Proc. SPIE 105541E (15 February 2018); https://doi.org/10.1117/12.2317660
13. H. M. Foronda, F. Wu, **C. Zollner**, M. E. Alif, B. Saifaddin, A. Almogbel, M. Iza, S. Nakamura, S. P. DenBaars, J. S. Speck: *Low threading dislocation density aluminum nitride on silicon carbide through the use of reduced temperature interlayers* J. Cryst. Growth 483 (2018) 134-139 https://doi.org/10.1016/j.jcrysgro.2017.11.027
14. J. K. Kawasaki, C. H. Kim, J. Nelson, S. Crisp, **C. J. Zollner**, E. Biegenwald, J. T. Heron, C. J. Fennie, D. G. Schlom, K. M. Shen, *Engineering Carrier Effective Masses in Ultrathin Quantum Wells of IrO_2.* Phys. Rev. Lett. 121 **17** 176802 (2018). https://doi.org/10.1103/PhysRevLett.121.176802
15. **C. J. Zollner**, T. I. Willett-Gies, S. Zollner, S. Choi: *Infrared to Vacuum-Ultraviolet Ellipsometry Studies of Spinel ($MgAl_2O_4$)* (2013) Thin Solid Films 571 689-694. http://dx.doi.org/10.1016/j.tsf.2013.11.141

Presentations

1. *UV LEDs Grown on SiC and sapphire substrates*
    a. PhD Defense Presentation, Santa Barbara, CA, January 2022
    b. SSLEEC Annual Review Conference, Santa Barbara, CA, November 2021
2. *Superlattice hole injection layers for GUV LEDs grown on SiC*
    a. SSLEEC Annual Review Conference, Santa Barbara, CA, November 2019
    b. UCSB-KACST Solid State Lighting Center Workshop, online, November 2020
3. *The Power of Light (UV LEDs for COVID-19 Disinfection)*
    a. KEYT video news interview, aired internationally, April 2020 https://keyt.com/news/top-stories/2020/04/17/ucsb-hoping-the-power-of-light-can-help-covid-19-fight/
    b. Speaker series seminar for building/operations managers through Gridium, Inc.
4. *Reduced dislocation density and residual tension in AlN grown on SiC by MOCVD*
    a. International Conference on Nitride Semiconductors (ICNS-13), Bellevue, WA, USA, July 2019
    b. Deutsche Physikalische Gesellschaft (DPG) Conference, Regensburg, Germany, April 2019
    c. The 2nd Swedish Terahertz Workshop, Linköping University, Sweden, March 2019
5. *Low threading dislocation density aluminum nitride: MOCVD on SiC and AlN substrates & high temperature annealing*
    a. SSLEEC Annual Review, November 2017.

6. *Engineering new limits to magnetostriction through metastability in iron-gallium alloys*
    a. Cornell Summer REU Undergraduate Symposium, August 2014.
    b. Cornell Physics Senior Research Symposium, November 2015.
    c. Physics and Chemistry of Surfaces and Interfaces (AVS) Conference, Santa Fe, NM, January 2016.
7. *Solid-State Synthesis of the Pyrochlore Iridate $Nd_2Ir_2O_7$ for Investigation of Novel Electronic Ground States*
    a. UCSB Undergraduate Summer Research Colloquium, August 2015.
8. *Infrared to Vacuum-Ultraviolet Ellipsometry Studies of Spinel ($MgAl_2O_4$)*
    a. AVS Chapter Meeting, Albuquerque New Mexico, May 2013.
    b. ICSE Conference, Kyoto, Japan, June 2013.
    c. Diversity in Scholarship and Engagement Symposium, Cornell University, September 2013.
    d. AVS Rio Grande Symposium, Albuquerque, NM, October 2013.
    e. ERN Conference, Washington DC, February 2014.

Patents

1. **C. J. Zollner**, J. S. Speck, S. P. DenBaars, S. Nakamura. *Fully transparent UV LED or far-UV LED.* Docket G&C 30794.0781USP1, Prepared by Gates & Cooper LLP (July 2020, pending PCT International)
2. V. Rienzi, **C. J. Zollner**, S. P. DenBaars, S. Nakamura. *III-nitride LED with UV emission by Auger carrier injection*. Docket 30794.0776WOU1, Prepared by Gates & Cooper LLP (May 2021, pending PCT International)
3. **C. J. Zollner**, S. P. DenBaars, S. Nakamura. *Multicolor III-nitride LED or Micro-LED Displays Using Wafer Bonding*. Docket 30794.0775USP1, Prepared by Gates & Cooper LLP (May 2020, pending)
4. A. Almogbel, B. Saifaddin, **C. Zollner**, M. Iza, *et al. Method for Fabricating Conductive Nitride Layers*. Docket 30794.0689USP1, Prepared by Gates & Cooper LLP (Aug 2018, provisional, unfiled)
5. **C. J. Zollner**, B. Saifaddin, A. Almogbel, M. Iza, S. P. DenBaars, J. S. Speck, S. Nakamura: *Method for the Fabrication of Electrically Conductive Layers* Docket 30794.0686-US-P1, Prepared by Gates & Cooper LLP (Jul 2018, PCT/US2019/042272, WO/2020/018709)
6. **C. J. Zollner**, M. Iza, S. P. DenBaars, J. S. Speck, S. Nakamura: *Method for Thermal Treatment of Semiconductor Layers with Reduced Evaporation* Docket 30794.663-US-P1, Prepared by Gates & Cooper LLP (Oct 2017, PCT/US2020/0243334A1, WO/2020/154674A1)
7. A. Almogbel, B. Saifaddin, **C. Zollner**, H. Foronda, M. Iza, S. P. DenBaars, J. S. Speck, S. Nakamura: *Method for Fabricating III-Nitride Layers* Docket 30794.660-US-P1, Prepared by Gates & Cooper LLP (Sept 2017, provisional, unfiled)

ABSTRACT

Ultraviolet Light Emitting Diodes Grown on Sapphire and Silicon Carbide Substrates

by

Christian J. Zollner

Germicidal ultraviolet (GUV) light with wavelengths between 250 nm and 300 nm was first discovered to have a strong disinfectant effect in the 19th century. GUV irradiation is a chemical-free, species-agnostic disinfection technology: some example applications include disinfection of medical equipment and buildings; municipal water treatment, residential water purification, and consumer devices like water bottles; air disinfection in offices, schools, planes, cruise ships, and retail spaces, and countless others. A low-cost, durable, portable, and efficient solid-state GUV light source could bring these disinfection applications to low-income and developing regions where most sewage enters waterways untreated, and the lack of sterile environments and equipment worsens healthcare outcomes.

The current incumbent technology for GUV light emission is the mercury lamp. This technology has remained largely unchanged for the past century—it is efficient and inexpensive, and has a large market in the form of phosphor-converted white light (“fluorescent lighting”). On the other hand, this technology relies on toxic mercury vapor contained within a hot quartz bulb, requires complex and inefficient driving electronics, and cannot be reliably dimmed or rapidly switched on/off. To meet growing demand for disinfection technologies, and for GUV to expand into residential, consumer, and smart applications, a solid-state GUV light emitter is needed. An efficient UV LED would have many benefits, much like the now-mature solid-state blue and white LEDs which have revolutionized the lighting and display industries. Semiconductor LEDs can be produced at smaller sizes, lower costs, higher efficiencies, and longer lifetimes than their 19th-century vapor lamp counterparts; these semiconductor devices can be dimmed or switched rapidly with no warm-up or flicker, and are readily produced in a variety of target wavelengths.

Currently available UV LED technologies based on the AlGaN materials system are much less efficient (3-5%) than Hg lamps (20-30%), due to a number of challenges related to AlGaN material quality, chemical purity, process technologies, and optical properties. Therefore, there is a strong desire to improve the efficiency, cost, and lifetime of UV emitters to match their visible LED counterparts, which have efficiencies well over 50% and lifetimes over 10,000 h. In this dissertation, I discuss the ways in which AlN and AlGaN defect density on foreign substrates has been greatly reduced using improved MOCVD growth methods, achieving a dislocation density of $2\text{x}10^8$ cm^{-2} on SiC. Next, I will explain why n-type and p-type doping (both of which are needed for LED operation) of AlGaN are challenging, and how both have been greatly improved using growth condition modification and polarization engineering, respectively. Using the methods outlined in this dissertation, we achieved n-type $Al_xGa_{1-x}N$ (x>0.65) resistivities below 10 mΩ-cm in material grown on three different substrate platforms (4H-SiC, 6H-SiC, and sapphire), and on two different MOCVD reactors. I will discuss active region engineering for increased light emission power, as well as an analysis of the various LED processing methods and packaging architectures used in the devices shown. Combining improvements in material quality, electrical conductivity, and optical quality, we have increased GUV LED external quantum efficiency from 2% to 10%.

Table of Contents

1 Introduction

1.1 Semiconductors

A semiconductor is a material that conducts electrical current (or doesn't) in a controllable way. Chemically pure semiconductors are often resistive but can be made conductive with the introduction of parts-per-million level impurities (dopants), with the strategic application of a voltage (as in a transistor), or under illumination (as in a photodiode).

Free electrons may have any energy. Within a crystal, electron energies are bound within certain bands. Each band can contain a finite number of electrons (per unit cell), so the bands fill in order of increasing energy as the number of electrons in a material increases. In a metal, there exists an energy band which is partially occupied (electrons in partially occupied bands can conduct electrical current readily), called the conduction band. In a band insulator there exists one energy band which is completely full, called the valence band, and another band above it which is unoccupied, called the conduction band. No partially occupied band exists, and therefore the insulator does not conduct electricity. A structurally perfect and chemically pure semiconductor is an insulator by this definition and is referred to as *intrinsic*.

The energy difference between the bottom of the conduction band and the top of the valence band is called the bandgap; it is closely related to the bond strength of neighboring atoms in the solid and is the most important physical property of a semiconductor. In insulators, the band gap is very large, whereas semiconductors usually have band gaps on the order of a few eV. A semiconductor's band gap is closely related to the feasibility for growth of high quality crystals (by way of the bond-strength dependence), and also determines the energy released when an electron transitions from the conduction band to the valence band. When this transition occurs via photon emission, the wavelength of the photon is determined by its energy, which is equal to the energy released by the electron transition, i.e. the band gap.

For a semiconductor to conduct electricity, a partially filled band must be created, either by the promotion of electrons into the conduction band (n-type conduction) or by the removal of electrons from the valence band (leaving behind positively charged holes, p-type conduction). In a field effect transistor, this might be achieved with the application of an electrical voltage to attract excess electrons into an accumulation region; in a photodiode, electrons are promoted from the valence band into the conduction band by the absorption of photons with energies above the bandgap energy.

Semiconductors can be made persistently conductive, n-type or p-type, with the addition of impurities. Heterovalent impurities (e.g. atoms that are just to the right or just to the left of the host atom they replace in the periodic table) add or remove a small fraction of one electron per unit cell, causing the conduction band to be slightly filled or the valence band to be partially emptied, and enabling electrical conduction. Defects with an extra electron and with states located close to the conduction band are called donors, because at finite temperatures some fraction of electrons populate the conduction band leading to n-type conduction. Likewise, defects with a missing electron located close to the valence band are called acceptors, because electrons from the valence band populate some of these states, leaving behind holes for p-type conduction[1]. Thus, as long as 1) the dopant energy levels are reasonably close to the semiconductor energy bands and 2) the materials technology for controlled doping is feasible, an insulator can be turned into a semiconductor.

---

[1] Formal definitions for those keeping score: donors are charge-neutral when electron-occupied and positively charged when unoccupied; acceptors are neutral when electron-unoccupied (hole-occupied), and negative when electron-occupied (hole-unoccupied).

1.2 Ultra-wide band gap semiconductors

The first commercially successful semiconductors had bandgaps on the order of 1 eV, wide enough to prevent unwanted conductivity at room temperature, but narrow enough to allow manipulation using voltages on the order of 1 V or less, and to enable efficient doping. The covalent bonds in these materials enabled high quality melt-grown crystals to be formed. Semiconductors with bandgaps on the order of 3 eV like SiC and GaN are more challenging to grow due to their stronger and more polar covalent bonds, and dopant atoms in these crystals produce energy levels further away from the semiconductor bands, reducing doping efficacy. However, the wide bandgaps of these materials enable excellent high-voltage performance and visible light emission (roughly 1.5 eV - 3 eV per photon). Since the 1990s, wide-bandgap semiconductor technology has progressed greatly, and now makes up a significant global market.

Semiconductors with band gaps above 5 eV are called ultrawide-bandgap semiconductors. The three most studied ultrawide gap semiconductors are gallium oxide, diamond, and aluminum nitride (AlN). These materials have very strong chemical bonds, affording them excellent mechanical and acoustic properties, making them physically and thermally resilient and reliably electrically insulating. For example, aluminum nitride has been used as a dielectric in the semiconductor industry for decades and is also an excellent piezoelectric material. Combining all these excellent dielectric properties with high-performance semiconducting properties would be a valuable proposition indeed.

AlN is the most technologically mature ultrawide gap semiconductor due to its close structural and chemical similarity to GaN. Like GaN, it can be doped n-type using silicon, and p-type using magnesium. It can be grown epitaxially with high structural quality, and its band gap is direct. By mixing the precursors for AlN and GaN together AlGaN is formed, a semiconductor alloy with properties smoothly varying between those of GaN and AlN. For instance, varying the $Al_xGa_{1-x}N$ composition, x, from zero to one changes the bandgap energy from 3.4 eV to 6.2 eV, covering the entire usable ultraviolet range from 380 nm to 200 nm [1], [2].

1.3 Ultraviolet LEDs based on AlGaN

Of particular interest is the alloy $Al_{0.5}Ga_{0.5}N$ (a 50/50 mixture of AlN and GaN in molar terms) with a band gap of 4.6 eV, corresponding to 270 nm photon emission. By epitaxially growing a multilayer structure of n-type $Al_{0.7}Ga_{0.3}N$:Si (70% AlN, 30% GaN), an active region with an $Al_{0.5}Ga_{0.5}N$ emitting layer, and a p-type structure such as $Al_{0.7}Ga_{0.3}N$:Mg, a UV-C emitting light emitting diode can be produced. This simple sounding recipe is nontrivial to achieve in practice. The device layers must have high crystal quality, meaning that they contain a low density of crystallographic defects, or deviations from the perfect AlGaN crystal structure. Point defects such as substitutional atoms or atomic vacancies and extended defects such as dislocations trap electrical carriers, diminishing both electrical and optical performance. Many of these layers must also have smooth interfaces and high conductivity.

With the application of an electrical bias voltage, electrons and holes are injected into the active region from the n- and p-sides, respectively, and recombination occurs. Recombination is the transition of an electron from the conduction band into an empty state (a hole) in the valence band. As mentioned above, recombination can be radiative, meaning that a photon is emitted. However, in the presence of defects in the active region, recombination can occur indirectly leading to non-radiative recombination. It is desirable to maximize the production of photons in the active region relative to the electron-hole-pair (ehp) supply in the active region, known as the radiative efficiency or internal quantum efficiency:

$$\mathrm{RE} = \mathrm{IQE} = \frac{\text{photons emitted by the active region per second}}{\text{electron} - \text{hole} - \text{pairs injected into the active region per second}}$$

Not all electron-hole recombination occurs in the active region. Especially in nitride deep-UV LEDs where n-type conduction is superior to p-type conduction, some of the electron current escapes or *overshoots* the active region, instead recombining with holes in the p-type region or being collected at the p-side metal contact. We define injection efficiency

$$\mathrm{IE} = \frac{\text{ehp recombining in active region}}{\text{ehp injected at metal contacts}} \approx 1 - \frac{\mathrm{J}_{n,p}}{\mathrm{J}_{\mathrm{total}}}$$

where $J_{n,p}$ is the electron current immediately above (to the p-side of) the active region, and J_{total} is the total current flowing through the device. The approximation corresponds to the assumption that hole overshoot into the n-side is zero. Taking the product of IQE and IE, we arrive total fraction of photons produced by the device relative to the total number of electrons injected at the ohmic contact[2]:

$$\mathrm{IQE} \times \mathrm{IE} \propto \frac{\text{optical emission rate (photons per second)}}{\text{electrical current (electrons per second)}}.$$

Further, the LED device should be transparent and designed to minimize internal reflections and absorption of the emitted light. As a rule, semiconductors with band gaps significantly above a given photon energy will be transparent to photons of that energy, hence

---

[2] There appear, to me, to be two different IQE conventions in the nitride LED literature. In this dissertation, IQE is defined to be the same as RE (equal to $\frac{Bn^2}{An+Bn^2+Cn^3}$), such that EQE=IQE*IE*LEE. There is another convention in which *IQE=RE*IE*, such that *EQE=IQE*LEE*. I have used the second convention in Refs. [32], [55] but have selected the first convention here to be in better agreement with the majority of the literature. Confusingly, in some contexts IE is assumed to be unity (perfect injection), making both conventions equivalent.

the choice of $Al_{0.7}Ga_{0.3}N$ doped layers for an $Al_{0.5}Ga_{0.5}N$ active region. The light extraction efficiency,

$$\mathrm{LEE} = \frac{\text{"useful" or "measured" light}}{\text{light emitted in active region}}\ ,$$

is a function of both the optical properties of the semiconductor layers, as well as the design and properties of the device packaging including metal contacts, mounting hardware, and encapsulation material.

The external quantum efficiency,

$$\mathrm{EQE} = \mathrm{IQE} \times \mathrm{IE} \times \mathrm{LEE}$$

is often reported among academic results as the most important figure of merit for UV LED devices; however EQE does not take into account electrical performance, i.e. how much energy is wasted in transporting the electrons and holes into the active region. This energy loss corresponds to a voltage (charge carriers with electrical charge, e, traversing a voltage difference Φ, dissipate an energy $e\Phi$, which is why carrier and photon energies are often reported in terms of the electron-volt, eV). Electrical efficiency,

$$\mathrm{EE} = \frac{\frac{hc}{\lambda}\ \text{[photon energy]}}{e\mathrm{V}_{\mathrm{diode}}\ \text{[electron energy]}}\,,$$

wherein h is Planck's constant, c is the speed of light, λ is the emission wavelength[3], and e is the charge of the electron, must be maximized in order to produce a device with optimal total

---

[3] Here and throughout this dissertation, the approximation of monochromatic light emission will be made for the sake of simplicity. Of course, real devices have some distribution of emitted power over a wavelength range, with a central or peak wavelength, λ. The errors introduced by this approximation are rarely significant, but the equations could be straightforwardly adapted to the case of a wavelength distribution. Unless otherwise stated, λ refers to the real-space wavelength, λ_0, of the light, whereas the wavelength in a medium will become λ_0/n where n is the refractive index of the material.

performance. For example, an LED emitting photons with energy 4.5 eV, operating at 9.0 V, has electrical efficiency 50%. Finally, we define the wall-plug efficiency

$$\mathrm{WPE} = \mathrm{EQE} \times \mathrm{EE} = \mathrm{IQE} \times \mathrm{IE} \times \mathrm{LEE} \times \mathrm{EE} = \frac{\mathrm{L}\ [\text{optical power out}]}{\mathrm{IV}_{\mathrm{diode}}\ [\text{electrical power in}]}$$

to represent the total power conversion efficiency of the device (this quantity is sometimes called PCE). Since all energy not emitted as light must inevitably turn into heat, maximizing WPE is crucial not only for energy savings, but also for device lifetime, thermal management, and reliability reasons. The current state of the art for commercial devices can be estimated as: IQE*IE=60%, VE≥80%, LEE≤10%, yielding WPE≤5%.

1.4 Challenges to UV LED development

The only known GUV-transparent semiconductor with n- and p-type conductivity is $\mathrm{Al}_x\mathrm{Ga}_{1-x}\mathrm{N}$. The properties of this semiconductor alloy can be tuned between those of GaN and AlN via the alloy fraction, x. It comprises nontoxic elements and can be produced at scale using metalorganic chemical vapor deposition (MOCVD). The bandgap remains direct throughout the alloy range, and the radiative lifetime is very short, providing excellent intrinsic optical emission properties [3]. Alloy composition and impurity concentrations are controllable using MOCVD, and atomically flat interfaces can be formed.

The fundamental LED performance metric of WPE can be increased in four ways: 1) lowering driving voltage, 2) increasing transparency and reflectivity of various components, 3) improving the injection of ehps into the active region, and 4) maximizing the radiative recombination rate while lowering the nonradiative. Some synergies exist: for instance, improving the conductivity of the p-type layer reduces excess voltage while improving injection efficiency. Unfortunately, many tradeoffs also exist: increasing the alloy fraction in the n-type $\mathrm{Al}_x\mathrm{Ga}_{1-x}\mathrm{N}$ layers improves optical transparency but also increases resistivity.

EQE is the most useful metric for evaluating research in which IQE and LEE are of interest, and VE is intentionally neglected, so the academic literature primarily reports EQE. To evaluate the readiness of UV LEDs for applications, EQE is not the most useful metric because it is difficult to compare on a systems-level, and with other UV lamp technologies[4]. Figure 1.1 summarizes the best reported WPE values from the literature. Commercially available GUV LEDs have WPE approaching 4%, whereas research results over 10% have been achieved through novel device designs. Plots similar to Figure 1.1 showing EQE [4] or IQE [5] have been reported elsewhere.

The technological challenges for achieving high WPE GUV LEDs can be divided into epitaxial growth and device fabrication. The most commercially successful method for epitaxial growth of nitride semiconductors is MOCVD, due to its relatively high growth rates and material quality. The precursor materials for MOCVD of AlGaN optoelectronics are trimethylaluminum (TMA), trimethylgallium (TMG), ammonia (NH_3), silane (SiH_4), and bis-cyclopentadienyl magnesium (Cp_2Mg). In some cases, triethylgallium (TEG), trimethylindium (TMI), and disilane (Si_2H_6) are used. The most popular substrate for all III-nitride optoelectronics research and commercial devices is sapphire, while other relevant substrate materials include bulk GaN and AlN, SiC, and Si.

---

[4] Consider a low-pressure Hg lamp operating at 30 W, 120 V and emitting 10 W of GUV flux at 254 nm (4.88 eV). This lamp has a WPE of 33%, but an EQE of over 800%. Eight photons are emitted for each injected high-voltage electron. Alternatively, consider a system of ten LEDs, each with EQE=10% and WPE=8%. Running in parallel, these LEDs form a system with WPE=8% and EQE=10%; wired in series, this system has WPE=8%, but EQE=100%.

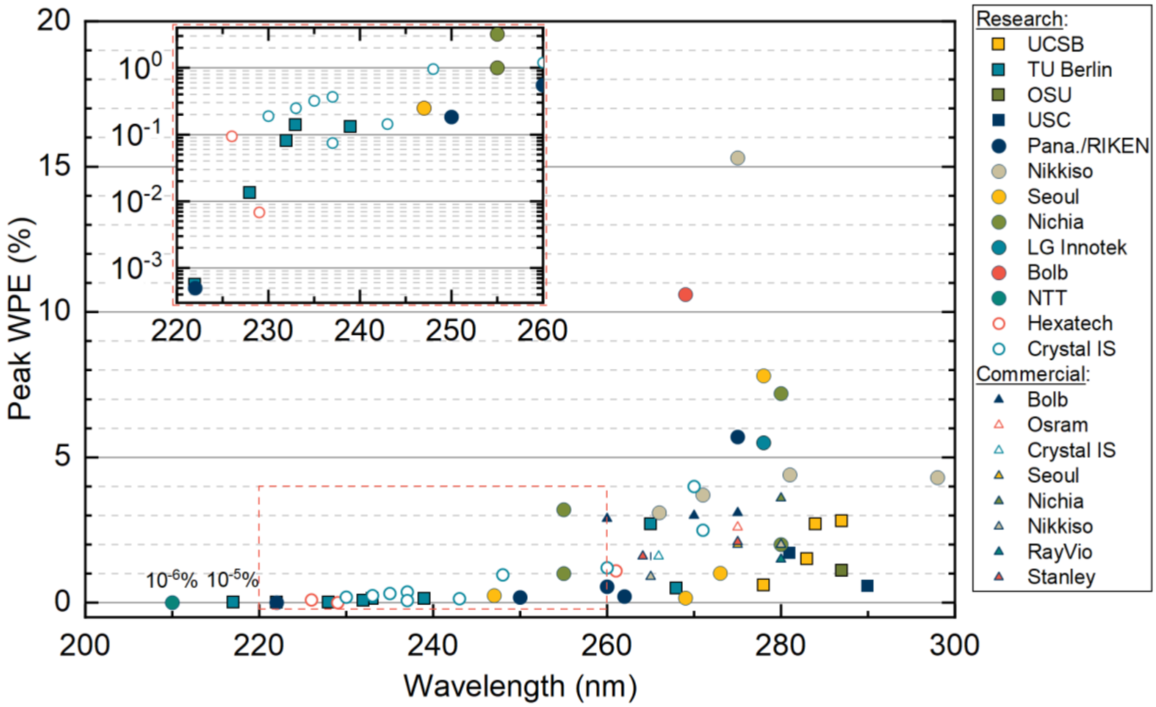

Figure 1.1: WPE for GUV LED research demonstrations and commercially available devices versus wavelength. WPE plotted as reported or calculated from reported voltage and wavelength. Publications reporting neither WPE nor voltage omitted. Academic results (squares) and research demonstrations from companies or partnerships between companies and universities (circles) show higher WPE than commercially available devices (triangles). GUV LEDs grown on bulk AlN wafers (open symbols) show similar WPE to GUV LEDs grown on foreign substrates (filled symbols). [6]–[41]

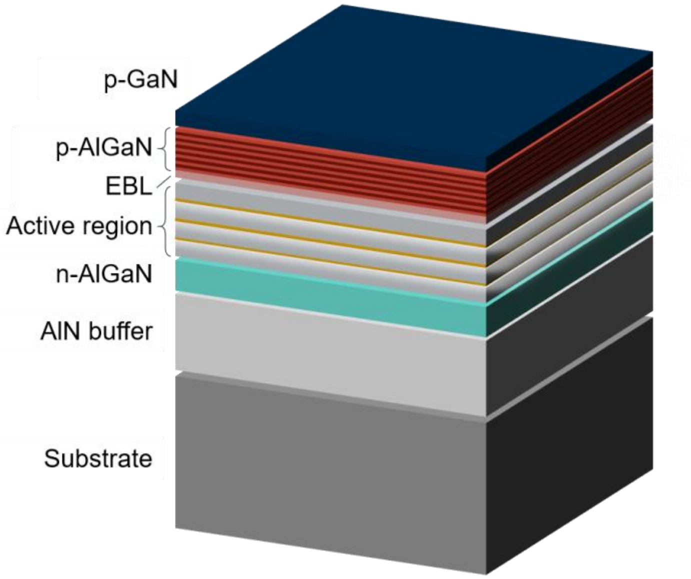

Figure 1.2: Epitaxial stack diagram for a typical UV-C LED grown on a sapphire wafer or free-standing AlN substrate. AlN buffer n-type AlGaN grown on the substrate, then the active region comprising barriers and wells. The p-side includes an EBL, p-AlGaN (typically a superlattice or a compositionally graded region). UV-LEDs contain a p-GaN contact layer for low voltage operation.

Figure 1.2 shows a diagram of the epitaxial stack of a typical UV LED. The substrate, AlN, and n-AlGaN are well understood and maturing technologies. The most important figures of merit are threading dislocation density and n-type conductivity, as well as film stress and smoothness. The active region comprises a multilayer stack of quantum wells and quantum barriers. The p-type AlGaN in modern devices usually comprises a superlattice (a stack of many thin layers of alternating alloy composition) or a compositionally graded region to enhance hole conduction. A p-GaN contact layer is used to provide adequate hole injection and low voltage, because it is impractical to make low-voltage conventional ohmic contacts directly to p-AlGaN.

2 Ultraviolet Disinfection

From the surface of a clear lake, there leaps suddenly a fish.

-Tibetan Poem

Nearly one third of the world’s population lacks access to clean drinking water [42]. In many developing regions, there is no incumbent disinfection technology for drinking, cooking, and bathing: water is either boiled or used as-collected from communal sources [43]. Diarrheal disease is the number one cause of death for children under 5 in the developing world, and the WHO estimates that *E. coli* alone accounts for one in four global cases of this disease. Every year, millions die from preventable, water-borne diseases, especially in the developing world [44] where 90% of all wastewater enters rivers and streams untreated and over 1 billion people completely lack access to sanitized water [45], [46]. There is a great need for a reliable, efficient, and low-cost technology for disinfection of water and medical equipment, especially in developing regions with limited or unreliable electrical infrastructure.

Nosocomial or healthcare-acquired infections (HAIs) are a major burden on healthcare costs and patient health outcomes. The World Health Organization lists delays and costs due to hospital equipment disinfection as a major limitation on access to life-saving surgeries in developing regions [47]. In the US, one out of 25 hospital admissions result in an HAI, leading to nearly 100 thousand deaths per year. Of these deaths, one in nine are attributable to drug-resistant Staphylococcus bacteria [48]. HAIs are the most common source of novel drug-resistant pathogens [49], which often escape the hospital to become community-spread pathogens. There is a strong incentive to reduce antibiotic drug use in treatment of HAIs, and to reduce the incidence of HAIs generally.

Water disinfection is the most quantitatively well-established case for UVGI implementation [50]. Chlorine, the current incumbent technology, leaches toxic and carcinogenic byproducts into the environment due to the interaction with various organic and manmade materials [51], [52]. Air disinfection using UVGI has been in use longer than water disinfection, but its efficacy is harder to quantify. The fastest-growing application of UVGI is surface disinfection. UV-C has also been shown to prolong the shelf life of meat, fruit, and other food products. UVGI emerged as one of the most promising methods for PPE disinfection [53], and commercial products for this purpose went into high volume production in 2020. For an up to date and comprehensive selection of research in the area of ultraviolet germicidal irradiation, readers are directed to the recent special issue in the Journal of Research of the National Institute of Standards and Technology [54], and to Ref. [55].

2.1 Germicidal Efficacy

The ultraviolet spectrum is conventionally broken down by wavelength into UV-A (315 nm - 400 nm), UV-B (280 nm - 315 nm), UV-C (200 nm - 280 nm), and vacuum-UV (10 nm - 200 nm). Solid-state light emitting devices throughout the UV-A, B, and C are anticipated to have many applications including horticulture, short-range communication, therapeutic applications, counterfeit currency detection, biosensing and other gas-phase sensing applications, and many others. All UV wavelengths have some photochemical effect [56], but UV germicidal efficacy is highest between 200 nm and 300 nm, defined as the GUV region. This may be further divided into far UV-C (200 nm – 225 nm, germicidal and potentially safe for humans, but difficult to generate) and conventional GUV (254 nm – 285 nm, strongly germicidal and easy to generate with lamps or LEDs, but unsafe for human eye and skin exposure).

UVGI is quantified by *dose*: the total GUV optical energy density incident upon the specimen (*not* the actual energy absorbed by the specimen). This energy density (mJ/cm^2) can be expressed as a product of intensity (mW/cm^2) and duration. A 2-log (99%) disinfection is considered sufficient for anti-bacterial surface disinfection, while 4-log (99.99%) is considered necessary in air and water applications [57]. More details on dose and rate constants are given in Ref. [55]. Data for the disinfection response to a given dose can be used to calculate the rate-constant, *k* (which can be thought of as a "susceptibility" or "germicidal efficacy").

Successful UVGI renders microorganisms unable to reproduce by effecting photochemical changes to their genetic material (plus other secondary effects). Genetic material (DNA and RNA) comprises long chains of nucleotide bases connected by a backbone. Upon GUV illumination, some pyrimidine bases (cytosine, thymine, and uracil) form double bonds to other nearby pyrimidines, leading to either *cross-linking* (if the nearby pyrimidine is on another strand of genetic material) or *dimerization* (if the nearby pyrimidine is a neighboring base on the same strand). Both cross-linking and dimerization lead to a reduction in replication ability, but pyrimidine dimerization is known to be the dominant mechanism of UVGI efficacy. The most important bases for this process are thymine in DNA, and its analog, uracil, in RNA [58]. The dominant wavelength for this photochemical pathway is around 265 nm, while others at 280 nm and below 240 nm may also be important [59], [60].

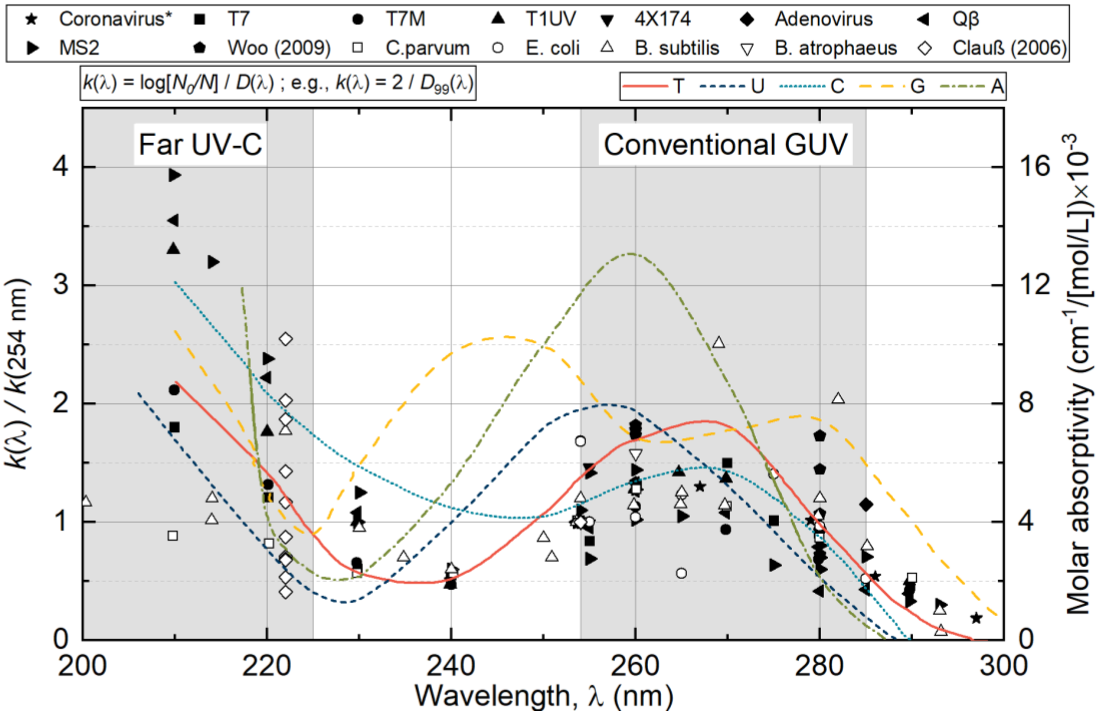

Figure 2.1: Wavelength dependence of germicidal efficacy. Rate constant (a measure of germicidal efficacy), *k*(λ), relative to *k*(254 nm) over the GUV region of 200 nm – 300 nm (symbols). Far UV-C (200 nm – 225 nm) and conventional GUV (254 nm – 285 nm) shaded. Data symbols for viral (filled) and other (open) pathogens by name, or by author for compilations [61]–[73]. Nucleotide base absorption spectra (curves) for pyrimidines: thymine, uracil, cytosine (T, U, C); and purines: guanine, adenine (G, A) in units of absorbance per molar concentration (cm^{-1}/M, or cm^{-1}/[mol/L]). Data from [74] normalized to estimated *k*(267 nm)/*k*(254 nm) ≈ 1.3 because no 254 nm reference was given. *Includes coronaviruses other than SARS-CoV-2.

2.2 Wavelength dependence of germicidal efficacy

The disinfection dose-response and reaction rates for some important pathogens are shown in Figure 2.1. [56], [74], [75], along with the absorption spectra of the nucleotide bases, in terms of the molar absorptivity (also called the molar attenuation coefficient). Molar absorptivity is a measure of the absorption of light by each species individually (so the total absorptivity of a solution is sum of the absorptivities of each component). The absorptivity spectrum of thymine matches the observed disinfection efficacy trends better than any commonly used fitting functions, rising to a maximum around 270 nm, then dipping to a minimum around 240 nm before rising steeply again in the far UV-C. Minimal germicidal efficacy is found at 240 nm, where thymine is least absorptive.

Some microorganisms, notably bacterial and fungal spores, have protection mechanisms like melanin that absorb UV light and prevent damage. These protection mechanisms can increase the required dose for disinfection by a factor of two. Many studies have shown a mixture of wavelengths to be more effective than monochromatic light for certain bacterial and fungal pathogens, related to strong protein absorption bands [60]. Deactivating enzymes responsible for repair mechanisms may enhance germicidal efficacy of some wavelengths, while other wavelengths may actually *enhance* photorepair mechanisms. Photodamage to enzymes is thought to be a broadband effect, as enzymes contribute little to the total absorption spectra. There have been a limited number of studies interrogating possible multi-wavelength synergistic effects using LEDs, but these theoretically predicted synergies have not yet been confirmed [65], [76]. Thus, a more comprehensive study of the wavelength response of pathogens including multi-wavelength synergy effects is needed (and UV LEDs are the only feasible technology to perform these experiments in a non-cost-prohibitive way.

The wavelength dependence of inactivation at the level of individual microorganisms also neglects other real-world considerations which may introduce additional wavelength dependence. For air disinfection applications, microorganisms are usually suspended in water droplets, leading to a droplet-size dependence due to scattering. For water disinfection, scattering effects can be significant when the microorganism size is comparable to the optical wavelength, as is the case for viruses.

2.3 GUV Light Sources

Around the middle of the 20th century, with the invention of germanium and silicon transistors, solid-state electronics began to replace vacuum tubes in amplification and digital computing. Shortly thereafter, with the development of the III-V compound semiconductors, solid-state light emitters quickly overtook vacuum tube and vapor lamp technologies for red and infrared wavelengths. Beginning around 1990, there has been a revolution in white lighting brought about by III-N-based solid-state light sources, which have mostly eliminated vacuum tubes, moving parts, and pressurized gases in illumination applications. The advantages of solid-state technologies over vacuum technologies include smaller size, lower power consumption, durability, reliability, lifetime, and lower cost. Light emitting diodes (LEDs) and laser diodes (LDs) already produce light at higher energy efficiencies than conventional lamp sources in the infrared, red, blue, and near-UV, and there are no fundamental physical reasons why this trend should not continue for solid-state deep-UV light sources.

Just as with the infrared and visible regions of the electromagnetic spectrum, there are a variety of light sources capable of producing GUV light, each with their own advantages and disadvantages. Recall the most important figure of merit for a light emitter: the wall-plug efficiency (WPE), or "energy efficiency," defined as

$$\mathrm{WPE} = \frac{\text{optical output power}}{\text{electrical driving power}} = \frac{P_{out}}{IV}$$

wherein the "output power" P_{out} is the useful radiant flux emitted by the light source, I is the electrical driving current, and V is the source voltage. In the case of AC-driven systems, time-averaged $\langle P_{\mathrm{out}} \rangle$ and $\langle IV \rangle$ are used (and there may be additional reactive losses). For broadband light sources, the *useful* radiant flux is defined as the integrated spectral radiant flux within the range of useful wavelengths: herein, the GUV.

Increasing LED WPE improves lifetime, increases power output per die, reduces cost per watt, reduces power consumption and operating temperature, and enables miniaturization, so it is considered the fundamental figure of merit from which all others are derived. Table 2-1 summarizes the important metrics for GUV light sources, along with two visible light sources for context, from manufacturers of the various light sources or Refs. [56], [77].

Table 2-1: Efficiency, power, cost, and other characteristics of the most important commercially available GUV light sources. LP Hg lamp data given for both conventional and cold-cathode (CC) varieties. Reference values for visible LEDs and compact fluorescent lamps are given as well, with radiant flux values based on visible light emission, rather than GUV. Blue LED *peak* WPE exceeds 60% (which is the operational WPE rated at 20 A/cm^2).

Source	GUV WPE	GUV radiant flux/device	Lifetime	Cost per watt of GUV output	Min. Size	Maximum efficiency	Effect of dimming/switching
UV LED	2-5%	5-50 mW	1,000-10,000h	\$100-\$400	<5 mm	Low power	Increases lifetime
MP Hg	15%	>10 W	10,000h	\$3	>10 cm	High power	Decreases lifetime
LP Hg	30-40%	1-20 W	10,000h	\$2	10 cm	High power	Decreases lifetime
LP Hg: CC	12%	1-2 W	20,000h	\$10	10 cm	Med. power	Little effect
Pulsed Xe	3%	10-30 W	100-1,000h	\$800	No	High power	Little effect
Excimer	1-2%	100-300 mW	4,000h	>\$1,000	10 cm	Low power	Increases lifetime
Blue LED	60%	0.1 W - 15 W	30,000-50,000h	\$1	<5 mm	Low power	Increases lifetime
White CFL	10%	1-10 W	10,000h	\$1-2	10-20cm	High power	Decreases lifetime

2.3.1 Mercury vapor lamps

Mercury vapor discharge lamps (Hg lamps) are efficient, reliable, and economical. The most common implementation of Hg lamps is in white lighting for general illumination, in which fluorescent phosphors down-convert the UV into white light. GUV Hg-lamps are similar to these "fluorescent" lamps, sans phosphor (in fact, many UV lamps can be directly installed in fixtures designed for fluorescent tubes, since the driving electronics and ballast are often identical).

Low-pressure (~10 torr) Hg vapor lamps (LP-Hg) predominantly emit at a single wavelength near 254 nm. The total WPE of a LP-Hg tube source is around 60%, with a useful GUV WPE of 50%. Driving electronics and ballast reduce system efficiency to below 40%. Medium pressure (~1000 torr) Hg vapor lamps (MP-Hg) have a similar total WPE to LP lamps, but have broadband emission including wavelengths outside the GUV, along with a number of sharp emission peaks between 250 nm and 340 nm, so their *useful* WPE is slightly lower.

All other GUV light emitter technologies besides Hg lamps and LEDs are inefficient and have small or highly specific niche applications, and are not described fully here. See Ref. [55] for a full description of the most important alternative GUV light sources.

2.3.2 GUV LEDs – the technology

UV LEDs are the fastest growing sector of GUV source technology. An LED is a device in which electrons are converted directly into photons by quantum-mechanical processes within a solid semiconductor (strictly, conduction-band electrons are converted into photons plus valence-band electrons). Unlike in the vapor lamp technologies discussed above, electrons are not accelerated to high excess energies to excite atomic transitions. Instead, in the ideal case, each electron is given (via a DC voltage) precisely the energy needed to produce a single photon of the desired wavelength.

An ideal light emitting diode can approach or even exceed 100% WPE [78]. LEDs emitting in the infrared and visible regions with peak WPE in excess of 80% are commonplace. Commercial GUV LEDs currently have efficiencies below 5%, with research results of 10-15% [6], [35], but this is expected to increase rapidly as technologies are improved.

From a system-wide efficiency perspective, the large size and non-directionality of Hg lamps mean that in almost all applications, much of the GUV light produced at the lamp is wasted. In the case of louvered upper-room air disinfection where the directionality of the GUV light emission is tightly controlled, current system efficiencies are around 5%. Because LEDs act approximately as point-sources, they can be combined with UV-transparent or reflective optical elements to produce precisely controlled directional emission with very little efficiency loss (this has been widely proven in visible LEDs, and recently demonstrated with UV LEDs including far UV-C LEDs [23]). Thus, even at a WPE of 5%, UV LEDs are already able to replace Hg lamp systems in certain applications.

2.3.3 GUV LEDs – the advantages

Like blue LEDs in white lighting applications, UV LEDs can be operated in parallel, generating high irradiance by combining the output of several devices. While large, high-power Hg lamps high may deliver a high average UV dose in an area, it is also important to consider dose uniformity. It is of no use if 90% of a space if fully sterilized, while the other 10% is shadowed and therefore unaffected. The total disinfection is still only 90%. In addition, very high doses near a single source maximize material degradation effects and safety risks. There is a benefit to distributing the UV power evenly throughout a space, among a wide array of small sources, rather than maximizing the power at a single source.

UV LEDs are unique among the commercially available GUV light sources in that they can be manufactured with a variety of emission wavelengths. Commercial devices with wavelengths down to about 250 nm are available, and research results in the academic literature include light emitters spanning nearly the full GUV range, down to 210 nm [1]. This wavelength tunability is considered a major advantage of UV LEDs. For instance, if the germicidal efficacy of a given pathogen of interest peaks at a particular wavelength, LEDs of that wavelength can be used for maximum efficiency. Or, a set of LEDs emitting at various wavelengths can be used to target multiple relevant germs, perhaps with some synergistic effects to prevent photorepair mechanisms [65], [76]. Particularly hazardous UV-B wavelengths can be suppressed, while safer far UV-C wavelengths are enhanced. This functionality is analogous to the "color mixing" used in visible LEDs, where fixtures can be set to a predetermined color or allow the color to be varied in real time.

LEDs can be dimmed and switched rapidly, so one of the fastest growing uses for GUV LEDs is in *smart* applications, combining these functionalities with occupancy sensors, flow meters, and microcontrollers. For example, point-of-use water purifiers using LEDs might switch on only when water is flowing or adjust power to match water flow rate. UVGI could interface with existing smart systems like climate control, plumbing, lighting, and others. Air and surface disinfection systems could be built into airplane cabins or hospital rooms, switching on between flights or after hours. Coupled with proximity sensors, such systems could detect when staff are nearby and locally switch off, dim to below the acceptable safe power value, or switch to a safer wavelength.

3 Aluminum nitride nucleation on foreign substrates

We can forgive a man for making a useful thing, so long as he does not admire it. The only excuse for making a useless thing is that one admires it intensely.

-Oscar Wilde

Sometimes it is tempting to try to produce perfect material with no defects, supposedly to perfectly match some predicted properties or achieve ultimate performance; but producing perfect material is costly and sometimes impossible. It is prudent to discern just how imperfect a material can be, while still providing desirable properties to be useful for devices. As it turns out, GaN optoelectronic devices have very high efficiency despite enormous defect densities, much higher than would be feasible in the conventional III-V materials. If it were not for this remarkable *defect tolerance*, it is unlikely that the solid-state lighting revolution would have ever occurred.

Crystal defects trap carriers at energy levels within the semiconductor band gap, leading to nonradiative Shockley-Read-Hall recombination. However, if the distance between nonradiative defects greatly exceeds the shorter of the two carrier diffusion lengths, then these carriers only “see” a nearly perfect local region, and radiative recombination can be highly efficient even in defective semiconductors[5] [79]. Thus, radiative efficiency is enhanced by 1) reducing carrier diffusion length in the active region, and 2) reducing the density of nonradiative defects. Hole diffusion lengths in the III-nitrides are much lower than in the

---

[5] In other words, the spatially-averaged nonradiative recombination rate is a function of both the recombination lifetime itself, and the effective carrier capture rate. For diffuse defects, the carrier capture rate is low.

conventional III-V semiconductors, greatly reducing the region of influence for any given nonradiative defect, and enabling much higher defect tolerance. It is therefore of value to reduce the density of defects[6] *just enough* that they do not greatly affect IQE, but one cannot expect that IQE will increase monotonically with decreasing defect density forever—eventually there will be diminishing returns.

Most point defects have limited room-temperature mobility in III-nitrides, so that they can be controlled locally during growth. That is, the point defect content in the active region depends, to first order, on the active region's growth conditions. Extended defects, on the other hand, propagate throughout many device layers, so that the growth conditions of each layer must be optimized in view of its effect on other layers. The extended defect content in a high-efficiency AlGaN-based active region is nearly independent of active region growth conditions, and depends much more on the AlN buffer layer.

The most important development enabling the GaN visible lighting revolution was the reduction of the *threading dislocation density* (TDD) in the nucleation layer. Threading dislocations are line-defects which propagate upward along the growth direction during epitaxial growth. In microstructural terms, dislocations can be thought of as the boundaries of missing (or extra) planes of atoms within a crystal lattice, or as the local distortions resulting from a row of atoms being displaced by a particular distance and direction. This displacement is called the Burgers vector. As dislocations are the boundaries of surfaces, they cannot terminate within a crystal.

---

[6] Some point defects are beneficial, most notably dopants! These are substitutional atomic point defects which are needed for device operation. I will refer to these intentional defects as dopants explicitly, and reserve the word defects for unintentional and/or detrimental ones. Unless otherwise noted, *defects* should be read as *unintentional defects*.

3.1 Review of Methods for AlN heteroepitaxy

The III-nitride semiconductors have strong covalent bonds with some ionic character[7], due primarily to the large electronegativity of nitrogen. Strong bonds afford the nitrides high breakdown electric fields and chemical and thermal stability, but also restrict wet etching methods and epitaxial growth quality. In the wurtzite nitrides, due to both strong bonds and hexagonal symmetry, there are no active slip systems for dislocation glide [80], so the primary form of relaxation of tensile stress is cracking [81].

Usually the preferred growth mode for semiconductor epitaxy is the step flow growth mechanism, named for the apparent motion of the atomic step-terrace structure across the sample surface as adatoms preferentially incorporate at the atomic step edges [82]. Step flow may proceed by many different pathways including Frank-van der Merwe growth (parallel steps or spirals without island formation), or Stranski-Krastonov growth in which small islands coexist with atomic step flow. In contrast, films grown with a large thermodynamic driving force, large mismatch, and low adatom mobility may exhibit Volmer-Weber island growth, in which stress-relaxed islands nucleate and grow due to the preferential incorporation of adatoms at the islands rather than at the heterointerface. Step flow growth is traditionally preferred due to finer control of composition, doping, and growth rates, and the greater barrier against dislocation generation in the planar geometry. The flat interfaces in this growth mode are preferred for many applications due to reduced optical scattering and carrier confinement.

In contrast to the conventional semiconductors, heteroepitaxy of III-nitrides benefits greatly from Volmer-Weber growth, in the following way. Due to the large structural and

---

[7] This is to say, the bonds are highly directional (leading to tetrahedral bonding and wurtzite/zincblende structures) and the valence electron density is high between neighboring atoms (covalent), *but* the electron density is pulled slightly toward the anion and away from the cation (ionicity) leading to a slight dipole moment within each unit cell.

chemical dissimilarity between GaN and all suitable foreign substrates, coherent Frank-van der Merwe nucleation is not feasible. Instead, low temperature MOCVD conditions are used to deposit a fully relaxed, highly disordered layer (LT-NL) via the Volmer-Weber mechanism—crystallographic coherency across the heterointerface is disrupted, however all lattice mismatch is accommodated. Next, the sample is heated to a high temperature (HT) and a second Volmer-Weber layer is deposited atop the first. The higher temperature enhances adatom mobility and large islands are formed, each of which is strain-relaxed and nearly structurally perfect. These islands grow and eventually coalesce into a planar film, with the slight tilt and twist misalignment of neighboring islands accommodated by threading dislocations of screw and edge character, respectively (in reality, most of the screw dislocation content exists in mixed dislocations, i.e. dislocations with screw and edge components).

Thus the threading dislocation density in the film depends primarily on the size of the Volmer-Weber islands deposited in the high-temperature nucleation layer step, and the degree of tilt and twist disorder in the islands [83]–[85]. The TDD in GaN grown this way is ~ 10^8 cm^{-2}, orders of magnitude lower than in a HT layer grown directly without LT-NL.

The chemical bonds in AlN are even stronger and more ionic than those in GaN. This leads to more pronounced spontaneous and piezoelectric polarization effects [86], reduced thermal expansion coefficient, and, most importantly, a reduced mobility of adsorbed precursor atoms during epitaxial growth [87]. The reduced mobility of aluminum precursor species in AlN epitaxy greatly reduce Volmer-Weber island size, and high TDD results [88].

Because dislocations cannot terminate within a crystal, here are the four approaches for reducing TDD in AlN (all of which have been demonstrated by us and in the literature with varying degrees of success):

1. *to reduce the total dislocation density formed at the nucleation layer initially*

2. *to enhance the formation of dislocation loops or half-loops*
3. *to produce free surfaces where the dislocations generated at nucleation might terminate*
4. *to create conditions in which dislocations can move freely to mutually fuse and annihilate*

The optimization of AlN nucleation conditions began with (*1*), via the enhancement of aluminum precursor mobility by increasing the growth temperature, with some studies using temperatures as high as 1600 °C [89], [90]. These early studies showed straightforward trends of improved surface smoothness, reduced TDD, and reduced impurity incorporation with increasing AlN growth temperature (after initial nucleation at reduced temperature) [91].

The second method used to enhance Al adatom mobility was the reduction of the ammonia supply. Active nitrogen is the excess species in AlN and GaN growth, so NH_3 flow can used to control the driving force for crystallization while also directly affecting the supersaturation of cation atoms on the growth surface[8]. When a slight surplus of group III precursor atoms are present on the growth surface, adatoms can move across the surface with a reduced diffusion barrier, at the risk of droplet formation or reduced crystal quality due to low driving force [92]. Increased NH_3 flow (increased thermodynamic driving force for crystallization) tends to increase AlN crystal quality at the expense of surface smoothness, while reduced NH_3 (metal-richer condition with a higher expected surface occupancy of group

---

[8] In CVD growth, the precursor partial pressures are determined by the total pressure and the molar precursor flow fractions. At the epitaxial surface, precursors are consumed and the partial pressure reduces to the vapor pressure of the solid crystal (In MOCVD growth, the vapor pressure is smaller than the precursor pressures, but it is not zero. *I.e.*, growth and etch are occurring simultaneously, with changes in reactor conditions causing the system to move in either direction. In this sense the growth is *close to equilibrium*.). In order to produce crystals with high quality, a strong thermodynamic driving force is needed, so a high supersaturation of precursor is needed at the crystal surface. If both precursors are introduced in a stoichiometric ratio, both partial pressures go to zero at the crystal surface and the driving force is small. On the other hand, if one precursor is used in excess, the partial pressure of that precursor remains high even at the sample surface; thus, the concentration of the excess species can be used to control the thermodynamic driving force for crystallization. An excess of metal (group III) leads to metal droplet formation, poor crystal quality, and increased defect densities. An excess of group V elements does not have this problem, and III-V semiconductors are grown with molar V/III ratios much greater than unity.

III adatoms) produces smooth step-flow conditions. In order to reduce the effective NH_3 flow without greatly degrading crystal quality, many research groups used pulsed-flow schemes in which the NH_3 flow is alternately turned on and off [55], creating momentary Al-rich conditions for enhanced precursor mobility in alternation with NH_3-rich conditions for efficient and coherent crystal growth [86] without inversion domain formation. This approach was used to produce the first high-efficiency UV-C LEDs in 2012 [15], [93].

Even at conventional MOCVD temperatures, but especially at the elevated temperatures used for AlGaN growth, trimethylaluminum (TMA) and ammonia (NH_3) are somewhat reactive in the gas phase. Gas-phase pre-reactions must be carefully controlled to avoid parasitic reactions and the formation of *adducts,* solid-phase byproducts of parasitic pre-reactions, which can degrade reactor performance, reduce precursor usage efficiency, and deposit debris on the wafer and reactor components.

AlN and AlGaN are therefore usually grown at reduced reactor pressures, on the order of 5-20 kPa or about one tenth of atmospheric pressure[9], which reduces the effect of pre-reactions. Thus, while the effective V/III ratio (the V/III ratio near the wafer surface[10], after

---

[9] A quick aside: one question which came up during my PhD was whether the gas pressure exiting the gas injection channel or nozzle could be assumed to be precisely that of the MOCVD chamber as a whole (it acts as a "free" gas flow), or whether the pressure at the moment the gas enters the flow channel is closer to that of the gas lines (held slightly above atmospheric pressure), indicative of a "duct"-like flow pattern in which the pressure reduces gradually throughout the duct. This matters because the pressure at the moment the gases mix is what determines whether pre-reactions will dominate.

At first glance, we can note that the gas velocities in all cases are well below Ma = 0.3, so we expect the incompressible approximation to hold. Gas velocity would need to be quite high in order to result in the compressible flow dynamics needed to sustain a pressure ratio above 2:1 within the flow channel duct. As a result, "*jet exit pressure equals atmospheric pressure.*" So, we can simply use the ideal gas law, $P = \rho RT$, to find the gas velocity at various pressures: $[\rho \cdot Area \cdot Velocity]_{in} = [\rho \cdot Area \cdot Velocity]_{out}$.

This result can be checked by setting the problem up using the Reynolds Transport Theorem and adiabatic sonic-point approach to determine what the duct geometry *would need to be* to support a large pressure differential. This is left as an exercise (See: *Fluid Mechanics*, F. M. White, 7th edition (2011), Ch. 3 and 9), but I believe the full solution illustrates that the gases immediately take on the MOCVD chamber pressure as soon as they exit the supply lines.

[10] At the top of the boundary layer

some TMA has been depleted) is decreased by pre-reactions, low pressures allow this effect to be reduced while growth rates are enhanced, and impurity incorporation reduced [87]. On the other hand, low growth pressures reduce the aluminum adatom mobility, perhaps because the supersaturation (in partial pressure terms) of Al is reduced. As will be discussed below, AlN nucleation layers are greatly improved when grown at slightly elevated pressures (up to 40 kPa), where enhanced Al mobility can be achieved without resorting to extremely low V/III ratios.

Precursor mobility is higher for gallium than it is for aluminum (and higher still for indium) due to the weaker bond strengths of these cations in III-N crystals. Thus, effective Al mobility can be enhanced with the introduction of even modest quantities of Ga [94], [95]. However, this approach has not been used successfully to produce AlGaN alloy nucleation layers, likely due to the formation of subpopulations of pure AlN and GaN islands rather than AlGaN islands.

Threading dislocations rarely propagate perfectly vertically. Dislocations in crystals have associated strain fields, which carry with them an elastic energy per unit dislocation length. If a dislocation is free to deform into any shape, it will tend toward being a straight line so that elastic strain energy is minimized, a tendency which is often described by analogy as a tension force along the dislocation line. More generally: if free to move, dislocations can do work by moving or deforming so as to reduce the strain energy of the crystal. The energy reduction per unit distance of motion is formalized as a force, called the Peach-Koehler force:

$$f_k = (\sigma_{iu} b_u)\zeta_j \epsilon_{ijk}$$

where ζ_j is the line vector of the dislocation and ε_{ijk} is the Levi-Civita symbol [96]. For instance, a vertically directed edge type dislocation with nonzero ζ_z and b_x, is subject to a force:

$$f_y = -\sigma_{xx} b_x \zeta_z.$$

Dislocations with similar strain fields (their Burgers vectors have a positive dot product) feel a repulsive Peach-Koehler force as their associated strain fields add to increase the total strain energy. Dislocations with opposing strain fields (Burgers vector dot product is negative) feel an attractive force as their strain fields cancel. If two dislocation lines come into contact with one another, a dislocation with Burgers vector equal to the sum of the Burgers vectors of the two contacting dislocations results—if the contacting dislocations have equal and opposite Burgers vectors, they mutually annihilate. Fusion and annihilation reactions result in reduced dislocation densities in nitride films if dislocations are either free to move (in *c*-plane growth of wurtzite films, glide is negligible and dislocation motion does not occur at moderate MOCVD temperatures) or free to grow at an inclined angle off the vertical growth direction. When inclined dislocations fuse or annihilate, dislocation half-loops can be formed.

AlN films are often grown to thicknesses between 1 μm and 4 μm to achieve reduced dislocation density via dislocation fusion and annihilation reactions (method *(2)*). These thick AlN films act as the foundation for subsequent device layer growth, and are referred to as *buffer layers* or *templates*. The downside to growing thick films (besides long growth durations) is the risk of cracking, which occurs in thick films under tension when no other stress relief mechanism is available.

Dislocation inclination in AlN can be enhanced using optimization of growth conditions [2]. However, the growth conditions which enhance TD inclination (reduced temperature, reduced V/III ratio, increased pressure) do not necessarily lead to optimal morphology and film stress (which tend to be optimal under high temperature, increased V/III, and reduced pressure conditions). To combine both beneficial conditions, multilayer stacks have been implemented by many researchers, as summarized in our publication on reduced temperature interlayers [97]. Silicon doping is also well understood to enhance dislocation inclination in AlGaN and AlN [55], leading to both dislocation reduction and generation of a stress gradient from compression towards tension [98].

There has been some success in the use of lateral overgrowth of AlN. In this approach (method (*3)*), voids or trenches are lithographically patterned on a previously grown AlN template, and then the sample is put back in the MOCVD for a regrowth. Dislocations near the edges of the patterned regrowth columns are attracted to the free surfaces, where many of them annihilate. Furthermore, because the remaining dislocations grow nearly vertically, the "wing" regions above the voids (where AlN grows laterally) are nearly dislocation free. Using this method, some groups were able to achieve very low TDDs, even into the 10^7 cm^{-2} range.

Finally, as will be discussed below, high temperature annealing of AlN films (above 1700 °C) can be used to enable dislocation climb, allowing dislocation motion under Peach-Koehler forces *(4)* leading to fusion and annihilation reactions, as well as motion toward free surfaces where dislocations annihilate.

3.2 AlN on SiC substrates

The vast majority of InGaN and AlGaN LEDs are grown on sapphire substrates. Sapphire is a low-cost, optically transparent, and thermally/mechanically/chemically robust material. GaN/sapphire with dislocation densities below 10^8 cm^{-2} can be routinely produced. However, for the reasons discussed in the previous section, AlN/sapphire growth is more challenging than GaN/sapphire, and only in the past few years has AlN/sapphire epi appeared on the commercial market with decent quality.

Silicon carbide, the original wide-bandgap semiconductor [99]–[102], has mature wafer-growth and processing technologies. Large-area wafer substrates are commercially available for a cost slightly higher than sapphire, but well below AlN. Unlike sapphire (corundum, trigonal R3c), a nonpolar oxide insulator with highly dissimilar crystal structure and lattice parameters to AlN (wurtzite, hexagonal $P6_3mc$), SiC ($P6_3mc$) is a polar semiconductor with only about a 1% in-plane lattice mismatch to AlN. The polar nature of the SiC structure has been observed to prevent the unwanted nucleation of N-polar III-nitride films on the SiC Si-face, whereas growth on sapphire may produce unwanted inversion domains under some growth conditions [103]–[106]. In principle, this closer structural and chemical similarity with the III-nitride system ought to make SiC an ideal foreign substrate for AlN growth. SiC is optically absorbing in the deep-UV and therefore must be removed during UV LED device processing; but, as I will discuss in a later Chapter 8, this is not as great a disadvantage as it may seem.

Recall that, for high-quality nitride heteroepitaxy, a population of nearly perfectly crystalline islands with limited tilt and twist disorder is needed to achieve low dislocation density. On SiC, it was predicted that the low-temperature nucleation layer could be foregone, and that large well-aligned islands could be grown directly on the SiC surface [88], [107]. In particular, the expectation was that the structural and chemical similarity between SiC and AlN would enable a comparatively low energetic barrier to island growth, by way of enhanced Al mobility on the SiC surface and/or a reduced energetic barrier to the formation of the AlN/SiC atomic interface.

In practice, low-TDD AlN/SiC was not achieved for many decades. It seems there are additional constraints on island size, and mechanisms for TD formation which we have not yet considered. Firstly, island size can be limited by substrate surface morphology. The mechanically polished substrates available from most manufacturers throughout the 1990s and 2000s were rough, greatly increasing the density of island nuclei on the surface at the initial stages of AlN growth. The surface could be improved by high temperature etching of the substrates under such harsh conditions as propane, hydrochloric acid, or hydrogen, at high temperatures [107]–[112]. Fortunately, SiC technologies continued to improve as a result of the material's applications in power and high-speed electronics, and atomically flat substrates (chemo-mechanically polished, and presumably also annealed/gas treated, although the details of the process are proprietary) are now readily available in large wafer diameters from manufacturers such as CREE.

On atomically flat SiC, a second constraint on island size arises. Wurtzite crystals (III-nitrides, SiC) comprise stacked monolayers of atoms, which can be positioned in one of three sites, called A, B, and C. Because the 4H (ABCB)—and in some cases 6H (ABCACB) [113]—SiC stacking sequence differs from that of 2H (ABAB) AlN, it has been predicted[114] that stacking mismatch may form dislocations in nitride/SiC epitaxy. On both SiC and AlN surfaces, the monolayer (i.e. half-unit cell for 2H, quarter-unit cell for 4H, etc.) step is the most common in nearly-on-axis step-terrace surfaces. Therefore, AlN islands nucleating on SiC terraces will be out of crystallographic registry by a displacement vector equal to one SiC monolayer (in the *c*-direction). When islands from neighboring terraces are in close vicinity, this *stacking mismatch boundary* results in an energetic barrier to coalescence. An anisotropic island size limitation thus appears, and films coalesce upon each terrace long before coalescing across steps. These stacking mismatch boundaries result in dislocation formation at step edges [113], [115], [116]. The effects of stacking mismatch can be greatly reduced if the substrate is prepared in such a way as to have half- (or better yet, full-) unit cell step heights, so that the difference in stacking sequence between AlN and SiC is obscured.[88] This was achieved using a variety of pre-growth treatments such as high temperature annealing under hydrogen gas flow, producing smooth or even atomically flat surfaces [117], and greatly improving nucleation conditions [95], [97], [113], [118]–[122].

Finally, there is one other important potential TD generation mechanism present in AlN/SiC nucleation which is not relevant in AlN/sapphire growth. Because of the 1% lattice mismatch between AlN and SiC, it is possible for a finite thickness of AlN to nucleate coherently on SiC (that is, the AlN *a*-parameter shrinks to match that of SiC, leading to a compressively strained film). After a critical thickness is grown, misfit dislocation networks may form, leading to stress relaxation[11]. These misfit dislocations may bend upward upon island coalescence, turning into threading dislocations of edge character. There are few reports of coherently strained (or nearly coherently strained) AlN/SiC nucleation, and little evidence of misfit dislocation networks until very recently, as will be discussed later in this chapter.

3.3 Early work on AlN

As discussed by Dr. Foronda in Ref. [97], MOCVD growth conditions were found to be very important for producing high-quality AlN material. In particular, we found that the optimal growth conditions for the initial nucleation of AlN on SiC were not necessarily the same as the growth conditions needed for subsequent growth of thick buffers at higher growth rates. The difference in growth conditions also led to significant differences in morphology, so that we were later able to troubleshoot reactor drift by correcting for morphology as measured

---

[11] This is essentially a statement that, while the AlN/SiC mismatch is much smaller than AlN/sapphire, it is not zero. On sapphire, an extremely high TDD is formed in the LT-NL, then overgrown and buried. In AlN/SiC, the LT-NL is not used, so some (smaller number of) TDs remain and propagate into the film.

by AFM. For example, reactor temperature drifts could be diagnosed using the reference AFM images shown in Figure 3.1.The details of the correlation between surface morphology and threading dislocation density reduction are given in both Foronda's original work [97] on mechanically polished SiC of both 4H and 6H polytype, as well as our follow up work [123] on chemomechanically polished 4H SiC purchased from CREE.

Figure 3.2 shows more detailed images of the "3D" spiral island morphology typical of AlN growth at reduced temperatures. Although the surface morphology does not have a unidirectional step flow orientation, it is still consistent with a step flow growth mode. Dislocations with screw components can be observed at the apex of most hillocks, indicated by the termination of atomic steps.

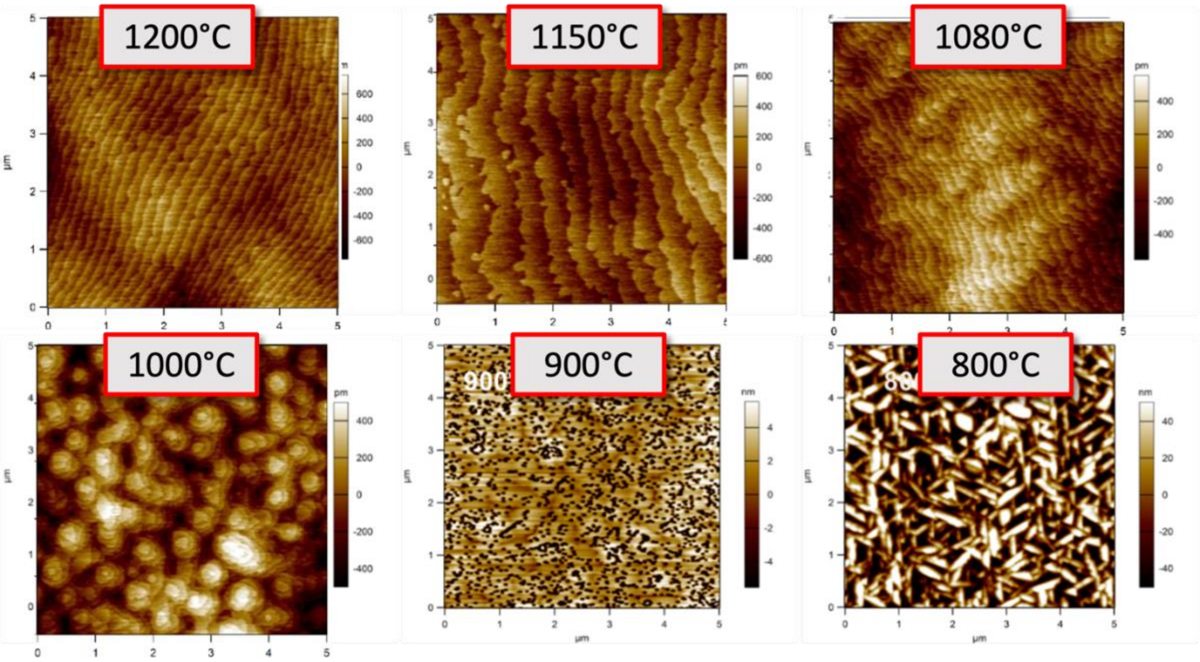

Figure 3.1: AFM of AlN versus temperature. As reactor temperature is decreased, AlN morphology changes from a smooth "2D" step-terrace structure (1200 °C), to a "3D" morphology with small islands a few unit-cells high (1000 °C) to a rough and low-quality structure below 900 °C. Temperatures measured using thermocouple on the older TNSC reactor, which reads about 150 °C lower than the new reactor used beginning in 2019.

Under low V/III conditions, the islands have a smoothly curved appearance; under higher V/III conditions (stronger driving force for crystal facet formation), islands have a crystallographically oriented triangular appearance and dislocation-related pits are no longer visible [124], [125]. The orientation of the triangular features in alternating directions is indicative of the half-unit cell height of the atomic steps; each half-unit cell (monolayer) has 3-fold symmetry, and the alternation between monolayers forms the overall 6_3 glide symmetry of the wurtzite structure.

We found that the MOCVD reactor used for these initial AlN growths produced high quality material but was not perfectly reliable. Over time, quartz reactor were coated up by parasitic pre-reactions, altering the thermal emissivity of these components and perhaps changing the effective substrate temperature during growth. Throughout the coating process, the molar efficiency of precursors changed from one growth to next. As shown in Figure 3.3, the quality of AlN material degraded over time, unless a "coating" run (such as a typical UV LED growth recipe) was performed daily (costly and time consuming because this reactor did not have an auto-cassette loading mechanism). SIMS measurements (data not shown) indicated a strong correlation between carbon impurity concentration and reduced material quality, indicating that a reactor coating or seasoning effect from coating may have been the reason for this trend. Thus, our options were essentially either to clean the reactor before every growth, or to grow a full LED stack before every run, neither of which were considered optimal.

In late 2018, the decision was made to switch to a new MOCVD reactor design, similar to the designs used in the other MOCVD reactors at UCSB for visible LED and LD research. This reactor was installed and then customized for high temperature and low pressure operation, and also featured an auto-loading cassette system for multiple unattended runs.

Initial experimental optimization shown in Figure 3.4 indicated that the optimal setpoint temperatures and precursor flow values were different. This is to be expected due to the different heater configuration and reactor size. Nonetheless, the qualitative trends in the most crucial parameters such as 3D (reduced temperature) temperature and 2D (high temperature) ammonia flow remained the same.

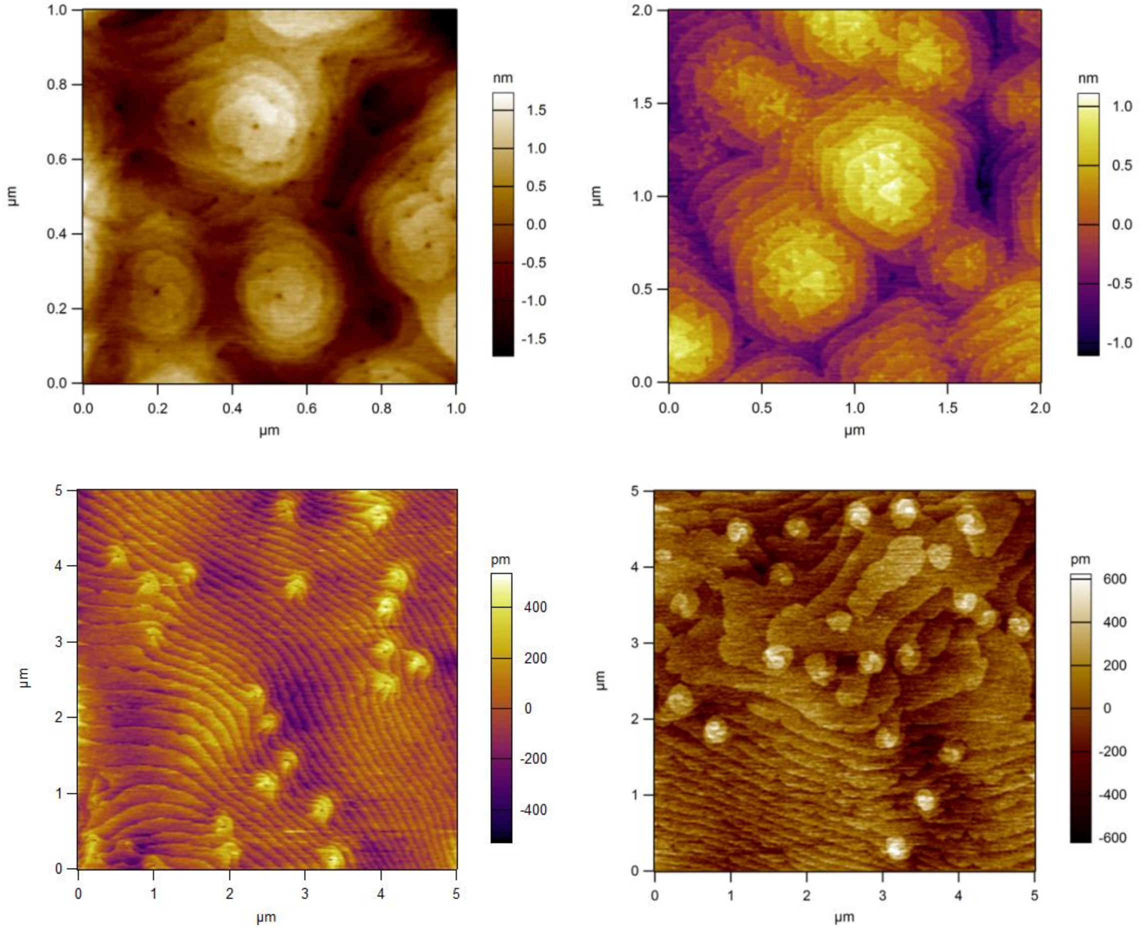

Figure 3.2: Magnified images of “3D” reduced temperature AlN layers grown on SiC showing the atomic step structure of these layers, and indicating that they are likely growing in a step-flow mode. The two upper images are of films grown under reduced temperature conditions, with low V/III ratio (left) and high V/III ratio (right). The two lower images were grown under intermediate temperatures (between the high temperature and reduced temperature condition), showing a mix of lateral and spiral step flow modes.

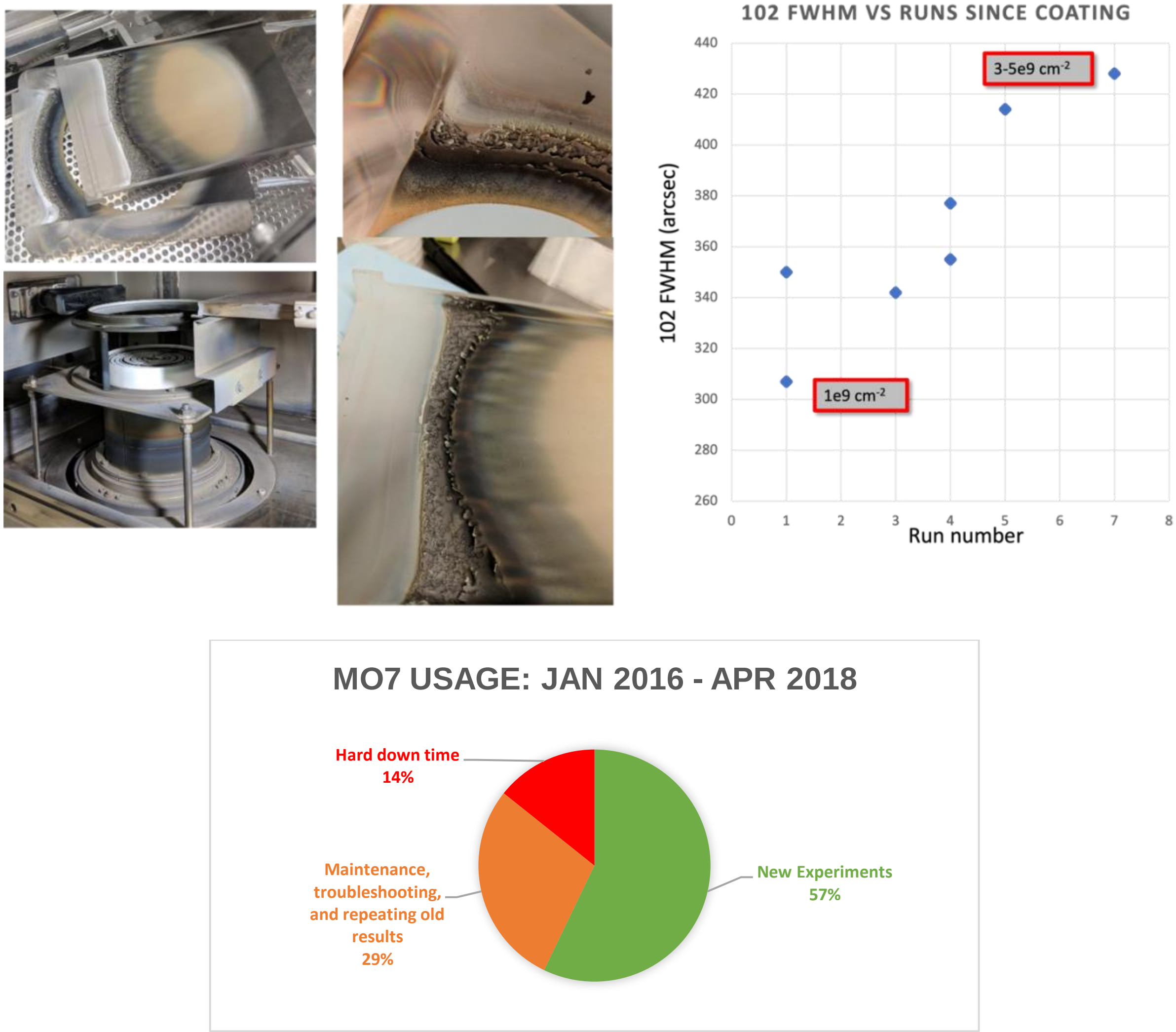

Figure 3.3: MOCVD reactor issues. **Top left**: images of quartz hardware after about 1-2 weeks of MOCVD growth, showing significant deposition of pre-reaction byproducts. **Top right**: plot of AlN (102) rocking curve FWHM over time, showing degradation of reactor performance even with repetitions of the same growth recipe. **Lower**: chart of reactor down-time caused by hardware issues and extended reactor recovery needed following each maintenance.

AFM studies of the initial reduced temperature nucleation layer grown at a very low pressure of 10 kPa showed a morphology which had not been previously observed, as shown in Figure 3.5. For reasons mostly related to supplier difficulties, we changed our SiC wafer type from a mechanically polished wafer type to a chemo-mechanically polished wafer type which was atomically flat and had a clear step-terrace structure (more details on these substrates will be given in the next section). As a result, we observed 3D nucleation islands aligned along the SiC atomic steps. As discussed in the previous section, this is explained by the energetically unfavorable coalescence of islands across 4H monolayer step edges. As the 3D layer was grown to greater thicknesses, trenches remained.

Growths performed at greatly reduced growth rates of 0.5 Å/s showed that even as the 3D nucleation layer was made much smoother, and completely coalesced into a planar film within the SiC atomic step terraces, the trenches at step edges remained. The only growth condition found to give fully coalesced AlN layers under reduced temperature conditions was a pulsed-NH_3 growth mode. The pulsed NH_3 mode enabled significantly higher lateral growth rates due to high Al adatom mobility and reduced crystallization driving force, but it did not result in high crystal quality. Notably, unlike the previous experiments on the old reactor,

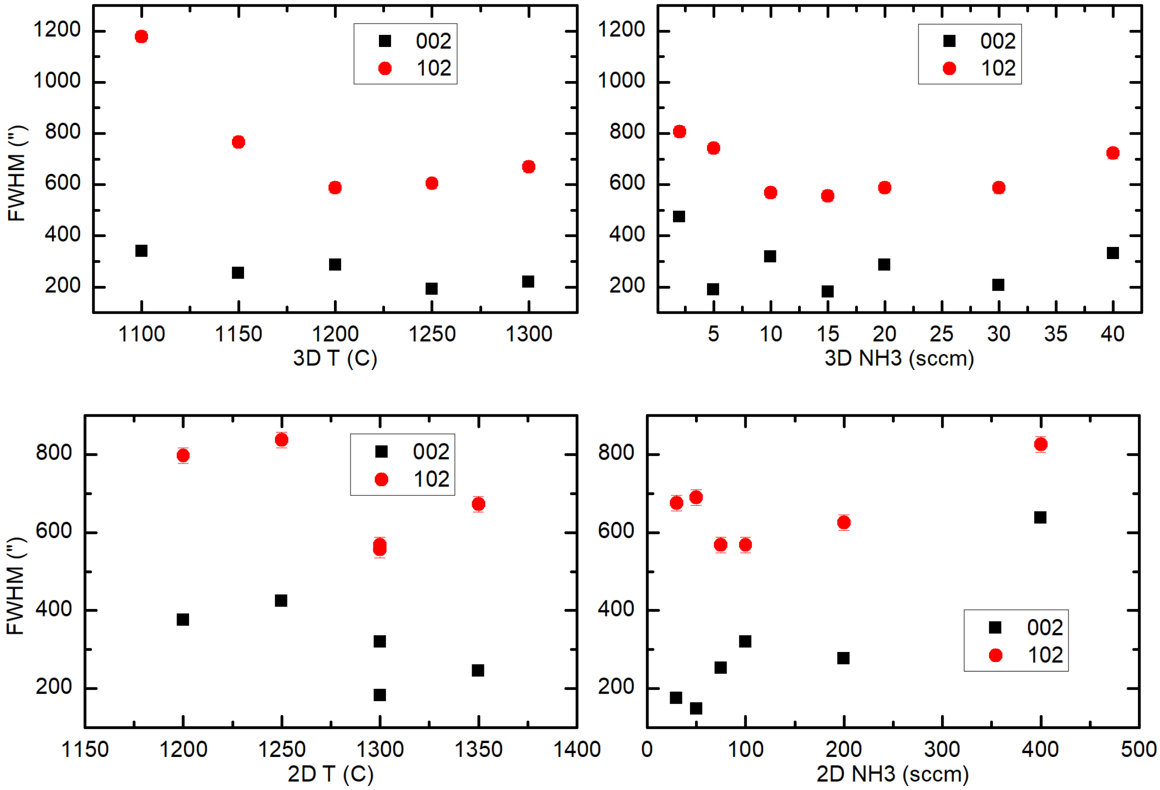

Figure 3.4: AlN temperature and ammonia flow optimization. While specific optimized values differed from those found on the previous reactor, the overall trends were similar. Crucially, the nucleation layer was found to have an optimal growth temperature, with films grown under very high nucleation temperatures having lower quality.

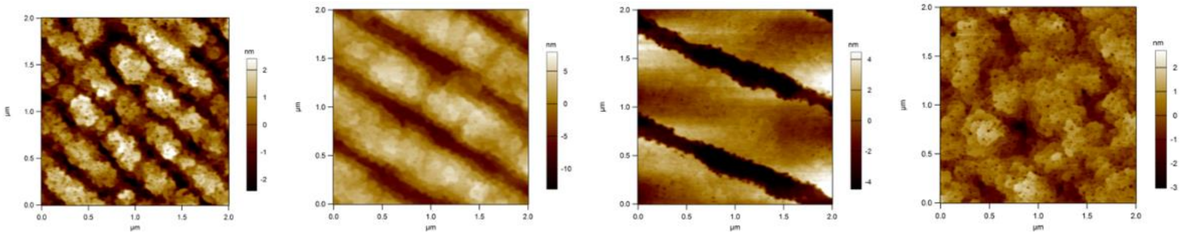

Figure 3.5: AFM of AlN with trenches attributed to SiC atomic step terraces. From left to right, images show: initial reduced temperature layer 30 nm thick, reduced temperature layer after 100 nm of growth, 30 nm of reduced temperature layer grown under a greatly reduced growth rate (from about 1.5 Å/s to 0.5 Å/s) showing locally flat regions separated by sharp trenches, and trench-free morphology of a 30 nm film grown under a pulsed NH_3 growth mode.

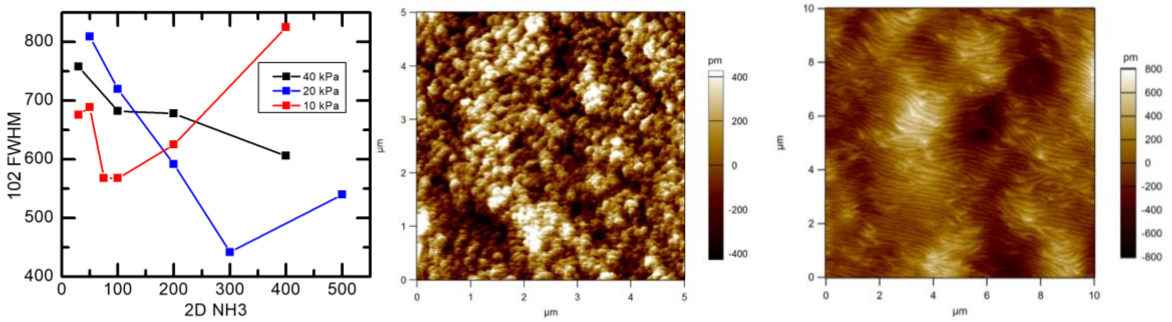

Figure 3.6: AlN at increased reactor pressures. Left: plot of crystal quality versus ammonia flow in the high-temperature (2D) AlN layer. Increased reactor pressure allowed for greater NH3 values to be used, perhaps due to the increased group-III over-pressure. Films grown at higher reactor pressures had significantly smoother surface morphologies indicative of a step-flow growth mode. Initial (center) and fully optimized (right) high temperature AlN layers shown.

growths on the new reactor and substrates performed at 10 kPa did not show a clear correlation between surface morphology and crystal quality. As shown in Figure 3.4, the lowest FWHM values achieved at 10 kPa were above 150” and 500” for the (002) and (102) reflections, respectively, and the surface morphologies for both the reduced and high temperature layers were very rough and did not have an appearance consistent with a step-flow growth mode.

We found that increasing the reactor pressure during AlN growth gave significantly improved crystal quality (Figure 3.6). Reactor pressures above 40 kPa did not give good quality or high growth rates, perhaps due to significant pre-reactions. But, a pressure of 20 kPa seemed to give an optimal combination of high Al precursor mobility, moderate driving force for growth, and manageable pre-reactions. Once growth conditions were again optimized at 20 kPa in the usual way, we found that the AlN surface morphology also improved. Therefore, we proceeded with 20 kPa. Future work may involve further optimization of this pressure, including for active or doped layers, where there may be some dependence of point defect density on reactor pressure.

Just as with the previous reactor, we found that several rounds of growths were needed to season the reactor after maintenance. However, once seasoning was finished, MOCVD characteristics such as growth rates, alloy compositions, and crystal quality remained stable and did not fluctuate as much as they had done on the old reactor. About one week of growths was needed for stabilization of crystal quality and alloy composition, and about two weeks for LED growths (as LED growths were improved and more robust growth conditions were found, these recovery times eventually reduced to about 1-3 days). This was a significant improvement over the old reactor which often required multiple weeks or even months of recovery and recalibrations after maintenance.

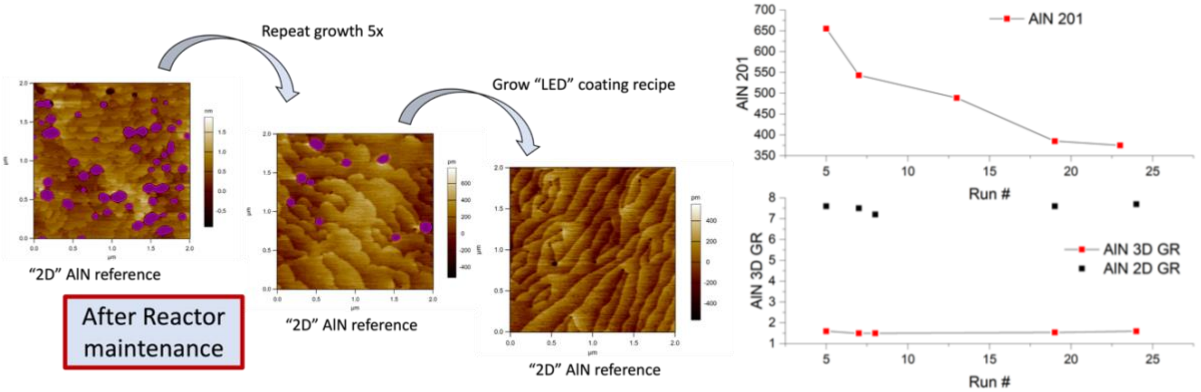

Figure 3.7: AFM and crystal quality improved with reactor coating. Growth rate was slightly higher after initial maintenance and stabilized within about 5 growths. However crystal quality did not fully stabilize until about 20-25 growths. Reactor coating using a LED recipe gave improved morphology compared to coating using pure AlN.

Preliminary experiments showed that elimination of sapphire corrals (and switching to graphite pucks with square cutouts) improved AlN crystal quality and reduced cracking, perhaps due to reduced oxygen contamination. This puck configuration was used for all growths on SiC as published in Refs. [32], [123], [126]. Later, when growing on sapphire (discussed below), we found that LED performance was more repeatable when using sapphire corrals instead of graphite pucks, perhaps because a pristine sapphire wafer could be used to ensure conditions were identical for every growth (whereas the graphite pucks were slowly coated over time). This tradeoff of slightly reduced epitaxial quality for greatly improved repeatability proved valuable for LED optimization, so we used sapphire corrals for all later growths on sapphire.

With these preliminary optimizations of reactor setup and growth conditions finished, we next turned to a detailed study of the ideal nucleation conditions for AlN on SiC, leveraging both post-growth and in-situ characterization methods.

3.4 Coherently strained AlN on SiC substrates

High quality AlN buffer layers needed for UV LED epitaxial structures must reduce dislocation density and eliminate residual tensile stresses in the film to avoid cracking,[80], [127]–[129] which becomes especially relevant in thick buffer layers. The most commonly reported mechanisms for tensile stress generation are thermal expansion coefficient (TEC) mismatch between AlN and SiC[87], dislocation inclination,[130], [131] and island coalescence.[132] The appearance of tensile stress in thin films grown by an island nucleation mechanism has been studied since the early years of metallic thin film deposition [133], and results from a thermodynamic driving force for coalescence when islands are nearly touching [132], [134]. When the distance between neighboring island sidewalls is small (on the order of one unit cell), total system energy can be released by reducing the film surface area via coalescence into a planar film, at the cost of some strain energy associated with the expansion of the neighboring islands. This effect leads to an in-plane tensile strain on the order of the distance between the island sidewalls at coalescence, divided by the island size. Thus, the island coalescence effect leads to a biaxial tensile stress which scales inversely with island size. (Notably: both dislocation density and film stress can be reduced by growing III-nitride nucleation layers with large islands.)

Threading dislocation inclination, by which edge-component TDs bend away from the vertical growth direction producing effective misfit components when projected onto the growth plane, are well known to lead to significant tension in nitride films grown with various techniques.[135]–[138] Edge- or mixed type dislocations with length l with a line tangent direction that is inclined by an angle, θ, with respect to the [0001] growth direction, can be said to have a threading component and a misfit component, with magnitudes proportional to $l\cos(\theta)$ and $l\sin(\theta)$, respectively. As a film grows, l increases, so that a stress gradient is generated, given by:

$$\bar{\epsilon} = \frac{1}{4} b \rho_{TD} h \tan(\theta)$$

as defined in [139], for edge type dislocations in c-plane nitrides inclined toward $\langle 1\bar{1}00 \rangle$, where b is the Burgers vector magnitude of the dislocation, ρ_{TD} is the density of relevant dislocations, and h is the film thickness.

In AlN and AlGaN, it is observed that the inclination of dislocations tends toward the generation of increasingly tensile stress gradients due to kinetic effects at the growth surface [128], [130], [131], [135], [137], [140]. The tensile stress generated by this mechanism increases with thickness and is highest for films with a high dislocation density and large inclination angle, so there is a tradeoff between dislocation annihilation/fusion and tensile stress generation for films with a high initial TDD.

Lattice mismatch[141] and TEC mismatch,[114] neither of which contributes to tension in AlN/sapphire growth, are somtimes ignored in AlN/SiC growth. We propose, however, that lattice (compressive) and TEC (tensile on cooling) mismatch can be dominant sources of stress in high-quality AlN/SiC growth, where other stress sources are minimized. At room temperature (RT), the difference in in-plane lattice parameter, a, for AlN (3.112 Å) and 4H-SiC (3.081 Å) corresponds to a 1.0% lattice mismatch, meaning that a coherently grown AlN/SiC film would have an in-plane compressive mismatch strain $\epsilon_m = -0.010$. Due to the difference in thermal expansion coefficient, $\Delta\alpha = \alpha_{AlN} - \alpha_{SiC} = 1.13 \times 10^{-6}\ ^{\circ}\mathrm{C}^{-1}$, this coherency strain increases upon heating to a growth temperature (GT) of 1400 °C to $\epsilon_m - \epsilon_{TEC} = -0.0115$. Lattice parameters and other important materials properties used in this chapter are tabulated in Table 3-1.

Table 3-1:Materials parameters for AlN and SiC used for calculations in this chapter. Measured values listed in parentheses compare well with expected parameters from the literature.

Parameters: (see, e.g., [142]**)**	**AlN**	**4H-SiC**
C_{11} (GPa)	396	501
C_{12} (GPa)	137	111
C_{13} (GPa)	108	52
C_{33} (GPa)	373	553
Biaxial Modulus ($\boldsymbol{\widetilde{E}}$, GPa) $\boldsymbol{\widetilde{E} = C_{11} + C_{12} - 2C_{13}^{2}/C_{33}}$	470	602
a (Å)	3.112	3.080
c (Å)	4.982 (4.983)	10.085 (10.084) [143]
TEC Mismatch (α_{AlN}-α_{SiC}, $\mathbf{10^{-6}}\ ^{\circ}\mathrm{C}^{-1}$)	0.9 (1.13) [143], [144]	

Relaxation of this compressive mismatch can occur by misfit dislocation (MD) formation near the AlN/SiC interface during initial stages of growth[12],[145] or by TD inclination, and can be quantified in terms of a relaxation strain, $\Delta\epsilon$, such that the total in-plane strain of the film becomes $\epsilon_m + \Delta\epsilon$ at RT, or $\epsilon_m - \epsilon_{TEC} + \Delta\epsilon$ at GT. Unlike the commonly reported percentage "degree of relaxation" ($\Delta\epsilon/\epsilon_m$ at RT, $\Delta\epsilon/(\epsilon_m - \epsilon_{TEC})$ at GT), the relaxation strain, $\Delta\epsilon$, is representative of the actual plastic relaxation of the film via MDs or TD inclination, and its value does not change upon a purely elastic deformation such as that which occurs during cooldown.

In this experiment, we showed that by controlling AlN nucleation using both substrate preparation and initial growth conditions, high-quality, crack-free films can be grown by MOCVD on SiC substrates. *In-situ* wafer curvature and *ex-situ* x-ray diffraction illustrate the evolution of compressive in-plane coherency strain during growth, suggesting the importance of structural similarity between AlN and SiC. We find that a suppression of relaxation between the strained AlN initiation layer and SiC substrate correlates directly with TDD reduction; that is, the more closely the in-plane lattice spacing of the initiation layer matches that of the substrate, the higher the quality of the resulting AlN. We refer to these films as nearly coherent, or coherently strained, because the AlN in-plane lattice parameter nearly matches that of SiC. A perfectly coherent interface would have zero dislocation content, and therefore it is not correct to refer to these films as coherent films, even though the degree of relaxation is very

---

[12] Misfit formation during the initial stages of growth can occur near island boundaries or other non-flat regions of the epitaxial surface where shear strains are large. However, once a film becomes planar, misfit dislocations could only be produced via injection of spontaneously formed dislocation half-loops from the surface, which is energetically unfavorable in wurtzite c-plane growth. Therefore, we find a qualitative difference in the relaxation mechanisms of very thin initiation layers (where MD formation is relevant and increases eventual TDD), and of thick buffer layers (which relax by TD inclination, and do not show evidence of new TD generation under optimal conditions relevant for UV LED epitaxy).

small. Finally, atomic force microscopy (AFM) and transmission electron microscopy (TEM) microstructure analysis inform our understanding of the optimal growth mechanism of AlN/SiC, and how it is qualitatively different from the mechanism expected for AlN/sapphire.

3.4.1.1 *Methods*

The AlN/SiC samples used in this study were grown by MOCVD with trimethylaluminum and NH_3 precursors. The AlN films were grown in two steps: first, a 250 nm thick initiation layer was grown at 1.5 Å/s at 1200 °C. Then, the wafer temperature was increased to about 1400 °C, and a 2.7 µm thick AlN layer with a growth rate around 6 Å/s was grown to reduce TDD and surface roughness.[97], [146]

SiC wafers from two suppliers were used for comparison of different substrate preparation methods. Substrates from Supplier A were 250 µm thick on-axis Si-face (0001) 4H-SiC with a 0.1° unintentional off-cut. These wafers were mechanically polished, with large polishing marks obscuring the atomic step structure, as shown in Figure 3.8(a). In contrast, substrates from Supplier B had well-defined step-terrace structures with quarter-unit-cell atomic steps (see Figure 3.8(b)). They were otherwise similar to substrates from Supplier A: nominally on-axis Si-face (0001) 4H-SiC with a thickness of 500 µm.

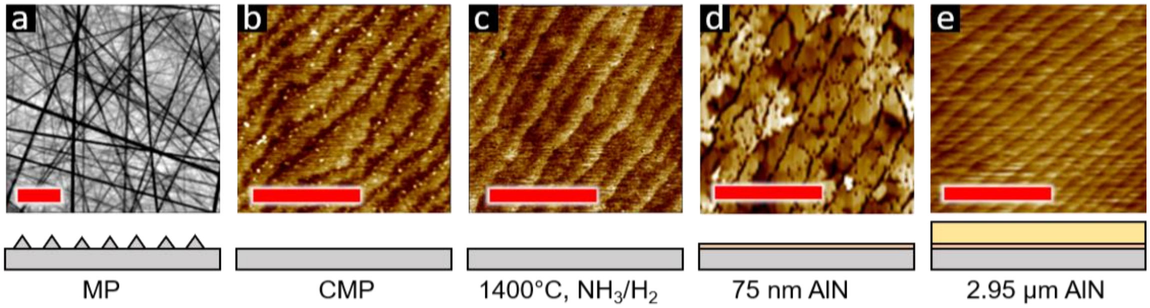

Figure 3.8: AFM images of commercially sourced SiC substrates: (a) Supplier A (mechanically polished), (b) Supplier B (chemomechanically polished), and (c) Supplier B after NH_3 pre-treatment. AFM after 75 nm (d) and 2.95 µm (e) of AlN growth by MOCVD show the initiation layer and smoothing layer morphologies. Scale bars equal 1 µm, and data color scales are 5 nm (a), 300 pm (b,c), 500 pm (d), 1 nm (e).

AFM was carried out with an Asylum Research MFP-3D AFM operated in AC mode with a high-frequency silicon cantilever. Images were flattened using second-order polynomial subtraction within Asylum's data analysis software. X-ray 2θ-ω measurements were taken in symmetric, triple-axis configuration to obtain high 2θ-resolution scans, and in double-axis open-detector configuration for rocking curves. High-resolution x-ray measurements of both 2θ-ω and reciprocal space maps (RSM) were used to assess in-plane and out-of-plane strain values. In addition, laser-based measurements (K-Space Associates) provided real-time surface curvature changes during MOCVD growth, providing in-situ measurements of film stress. TEM samples were prepared using a FEI Helios Dualbeam Nanolab 650 focused ion beam, and images were recorded with FEI Tecnai G2 Sphera at 200 kV.

3.4.1.2 Stress and relaxation

The compressively stressed AlN/SiC layers have been evaluated with multiple complementary methods, to improve the accuracy of the measured degree of relaxation. The most popular stress measurements in the AlN epitaxy literature are x-ray diffraction (2θ-ω) measurements of the *c* lattice parameter,[147] and measurements of a shift in certain peaks in the Raman spectrum.[148], [149] Both techniques are precise for relative comparisons between similar samples. However, to accurately determine equibiaxial in-plane stress, they require assumptions to be made of materials constants for the film, such as relaxed room temperature lattice parameters, elastic constants, and Raman-stress factors;[150] and, when one relies on small differences between measured values and assumed constants, large errors can result from very small uncertainty in assumed constants or instrumental offsets. X-ray reciprocal space mapping (RSM) is also often used to assess in-plane and out-of-plane strain, but still requires assumptions of elastic constants and relaxed lattice parameters, and has limited 2θ resolution when using semiconductor array detectors.

RSM scans in this work used a 2-bounce monochromator and a Pixcel 3D detector in scanning line mode. Off-axis RSM scans used an asymmetric orientation: χ is set to zero, and the surface normal is moved into the equatorial plane (defined by the incident and scattered wavevectors $\mathbf{S_0}$ and $\mathbf{S}$)[151] via an offset term, Δω, such that 2θ is twice (ω-Δω). Then, reciprocal lattice vectors of length $Q = 1/d = 2\sin\theta/\lambda$ can be decomposed into $Q_x = Q\sin\Delta\omega$ within the plane and $Q_z = Q\cos\Delta\omega$ along the *c*-direction.[151] RSM peaks were fit to 2D Gaussian functions using a nonlinear least-squares regression in Matlab.

The in-plane lattice spacings were investigated using RSM of the AlN $10\bar{1}5$ and SiC $10\bar{1}\,10$ (in *hkil* notation, *l*=5 for 2H-AlN and *l*=10 for 4H-SiC) reflections. These scans, shown in Figure 3.9, illustrate the very limited degree of relaxation in the thin AlN initiation layer (75 nm thick, blue) grown on Substrate B with NH_3 pre-treatment. The nearly vertical alignment between the SiC peak and the AlN peak in the thin initiation layer sample indicates a qualitative match in *a*-lattice spacing between the substrate and film. The spreading of the peak is due to a mixture of strain states from nearly coherently strained to partially relaxed, present in the form of a vertical strain gradient or in a laterally inhomogeneous strain distribution. After growing another film to a greater thickness (2.95 µm thick, red), it relaxed more fully. X-ray 2θ-ω and wafer curvature measurements (see Figure 3.15 and Figure 3.12) quantitatively confirm these results: the semi-coherent initiation layer is at first nearly fully strained, and then gradually relaxes to an average in-plane relaxation of $\Delta\epsilon = 0.31\%$. Then, the high growth rate layer relaxes via TD inclination so that its room temperature lattice spacing matches literature values.

Gradual stress relaxation by TD inclination—whereby the stress gradually decreases throughout the thickness of the film—appears in the RSM (Figure 3.9) as a spreading of both AlN peaks along a “relaxation line” defined by the lattice parameters and elastic properties of the film (see Ref. [123], supplemental).

In addition to 2θ-ω and RSM, the radius of curvature method has been used to measure directly the films’ mean residual (equibiaxial, in-plane) stress, where the only constants needed are the elastic properties of the bulk substrate; relative errors in calculated stress are no larger than the relative errors in these constants (or in film or substrate thickness, which can be measured with confidence).[152] *In-situ* laser-based measurements (K-Space Associates) provided real-time surface curvature values during MOCVD growth, relative to the wafer curvature prior to the initiation of growth. The laser monitor was calibrated by the manufacturer, and this calibration was confirmed on AlN/SiC films using the x-ray curvature method [139], a direct and absolute measure of film stress.[152], [153]

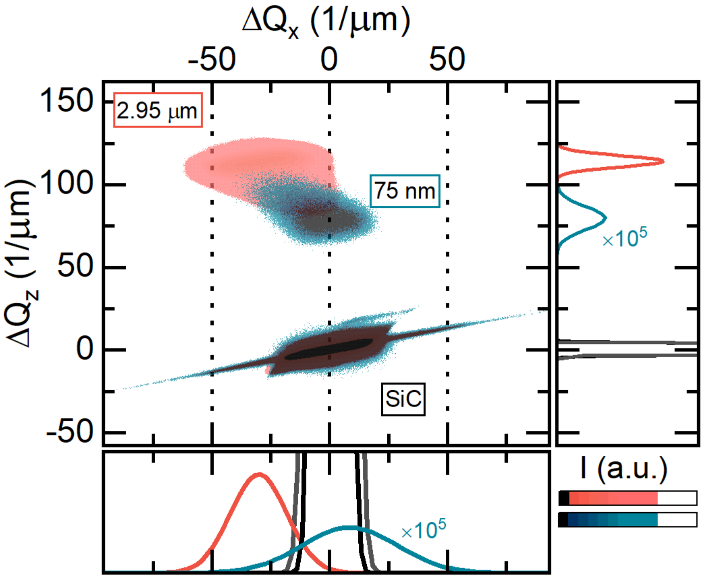

Figure 3.9: Reciprocal space maps for 75 nm initiation layer (blue) and 2.95 µm (red) AlN. Color scales differ and do not depict quantitative scattering intensity. SiC peak is broadened by finite monochromator resolution and a beam-size artifact. Projections of 2D Gaussian fits along both axes.

The Stoney formula,[152]

$$\kappa = \frac{6\, h_f \sigma}{\tilde{E}_s {h_s}^2} \ ,$$

relates a measured curvature, κ, to a product of film thickness, h_f, and average equibiaxial plane stress, σ ($h_f\sigma$ is commonly referred to as stress-thickness product), as well as the substrate thickness, h_s, and substrate biaxial modulus,

$$\tilde{E} = C_{11} + C_{12} - 2{C_{13}}^2/C_{33} = 602 \text{ GPa}$$

for SiC[142] (see Table 2-1). Thus, after converting κ vs. time into κ vs. thickness via the measured *in-situ* growth-rate (not shown here), one can plot the evolution of stress and equibiaxial strain, ϵ, as the slope of the data:

$$\frac{d\kappa}{dh_f} = \left(\frac{6}{\tilde{E}_s {h_s}^2}\right)\sigma = \left(\frac{6\tilde{E}_f}{\tilde{E}_s {h_s}^2}\right)\epsilon \ .$$

For example, extracting a slope of $0.134 \text{ m}^{-1}/9000$ Å from the data for Substrate A (see Figure 3.12) between 75 and 100 minutes (with a known growth rate of 6 Å/s), we used the Stoney formula to calculate a stress of 0.9 GPa. Cracking can be observed in the kink at 120 minutes (around 1.9 µm thickness) in the curvature plot, where the tension was released.

3.4.1.3 Experimental Results

The first consideration in preparation of SiC substrates is the smoothness of the surface. As measured by AFM, Substrate A had a rough surface with polishing marks, while Substrate B had an atomically flat surface (Figure 3.8 (a,b)). For the same growth conditions, AlN deposited on Substrate B showed reductions in tensile stress (Figure 3.10) and cracking (Figure 3.11) when compared with films on Substrate A. The marked reduction in tension when switching to smooth substrates suggests that small island size is a primary driver of stress generation on rough substrates.

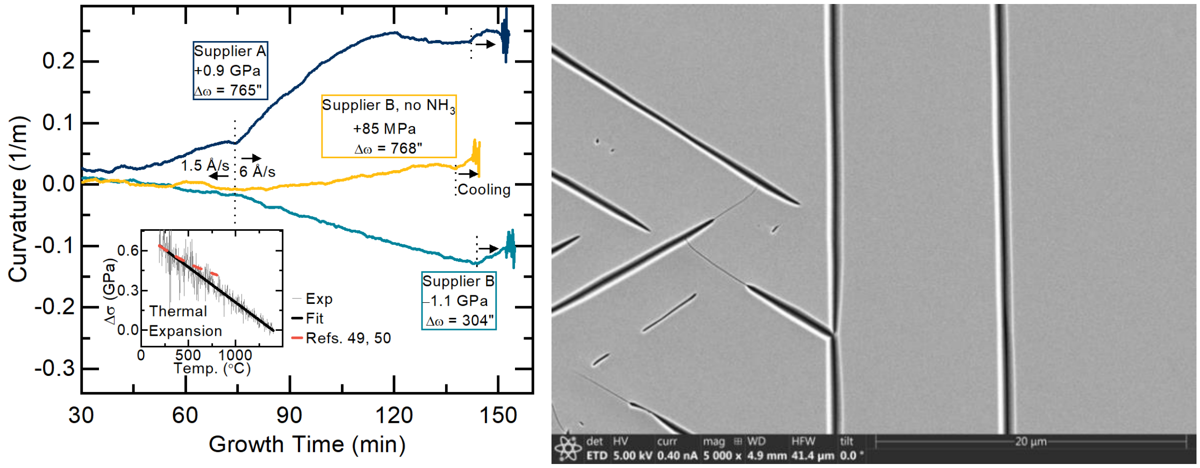

Figure 3.10: **Left**: *In-situ* curvature of AlN template on three SiC substrate types: rough SiC with NH_3 pre-treatment (top, tensile), smooth substrate (middle, weakly tensile), and smooth substrate with NH_3 treatment (bottom, highly compressive). Growth stress and $20\bar{2}1$ FWHM, Δω, listed. **Inset**: thermal expansion mismatch stress. Data (gray) are compared with literature models (red, dashed) and a linear least-squares fit (black, solid). **Right**: SEM image of cracks. The thick cracks appear to have occurred during growth and were then widened during the growth. The very thin cracks may have occurred on cooldown, with no evidence of growth above the crack.

Next, we explored the impact of *in-situ* substrate pre-treatments before AlN growth. One sample was pre-treated at 1400 °C and 10 kPa under flowing NH_3/H_2 for 10 minutes before growth, while the other was pre-treated under flowing H_2 only. Stress values (calculated as shown above) are shown for each data set in Figure 3.10; in particular, for the pre-treated Substrate B, we calculate a stress of -1.1 GPa. That is, with the introduction of NH_3 pre-treatment, AlN films grown on atomically flat substrates changed from a slightly tensile stress state (with some risk of cracking for thick films), to a strongly compressive stress state (crack-free up to 5 µm). XRC full-width at half-maximum (FWHM) values are shown in Figure 3.10 as well, showing that the combination of smooth substrates and pre-treatment produces higher film quality than either preparation alone.

Closer inspection of the SiC wafer after NH_3 pre-treatment, but before AlN growth, suggests a change in surface morphology. As shown in Figure 3.8(b), the as-received substrates have a step-spacing of about 165 nm, corresponding to quarter-unit-cell (Si-C monolayer) step heights, which are known to result in stacking mismatch and increased TDD[113]. After high-temperature chemical pre-treatment (Figure 3.8(c)), the SiC surface had larger steps with 330 nm spacing, corresponding to half-unit-cell (bilayer) step heights. No step-bunching or macro-steps were observed, and the morphology remained unchanged when increasing the pre-treatment duration beyond 10 minutes. *In situ* optical reflectance data showed a slight decrease in film reflectivity upon initiation of NH3 flow at 1400 °C. This could be related to the formation or removal of some very thin surface layer, but this was not investigated further, as we could not rule out that it could be an artifact related to slight differences in sample position caused by changes in gas flow velocity and reactor pressure. Other experiments suggest that 1400 °C is needed for effective NH_3 pre-treatment; annealing at 1300 °C or lower has no effect. For the highest quality samples, FWHM values for 0002 and $20\bar{2}1$ reflections were 123″ and 304″, and the films were atomically flat (Figure 3.8 (e)) with a well-defined structure consistent with step-flow growth. All subsequent experiments were conducted using Substrate B, with pre-annealing.

3.4.1.4 Crystal Quality Measurement Details

AlN film quality was optimized with the x-ray rocking curve (XRC) technique,[83], [85], [141] using a Panalytical X'Pert Pro MRD to measure the 0002 and $20\bar{2}1$ reflections. We scanned the sample angle ω (fixing the detector angle 2θ), with an open detector in a double-axis configuration and a two-bounce hybrid monochromator with intensifier in the incident beam. For the $20\bar{2}1$ measurement we used a skew-symmetric orientation: 2θ was twice ω, and the sample was tilted along χ (the axis perpendicular to the 2θ-ω axis within the scattering plane, sometimes called ψ).[151]

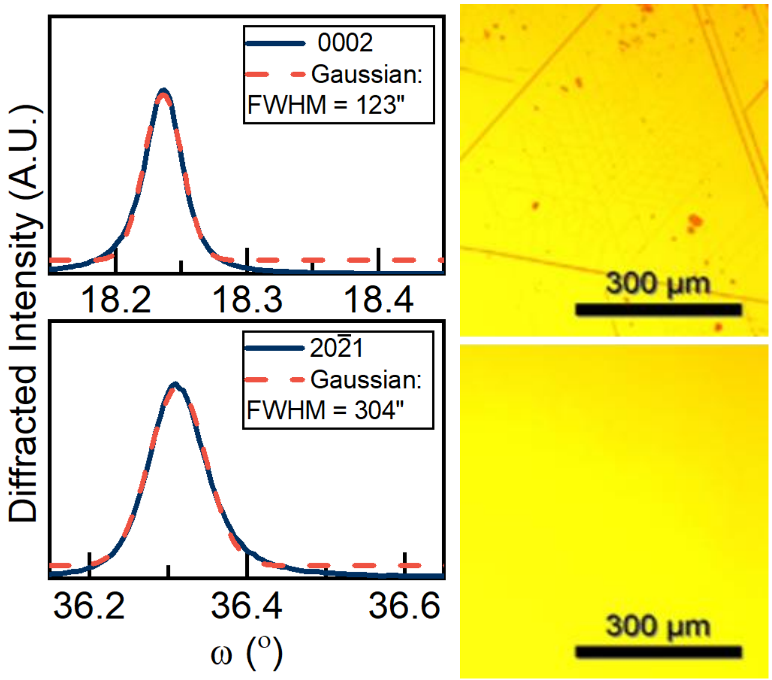

Figure 3.11: Typical 0002 and $20\bar{2}1$ x-ray ω-rocking curve scans (left) for uncracked AlN samples grown on SiC, with thickness of 2.95 µm: measured (solid) and a Gaussian fit (dashed). Nomarski-contrast optical microscope images for cracked (top right) and uncracked (bottom right) AlN films.

Figure 3.11 presents typical XRC scans for the highest quality 2.95 µm thick AlN films grown on substrates from Supplier B, with pre-treatment. Gaussian best-fit FWHM values for 0002 and $20\bar{2}1$ reflections were $123''$ and $304''$. Additionally, Nomarski-contrast optical microscope images of cracked (without pre-treatment) and uncracked (with pretreatment) AlN films on SiC are shown in Figure 3.11.

3.4.1.5 Importance of Initiation Layer Temperature

Upon varying the initiation layer growth temperature, changes in crystal quality and stress are observed, as shown in Figure 3.12. For reference, straight lines corresponding to a coherently strained film ($\epsilon_{11} = -1.15\%$) and a film with 0.31% relaxation ($\epsilon_{11} = -0.84\%$) are superimposed with the measured curvature data—the resolution of the laser monitor is insufficient to distinguish the two for initiation layers thinner than 250 nm.

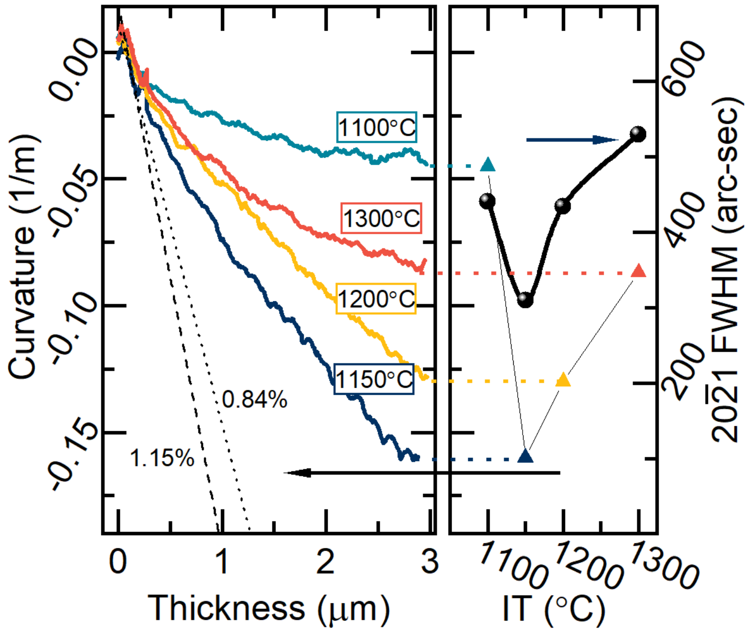

Figure 3.12: Thickness-dependent *in-situ* curvature compared to x-ray FWHM for AlN films grown with various initiation temperatures (IT). Hypothetical curvature trends for AlN on SiC with -1.15% (coherent, dashed) and -0.84% (0.31% relaxed, dotted) biaxial compressive strain.

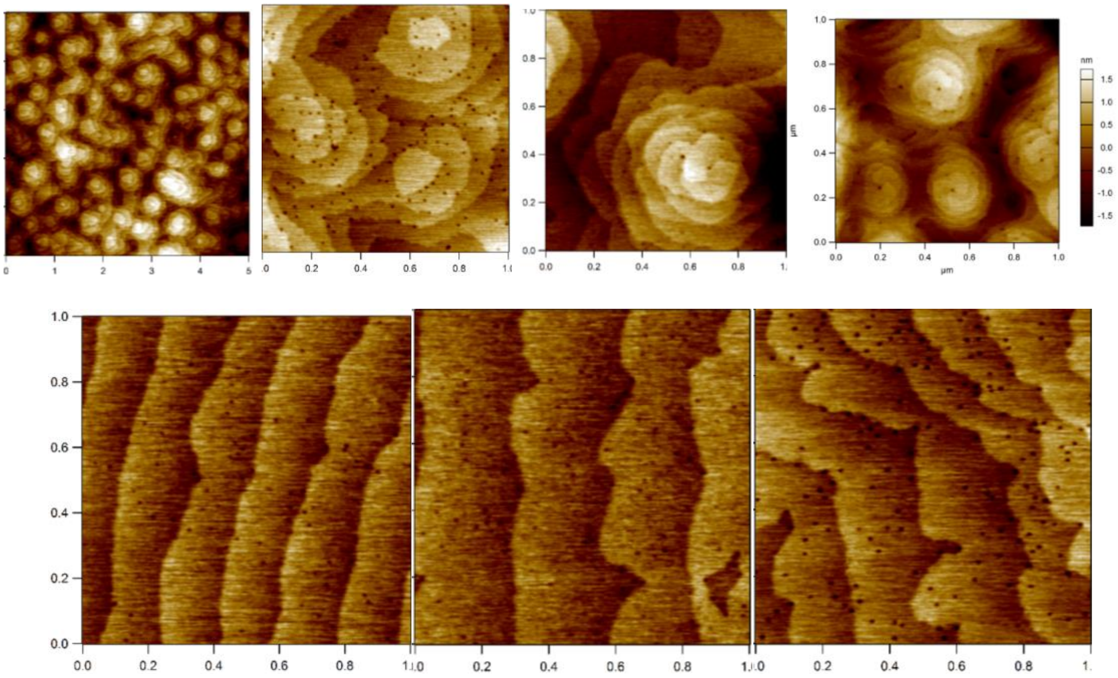

Figure 3.13:Detailed AFM images of optimized AlN. **Top row**: AFM details of optimized 3D AlN layer, grown atop an atomically flat thick 2D buffer. Due to the high growth pressures (high group III over-pressure) used here, dislocations appear as small black dots or pits. A mixture of dislocation mediated spiral islands, and non-dislocation-mediated step islands are observed. All films are nearly atomically flat with atomic step-terrace structure clearly visible. **Bottom row**: AFM images of 3D films grown atop 2D buffers at different temperatures, showing the gradual change from 2D to 3D growth mode with decreasing temperatures (from **left** to **right**: 1350 °C, 1300 °C, 1200 °C).

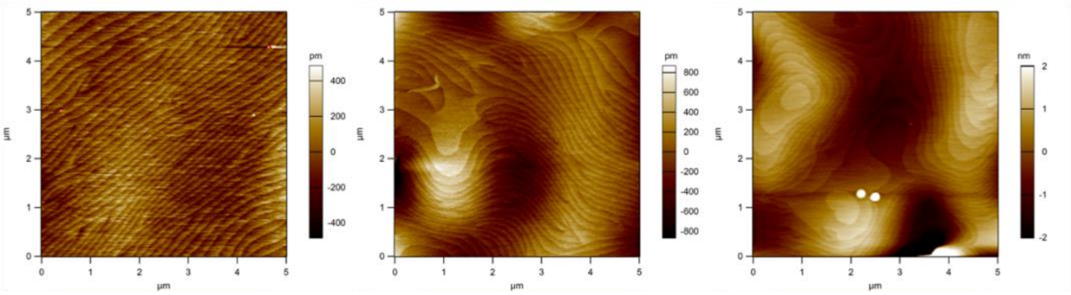

B190415DA
TMA = 18
RMS=100pm

B190416DA
TMA = 24
RMS=250pm

B190416EA
TMA = 36
RMS=800pm

Figure 3.14: 2D morphology versus growth rate. The 2D layer was optimized for atomically flat surface morphology (not shown in Ref. [123]), in addition to the equally crucial strain and TDD optimizations shown in the publication. All growth conditions discussed in the publication were developed under the constraint that they provide good surface quality as well. Here, I show an example of the effect of growth rate, with slower growth rates favoring a 2D step flow growth mode.

Crucially, the optimal initiation temperature at 1150 °C had the lowest relaxation strain (most negative curvature), likely due to the undulating spiral- or “3D” growth mode[97] expected to suppresses MD nucleation.[145] When the initiation temperature exceeded 1200 °C, high precursor mobility favored an atomically flat “2D” growth mode, and MDs likely nucleated with a higher density. Surface morphology of the optimal 3D growth condition (Figure 3.13, top row), other 3D growth temperatures (Figure 3.13, bottom row), and the optimal 2D growth condition (Figure 3.14), indicate that the initial nucleation morphology may also differ under these conditions.

To quantify *c* lattice spacings for very thin samples (where the uncertainty in stress from curvature is greatest), symmetric 2θ-ω scans of the AlN 0002 (and SiC 0004) reflections were taken, whereby $d_{hkil} = \frac{\lambda_{Cu,k_\alpha}}{2\sin\theta_{hkil}}$. Figure 3.15 compares these scans for initiation layer growth-interrupt samples with and without NH_3 pre-treatment: the non-pre-treated initiation layer (75 nm) has a greatly reduced *c* spacing of 4.969 Å. This corresponds to out-of-plane strain $\epsilon_{33} = -0.26\%$, and equibiaxial in-plane strain $\epsilon_{11} = -\left(\frac{C_{33}}{2C_{13}}\right)\epsilon_{33} = +0.45\%$, indicating a strong tensile stress state. This strong tension of 2.1 GPa leads to cracking[152] in films thicker than 1 μm. On the other hand, the initiation layer grown on a pre-treated substrate (75 nm) had an equibiaxial in-plane strain $\epsilon_{11} = -0.69\%$. Since a misfit strain of $\epsilon_m = -1.0\%$ (RT) is expected, this suggests that the misfit relaxation strain is $\Delta\epsilon = 0.31\%$ (displayed as a dotted line in Figure 3.12, as discussed above). [13]

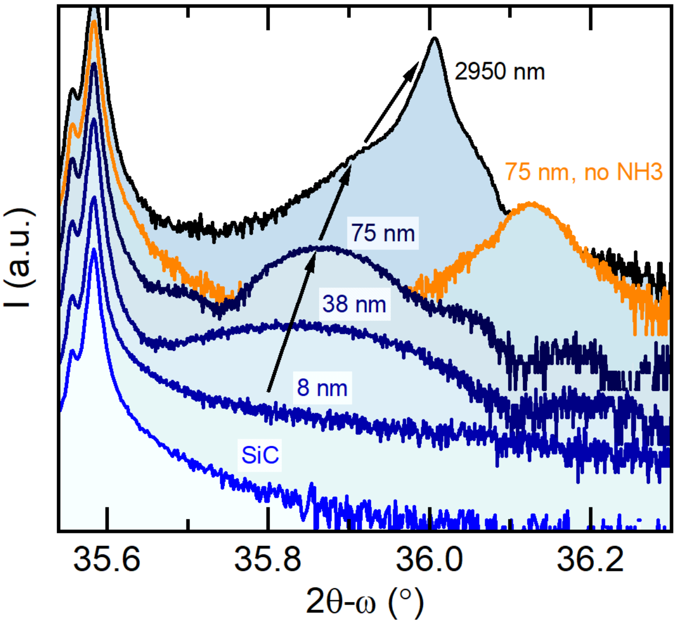

Figure 3.15: Symmetric triple-axis 2θ-ω scans of AlN/SiC films, with SiC double-peak for reference.[154]–[156] Bottom to top: bare SiC (blue), 8 nm, 38 nm, 75 nm, 75 nm without NH_3 pre-treatment (orange), and full 2.95 μm AlN thickness template (black). Logarithmic intensity scale.

Figure 3.15 shows additional scans for a thickness series grown on Substrate B, with pre-treatment, with AlN thicknesses of 8 nm, 38 nm, and 2.95 μm. SiC substrate peaks (strong 0004 peak and a much weaker 3C-related disorder peak) are included as a reference.[154]–

---

[13] I'd like to note here that care should be taken when using 2θ-ω to measure lattice spacings of films thinner than 300 nm. In very thin films, dynamical effects cause the film peak to shift very slightly toward the substrate peak. This shift is on the order of 10s to 100s of arcsec. In this particular dataset, the shift is negligible compared to the large peak shifts caused by strain differences, but in other datasets it may be important. See, e.g., Ref. [322]. Datasets for thin films must be modeled using dynamical simulation software such as those provided by the Rigaku HRXRD software package, and are strictly speaking only approximated by differential Bragg's law analysis.

[156] The thinnest sample for which a peak position can be extracted (38 nm) yields a calculated $\epsilon_{11} = -0.83\%$, corresponding to an even lower relaxation of $\Delta\epsilon = 0.17\%$. The full 2.95 µm AlN template film had a *c* parameter of 4.983 Å, corresponding to a negligible residual tension of $\epsilon_{11} = 2 \times 10^{-4}$.

3.4.1.6 Thermal Expansion coefficient mismatch of AlN and SiC

High-temperature TEC data are not readily available for AlN and SiC, so the laser monitor was used to measure mismatch stress (Figure 3.10, inset). The linear best-fit slope, $\frac{d\sigma}{dT} = 532\ \mathrm{kPa/°C}$ yields a constant thermal expansion coefficient mismatch $\Delta\alpha = \frac{d\sigma}{dT}/\tilde{E} = 1.13 \times 10^{-6}\ \mathrm{°C^{-1}}$, corresponding to a slight increase in AlN/SiC lattice mismatch $\epsilon_{TEC} = 1375\ \mathrm{°C} \times 1.13 \times 10^{-6}\ \mathrm{°C^{-1}} = 0.15\%$, when heating from RT to GT, as discussed above. Thus, a thick layer (>3 µm) which is fully relaxed at GT will develop a strong tensile stress $\tilde{E} \times \epsilon_{TEC} = 731$ MPa upon cooldown to RT, likely enough to cause cracking (see Figure 3.10, Figure 3.11). This $\Delta\alpha$ value is in good agreement with expected room temperature values,[114] as well as polynomial models from Refs. [143], [144] (tabulated only up to 800 °C), shown as a dashed curve in (Figure 3.10, inset).

3.4.1.7 TEM images of AlN/SiC

TEM foils were prepared in cross section and plan view geometries to investigate the microstructure of one 2.95 µm thick AlN/SiC film. Figure 3.16(a,b) depicts cross-sections highlighting screw-component and edge-component dislocations, respectively. As expected,[85] most dislocations had some edge character. Many instances of dislocation inclination (away from the vertical growth direction), bending, and annihilation and fusion reactions confirmed the dislocation reduction mechanism we have suggested previously.[97]

Additionally, the dislocation inclination observed in the TEM images explains the gradual stress relaxation measured via *in-situ* curvature and x-ray.

An additional plan view TEM foil was taken from the AlN/SiC interface (see Figure 3.16 (c,d)). MD networks were clearly resolved, forming dense rows spaced 300-600 nm apart, attributed to the large terrace width shown in Figure 3.8(c) after NH_3 pre-treatment. Between the rows, MD density is low. Measuring (Figure 3.16 (c,d)) a lateral spacing between misfit dislocations (in the low MD density regions) of about 200 nm and assuming a Burgers vector[132] of 0.3112 nm, we calculate[145] a degree of relaxation of $\Delta\epsilon = \rho_{MD} b_{\parallel} = 0.33\%$, where ρ_{MD} is the MD density assuming a regular two-dimensional grid, and $b_{\parallel}$ is the edge-component of the Burgers vector projected within the plane of the AlN/SiC interface. This agrees well with the measured relaxation value of $\Delta\epsilon = 0.31\%$, suggesting that the dense dislocation rows at atomic steps contribute little to overall misfit relaxation, and are more likely associated with stacking mismatch or local stress effects.[110], [113] Since MD density on terraces is minimal, the dense rows of MDs likely form the majority of TDs, as evidenced by the rows of pits observed in AFM of a separate sample (see Figure 3.8(d)), again with spacings of about 300 nm.

A plan-view TEM specimen near the film surface was imaged (Figure 3.17) to quantify TDD. This specimen was taken from close to the center of the sample and is representative of the film. By imaging a large region (>40 μm^2) and counting over 100 individual dislocations, a value of $\rho_{TDD} = 2.4 \times 10^8$ cm^{-2} can be calculated with a relative uncertainty ($N^{-1/2}$) of at most 10% assuming a random distribution of threading dislocations.[157]

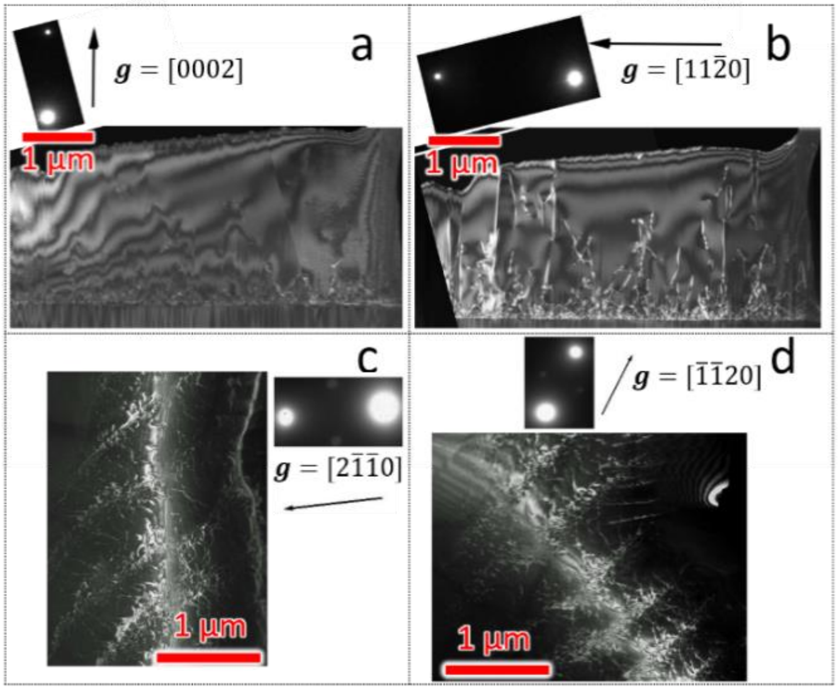

Figure 3.16: Cross-section TEM of AlN/SiC; screw (a) and edge (b) components of threading dislocations. Plan view TEM (c,d) of the AlN/SiC interface highlights the misfit dislocation networks formed in rows along SiC step edges. In the step-terrace regions between these rows, very low dislocation density is observed.

The studies of Okumura *et al.* have proven that AlN can be grown with high quality—and with compressive in-plane coherency strain[120]—on SiC by MBE, via precise control of substrate morphology and initial growth mode[95], [113], [119]. In those studies, SiC substrates were treated with high-temperature gas annealing at low pressures under flowing H_2 or HCl at temperatures exceeding 1400 °C, producing atomically flat SiC substrate surfaces with well-controlled step heights, and enabling low-TDD AlN layers.

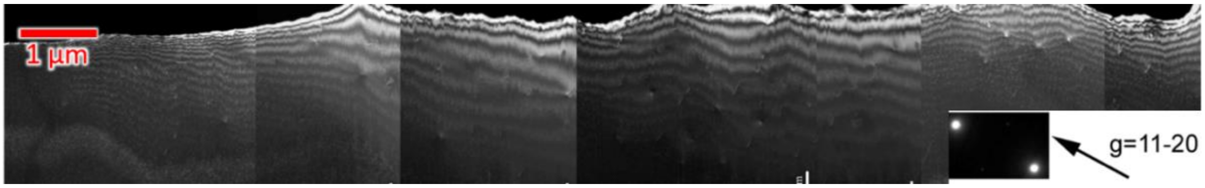

Figure 3.17: Plan-view TEM image of ~40 μm^2 of AlN film surface. A dislocation density of 2.4 x 10^8 cm^{-2} is calculated.

In this section, we demonstrate that the high-temperature pre-treatment approach can be applied in MOCVD growth of AlN on chemomechanically polished SiC as well, with the added advantage of performing the pre-anneal *in-situ*, immediately before film growth. The change in SiC substrate surface morphology shown in Figure 3.8(b,c) is consistent with the TDD reduction mechanism by reduction of stacking mismatch[110], [121]. There could also be a beneficial effect from surface cleaning or oxide layer removal[158], [159]. With substrate pre-treatment, misfit dislocation formation is greatly reduced upon the SiC atomic terraces, where AlN nucleation occurs semi-coherently (Figure 3.16(c,d)). On the other hand, high-density misfit networks form at step edges, due to locally maximized strain and possible stacking mismatch[110], [113]. If it were the case that these AlN films were nucleating by the typical AlN/sapphire model, one would expect misfit dislocations randomly distributed all throughout the AlN/SiC interface, and full strain relaxation almost immediately after nucleation.

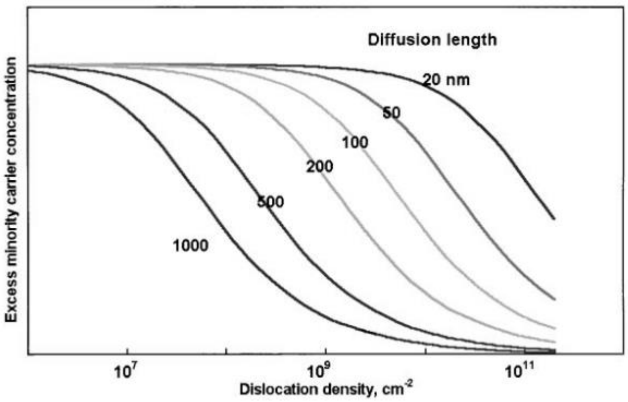

Figure 3.18: Excess minority carrier concentration, a proxy for radiative efficiency or IQE, versus dislocation density for various minority carrier diffusion lengths. Diffusion lengths of at most 50 nm are expected for AlGaN (in contrast to 1,000 nm or more for conventional III-Vs), suggesting that the benefit of reduced TDD is negligible below 10^9 cm^{-2}. Reproduced under Fair Use from [160].

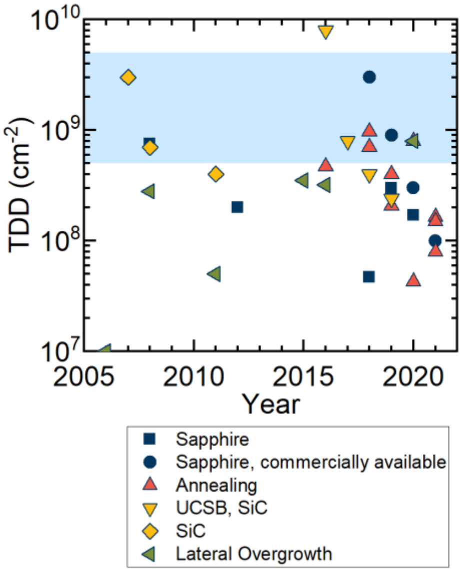

Figure 3.19: Selected heteroepitaxial AlN TDD by year of publication. Ultralow TDD was first achieved by lateral overgrowth. Since 2010, low TDD has also been achieved on sapphire and SiC without lateral overgrowth. Since 2016, high temperature annealing has rapidly improved to provide low dislocation density AlN. Commercially available AlN/sapphire templates now have TDD in the low 10^8 cm^{-2} range. The shaded region (5×10^8 cm^{-2} – 5×10^9 cm^{-2}) represents the approximate TDD in commercially available devices on sapphire, as well as the current record WPE and EQE. [24], [97], [119], [123], [141], [147], [161]–[180]

3.5 Bulk AlN substrates – advantages and challenges

Much has been made of the promise of bulk or free-standing AlN substrates, grown using physical vapor transport (PVT), with TDD as low as 10^3-10^5 cm^{-2}, several orders of magnitude lower than that achievable on foreign substrates. So it is interesting that nearly all of the most efficient UV LED results in the literature are not on free-standing substrates, but rather on foreign substrates with dislocation densities between $5x10^8$ and $5x10^9$ cm^{-2}. Currently available bulk AlN substrates have high optical absorption in the UV in the tens or hundreds of cm^{-1} (and often in the visible as well, so that most wafers have a yellow or brown appearance).

Due to the high cost and poor optical transparency of free standing AlN substrates, the benefit of ultralow TDD would have to be great to justify their use. There are many analyses of the impact of TDD on III-nitride LED radiative efficiency in the literature [181], [182], and the details of their quantitative outcomes vary widely. This variation is well captured by Figure 3.18, which considers a concise model of the interaction between dislocations and charge carriers and shows that: *for a given effective minority carrier diffusion length, there exists a range in which the TDD-dependence of IQE is strong, with only a weak dependence above or below that range* [160]. Once the average distance between adjacent dislocations greatly exceeds the effective minority carrier diffusion length (or the average distance between relevant point defects), then further decreases in TDD do not impact IQE. Furthermore, due to the low hole diffusion length and short fundamental radiative lifetime, AlGaN appears to be even less sensitive to TDD than InGaN.[14] Some reports have suggested a threshold as high as 10^{10} cm^{-2}, below which TDD has little effect on room temperature UV LED IQE [182]. In practice, it is observed that TDD around $0.5\text{-}5\times10^{9}$ cm^{-2} (the blue-shaded region in Figure 3.19) is low enough to achieve the highest reported EQE [26] and WPE [6], [35].

The threading dislocation density in commercially available devices on sapphire is remarkably high—typical commercial devices on sapphire have estimated TDD of 10^{9} cm^{-2} or higher, based on TEM and x-ray data. IQE is thought to be above 60% for commercial devices,

---

[14] The remarkable robustness of InGaN active regions against TDD, when compared with the conventional III-Vs, is related to the short hole diffusion length and short recombination lifetime for this wide bandgap material (and the lack of dislocation glide in *c*-plane devices). In addition, alloy clustering or disorder leads to carrier localization which may mask the effect of dislocations [323]. Strong alloy clustering is not observed in high-TDD AlGaN [31], however the very high alloy disorder near 50% composition as used for UV active regions may produce localization effects [234].

in which point defect densities are greatly reduced by optimized MOCVD growth conditions [4]. Some research results suggest that IQE values above 80% have already been achieved, and as discussed above there are no fundamental reasons to doubt the plausibility of such values [5]. EQE is currently limited mostly by carrier injection (electron overshoot) and Auger, not TDD.

Preliminary results for characterization and device growth on AlN substrates carried out at UCSB are shown in Figure 3.20. These substrates had some UV absorption, as measured by Filmetrics and modeled using Gaussian absorption peaks. The model was fitted using a nonlinear least-squares Levenberg-Marquardt algorithm (open-source “Fityk” software). The fit had 15 parameters total, with 1500 total data points, and gave a chi-square of 32.48. A bandgap of 191 nm was modeled, however equipment limitations prevented measurements at wavelengths below 200 nm so this cannot be considered a reliable measurement. Despite the UV absorption, the high structural quality of the bulk AlN substrate provided significant improvement in LED power, measured in a very preliminary fashion using fiber-collected EL intensity. Despite the promising initial results, this project was not pursued further due to a lack of reliable substrate supply, high substrate cost, and the relative success of AlN growth on SiC (above) and sapphire (discussed later in this section).

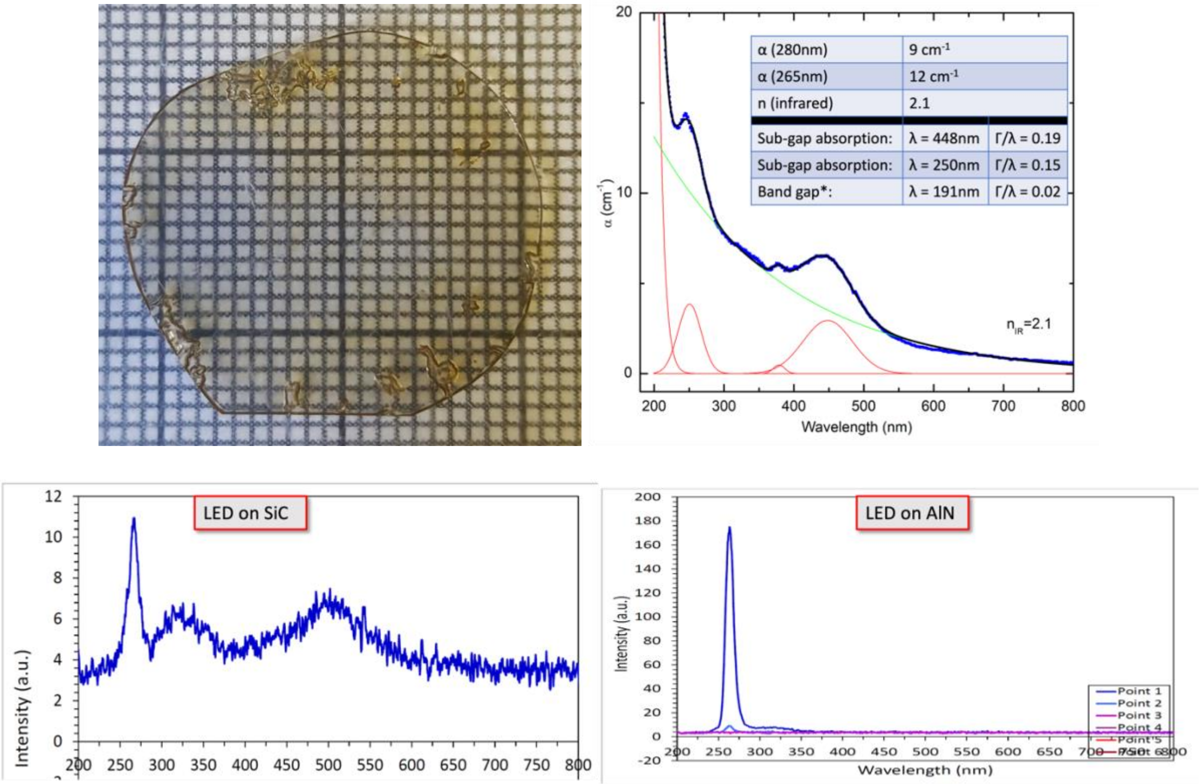

Figure 3.20: Preliminary AlN bulk results. Wafer appearance (**top left**) was clear with a slight yellow-brown appearance typical of early AlN samples available around 2017. UV-visible (Filmetrics) transmission data (**top right**) were used to calculate optical absorption, which is well modeled using a band-edge at 191 nm, and two broad sub-gap absorption peaks attributed to point defects. Preliminary LED growths showed significant improvements in LED output power indicated here by an increased EL intensity, however processed device EQE was very low because these LEDs were grown before a reliable high-power LED recipe had been developed.

3.6 High-quality AlN by high temperature annealing

The most exciting recent development in AlN TDD reduction is via post-growth annealing at around 1600 °C or higher. Such high temperatures, an appreciable fraction of the sublimation point of AlN, enable dislocation climb whereby dislocations move laterally within the solid crystal. Dislocations may then fuse and annihilate with other dislocations or at free surfaces. The most promising aspect of this method is its applicability to AlN grown by MOCVD, MBE, and sputtering, producing LED-grade dislocation densities from material with as-grown TDD of 10^{10} cm^{-2} or higher. The first reported use of this method was by Miyake *et al.* [163], and there have since been a flurry of reports exploring the application of this method to AlN grown by various methods on sapphire and SiC. The presence and mobility of vacancy defects has been proposed as a likely mechanism by which TD reduction is mediated [183], as mobile vacancies are known to mediate dislocation climb. Other reports suggest that stress relaxation is a major driver of TD motion [167], [184]. Novel variations on the annealing technique such as combined annealing with lateral overgrowth [169] and repeated sputtering and annealing [168] continue to be developed. The most advanced form of this technique uses variable temperature annealing to achieve TDD below 2×10^{8} cm^{-2} [175].

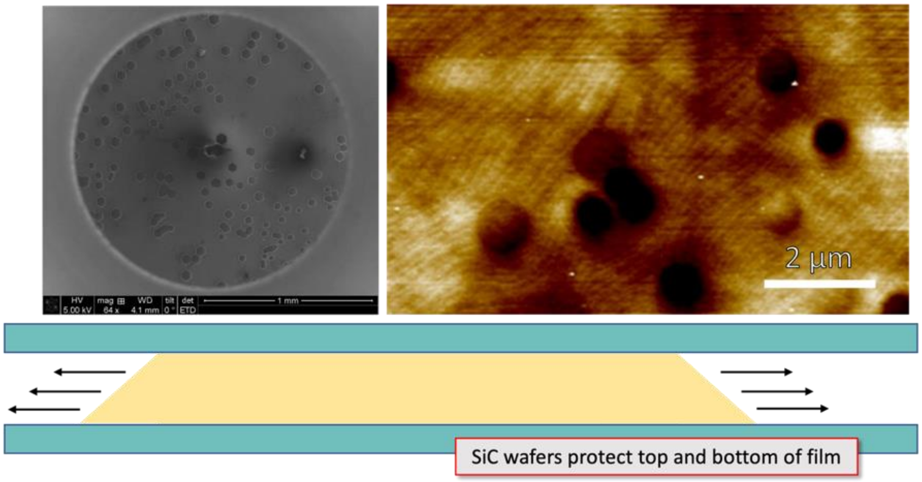

Figure 3.21: SiC cap wafer during AlN anneal prevents film sublimation. Without capping, AlN films developed hexagonal pits shown in SEM (**top left**) and AFM (**top right**) for short anneal durations less than 15 minutes. For longer durations of 30-60 minutes needed for TD reduction, films decomposed entirely.

AlN samples grown at UCSB using the methods of Ref. [97] were annealed using a SiC capping wafer to prevent AlN sublimation, as shown in Figure 3.21. Figure 3.22 shows that only an hour is needed for TDD reduction, and TD reduction (measured by reduction in AlN 102 rocking curve FWHM) is more or less uniform for all film thicknesses investigated.

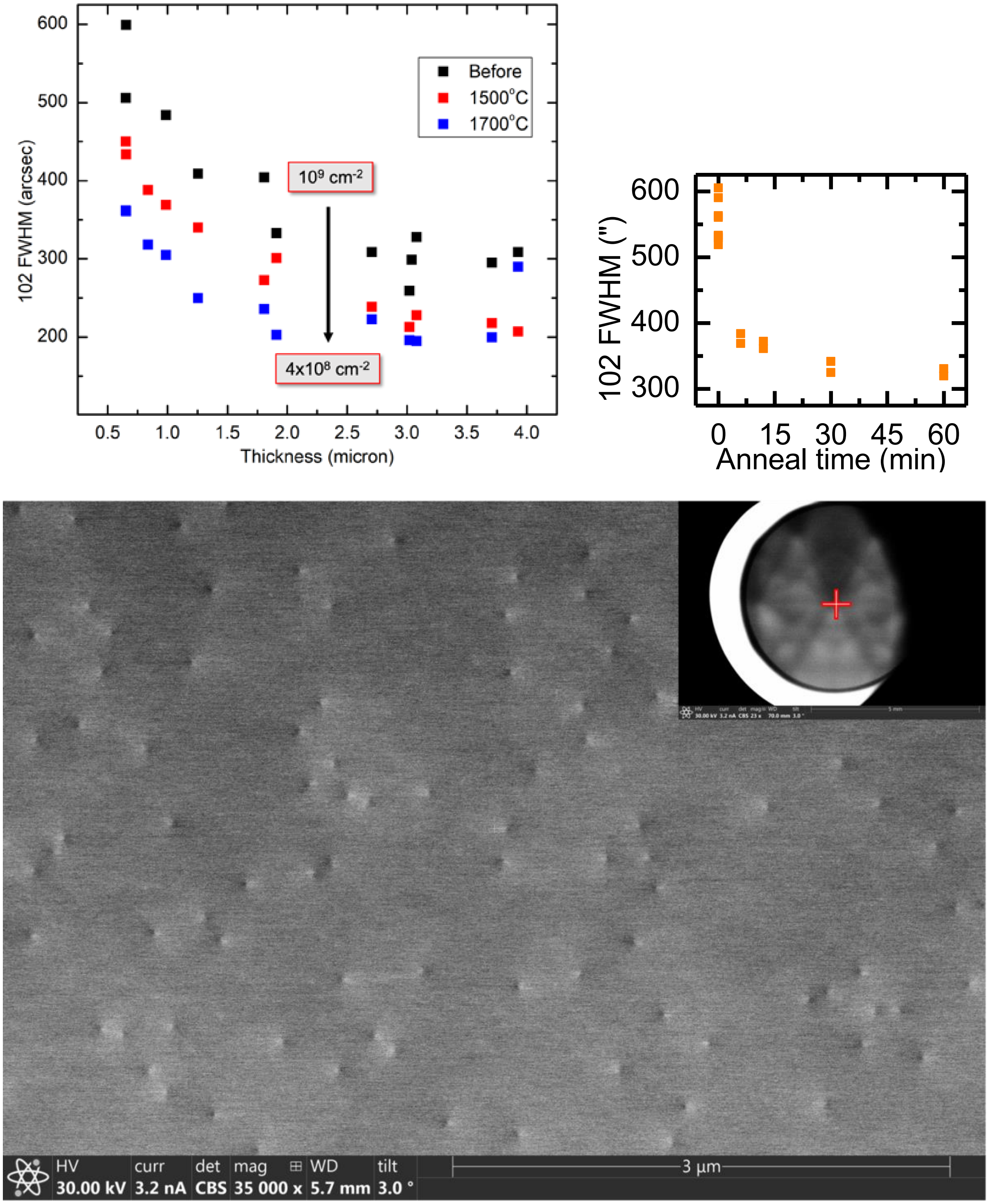

Figure 3.22: Dislocation reduction after annealing. X-ray rocking curve FWHM of the 102 AlN reflection indicates a strong TD reduction with both increased film thickness (due to TD inclination) and annealing temperature, with higher temperatures giving greater TD reduction. TEM-confirmed TDD values (inset) show that over half the TDs are annihilated. Annealing time (right) shows that very little time is needed for TD reduction, so that anneals need not take any longer than 1 hour. Electron channeling contrast imaging (ECCI) using SEM confirms this TDD on a larger number of samples.

Electron channeling contrast imaging (ECCI) indicates low TDD in annealed films (Figure 3.22); the best films were then characterized by TEM as shown in Figure 3.23. The dislocations in this image take on a curved shape, which is a high-energy configuration as discussed in Section 3.1. This suggests that some other, stronger driving force might be present, forcing the dislocations to move from their initially straight shapes into these curved forms. It could be the case the strain gradients present in the epitaxial growth cause this, or that it is due to the proximity of the dislocations to the film surface (since free surfaces attract dislocations). Plan view data shows that TDD was reduced from 8x10^{8} cm^{-2} to 4x10^{8} cm^{-2}, a 50% reduction, in good agreement with preliminary ECCI measurements.

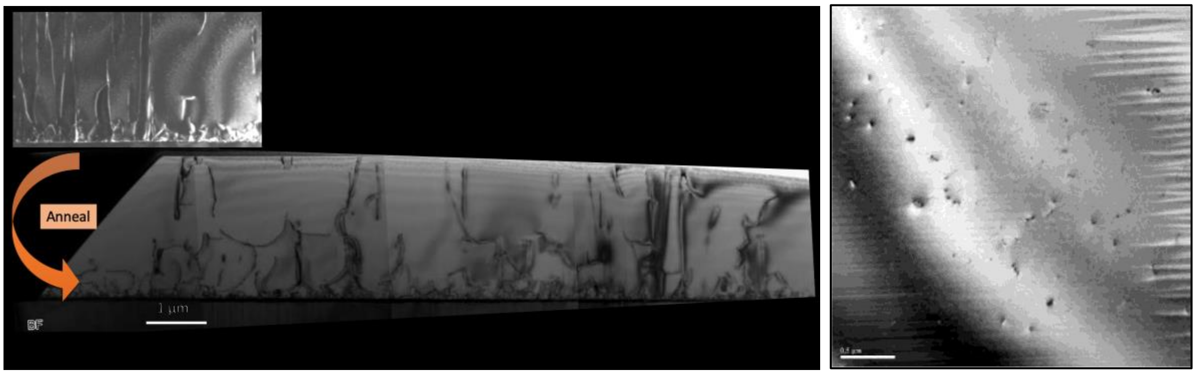

Figure 3.23: TEM of annealed AlN samples in cross-section (**left**) shows a significant change in TD geometry. Dislocations bend into curved forms during annealing. TDD near the substrate remains relatively high, while TDD near the film surface is greatly reduced. Plan view (**right**) shows an edge dislocation density of 4x10^{8} cm^{-2}.

To further understand the TD reduction mechanism, film stress was measured using the x-ray crystallographic curvature method [139]. Film stress was uniformly reduced for almost all films investigated, with only a few exceptions perhaps due to cracking or other nonidealities. Notably, the stress reduction was greater at higher annealing temperatures (see Figure 3.24) and for longer annealing durations (data not shown), indicating that a dislocation-motion mediated stress reduction via a Peach-Koehler strain energy minimization is plausible.

At this point it was not yet clear whether the overall reduction in average film stress was the driving force for TD reduction, or whether it was simply a consequence of largely random TD motion with just a slight bias toward film stress reduction.

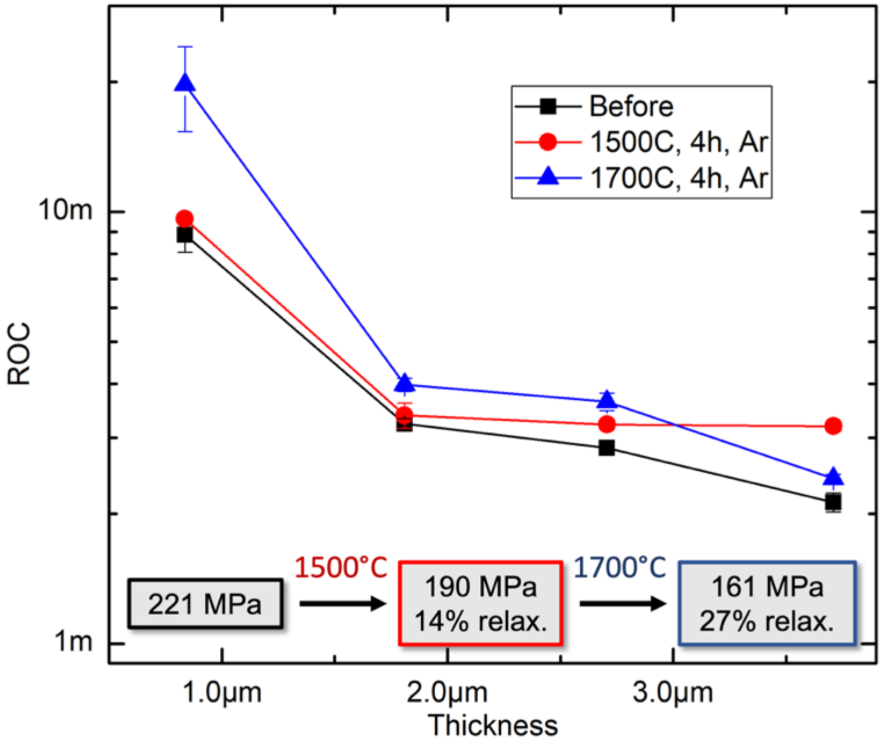

Figure 3.24: Radius of curvature and stress for annealed AlN films, showing a reasonably consistent reduction in tensile stress for almost all films.

TD motion by climb would explain the TD reduction and stress reduction. This could be the case if diffusion is occurring at these high temperatures. It is difficult to measure self-diffusion of, say, Al in AlN, because the Al atoms are all identical. We performed SIMS to look at known substitutional impurities, Si on the Al site, and O on the N site, to see if these species appeared to be diffusing during annealing (thereby indicating the plausibility of dislocation climb). The SIMS results are shown in Figure 3.25.

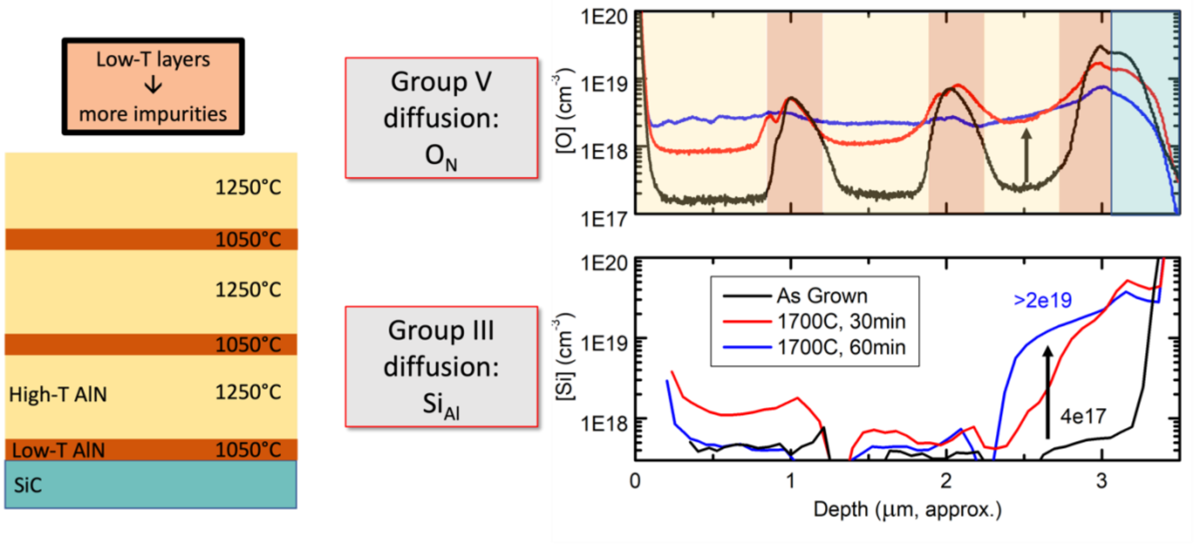

Figure 3.25: SIMS shows diffusion of both ON and SiAl in AlN films grown by MOCVD then annealed at high temperatures. This further confirms that dislocation climb is possible, and indicates a potential route to doping n-AlN using Si diffusion from a SiC substrate.

SIMS indicates that the reduced temperature AlN interlayers (as discussed in Ref. [97], and used in all our AlN and UV LED work before 2019) had higher O concentration than the surrounding high-temperature layers, attributed to the high growth pressure of 40 kPa in the reduced-temperature layers. During annealing, this oxygen diffused so that it was uniform after 60 minutes at 1700 °C. The case of Si was less clear because there were no spikes in the 3D layer. However, there was a clearly visible increase in Si near the AlN/SiC interface, perhaps due to bulk diffusion of Si from the substrate into the film. This indicated that the group III sites, as well as the group V sites, were mobile during annealing, further confirming that dislocation climb is plausible. The high Si concentration in the first 1000 nm of AlN suggested a possible route to n-type doping of AlN, which is difficult to achieve by conventional MOCVD. Initial experiments indicated that thin AlN films annealed using this method were indeed conductive, but no further work was conducted because the annealing furnace went down due to malfunctions and was never repaired.

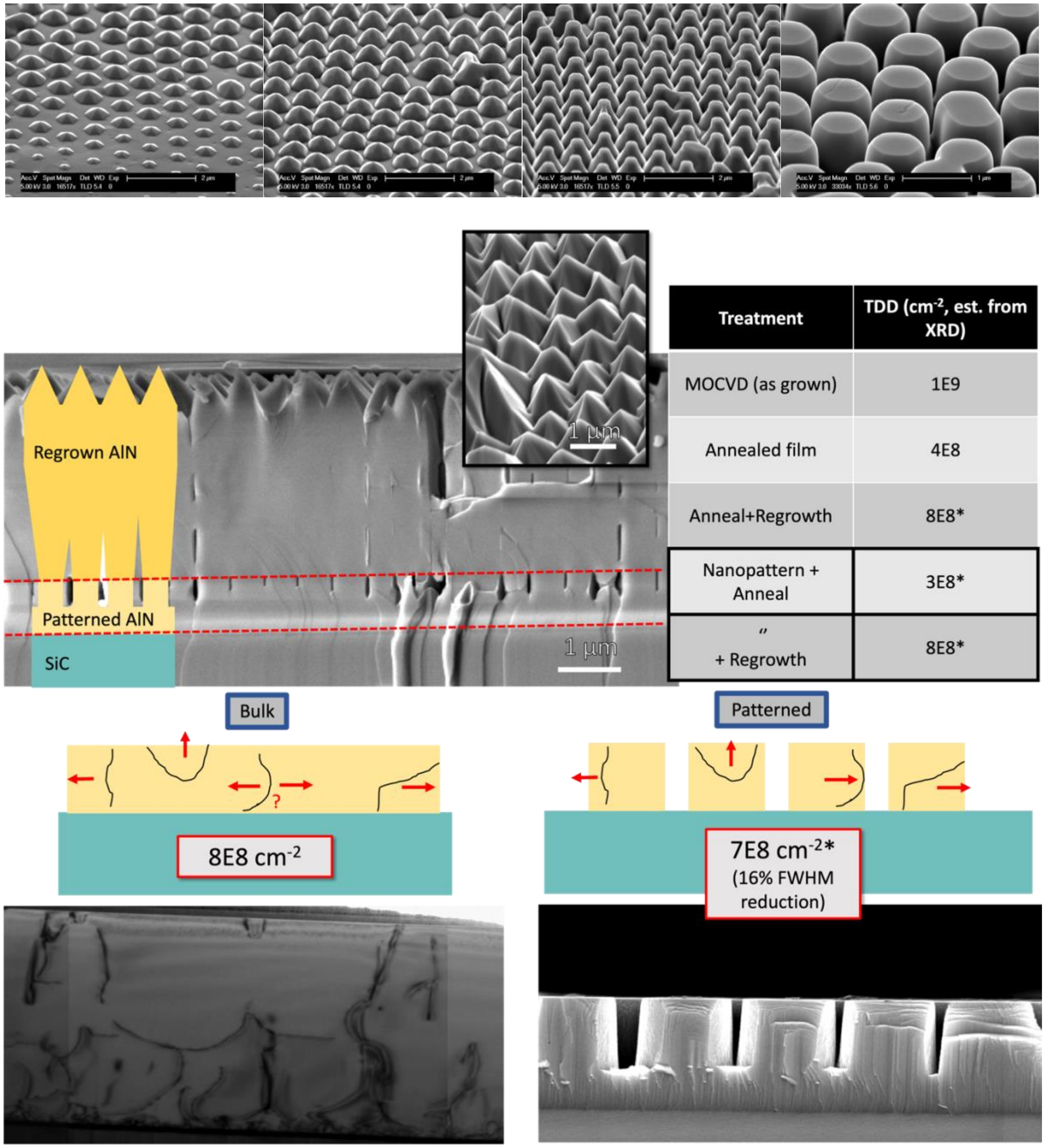

Treatment	TDD (cm^{-2}, est. from XRD)
MOCVD (as grown)	1E9
Annealed film	4E8
Anneal+Regrowth	8E8*
Nanopattern + Anneal	3E8*
〃 + Regrowth	8E8*

Figure 3.26: Nano-patterned AlN annealing study summary. **Top row** of images show a bird's eye view of annealed micropillars near the edge of the wafer (**left**) toward the center (**right**). The varying degree of pillar sublimation illustrates the effect of the capping wafer which is ineffective near the edges, but quite effective at the wafer center. After regrowth, the AlN film coalesces almost entirely but remains faceted (**middle row**). TD reduction of nanopillar AlN is only 16%, significantly less than uniform films. After unoptimized regrowth, TD returns to its initial value. *TDD values with an asterisk are estimated from XRD and ECCI, other values were measured using TEM.

In order to investigate whether stress reduction was driving TDD reduction in annealed AlN, films were patterned into micron-scale pillars using the colloidal nanolithography approach by Dr. Ley. This is a reliable and low-cost nanopatterning method which could potentially improve crystal quality by providing additional free surface area for TDs to annihilate. On the other hand, the reduced film stress in these pillars may lead to a reduction in TDD improvement, if it is the case that TDD reduction is driven by strain.

Figure 3.26 summarizes the preliminary efforts in this project, showing a slight TDD reduction estimated around 16% by XRD. Compared to 50% reductions found for planar films, this reduction was less than expected. This may be an indication that stress is a driving force for TDD reduction in annealed AlN films, and that TD fusion and mutual annihilation are more important than TD annihilation at free surfaces.

After annealing, planar AlN films were regrown. This growth was highly unoptimized, and while it did nearly fully coalesce, the film remained faceted. Additional growths would have been needed to optimize the lateral growth rate, as has been shown extensively in the literature. The TDD of regrown AlN increased only very slightly—while this did unfortunately wipe out the TD improvement from annealing, we found it promising that this could be achieved using only a few growths and without any optimization. Finally, as shown in Figure 3.27, regrowths on patterned AlN actually slightly outperformed planar regrowths, suggesting a potential synergy between annealing and lateral overgrowth effects, as was later confirmed by Susilo *et al.* [22].

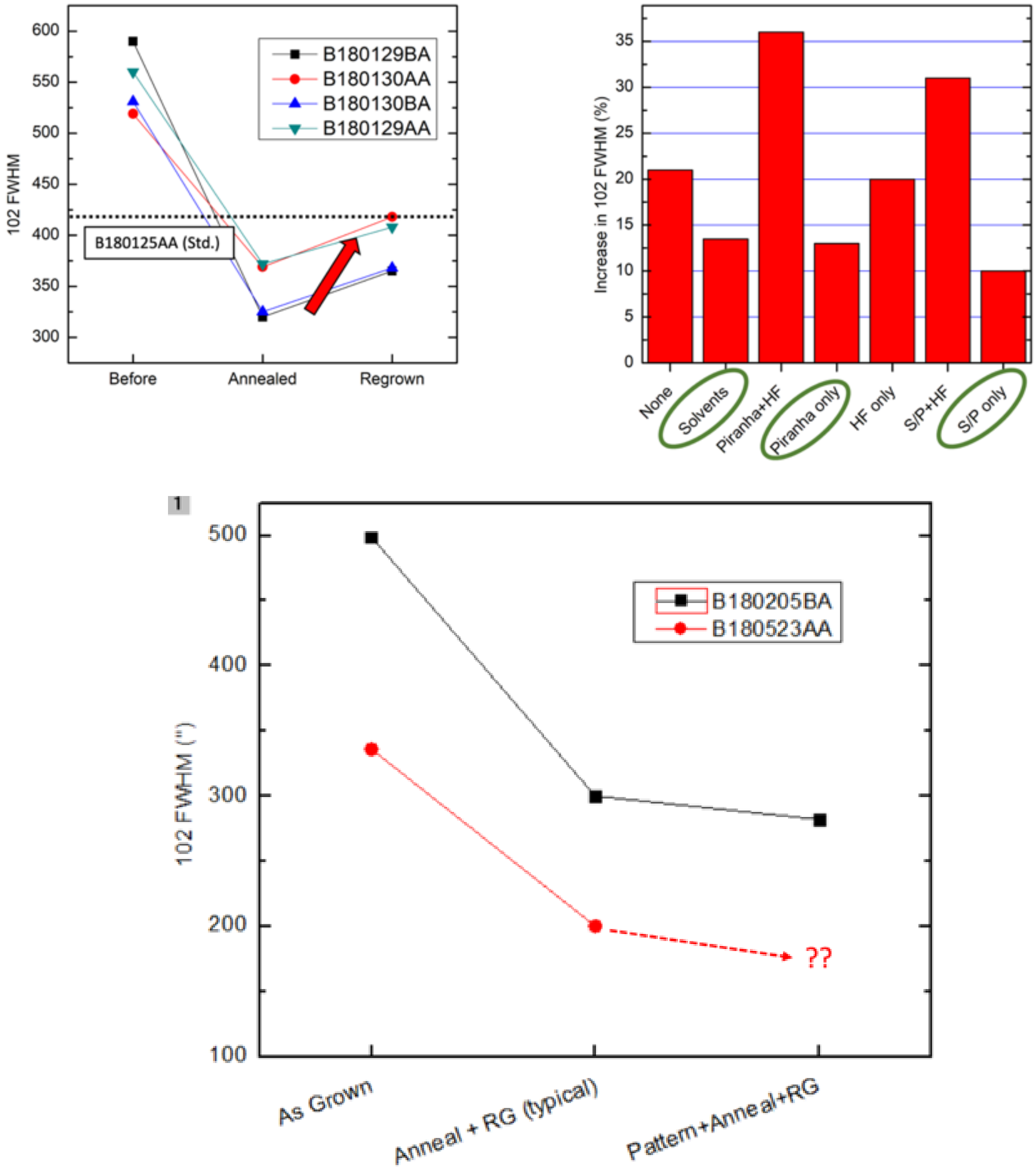

Figure 3.27: AlN regrowth on annealed films. Solvent cleaning and piranha cleaning gave better results than acid etching.

3.7 AlN on sapphire – commercial templates

When I began my PhD in 2016, there was no commercially available AlN with TDD below 10^{10} cm^{-2} to be had; by 2020, we are aware of half a dozen manufacturers offering this product, with others likely to follow. There has been a significant paradigm shift in the past 5 years, and low-cost high quality AlN/sapphire is increasingly available. These substrates are optically transparent, and can be purchased at costs comparable to SiC or other conventional compound semiconductor wafers (i.e. an order of magnitude less than bulk AlN). Some of these wafers are produced by a high-temperature annealing method, others are produced by advanced MOCVD techniques with dislocation filtering—all are produced using proprietary secret methods which might combine many of these advances.

In late 2020 we acquired AlN/sapphire from a handful of suppliers, and quickly found that the quality was excellent, and that these wafers were highly uniform. This enabled more repeatable UV LED experiments, and simplified device processing as will be discussed in the Chapters below. A bit of work was needed initially to bring up AlN growth on these wafers, which was now quasi-homoepitaxial so slightly different growth conditions were needed.

One growth defect we observed under unoptimized conditions was inversion domains, which we found by etching the AlN in dilute KOH. KOH selectively etches the N-polar face of AlN, so that inversion domains appeared on the wafers as prismatic pits shown in Figure 3.28. By using a single-step regrowth using our low-pressure, high V/III, high temperature AlN growth condition (the "2D" condition), inversion domains were eliminated and crystal quality improved. We confirmed negligible TD formation at the regrowth interface.

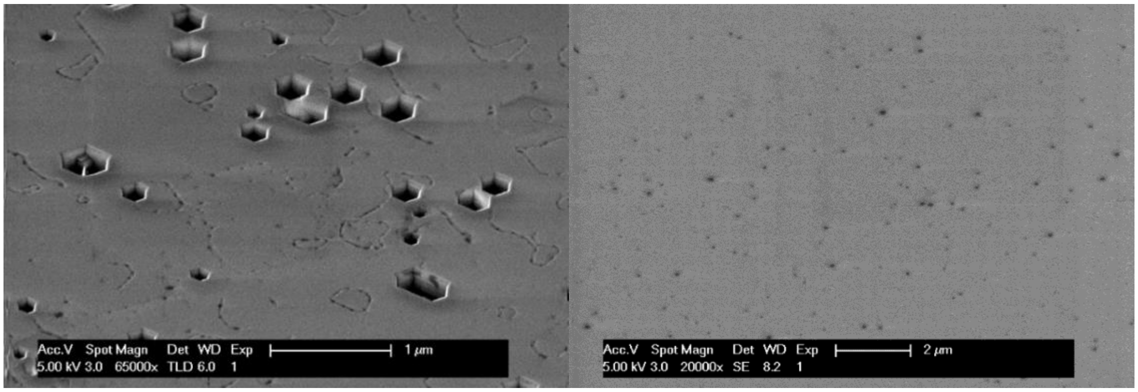

Figure 3.28: KOH etch pits show inversion domains in initial unoptimized AlN. By switching to a standard high V/III ratio, high temperature, low-pressure AlN growth condition for regrowth on AlN/sapphire substrates, inversion domains were eliminated.

TEM images of AlN grown on AlN/sapphire templates from two major suppliers (supplier 1 and supplier 2) are shown in Figure 3.29. A slight feature can be seen in the middle of the AlN/sapphire provided by supplier 1, where the threading dislocations suddenly bend (this is not the UCSB material's regrowth interface—this interface is present in the as-received material). Higher up in the stack, a faint distinction can be seen at our regrowth interface. The commercial template/UCSB interface is notable mainly by its absence; there is no measurable TD nucleation or any other contrast at this interface, suggesting it is a coherent homoepitaxial interface. Subsequent AlGaN layers can also be seen, giving additional TD bending, but no significant nucleation of new TDs.

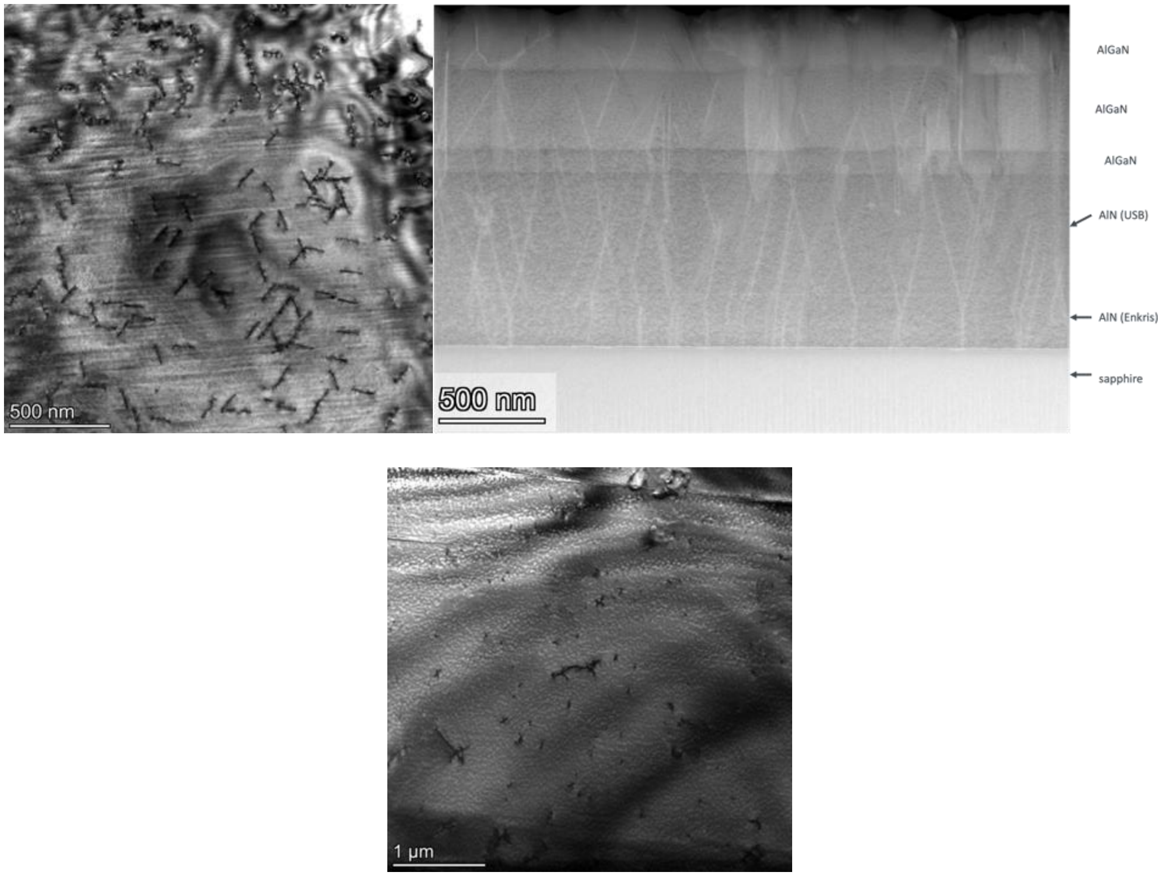

Figure 3.29: TEM of AlN regrown on commercially available AlN/sapphire templates. **Top**: plan view and cross-section TEM of substrates from supplier 1 showing a TDD of 3×10^{9} cm^{-2}, and negligible TD formation at the AlN/AlN regrowth interface. **Bottom**: plan view TEM of AlN regrown on AlN/sapphire from supplier 2, showing a TDD of 6×10^{8} cm^{-2}.

4 n-type AlGaN for UV LEDs

So often men trip by being in a rush. If one were properly to perform a difficult and subtle task, he should first inspect the end to be achieved and then, once he had accepted the end as desirable, he should forget it completely and concentrate solely on the means. By this method he would not be moved to false action by anxiety or hurry or fear.

-John Steinbeck

The change to the new reactor and new substrate materials forced us to take a step back and fully characterize our layers (we had no choice in this; we had to develop new methods from scratch anyway), giving us an opportunity to invest in some slow, methodical experiments. We began by optimizing the AlN as discussed in the previous chapter, and set aside time to fully understand the growth of n-AlGaN. Then, only after fully optimizing the AlN and n-AlGaN, we grew our first LEDs and very quickly achieved greatly improved device performance.

In this Chapter, I will first discuss some general points regarding AlGaN growth, characterization, and properties. I will then move to a more detailed discussion of Si-doped AlGaN, as this is the most challenging to grow and formed the bulk of our work regarding epitaxial growth conditions.

4.1 AlGaN MOCVD growth and characterization

The standard method for determining the composition of heteroepitaxial compound semiconductor thin films is using x-ray diffraction. This method directly measures the lattice parameter of the film: on-axis measurements (such as AlN 002) are sensitive to the *c*-lattice parameter, and off-axis measurements are sensitive to differences in both the *c*- and *a*-lattice parameters. In relatively thin, low-defect density samples, the film is assumed to be coherently strained to the substrate, so that only one in-plane measurement is needed to determine the composition; in combination with an analyzer crystal, this on-axis measurement can also determine film thickness from the fringes in the diffraction pattern.

On the other hand, for thick films with higher dislocation content, the assumption that the in-plane lattice parameters are equal cannot be made, and an analysis of off-axis peaks is needed to decouple in-plane and out-of-plane lattice parameters. A measurement of both lattice parameters using, e.g., a reciprocal space map (RSM) can be used to determine film stress and composition if alloy lattice parameters and elastic properties are known. Some details of this method are given in Bauer & Richter [151], and a full treatment specific to the wurtzite crystal structure is left as an exercise.

Example RSMs of AlGaN grown on AlN/SiC templates are shown in Figure 4.1. In this dataset, the “standard” sample shown on the far right is a typical UV LED n-AlGaN growth condition which should give 65-70% Al. As shown in the other RSMs, the composition was much lower (and the growth rate faster, indicating higher Ga uptake) when a brand new graphite puck was used. As the puck was coated, the growth rate and composition stabilized. Pucks were therefore typically coated ~10 times before using them for growth; another 20-30 quality growths could occur before pucks became overly coated and needed cleaning. After several rounds of cleaning and re-coating, pucks were discarded to reduce variability between pucks.

Well-coated pucks were found to give lower AlN TDD and more repeatable alloy compositions and growth rates than brand new graphite pucks, so this method was favored in early growths. On the other hand, the slightly variable quantity of coating material on the graphite pucks appeared to introduce a bit too much process variability as we moved into greater volumes of LED growths, so we eventually began using sapphire corral wafers surrounding the LED growth substrate. This enabled better process repeatability since a new corral wafer could be used every time. Even so, we found that the most repeatable LED growth process involved 1) reactor coating with something like an LED recipe each morning or after any duration of reactor downtime, 2) reactor baking under H_2 at 1200 °C or higher, 3) experimental growth, 4) bake, 5) experiment, and so on. Reactor coating was crucial for AlGaN composition and growth rate stability, whereas reactor baking was found to be most important for the reduction of background Mg levels.

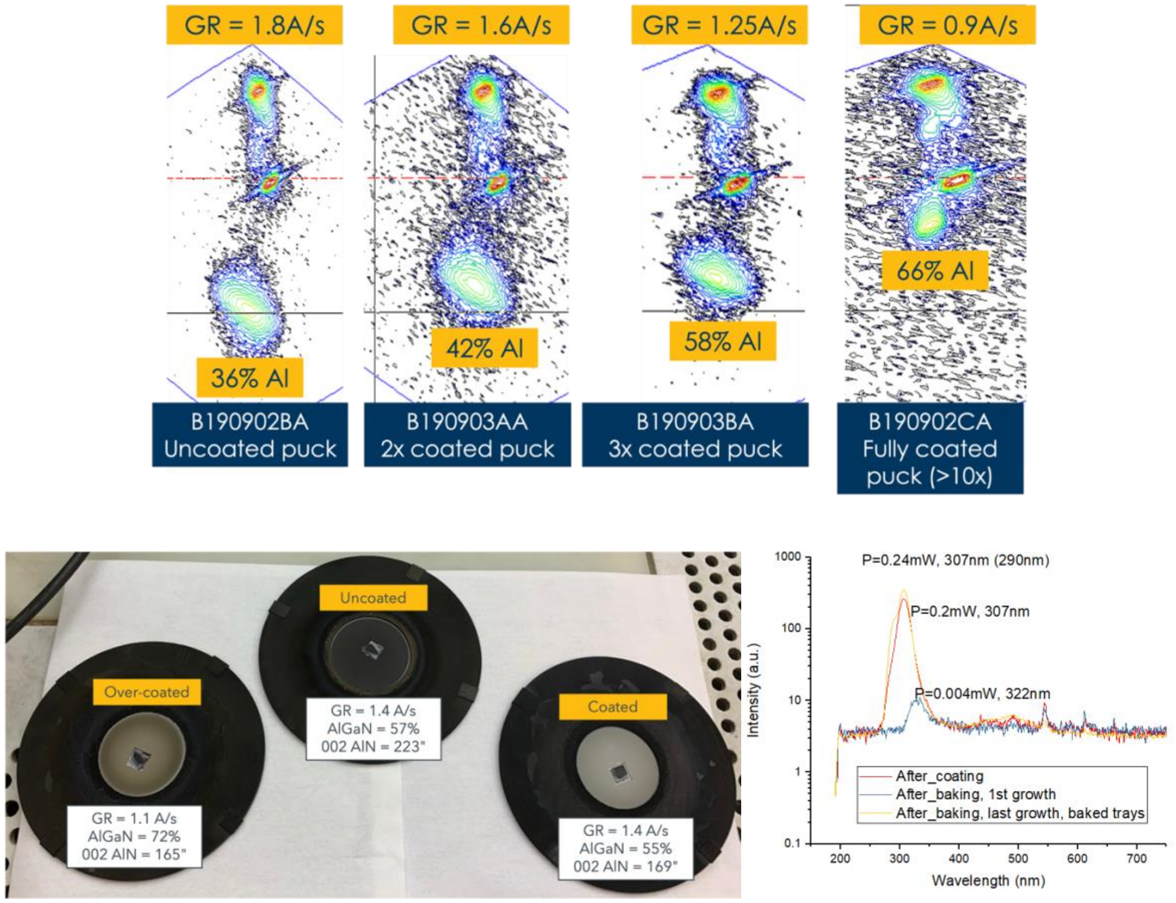

Figure 4.1: AlGaN RSM shows that puck coating significantly affects both growth rate and TMG uptake. Puck coating is illustrated below, as is a preliminary study of LED output power showing the importance of reactor coating and reactor baking.

4.1.1 Strain in thick n-type AlGaN

$Al_xGa_{1-x}N$ alloys with $x < 75\%$ have significant compressive in-plane biaxial stress when grown on AlN. This stress can be relaxed if the AlGaN layers are grown via island nucleation on the AlN template, but this introduces a high density of new threading dislocations, and is not a relevant growth mode for high-WPE UV LED devices. Another mode for stress relaxation is via dislocation inclination [98], [123], [139], which generates a gradient from compression towards tension, as illustrated in Figure 4.2. It should be noted that this relaxation is not *caused* by the compressive stress; it is rather a mechanism of tensile stress generation which occurs in nearly all *c*-axis nitride growth, as discussed in Chapter 3.

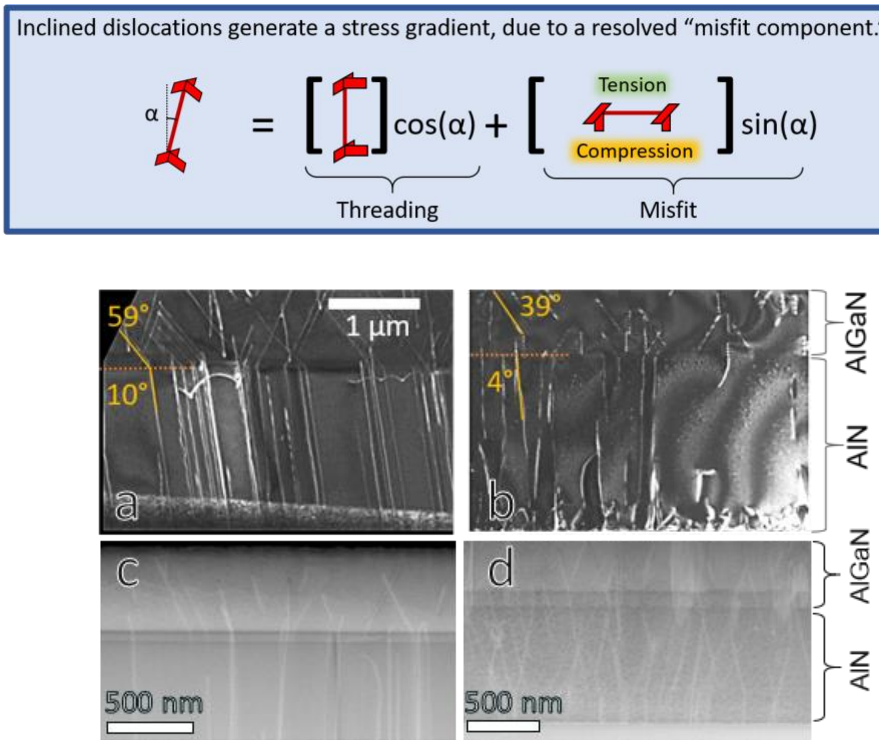

Figure 4.2: Dislocation inclination generates a strain gradient in nitride epitaxial films. **Top**: illustration of the decomposition of a TD with some horizontal component into an equivalent sum of a threading and misfit component. (a,b) TEM images for material discussed in Ref. [97], [185], showing dislocation inclination in AlGaN/AlN films grown on SiC substrates. Small but nonzero inclination in AlN; larger inclination in the silicon doped AlGaN layer above. (c) TEM of lower portion of LED from [32] showing that dislocations remain nearly vertical at AlN/UID-AlGaN interface, and become inclined in the n-doped AlGaN. (d) AlGaN on commercially available MOCVD AlN/sapphire, grown using TD reduction by inclination in the AlN.

Dislocation inclination is enhanced by Si doping [98], [139], [186], and can lead to tensile stress well beyond full relaxation [187], going even into significant tension and cracking. This effect is relevant for samples with high dislocation densities and high resistivity, because high resistivity films must be grown very thick to achieve low sheet resistance. On the other hand, for n-AlGaN with dislocation densities below about 10^9 cm^{-2}, and with resistivity below 10 mΩ-cm, concerns around relaxation and tension can be avoided by keeping film thicknesses below about 500 nm. Other reasons for avoiding AlGaN film relaxation will be discussed in Chapter 6.

4.1.2 Luminescence of n-type AlGaN

Historically, excellent agreement had always been found between AlGaN alloy composition determined by x-ray and luminescence methods, as discussed in the dissertations of Dr. Almogbel and Dr. Foronda. SEM-based cathodoluminescence (CL) was used as a fast and reliable determination of the alloys' luminescence band edge, agreeing perfectly with bandgap calculations using Vegard's law and a bowing parameter as discussed in Ref. [126]. For these samples, little difference was seen between p-type, n-type, or undoped AlGaN (this n-type material was a factor of 50-100 more resistive than our later, fully optimized material).

After fully optimizing AlGaN growth for n-type material (using major changes to growth conditions such as reduced temperature and ultralow V/III ratio, as discussed in the following sections), we no longer observed good agreement between composition and expected luminescence wavelength. As shown in Figure 4.3, an additional CL peak about 600 meV below the bandgap appeared in these samples (and many samples only had the low energy peak, with no observable band edge peak). The energy of the peak indicated it may be a defect peak such as an acceptor or donor-acceptor-pair transition; on the other hand, it was quite strong and sharp, which would not be expected for a defect emission line.

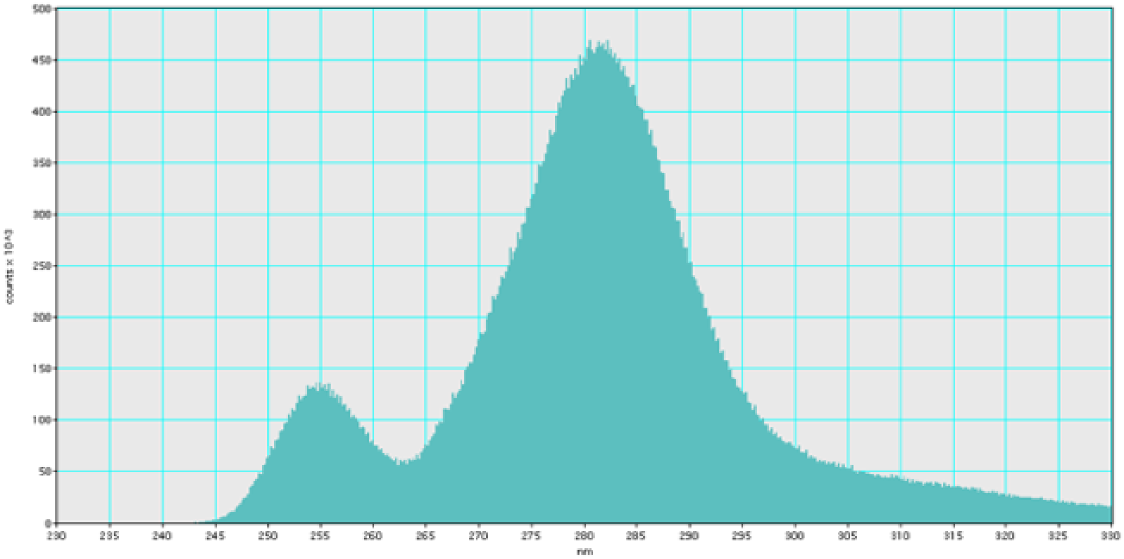

Figure 4.3: Cathodoluminescence of strongly n-type AlGaN, showing a band-edge luminescence peak at high energies, in addition to a much stronger peak about 600 meV below the bandgap.

In photoluminescence (PL) experiments of heavily doped AlGaN, we observed this low-energy peak again, as shown in Figure 4.4[15]. Next, we used other methods to measure the composition, including: spectroscopic ellipsometry (which measures the band gap as both a step in absorption and a peak in the dielectric constant), x-ray photoemission spectroscopy, SIMS, and atom probe tomography. Some of these methods are more quantitative than others; some are surface sensitive whereas others are bulk sensitive; these methods operate on fundamentally different physical principles, and they all returned the same answer: there was no reason to believe our composition measurements were incorrect.

---

[15] The strength and sharpness of the peak so resembled a band-edge luminescence peak that for a while I was very concerned that we may have made a mistake in our composition determination by XRD. After looking over the math multiple times and checking with colleagues, we concluded that no errors could be found in the XRD analysis or data collection methods.

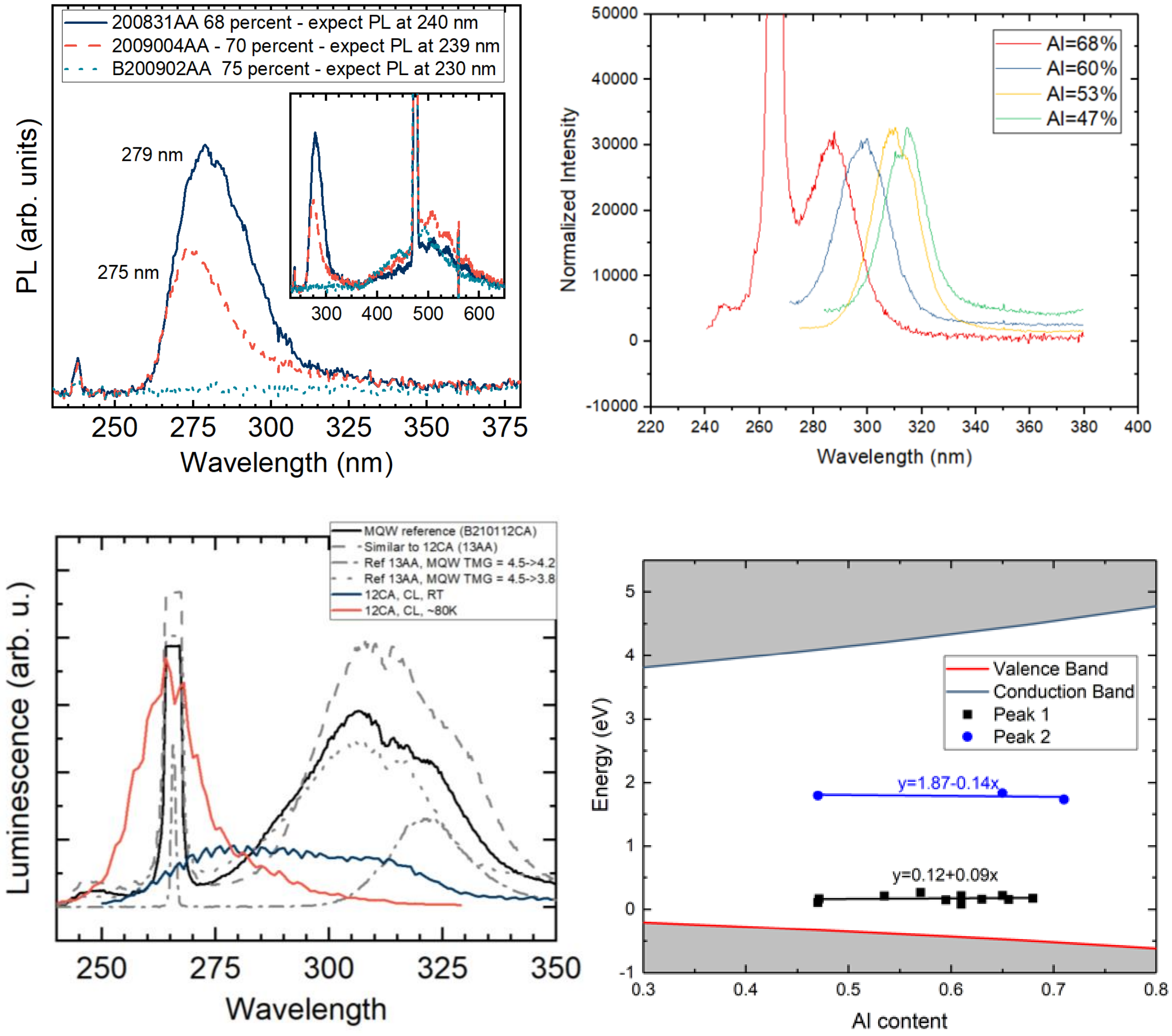

Figure 4.4: A strong PL peak 600-800 meV below the bandgap appears in heavily n-type films. **Top left**: PL collected using a laser with 234 nm wavelength, which excites only layers with bandgaps wider than ~5.3 eV (no emission from 75% Al). Both samples emit a single strong PL peak 700 meV below the bandedge. **Top right**: PL collected using a 263 nm laser, showing a wide variety of alloy compositions all giving emission redshifted by 600-800 meV. **Bottom left**: CL spectra and PL spectra of a MQW sample (solid curves). Black data is PL, showing the red-shifted peak as expected, attributed to the surrounding bulk n-AlGaN. Blue data is room temperature CL, showing a mixture of emission from the n-AlGaN and other layers including the undoped high-Al layer deeper in the device, and perhaps some MQW emission. Red data shows the low-T CL, showing the expected MQW wmission wavelength of ~265 nm. **Bottom right**: compilation of PL data for a large number of samples, showing that the wavelength of the redshifted emission is consistent with a CB-to-deep-acceptor transition.

So, we proceeded to further characterize the strong luminescence peak which we now attributed to some highly radiative defect pathway. Luminescent defects in GaN have been scrutinized for many years [188], and there is an increasingly large library of references for

AlN luminescence as well [189]. The literature for luminescence properties of defects in AlGaN is comparatively thin, but some insight may be gleaned from the literature of the related binaries. It seems plausible that the luminescence line consistently found 0.5-0.8 eV below the bandgap in the highly doped alloys is caused by an acceptor defect; acceptors are known to be present in highly doped AlGaN where they act as compensation centers.

Temperature dependent PL spectra are shown in Figure 4.5. The expected near-band-edge emission at 4.5 eV is missing, and the highest-energy peak observed is at 4 eV. This peak (Peak 1 in Figure 4.4, bottom right) is labeled “blue” by analogy with the acceptor-related blue emitting peak in GaN that is known to be highly radiative and likely caused by Mg. (It could also be attributed to a group-III vacancy which is a multiply charged acceptor defect that may have a strong carrier capture rate). Another very broad visible-wavelength peak labeled as “yellow” is also shown; this peak was only present in heavily doped samples with significant dopant compensation (Peak 2 in Figure 4.4), and therefore may correspond to a different point defect such as a vacancy complex [190], [191]. The specific identities, energies, and optical properties of acceptor defects including vacancies in AlGaN are not fully understood, so it’s possible that these analogies are not relevant at all. For instance, the “yellow” luminescence line in GaN is understood to be from an acceptor about 800 meV above the valence band, which may be a closer analog to the strong luminescence observed in these samples.

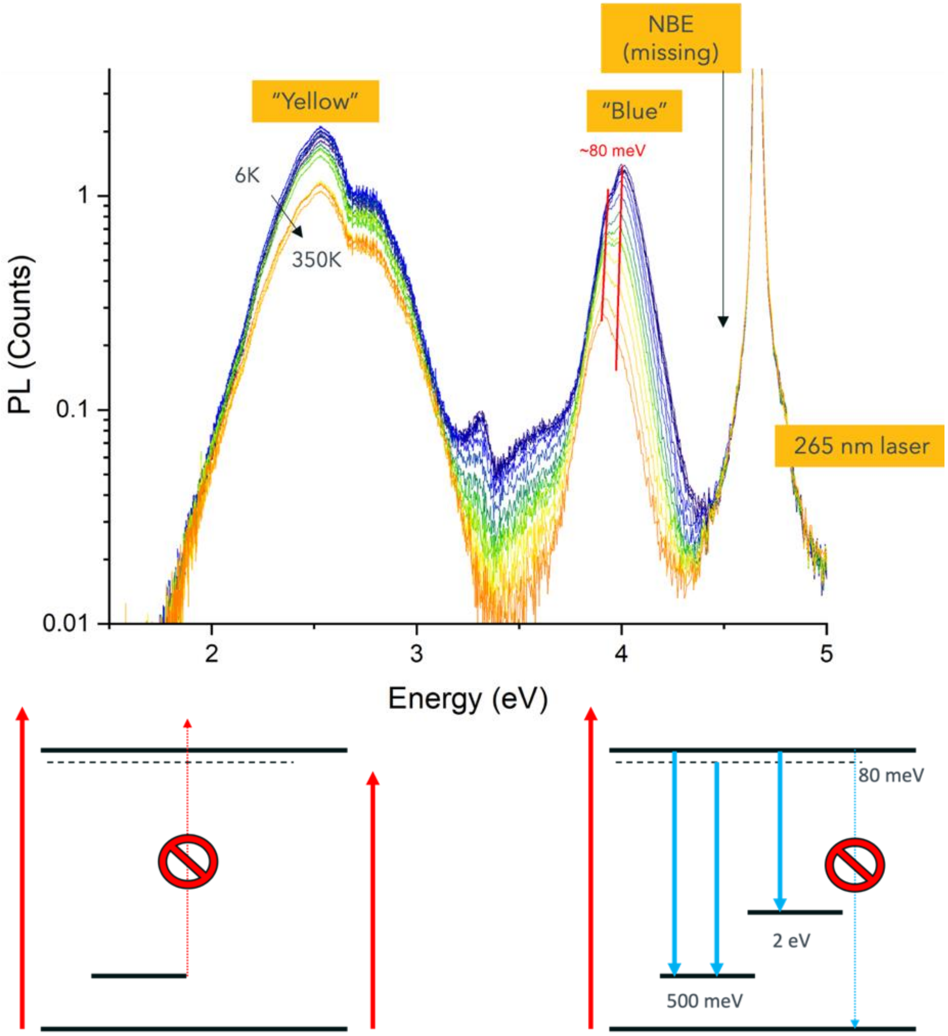

Figure 4.5: Temperature dependent PL spectrum of a 47% Al n-AlGaN sample (top). Peak labels correspond not to true emission wavelength colors, but to labels used in the (hypothetically) analogous GaN luminescence spectra. (bottom) Diagram illustrating the photo-pumping behavior (left) and emission behavior (right) observed for such samples.

In the lower portion of Figure 4.5 I present a schematic illustration of the PL behavior of these samples. Because the acceptor levels are spatially diffuse and have a relatively slow capture rate of electrons from the valence band, the number of carriers pumped from this level to the conduction band (CB) is negligible, illustrated by the crossed out dotted arrow. Instead, the most relevant pathway for carriers pumped by laser illumination is shown with the bold red arrow, going directly from the valence band (VB) to the conduction band (VB→CB), or from the VB into a hydrogenic donor level (probably via relaxation from the CB).

In terms of experimentally measurable implications, this predicts that a laser wavelength above the bandgap energy is needed to excite bright luminesence, even if the resulting luminescence energy is significantly lower than the absorption band-edge. That is indeed what we observe, although there is a rather wide region of wavelengths near the expected band edge which give significant luminescence intensity: for instance, sample with a band edge around 260 nm often still give luminescence when excited by 263 nm laser illumination, but samples with band edges below 250 nm did not. Those samples could only be excited by a 233 nm laser. The 233 nm laser could not excite samples with band edges below 230 nm (see Figure 4.4). Thus, by measuring many samples with different expected band gaps against these two laser wavelengths, we can confirm that the laser energy must be greater than the approximate alloy bandgap to produce PL, further confirming that our composition calibrations are correct.

The data for several AlGaN samples with different compositions is shown in the lower-right of Figure 4.4 (courtesy of Y. Yao). Modeling the strong luminescence peak as an acceptor (which is to say, considering the transition energy to be an energy difference between the CB and a state low in the gap) yields an acceptor level which does not follow the valence band, but rather remains mostly flat versus alloy composition, characteristic of a deep acceptor.

In the lower right portion of Figure 4.5, proposed emission lines are illustrated. The 2 eV emission line is not particularly well studied here, but the acceptor like defect emission line 0.5-0.8 eV away from the valence band is of particular interest because of its strength, sharpness, and persistent appearance in all films grown under the low V/III conditions discussed in this Chapter (for simplicity I am showing it as 0.5 eV in this figure, but the exact energy difference was not the same in all samples, and varied between 0.5 and 0.8 eV). Also illustrated is a donor level 80 meV below the conduction band, perhaps explaining the appearance of two small peaks within the overall 0.5 eV luminescence feature in Figure 4.5. I should note that if that is the explanation for the small splitting of that peak, one would expect the higher-energy band-to-acceptor transition to become dominant at higher temperatures, and the lower-energy donor-to-acceptor transition to dominate at lower temperatures where more electrons are localized in the donor state. The close resemblance of the values 80 meV and 500 meV to the expected ionization energies of Si and Mg, respectively, might be coincidental. Due to the known low Mg concentration in our n-type material, another intrinsic acceptor such as a group III vacancy or silicon-vacancy complex may be more plausible, and this is also expected to have an energy around 0.5-0.8 eV above the valence band [192]. Potential future work could include time-dependent PL or power-dependent PL to further understand the origin of this defect luminescence peak.

4.2 Silicon-doped AlGaN

The ideal silicon doped n-$Al_xGa_{1-x}N$ layer provides electrons to the active region while adding a minimal driving voltage due to series resistance. This includes contact resistance and sheet resistance contributions, both of which depend strongly on the concentration of intentionally introduced silicon donors in the AlGaN crystal. Substitutional Si_{III} impurities in AlGaN contain one more valence electron than the atom they replace in the lattice and are called donors because they are neutral when occupied, and positively charged when unoccupied. This extra electron occupies the conduction band but is bound near the donor atom by the Coulomb interaction. At finite temperature the extra electron may have enough energy to escape the donor atom and move freely through the semiconductor crystal. The energy difference between an electron bound to a donor site and a free conduction electron, E_{CB}-E_D, is determined by the properties of the donor and of the host lattice. E_{CB}-E_D is on the order of 50 meV for $Al_xGa_{1-x}N$:Si with $x < 0.65$, but increases to around 200 meV for $x > 0.95$ [193].

As shown in Figure 4.6, a very wide range of voltage efficiencies have been reported in the high-EQE UV LED literature. Commercial devices now have peak VE around 80%, and there are even many academic results above 70%. This suggests that VE should not be considered a major fundamental bottleneck preventing UV LED progress, only a technological challenge to be overcome. In this section, I will discuss the latest technology of low-resistance n-AlGaN, enabling high VE UV LED operation.

A sheet resistance of no more than 100 Ω/□ is needed to enable uniform, low-voltage-drop current injection (without n-side current crowding) in UV LEDs with mesa sizes on the order of 0.1 mm^2 [194]. Resistive n-AlGaN can result in current crowding, especially at high current densities. This occurs when the lateral resistance is high compared to the vertical (p-side) resistance. The characteristic current spreading length and series resistance are proportional to $R_{sh}^{-1/2}$ and R_{sh}, respectively (wherein R_{sh} is the sheet resistance of the n-AlGaN layer, $R_{sh} = \rho/t$, where ρ is the electrical resistivity and t is the n-AlGaN thickness).

Bulk n-type resistivity can be written as $\rho^{-1}=en\mu$, where e is the electron charge, n is the electron concentration, and μ is the electron mobility. Thus, the sheet resistance can be reduced by (1) increasing the n-AlGaN thickness, (2) increasing the electron concentration, and (3) increasing the electron mobility. There are some reports of deep UV optoelectronic devices with very thick n-AlGaN [6], [24], [195], showing that it is feasible to produce high-

WPE devices using this approach, but there are some risks to growing n-AlGaN to thicknesses greater than 1 μm (see Ref. [196] for details).

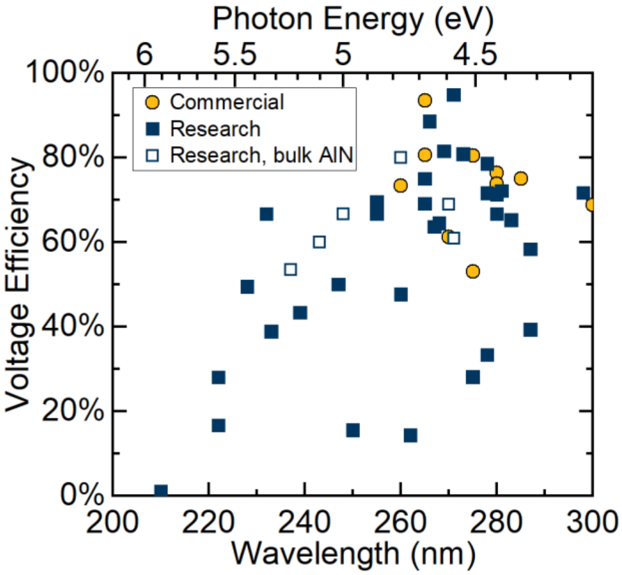

Figure 4.6: Peak voltage efficiency for a selection of the best WPE reports, showing that VE peaks around 260 nm – 280 nm, where most research resources have been spent. Commercial devices (circles) have similar VE to state-of-the-art research devices on both foreign substrates (filled squares) and bulk AlN substrates (open symbols).

4.2.1 Bulk resistivity of n-AlGaN

Strongly n-type $Al_xGa_{1-x}N$ with 60% < x < 75%, is needed for LEDs emitting in the conventional GUV. Good n-type conductivity in this composition range has been achieved for both *c*-plane (see Figure 4.7) and semipolar [197] AlGaN, and is no longer the primary obstacle to high electrical efficiency GUV LEDs; in this section, we discuss how we achieved low-resistance n-type AlGaN using optimized MOCVD growth conditions. These results enabled us to produce high voltage efficiency LEDs, and are also relevant for applications in high-voltage ultrawide bandgap electronics (which have demonstrated outstanding critical breakdown field values, but are currently mostly limited by series resistance and mobility constraints from high contact resistance and bulk n-type resistivity of AlGaN with an Al molar fraction above 50%).

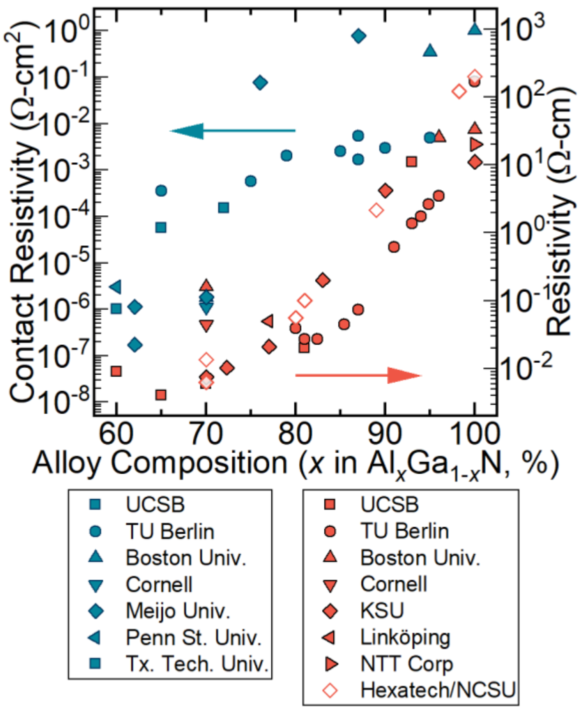

Figure 4.7: Contact resistivity (left, blue) and bulk or sheet resistivity (right, red) versus alloy composition for $0.6 < x < 1.0$. The n-type ohmic contact resistivity is on the order of 10^{-6} Ω-cm² below $x = 0.7$, then increases by three orders of magnitude for $x > 0.7$. Bulk resistivity as measured by Hall effect increases smoothly with respect to alloy composition. Data compiled from Refs. [198]–[205] (contact) [1], [193], [198], [205]–[211] (bulk), as well as UCSB results [126], [196].

4.2.2 MOCVD growth of highly conductive n-AlGaN

Electron mobility in highly conductive n-AlGaN is lower than in GaN: it is typically between 5 and 100 cm²/Vs in material used for GUV LEDs. As a result, electron concentrations (and thus, silicon concentrations) must be above 10^{19} cm^{-3} for low resistivity. Arbitrarily high [Si] can be achieved by metal–organic chemical vapor deposition (MOCVD), but above some threshold [Si], additional impurity incorporation ceases to provide additional free electrons. For very high [Si] = $[\mathrm{Si}]_{knee}$, there is usually an inversion of the relationship between [Si] and *n*, meaning that the additional Si atoms above this threshold either cease to act as shallow donors or are compensated by acceptor defects [191], [211]–[213]. This effect is referred to in the literature as self-compensation, and the threshold or *knee* value is not a fundamental property, but a variable [126], [196], [208], [212], [214], [215] which depends on growth conditions such as growth temperature, growth rate, V/III ratio, and others.

4.2.2.1 Materials and Methods

The experiments presented in this section were performed on a wide variety of substrates (4H SiC, 6H SiC, and multiple AlN/sapphire wafers of different thicknesses from different suppliers, and produced by different methods), and on material grown on two different MOCVD reactors. We found that the trends were identical between all substrate types and reactors, only the measured thermocouple temperature and V/III ratios differed between reactors. This agreement suggests that the trends identified in our experiments are likely to apply to a wide variety of systems and substrates.

AlN/SiC templates were grown by MOCVD using the methods discussed in either [97] (TNSC reactor) or [123] (UCSB custom reactor). AlN/sapphire templates were obtained commercially. AlN templates were then used to grow 50 nm thick undoped $Al_{0.85}Ga_{0.15}N$ interlayers. Next, Si-doped $Al_{0.65}Ga_{0.35}N$ films up to 700 nm thick were grown using various thermocouple temperatures, various V/III ratios, and a reactor pressure of 20 kPa[16].

Samples were fabricated into Van der Pauw patterns for Hall measurements and circular transmission line method (CTLM) structures for characterizing contact resistivity. Dry etching was performed using $SiCl_4$-based reactive ion etching, and contacts were deposited using electron beam deposition and then annealed using a rapid thermal annealing (RTA) system under N_2 ambient at temperatures between 700 and 940 °C for 30 seconds.

---

[16] Reactor pressures and V/III ratios are not universally reported in the high-Al AlGaN literature; based on the limited number of reports, we expect that these are among the highest pressure and lowest V/III ratios reported for highly conductive $Al_xGa_{1-x}N$ with $x > 0.5$.

Hall measurements were conducted using both annealed V-based contacts (discussed below) and soldered indium contacts. Lithographically defined Van der Pauw structures enabled precise, local measurements of carrier concentration and mobility, whereas indium contacts provided approximate, average values across the entire epitaxy surface. Magnetic fields of ±0.2 T, ±0.4 T, and ±0.6 T were used with currents up to 0.1 mA. Good agreement (<5%) was found among both contact types and all magnetic fields, indicating good epitaxial uniformity.

Atomic force microscopy (AFM) was carried out using an Asylum MFP-3D in AC mode with a high-stiffness cantilever. High-angle annular dark field (HAADF) scanning transmission electron microscopy (STEM) and Energy-Dispersive X-Ray Spectroscopy (EDS) mapping were performed with a ThermoFisher Talos G2 200X TEM/STEM system operated at 200 kV. The sample for HAADF-STEM and EDS was prepared by the focused ion beam (FIB) technique with FEI Helios Dualbeam Nanolab 600.

RSM data (not shown) indicated a low degree of relaxation for the n-AlGaN layers studied in this report. Dynamic secondary ion mass spectroscopy (Cameca IMS 7f auto SIMS) with a magnetic-sector mass filter was used to measure the concentration of Si and other impurities in AlGaN films. The Cs^+ primary beam energy was 15 kV, and measurements were performed using high mass resolution to distinguish between ^{28}Si, N_2, and $^{27}Al^1H$ ions.

Positron annihilation spectroscopy (PAS) experiments in the Doppler broadening mode were conducted with a slow positron beam at 10 keV to estimate the concentrations of negative and neutral cation vacancies (V_{III} and V_{III}-related complexes) in the AlGaN:Si layers. High purity germanium detectors with resolution of 1.25 keV at the 511 keV annihilation line were employed to collect approximately 10^6 counts in the annihilation spectra. The S parameter was defined as the fraction of counts around the < 0.96 keV-wide central region of the peak, and the W parameter is the fraction of counts in the tail of the peak at the energy range of ±(3.00-7.60 keV) from the center. Details of the experiments and analyses are in Refs. [216],[217].

4.2.2.2 Temperature, growth rate, and TMI surfactant

Historically it was believed that AlGaN must be grown at very high temperatures due to the Al precursor mobility issues discussed in Chapter 3. While high temperatures *did* favor smooth surface morphologies, reduced temperatures were in fact optimal for n-type doping. As detailed in Ref. [91], we found that the optimal temperature window (on the TNSC reactor) for n-AlGaN growth was above 1000 °C (high enough to prevent C incorporation), but below 1250 °C to improve n-type conductivity.

We grew n-AlGaN samples with 65% Al content at three temperatures: 1050 °C, 1115 °C, and 1175 °C (TNSC thermocouple design), each with various disilane precursor flow rates (see Figure 4.8). At each temperature, optimized silicon flow for lowest resistivity, but the trends with respect to electron concentration were notably different. At 1175 °C, we observed the typical knee behavior described above. However, at 1115 °C and 1050 °C, we instead observed a flattening or saturation of the electron concentration. The samples grown at 1175 ºC also had a lower growth rate, so we cannot conclusively state whether the qualitatively different over-doping behavior is due to growth rate, temperature, or both. Other experiments conducted by Dr. Almogbel (not shown) indicated that samples grown at 1 Å/s at 1175 ºC showed the same knee behavior as the data pictured in Figure 4.8, suggesting that growth temperature is the stronger effect.

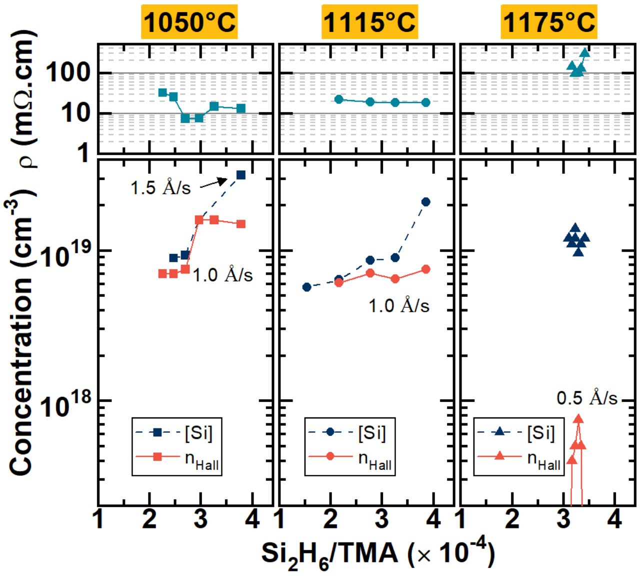

Figure 4.8: Temperature dependence of *n* and [Si]. The dependence of the electron concentration determined by Hall measurements on disilane/TMA molar ratio for various growth conditions: fast growth at 1050 ºC, fast growth at 1115 ºC, and slow growth at 1175 ºC. AlGaN:Si grown at lower temperatures had wider optimal doping window, higher *n* and lower resistivities, while AlGaN:Si grown at higher temperature had narrower optimal doping window and experienced earlier onset of overdoping-like behavior. In all growth modes, the free electron concentration *n* peaked at approximately the same optimal disilane/TMA molar ratio, *n* was found to saturate at some temperature-dependent limit even when the silicon concentration increased. (Temperatures refer to the thermocouple reading of the TNSC reactor design used 2016-2018, 150 ºC lower than the UCSB custom reactor used 2019-present).

We also found a significant difference in surface morphology in the silicon doped samples, compared to undoped AlGaN of the same composition, as shown in Figure 4.9. The undoped AlGaN showed atomically flat, 2D step flow morphology at all temperatures above 1050 ºC. The strongly Si-doped material showed a hillock-morphology with an RMS roughness around 2 nm, regardless of growth rate or temperature. This strong dependence on Si concentration (with no discernable effect of temperature or growth rate) illustrates the anti-surfactant nature of Si during MOCVD growth.

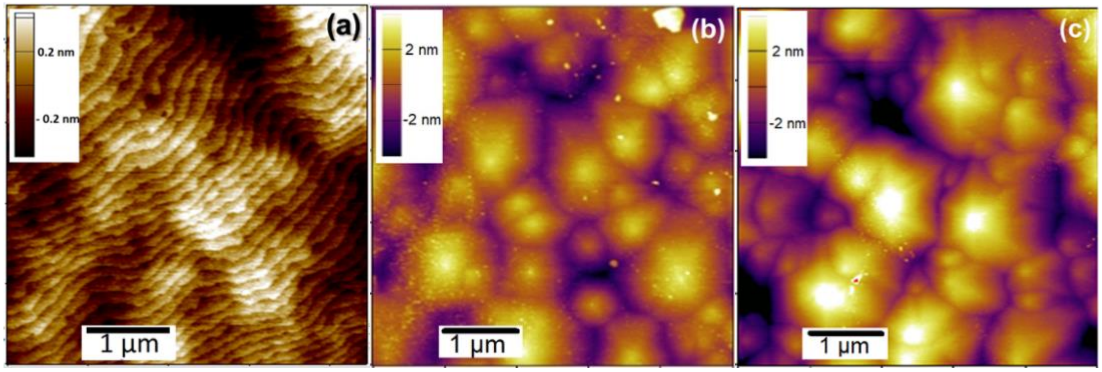

Figure 4.9: AFM images of AlGaN:Si layers (optimized with respect to resistivity) grown at different temperatures. (a) undoped AlGaN. (b) AlGaN:Si grown at T = 1050 ºC (RMS = 1.4nm) (c) AlGaN:Si grown at T = 1175 ºC (RMS = 1.9nm). These films were grown at 1 Å/s, samples grown at slower growth rate of 0.5 Å/s exhibited similar hillocks-mediated surface morphology with comparable smoothness, likely indicating that the silicon-induced roughening is controlling AlGaN:Si surface quality more than the growth temperature or growth rate in this growth regime.

All the films studied in this experiment were degenerately doped—that is, the electron concentration exceeded the conduction band density of states (which is in the low 10^{18} cm^{-3} range for AlGaN)—so they showed negligible temperature dependence in electron concentration. This is unfortunate, because in non-degenerate samples, temperature dependent Hall effect measurements provide useful insights into compensation and defects in doped materials. We *could* have measured temperature dependent Hall of lightly doped samples, but that would defeat the purpose of studying the unique compensation effects in over-doped samples. Because the doping is degenerate, we can assume near-unity ionization of donors, and therefore any difference between electron concentration, n, and silicon concentration [Si], must be due to *compensation*—that is, the presence of acceptors which trap electrons.

We were unable to find any of the most common compensating defects using SIMS, as shown in Figure 4.10. The group of Prof. Tuomisto performed PAS to identify the signature of negative and neutral defects in the material, but these were not found in significant concentrations either. Thus, the exact identity of the compensating defect which explains the large discrepancy between n and [Si] remains a mystery for now.

At 1175 ºC, we found that resistivity could be reduced in half by doubling the growth rate from 0.5 Å/s to 1.0 Å/s, with a further slight improvement when increasing the growth rate further to 1.5 Å/s. The effect was less pronounced at 1050 ºC where resistivity was lower for all growth rates generally. At 1050 ºC, we next introduced a TMI surfactant flow during all growths. While it did not give the expected morphology improvement, it did greatly reduce the observed resistivity, achieving our best values of 4 mΩ-cm (65% Al), 6 mΩ-cm (70% Al), and 20 mΩ-cm (83% Al). Finally, we then transferred this approach to the new UCSB custom-designed MOCVD reactor, achieving similarly low resistivities.

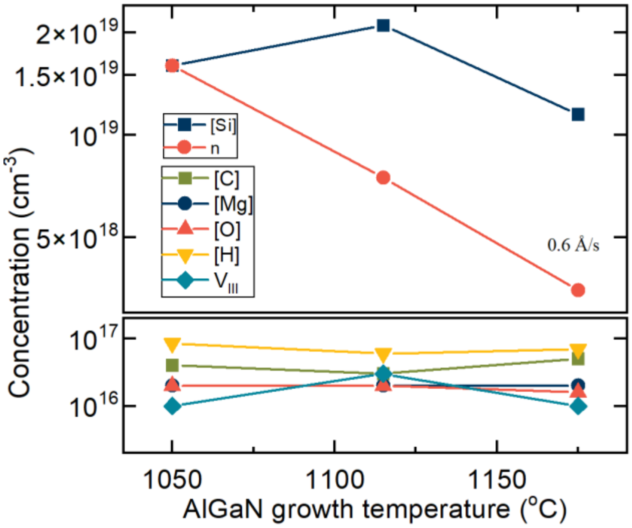

Figure 4.10: Comparison of silicon, carbon, magnesium, oxygen, and hydrogen concentration from SIMS as well as electron concentration from Hall measurements and group-III monovacancy estimates from PAS. No atomic impurities can explain donor compensation behavior. All films were grown at TMA = 10 sccm. All SIMS measurements were calibrated using relative sensitivity factors from ion-implanted AlGaN standards, and have relative uncertainties of ~20%.

4.2.2.3 V/III ratio

Next, we explored the effect of the molar ratio of group V (NH_3) and group III (TMA and TMG) MOCVD precursors, the V/III ratio, on the composition and n-type conductivity of $Al_xGa_{1-x}N$:Si with $x = 0.65 \pm 0.05$. These growths were all performed on the new UCSB custom

MOCVD reactor, using the same methods as above. The optimal growth temperature on the new reactor was found to be 1200 ºC, which we attribute to a 150 ºC thermocouple temperature difference due to different heater and TC designs[17]. We confirmed these conditions work well on SiC substrates, but all the experimental data shown in this section is for sapphire substrates.

First, the relationship between NH_3 flow and molar efficiency for TMG and TMA was investigated to for growth conditions giving 65% AlGaN at a growth rate (GR) of 2 Å/s, over a wide range of V/III ratios. It was found that V/III had some effect on GR, such that a decrease of about a factor of one-half in TMA was needed to maintain constant GR and composition at the highest NH_3 values. On the other hand, the necessary TMG to maintain 65% composition (see Figure 4.11) reduced by nearly an order of magnitude between NH_3 flows of 4 sccm and 400 sccm (corresponding to V/III of 10 and 6,000, respectively). As NH_3 flow was increased further above 400 sccm, the necessary TMG flow increased again.

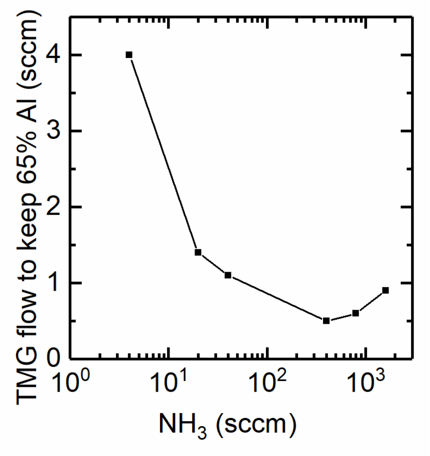

Figure 4.11: TMG flow needed to achieve 65% AlGaN over a wide range of ammonia flow levels, while adjusting the TMA flow between 2 and 4 sccm to maintain a constant growth rate around 2 Å/s. Data span V/III ratios from 10 to 16,000.

---

[17] This temperature offset was based on data from AlN crystal quality and morphology, AlGaN morphology and conductivity, and emissivity measurements using a pyrometer (which are not particularly accurate either, but were consistent nonetheless). The higher temperature reading is not unexpected because the thermocouple in the UCSB custom system is located physically closer to the susceptor than in the TNSC reactor.

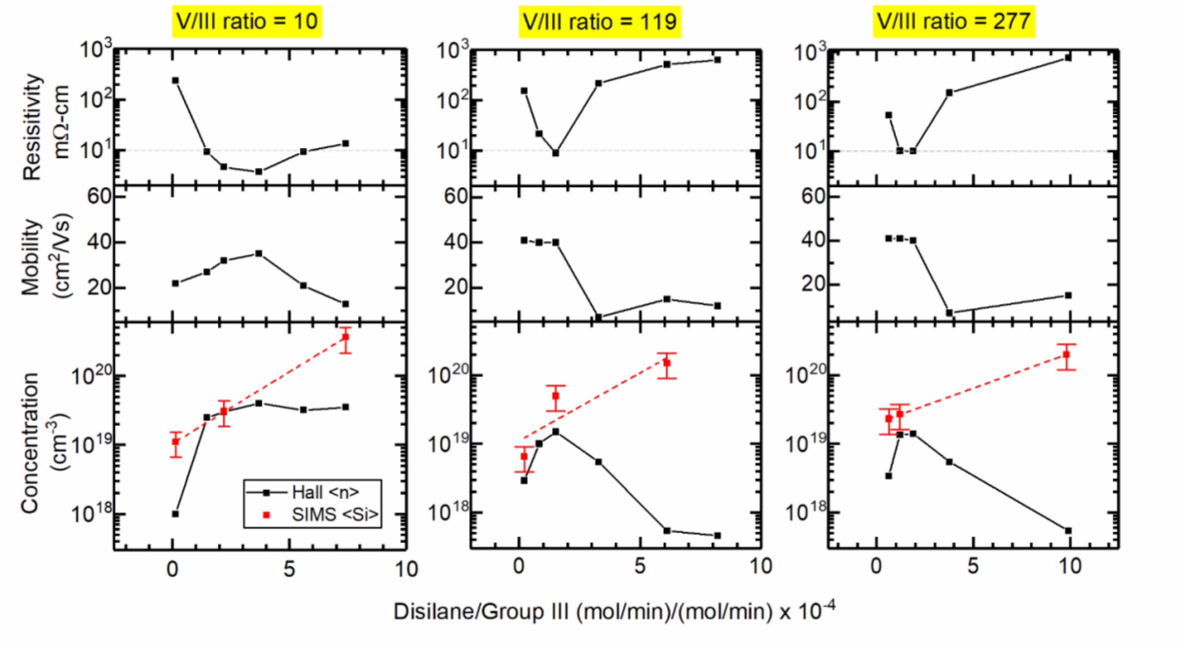

Figure 4.12**:** Resistivity, electron mobility, electron concentration (Hall), and silicon concentration (SIMS) for the three lowest V/III ratio conditions investigated. In all cases, [Si] increased monotonically with disilane flow. Knee behavior in electron concentration was observed for V/III > 100 but not for V/III = 10. Knee behavior also corresponds to drastic reduction in mobility for V/III > 100, which is in contrast to the gradual change in mobility for V/III = 10. As a result of the qualitative differences in electron concentration and mobility trends, growths at V/III = 10 show a much wider doping window than growths at V/III > 100.

A steady increase in Si incorporation with increasing disilane flow (shown in Figure 4.12, with log-linear trendlines to guide the eye) was observed for all growth conditions. For V/III ratios > 1,000, no highly conductive films were observed. In the three lowest V/III conditions, shown in Figure 4.12, increasing [Si] > 3×10^{19} cm^{-3} failed to increase the electron concentration, *n*, in the material. Instead, the additional silicon either led to a knee behavior (in the V/III = 119 and 277 cases), or to a saturation in electron concentration (in the V/III = 10 case). Additional SIMS data (not shown, but similar to Figure 4.10) confirmed that [C] incorporation was too low to account for the observed compensation, and the threading dislocation density was low enough that compensation by dislocations could be neglected [208]. The lowest achieved resistivity using V/III = 10 was 4 mΩ-cm for 65% Al molar fraction, with samples above 70% Al exhibiting resistivities as low as 9 mΩ-cm. The growth window—i.e., the range of disilane/III molar ratios over which $\rho < 10$ mΩ-cm was achieved—was 5×10^{-4} for V/III = 10 but narrowed to $<10^{-4}$ for V/III > 100.

For V/III ratios > 100, the inversion of the [Si] vs. *n* relation also corresponds to a sharp reduction in electron mobility from around 40 cm^2/Vs to below 10 cm^2/Vs. As a result, the window of optimal doping conditions was quite narrow, since both electron concentration and mobility sharply decreased above $[\text{Si}]_{knee}$. In contrast, there was only a very slight reduction in electron mobility at high [Si] in the V/III = 10 growths—resulting in a wider doping window.

Figure 4.13 shows the effect of V/III on surface morphology. The initial MOCVD-grown AlN buffer had an atomically flat surface with sub-nm RMS roughness. AlGaN:Si grown under the lowest V/III conditions had an "undulating" or "hillock" morphology—atomically flat on a local, sub-µm length scale. Most hillocks were terminated by a small pit, indicative of a dislocation-mediated hillock step flow growth mechanism [124], [125], [218]. A mixture of pits with and without step termination (indicative of screw-component and pure-edge dislocations, respectively) was observed on closer inspection (not shown). Slight differences between Figure 4.9 and Figure 4.13 may be related to the threading dislocation density, which was in the mid-10^8 cm^{-2} range on SiC, but in the 3-5×10^9 cm^{-2} range on sapphire.

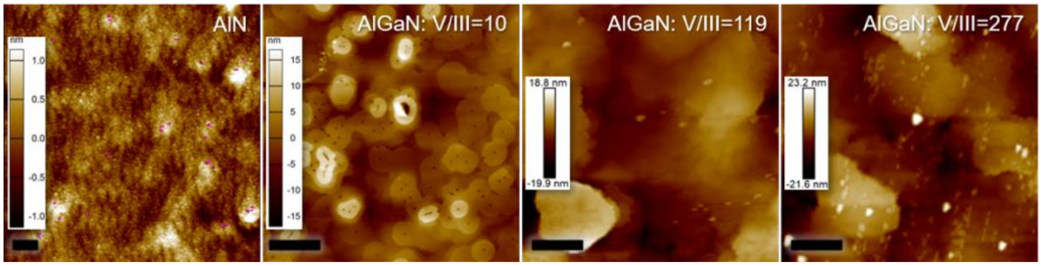

Figure 4.13: AFM micrographs of AlN and AlGaN:Si surfaces as grown by MOCVD. With V/III=10, the atomic step-terrace structure provides evidence of optimal step-flow growth mode. AlGaN:Si grown with higher NH_3 flow shows a large-hillock morphology RMS roughness below 6 nm. Scale bars 1 µm.

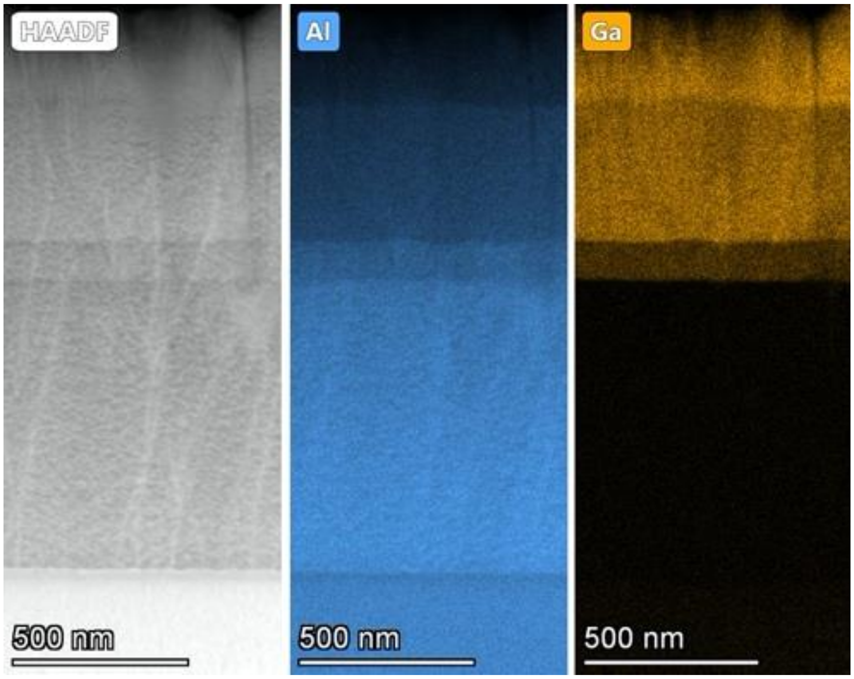

Figure 4.14: TEM and EDS images of a sample comprising two thick Si:AlGaN layers grown with V/III = 10, above a thin UID interlayer, an AlN template, and a sapphire substrate. No additional threading dislocations are formed at the AlGaN/AlN interface, and heterointerfaces are abrupt.

For V/III ratios > 100, the width and height of the hillock features increased, leading to a rougher morphology with sharper features more typical of highly Si doped AlGaN [219], [220]. RMS roughness of 4 nm, 5 nm, and 6 nm were calculated for n-AlGaN films grown under V/III = 10, 119, and 277, respectively. Smoother morphology could be achieved by, e.g., increasing growth temperature, increasing V/III, or reducing growth rate, but these changes lead to reduced conductivity [91].

Electron microscopy images of a sample with an undoped interlayer and two thick n-AlGaN layers with different compositions are shown in Figure 4.14. Cross-sectional TEM confirmed that the growth of AlGaN occurred coherently on the AlN template, with no generation of additional dislocations at the AlGaN/AlN interface. TEM-EDS indicated smooth, sharp interfaces between regions of different AlGaN molar composition and spatially uniform compositions. The undulating morphology of the thick AlGaN:Si layer can be observed most clearly in the Ga signal. The interface between the topmost AlGaN layer and the layer below it appears less sharp due to surface roughness.

4.2.3 Explanations for knee behavior in n-AlGaN

Extrinsic impurities have been overwhelmingly ruled out as the main compensating defects in over-doped n-AlGaN using secondary ion mass spectroscopy (SIMS) [126], [211]–[213], [215]. A number of intrinsic compensating point defects have been proposed based on theoretical calculations, in reasonable agreement with optical and electrical spectroscopy and transport data. The most likely origin of compensation in over-doped n-AlGaN is by group-III vacancies (V_{III}), which can be quantified in order-of-magnitude terms by PAS if certain assumptions are made about the properties of the predicted vacancies and vacancy-defect complexes [190], [215]. [212][215], and have also been inferred based on defect energy levels detected by DLTS/DLOS [213].

An additional concern for high alloy compositions is the tendency of Si to undergo a *DX* transition, whereby the Si donor is displaced from a substitutional Si_{III} site toward an interstitial site, and changes from a shallow donor to a compensating defect. This *DX* configuration greatly deforms the surrounding lattice and results in reduced atom density at the wurtzite group III site, so it is a vacancy-like point defect for the purposes of electronic states and PAS signature [221], [222] (one could think of it as an interstitial-vacancy complex, Si_i-V_{III}).

The *DX* transition becomes energetically favorable at high average Al compositions ($x_{DX} \approx 0.84$ is often cited [223]). However, this value is based on calculations which do not consider alloy disorder or local coordination, but rather simulate alloying by artificially varying the bandgap (via deformation of the lattice constant), called the virtual crystal approximation.

The effect of biaxial stress in alloys on *DX* center formation has not been studied, but it may play a role either directly via changes to the local interatomic spacings, or indirectly via changes in growth kinetics that affect the incorporation and local coordination of Si impurities. Furthermore, if it is the case that *DX* center formation can be determined by local coordination (i.e. strongly influenced by alloy disorder or inhomogeneity), then it is to be expected that populations of Si donors and *DX* centers can be observed to coexist in the same crystal.[18]

4.2.3.1 Discussion of experimental results

We found that reducing the growth temperature from 1175 °C to 1050 °C (TNSC, equiv. to 1325 °C and 1200 °C on UCSB reactor) qualitatively changed the over-doping behavior of strongly Si-doped n-AlGaN samples from a sharp knee-behavior to a more gradual or even eliminated knee behavior [91]. We used SIMS and PAS to rule out many of the commonly reported compensating defects in our material. We also found that increased growth rates above 1.5 Å/s and TMI surfactant flow greatly improve conductivity, both of which could be interpreted as ways of increasing the group III supersaturation on the sample surface.

In our subsequent experiments, we first confirmed that the growth conditions developed for the old TNSC reactor on SiC substrates transferred to a new custom reactor design, and then to a new AlN/sapphire platform. We then turned our focus to the V/III ratio of the n-type AlGaN, confirming that the knee behavior can be reduced and even eliminated

---

[18] While the problem of *DX* centers in AlGaN is still the topic of ongoing study and debate, the case of *DX* centers in $Al_xGa_{1-x}As$ is better understood, with a well-known "onset" at x=22% [324]. However, it has also been observed [325] that a *DX* transition can be triggered in AlGaAs with x as low as 4% under very highly doped conditions, on the order of 10^{19} cm^{-3}, as are used in n-AlGaN. Because the elastic deformation and electronic states associated with Si *DX* centers are highly localized, the transition of a particular Si impurity to a *DX* configuration is strongly dependent on local coordination, which depends only probabilistically on overall alloy composition, and is strongly influenced by alloy disorder or inhomogeneity. Computational results [326] suggest that *DX* center formation may be enhanced by local strain fields surrounding dislocations, and experimental evidence [327], [328] shows a strong dependence of Si *DX* behavior on the nearest group-III neighbors surrounding a Si impurity in AlGaAs.

entirely with optimal growth conditions. We reported for the first time that using a V/III ratio < 100 greatly reduces the self-compensation effect, producing an n vs. [Si] vs. relation, which flattens at around $n = 3\times10^{19}$ cm^{-3} rather than decreasing (no knee behavior) [196].

By growing with an elevated reactor pressure of 20 kPa (150 Torr), the thermodynamic driving force for AlGaN growth can be increased without the need for an increased V/III ratio [224]. Washiyama *et al.* explained that Si-AlGaN should be grown under a high degree of group III supersaturation and reduced temperature, in good agreement with our results [208], [224]. We speculate that increased growth rate (i.e. increased group III precursor partial pressure via increased molar ratio) [225], TMI precursor (presence of an additional group III species), increased reactor pressure (increased group III partial pressure via increased total pressure), and decreased V/III ratio (increased group III molar ratio), all combine to increase the group III supersaturation. From a crystal growth and morphology perspective, it seems reasonable that elevated reactor pressures enable growth of AlGaN at V/III ratios below 100, which may not be feasible at more typical reactor pressures used for AlGaN (<10 kPa).

There are a few reports of the dependence of electron mobility on silicon concentration in heavily doped n-AlGaN samples [209], [210], [226]. As shown in Figure 4.12, the onset of knee behavior in n clearly accompanies a sharp drop in μ above $[\mathrm{Si}]_{knee}$. This order-of-magnitude decrease in mobility (which we first observed back in 2016, see Dr. Foronda's PhD dissertation) is attributed to ionized impurity scattering[19], likely by the same compensating

---

[19] Ionized impurity scattering is usually discussed in reference to ionized dopants, e.g. ionized Si donors in n-type AlGaN. These become positively charged when the electron leaves the donor behind, creating fluctuations in the real-space electric field profile that lead to scattering. There are also acceptors in the n-type material, i.e. compensating defects, which are negatively charged when holding a trapped electron. These charged compensating acceptors also lead to ionized impurity scattering. Both donors and compensating acceptors could therefore contribute to ionized impurity scattering and limit mobility in heavily doped, heavily compensated, n-type AlGaN.

defects that reduce *n*. In the lowest V/III dataset, there is no drastic drop in μ, in good agreement with the trend in *n* which does not suggest any significant charged compensating defect formation above [Si] = 3×10^{19} cm^{-3}. The lack of knee behavior in *n*, combined with the more gradual decrease in μ, leads to a wider doping window in the V/III=10 condition, improving repeatability and uniformity.

It is plausible that the excess [Si] > 3×10^{19} cm^{-3} in the reduced temperature (Figure 4.8) and reduced V/III (Figure 4.12) cases (which do not contribute to *n*) may be incorporating in some *neutral* defect configuration; this would explain the lack of donor compensation *and* the much weaker reduction in μ. Harris *et al.* proposed that numerous $V_{III} + nSi_{III}$ complexes are stable in n-type AlGaN [190]. Whereas $V_{III} + 1Si_{III}$ and $V_{III} + 2Si_{III}$ are acceptors in n-type AlGaN, $V_{III} + 3Si_{III}$ is most stable in a charge-neutral configuration. It may be the case that the extreme conditions of reduced temperature, ultralow V/III, high reactor pressure, TMI surfactant, and high disilane injection [227] promote the formation of $V_{III} + 3Si_{III}$ or some other neutral vacancy complex not routinely observed under conventional growth conditions for n-AlGaN (temperatures above 1200 °C, pressures below 10 kPa, V/III > 500, silane precursor, and no TMI surfactant).

4.3 Contact resistance and ohmic contacts to n-AlGaN

Below 60% Al, ohmic contacts (contacts having a linear IV relation) can readily be formed using annealed Ti/Al-based metal stacks, similar to well-established n-GaN technologies [228], as developed by SaifAddin *et al.* in our early publications on UV-C LEDs using 58%-60% Al. HCl etching was found to improve yield and reliability of ohmic contacts which are quite sensitive to annealing temperature. As seen in Figure 4.15, 10 minutes of HCl etching gave reduced contact resistivity regardless of RTA anneal temperature, whereas 2 minutes of HCl only gave significant improvements in when the RTA temperature was at its optimal value of 830 °C (for 60% Al). However, in all cases, perfectly linear ohmic contacts could not be achieved, and contact resistivity remained higher than desired for high-WPE devices. These early samples had electron concentrations in the low-mid 10^{18} cm^{-3}.

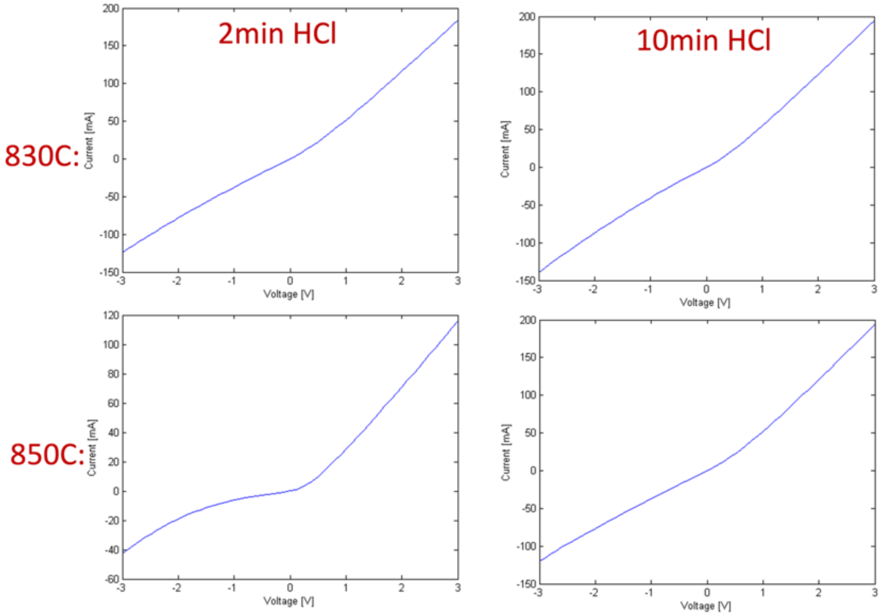

Figure 4.15: HCl etching improves ohmic contact character, especially when RTA temperature is not optimal. At the optimal temperature of 830 °C for these 60% Al samples, only 2 minutes were needed. At a sub-optimal temperature of 850 °C, only samples with 10 minutes of HCl etching gave conductive contacts.

In order to improve carrier confinement, reduce strain, and increase optical transparency, we decided to change to n-type AlGaN with 65%-70% Al beginning around Ref. [31], which required us to change to a different n-ohmic contact technology. Above about x = 0.6, there are no reports of ohmic Ti/Al-based contacts to n-$Al_xGa_{1-x}N$, and V/Al-based contacts are used instead [202], [229]. The mechanism of Ti/Al and V/Al ohmic contact formation is thought to be based on the formation of AlN, TiN, and/or VN compounds at the metal-semiconductor interface, which can be achieved by thermal annealing in air or nitrogen between 700 °C and 900 °C [202], [229]. The metallic nitrides TiN and VN have work functions lower than any commonly used elemental metals, with VN having the lowest work function (3.5 eV) of any experimentally investigated contact material (for comparison, TaN, WN, MoN, TiN, Ti, and V all have work functions above 4 eV) [230].

Contact resistivity is measured by the CTLM method [231]. For the samples studied in Ref. [91] and [196], we used currents up to 500 mA, constant inner pad radius, L, and varying gap distance, *d*. The contact resistivity, R_c, can be calculated from total resistance values, *R*, using the full CTLM solution:

$$R = \frac{R_{sh}}{2\pi}\left[\frac{L_T}{L}\frac{I_0\left(\frac{L}{L_T}\right)}{I_1\left(\frac{L}{L_T}\right)} + \frac{L_T}{(L+d)}\frac{K_0\left(\frac{L+d}{L_T}\right)}{K_1\left(\frac{L+d}{L_T}\right)} + \ln\left(\frac{L+d}{L}\right)\right],$$

via $R_C = L_T^2 R_{sh}$, where L_T is the transfer length and R_{sh} is the sheet resistance of the film. I_0, I_1, K_0, and K_1 are the hyperbolic Bessel function solutions of the first kind and second kind. Y. Yao standardized our testing and data analysis for this method, improving on my older method which made a number of approximations.

Using the optimized AlGaN:Si conditions shown above, we compared ohmic contact formation methods. In Figure 4.16, we compare Ti- and V-based metal stacks, all annealed at 900 °C. Replacing the Ti contact layer (the first deposited layer) with V greatly improved contact resistance [200], as did replacing the second V layer with Ni, perhaps because it reduced the intermixing between Au and Al. Increasing the Ni thickness from 20 to 150 nm did not provide any benefit. An anneal temperature of 900 °C was found to be best (Figure 4.16), yielding a contact resistance of 7×10^{-5} Ω-cm^2 and a sheet resistance of 90 Ω/□, as shown in Figure 4.17. This sheet resistance is in good agreement with the sheet resistance determined by the Van der Pauw method (Figure 4.12), and it is sufficiently low to prevent current crowding in a UV LED device.

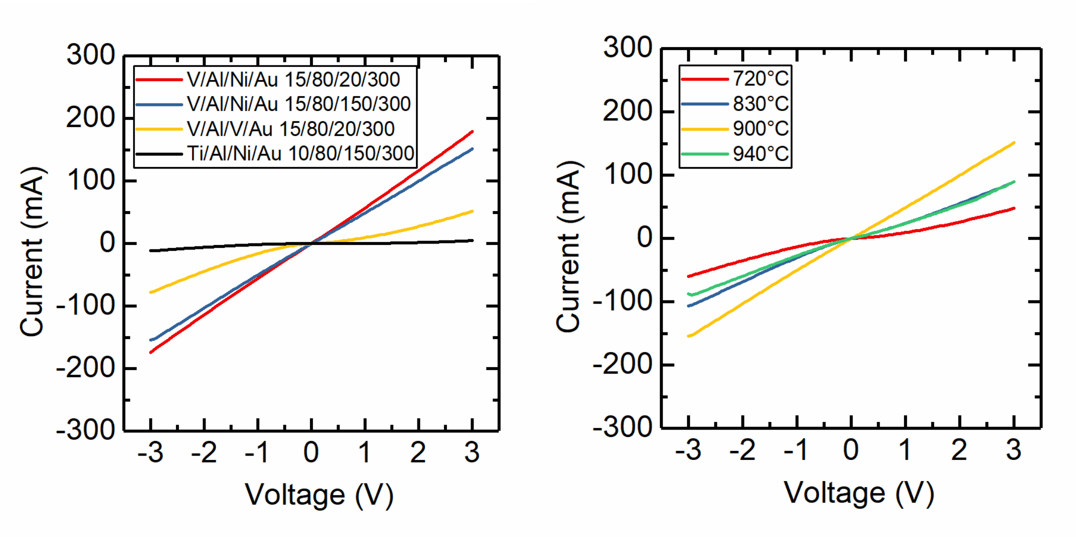

Figure 4.16: Ohmic contacts to n-$Al_{0.65}Ga_{0.35}N$ for different metal stacks and rapid thermal annealing conditions. (left) The thickness (values given in nm) and type of metal used for the diffusion barrier has a strong effect on contact resistance, with Ni-containing stacks outperforming V/Al/V/Au stacks; (right) the optimal anneal temperature was found to be 900 °C. (Figure credit: Y. Yao)

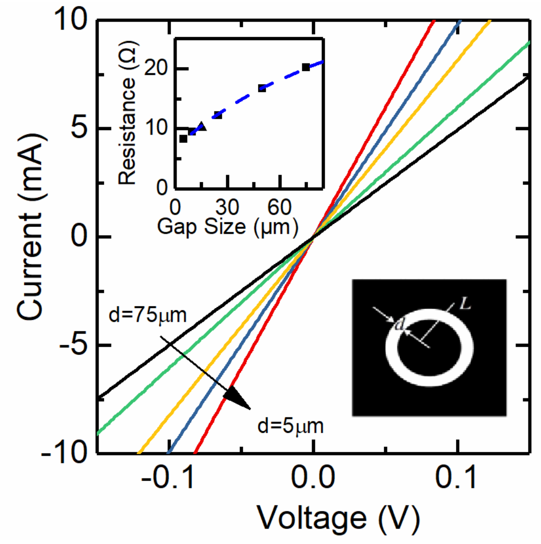

Figure 4.17: Details of CTLM measurement and data for a V-based ohmic contact to n-AlGaN. Linear fits (not shown) to the IV data (solid lines) for the CTLM patterns of varying gap length, d, and inner radius, L, (see inset schematic) were used to extract resistance values, plotted (square symbols) in the inset. These resistance values were fit to the CTLM Equation (dashed curve) to determine the sheet resistance. (Figure credit: Y. Yao)

5 p-type AlGaN for UV LEDs

We shall not cease from exploration. And the end of all our exploring shall be to arrive where we started and know the place for the first time.

-T. S. Eliot

5.1 Improving p-type AlGaN – Theory

In conventional semiconductors like GaAs, the valence bands have rather high energy in absolute terms (the difference between the valence band energy and the vacuum level is smaller), and thus acceptor atoms with low energies lying within the valence band can be found. The holes introduced by these *shallow* acceptors lower their energy by *populating the valence band,* and are bound to the acceptor only weakly by Coulomb interaction, resulting in low ionization energies (this state obeys the physics of a hydrogenic potential, with an effective mass governed by the properties of the valence band, and is often called a *hydrogenic* or *effective-mass* state).

The valence bands in nitride semiconductors are derived mainly from the nitrogen 2p-like orbitals, and therefore have very low energies. As a result, the energies of all known dopants sit above the valence band, in the semiconductor gap, and result in "deep" acceptor states. Holes bound to these deep acceptors do not populate the valence band, but rather sit in localized states at or near the acceptor. In other words, the crystal lowers its total energy by producing a mostly unoccupied localized electronic state near the atomic p-orbital energy of the acceptor atom. (Note that this is a localized state, not a state of a dispersive band. So, it does not make sense to refer to the hole there as having an effective mass, which is a property of a band, i.e. of a large, periodic crystal). There are no known III-N compatible acceptor dopants with p-orbitals having energies below that of the N p-orbital [232].

The most widely used deep acceptor in nitride semiconductors is Mg, with an acceptor ionization energy of around 200 meV for GaN, increasing linearly with alloy composition to well over 500 meV for AlN [4], [233], [234]. The hole mobility in p-type nitrides is also rather low, due to the large valence band effective masses. This results in *asymmetric* carrier injection, as electrons can be injected efficiently but holes cannot.

There are a few reports of bulk p-AlGaN layers with much lower activation energies than those which were initially predicted [4]. Once Mg concentration exceeds 10^{19} cm^{-3}, a significant reduction of activation energy can be observed at room temperature. As temperature is increased, the activation energy eventually returns to its large value. This anomalously low activation energy has been attributed to hopping- or impurity band conduction, which occurs when the concentration of dopants is so high that their carrier wavefunctions overlap.

The spatial extent of hole wavefunctions at Mg acceptor sites as determined by DFT [232] is about one nanometer, meaning that an acceptor density of well over 10^{20} cm^{-3} would be needed for wavefunction overlap by the conventional Mott transition model [235]. Previous reports have estimated critical acceptor concentrations two orders of magnitude lower than this by using a Bohr radius for free holes based on a valence band effective mass, which might not apply for holes bound to deep acceptors[20].

There are also some questions raised by the experimental data itself. Impurity band conduction occurs when the free carrier density (as observed by Hall, e.g.) is nearly equal to

---

[20] The Coulombic (a.k.a. hydrogenic) bound valence band hole state is not the *ground* state of the acceptor, but it does exist, so it is not impossible that a hydrogenic shallow state could play a role in hopping conduction even with deep acceptors.

dopant density [236]. In other words, impurity band conduction in p-AlGaN should result in Mg activation fraction remaining anomalously *high* at low temperatures, not *just* in a weak temperature dependence of carrier density. The experimental reports in p-AlGaN [237] and p-AlN [238] only show low activation energies at very *low* activation fraction, suggesting that *only a small sub-population of Mg acceptors contribute to hopping transport* (compensation is ruled out [237] because hole activation increases to near-unity at high temperatures). To explain this result, a percolative model of hopping transport might apply: even if the *average* spacing of Mg acceptors exceeds the wavefunction extent (preventing conventional hopping conduction or impurity band formation), the random positioning of acceptors leads to a subset of acceptors which are spaced closely enough that some small wavefunction overlap occurs. This would explain the onset of a hopping conduction mechanism for a hole concentration much lower than the acceptor concentration, and with a very low mobility of 1cm^2/Vs or less resulting from the very small wavefunction overlap.

5.1.1 Is hole transport in UV LEDs space-charge limited?

Consider an interface between a high hole density p+ region and a low hole density p-region, like the one found at the p-GaN/p-AlGaN interface in a UV LED. When current is injected from the p+ region into the p- region, the holes in the p- region must have much higher velocity to conserve the current, because $J = epv$. If p is constant, increasing currents must be accommodated by increasing v, until v reaches v_{sat} (which is a materials constant, to first order [239]). At this point, the only possible way to increase current further is for additional holes to be *injected* from the p+ region, into the p- region[21]. This condition is called saturated

---

[21] There is also a contribution from hole diffusion in this case, due to the large difference in hole concentration. This term is comparatively small, and decays quickly.

transport, and is an example of space-charge limited transport because the injected holes produce an unbalanced space charge that sets up a voltage *opposite* the applied voltage. The opposing voltage is proportional to the injected charge, p-p_0, and quadratic with the space charge region thickness, L.

Under the saturation approximation, the injection of holes is linear with $\mathcal{E} - \mathcal{E}_{crit}$, so we conclude that (like the Poole-Frenkel effect) the enhancement of hole concentration in a given p-AlGaN layer is simply a function of the voltage drop across it: if we consider a 50 nm p-AlGaN layer, the voltage drop would need to be at least 5 V to produce a 10x enhancement in hole concentration. While critical fields and saturation velocities for p-AlGaN are not known, a reasonable guess on the order of 10-100 kV/cm based on data for p-GaN [239] suggests that $\mathcal{E}_{crit}$ may be reached in LDs, but not for efficient LEDs.

However, in p-type III-nitrides, it is possible for space-charge limited transport to occur even if the saturation velocity has not yet been reached, so we must also consider that possibility. In thin layers with very low mobility, carrier injection occurs when the voltage penalty associated with space charge injection is less than the ohmic voltage drop. In this general case, the voltage across a semiconductor region in ohmic and space-charge terms is:

$$\Delta V = \frac{JL}{p\mu e} + \frac{ep_{inj}L^2}{4\epsilon},$$

where the total hole concentration is $p=p_0+p_{\mathrm{inj}}$. Space-charge limited current can be experimentally verified by a characteristic current-voltage relation $J = \epsilon\mu\frac{V^2}{L^3}$ [240].[22] If $p_{inj} > p_0$, then we find that:

---

[22] This is exact only if p_{inj} is a constant. Mott & Gurney (p. 172 in [240]) find that the full solution allowing for a spatially varying injected carrier concentration deviates from this approximation only by a factor of 9/8, as used by the authors of Ref. [329].

$$p_{inj} \approx \sqrt{\frac{4\epsilon J}{L\mu e^2}}$$

giving $p_{inj} \approx$ 1-5×10^{16} cm^{-3} for a p-AlGaN layer with μ = 1 cm^2/Vs, thickness L = 50 nm, $\varepsilon = 9\varepsilon_0$, and J = 10-100 A/$\text{cm}^2$ (notice that for conventional semiconductor mobilities on the order of 100 cm^2/Vs or more, this term becomes negligible). The radical results in a weak increase in low-field carrier injection even at high current densities such as those in laser diodes, increasing only to around 10^{18} cm^{-3} for J = 40 kA/cm^2. (real UV-C laser diodes use polarization enhancements discussed below, so p is likely already higher than this anyway).

We conclude that space-charge limited hole injection enhancement may be measurable in very high-voltage research results, but is not relevant for commercial devices or polarization-enhanced devices (discussed below), and is weaker than the Poole-Frenkel enhancement. This is confirmed by both back-of-the-envelope saturation velocity arguments and the full space-charge limited transport treatment (which considers space-charge limited transport even before the saturation velocity has been reached).

5.1.2 Acceptor doping in p-AlGaN

Mg incorporation can be enhanced by increasing the V/III ratio [241] as shown in Figure 5.1; this also suppresses the incorporation of donor-like nitrogen vacancies [192], [242]. If [Mg] exceeds ~3×10^{19} cm^{-3}, structural degradation such as inversion domain formation usually occurs [243], [244] (although there are some reports of successful Mg doping above 10^{20} cm^{-3} [245]). Structural degradation can be reduced, and hole concentration increased, using indium surfactant in both MBE [246] and MOCVD [247]. With optimized growth conditions, the best achieved bulk p-AlGaN free hole concentrations are ~10^{17} cm^{-3} for x = 0.7 [237], and 5×10^{18} cm^{-3} for x = 0.4 [247].

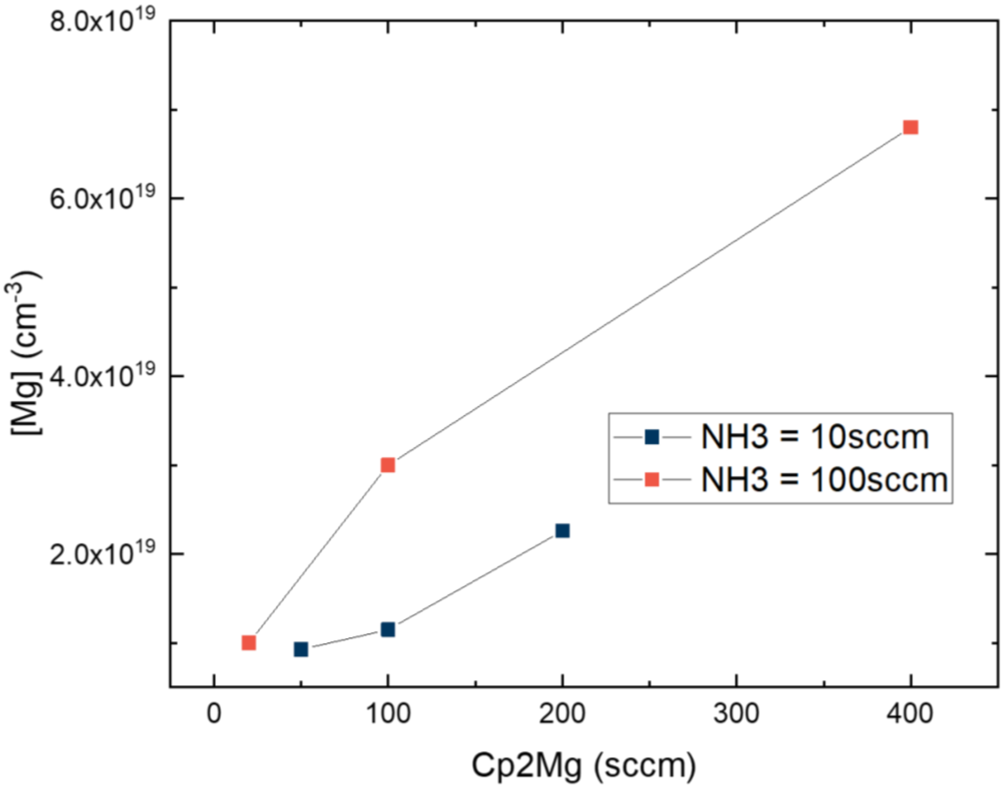

Figure 5.1: Mg incorporation increases with V/III, and with Cp_2Mg flow rate.

5.1.3 Polarization-enhanced p-type doping of AlGaN

The polar covalent bonds in nitride semiconductors, combined with the $P6_3mc$ symmetry, result in a nonzero dielectric *polarization*, $\boldsymbol{P}$. The direction of this polarization is always parallel to the *c*-axis (absent shear strain) due to crystallographic symmetry, but the magnitude of the polarization is a function of both alloy composition (the spontaneous, or pyroelectric contribution) and strain (the piezoelectric contribution). The electric field generated by a polar material is equal to that of a bound sheet charge $\sigma_b = \boldsymbol{P} \cdot \hat{\boldsymbol{n}}$ at the boundary of the material, where $\hat{\boldsymbol{n}}$ is the outward surface normal; if the material has spatially varying polarization $\boldsymbol{P}(\boldsymbol{r})$, there is a bound space charge, $\rho_b = -\boldsymbol{\nabla} \cdot \boldsymbol{P}$. At an interface between two polar materials with different $\boldsymbol{P}$, the bound sheet charge has a magnitude $\Delta\boldsymbol{P} \cdot \hat{\boldsymbol{n}}$, where $\Delta\boldsymbol{P}$ is the polarization difference between the two materials. In the III-nitrides, where polarization differences at heterointerfaces can be large, this results in significant electric fields due to bound charges. In compositionally graded AlGaN layers, the spatially varying polarization produces a bound space charge, which greatly effects the behavior of mobile charge carriers.

The Fermi level inside a graded p-AlGaN region is calculated in the usual way, except that the polarization charge must be accounted for. The number of negatively charged (electron-occupied) acceptor states, N_A^-, is given by:

$$\frac{N_A^-}{N_A} = f_4(E_A) = \frac{1}{\frac{1}{4}\exp\left(\frac{E_A - E_F}{kT}\right) + 1}$$

where $f_4(E)$ is the Fermi occupancy function for a band with degeneracy of 4. Simultaneously, the total hole concentration at equilibrium is defined (in the Boltzmann approximation, which holds for this non-degenerate case):

$$E_F \approx E_V - kT \ln\left(\frac{p}{N_V}\right)$$

where N_V is the valence band effective density of states, and p is the total hole concentration (i.e., not just the concentration of ionized acceptors) [248]. The Fermi level at a given carrier concentration is found by solving these two equations under the constraint of charge neutrality. In the presence of spatially varying polarization (i.e. nonzero bound polarization charge), and neglecting compensating donors and free electrons, charge neutrality means: $ep = eN_A{}^- - \rho_b$, wherein ρ_b is the polarization charge $-\boldsymbol{\nabla} \cdot \boldsymbol{P}$ (for a downward composition gradient along the [0001] direction, $\rho_b < 0$). The ρ_b term pulls the Fermi level towards the valence band, greatly increasing the hole concentration while decreasing the acceptor ionization fraction.

For example, for a UV LED with p-AlGaN having: $N_A = 5\times10^{19}$ cm^{-3}, $N_V = 10^{20}$ cm^{-3}, and E_A-E_V = 300 meV, the free hole concentration is 3.7×10^{17} cm^{-3} and the Fermi level is 143 meV above the valence band in the polarization-free case (approximately halfway between the acceptor level and valence band, as expected). In the polarization-enhanced case, with $-\rho_b/e$ = 5×10^{18} cm^{-3}, the total free hole concentration increases to ~5×10^{18} cm^{-3}, while *the ionized acceptor concentration decreases* to 2.5×10^{16} cm^{-3} and the Fermi level becomes 75 meV above the valence band. In practice, polarization charge densities of 5×10^{18} cm^{-3} can be achieved using a composition gradient around 1%/nm [5], [249]–[251].

It is important to note that *there is no local enhancement of acceptor ionization* within a 3D polarization enhanced p-AlGaN region. To the contrary: local Mg acceptor ionization fraction *decreases*, because the Fermi level moves closer to the valence band, while the ionization energy does not change. Instead, the excess holes originate *elsewhere* in the structure (e.g., in a remote acceptor doped region, at surface defects, in a metal contact which acts as a source of charge, etc.), and are swept into the bulk 3D polarization charge region to offset the bound polarization charge. The Mg acceptors in the bulk of the material are neither "field ionized" [250], nor is this a Poole-Frenkel ionization effect, as has been occasionally reported.

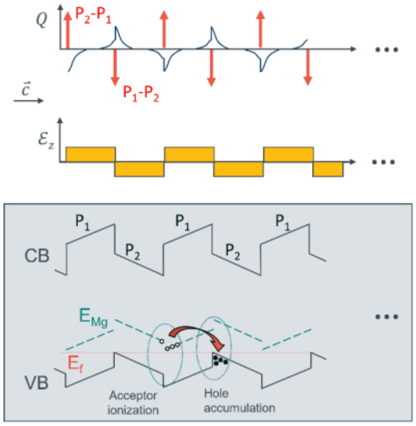

Figure 5.2: The space charge, electric field, and band diagrams of a p-AlGaN superlattice. Polarization sheet charges in red; free hole charge (positive) and ionized-acceptor charge (negative) shown in blue. The alternating polarization charges produce local regions of high Mg ionization (indicated by open circles), and nearby regions of high hole concentration sometimes called 2D hole gases (filled circles). In this figure, the Al-polar face of the crystal is on the right hand side.

The case above is an example of *3D polarization enhanced* p-AlGaN, in which the polarization charge is a *space* charge. Many reports of polarization enhancement use sheet charges $\Delta \boldsymbol{P} \cdot \hat{\boldsymbol{n}}$, resulting in 2D hole gases at abrupt heterointerfaces between AlGaN alloys of different compositions. These sheet charges are usually stacked in superlattices. The valence band variation produced by the 2D bound charges at each interface produce local regions of high Mg acceptor activation [252], as shown in Figure 5.2. The local electric field strength $\Delta \boldsymbol{P}/\varepsilon$ within such a superlattice is on the order of $\sim 6\ \mathrm{MV/cm}$ for a superlattice with compositions of, e.g., 20% and 80%. This could provide a significant additional Poole-Frenkel enhancement in Mg activation, as discussed below. As a result, high hole concentration and reduced effective Mg activation energy are observed in p-AlGaN superlattices. Using this method, hole concentrations as high as 10^{18} cm^{-3} have been observed in SLs with average composition of x = 0.8 [253]. Numerical simulations of such superlattices performed by Y. Yao are shown in Figure 5.3.

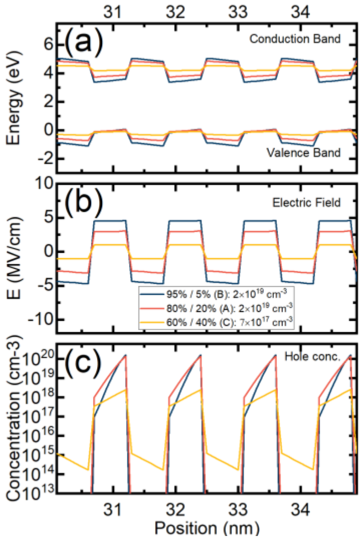

Figure 5.3: Superlattice simulations computed by Y. Yao, showing quantitatively the electric field strengths, band energies, and hole concentrations which can be achieved with p-type AlGaN/AlGaN superlattices with the compositions shown. These structures were later confirmed experimentally to give high injection efficiency, as discussed below. In these figures, the Al-polar face of the crystal is on the left hand side (opposite Figure 5.2).

When the hole gases are close enough together to enable tunneling between them (around a few nanometers), efficient vertical transport can be achieved. Such superlattices are sometimes referred to as short-period superlattices, and have many optical, electrical, and material benefits [254]. The quantum confinement of the very thin low-composition constituent layers raises the optical absorption edge above the bulk value, so that low-Al content alloys can be used without LEE penalty [32], [255]. The growth mode for short-period superlattices is necessarily a pulsed growth mode, which enhances Mg incorporation. This growth method can readily incorporate delta doping [247], flow modulation effects [256], [257], and other beneficial MOCVD growth principles for enhanced doping [258]. There are reports of p-SPSLs with both AlN and AlGaN barriers [6], [254]. Alloy barriers improve hole transport due to lower potential barriers and percolation paths [234], but they may also reduce mobility due to alloy scattering.

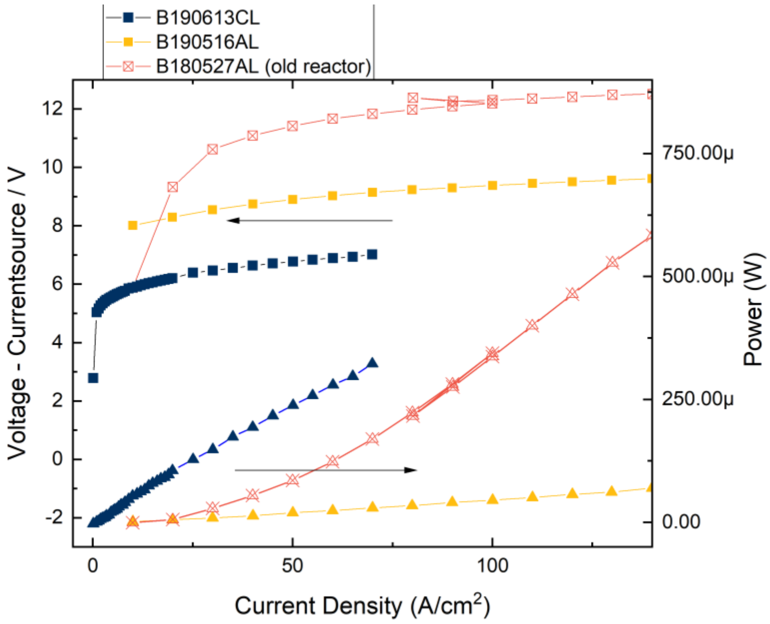

Figure 5.4: Comparison of LED power after reactor switch. The first LEDs shown in yellow had much lower power than previous results on the TNSC reactor, although they also had much better voltage. Power was immediately greatly improved by increasing the Mg concentration in the p-AlGaN from approximately high-10^{18} cm^{-2} levels (yellow) to 3x10^{19} cm^{-2} (blue).

5.2 Superlattice hole injection layers – experiment

In May of 2019, we had successfully transferred over our high-quality AlN and n-type AlGaN to the new reactor, and had met or exceeded our previous benchmark values in each of those areas, as discussed in the previous chapters. As a result, our LED voltage was lower than before. However, LED output power (shown in Figure 5.4) was much lower than the previous benchmark values. In order to improve EQE, our first area of interest was injection efficiency, which we expected would be most strongly improved by enhancing our hole-supply layers, i.e. the p-type AlGaN.

These samples (shown in Figure 5.4) all had p-type AlGaN layers with compositions around 20%. We found that every time we attempted to increase the composition above this value, LED power went to zero, and the IV characteristics became non-diode like and highly resistive. This suggests that those AlGaN layers were not sufficiently p-type to form a diode structure, and there was significant electron leakage to the p-GaN. In efficiency terms, we refer to this as poor IE caused by electron overshoot.

In this section, I will go over the experiments we performed next in optimizing polarization enhanced hole supply layers for our UV-LEDs. Similar to Chapter 4, these experiments took place over a long period of time, with a combination of data from both SiC and sapphire substrates. In particular, our results on SiC substrates can be found in Ref. [32], and our results on sapphire are summarized in Ref. [259] (under review).

5.2.1 Replacing bulk AlGaN with superlattice AlGaN

In the first set of experiments, we explore UV LEDs grown by MOCVD on SiC substrates, fabricated into thin-film flip chip devices (see Chapters 7,8). Replacing the *uniform* p-$Al_xGa_{1-x}N$ layer ($x = 0.2$) with a *short-period-superlattice* of alternating ($x = 0.1$ and 0.8) Al-composition improved EQE from 1.3% to 2.7% (3.2% with encapsulation) at 20 A/cm^2. Peak EQE and WPE values of 4.8% and 2.8% (287 nm) were measured at current densities below 2 A/cm^2, and maximum output power of 7.4 mW (76 mW/mm^2) was achieved at 284 nm.

Next, further optimization of the superlattice was performed on devices grown on sapphire substrates. As will be discussed in Chapter 8, the devices on sapphire had significantly lower light extraction efficiency, so that total EQE was slightly reduced although estimated IQE was increased. The results in this section will be discussed in terms of IQE, EQE, and WPE, assuming an LEE of 33% for the TFFC structure on SiC, and 18% for the vertically packaged devices on sapphire (see Chapter 8).

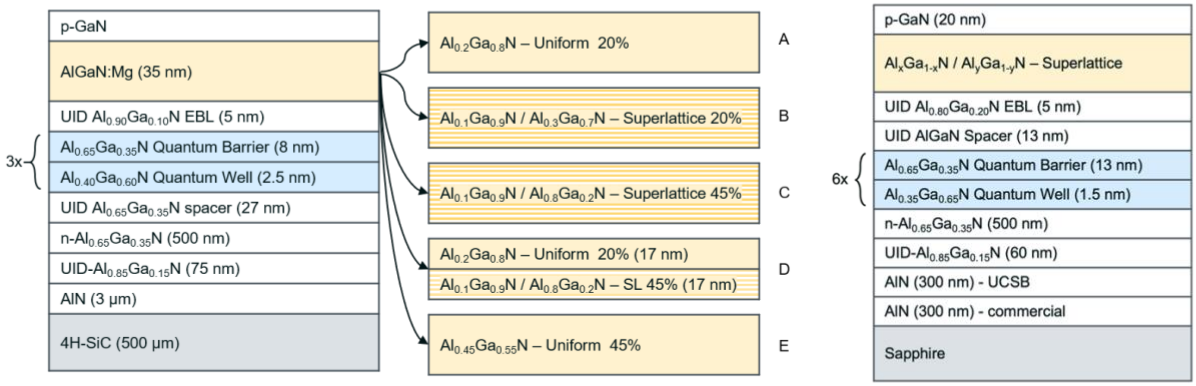

Figure 5.5: Epitaxial layer stacks with nominal thicknesses and compositions, for experiments performed on epi grown on SiC (left) and sapphire (right). For all devices, the buffer, unintentionally doped (UID), n-type, and active region layers were identical. Mg-doped AlGaN layers were either uniform, superlattice, or a combination of both layer types. The epitaxial stack for experiments on sapphire differed slightly from that used on SiC, but the overall device structure was very similar.

SaifAddin *et al.* originally demonstrated up to 2% EQE (IQE*IE=6%) UV-C LEDs [31] on SiC via substrate removal and backside roughening [185]. Then, we made improvements in n-type conductivity in $Al_xGa_{1-x}N$ with composition, x, greater than 0.6 [91] and reduced AlN/SiC dislocation density to 2×10^8 cm^{-2} [123]. These results enabled us to replicate those previous results and achieve a baseline EQE around 1-2%, corresponding to an estimated IQE*IE of 3-6%. IQE is related to both defect density in the active region (known to be low for these samples), and active region design[23]. IE depends to first order on the hole concentration in the p-side of the device.

5.2.2 Methods

The UV LED layer structure is represented schematically in Figure 5.5. All AlN and AlGaN layer thicknesses were confirmed by a combination of *in-situ* monitoring, reflectometry, and TEM. The AlGaN:Mg layers were grown with elevated V/III (i.e. NH_3/[TMAl + TMGa]) ratios between ~2,000 for 20% composition, and ~6,000 for 80%. All were grown with a constant V/[TMAl]—differences in V/III were due to differing TMGa flow, used to control composition. In the first round of experiments, AlGaN:Mg multilayer structures had constant nominal total thickness of 35 nm, while composition and superlattice structure were varied as shown in Figure 5.5. Short-period superlattice structures were grown with total period 17 Å, wherein the thicknesses of the high- and low-Al composition layers were roughly the same. The list of various combinations of uniform and superlattice AlGaN:Mg structures is given in the second column of Table 5-1.

In the second round of experiments, grown on sapphire substrates, we explored many additional parameters including compositional contrast, total thickness, period thickness, and Mg doping level, as discussed in Table 5-2. The AFM images of these superlattices are represented in Figure 5.7. The morphology of the 80%/40% superlattice appears to be atomically flat, similar to a bulk p-type AlGaN sample as shown in Figure 5.8. This is attributed to the high V/III ratio of the Mg-doped growth condition, giving a high thermodynamic driving

---

[23] The samples discussed in this section were developed using a highly simplified active region with unoptimized well and barrier thicknesses, using the growth condition of the n-AlGaN. We focused here on the p-side of the device, with a plan to optimize the active region later, after the p-superlattice had been implemented. Because active region design has a strong effect on both IQE and IE, whereas p-AlGaN design primarily effects IE only, our approach was to begin with the p-AlGaN.

force for crystal growth and enhancing the stability of the c-plane facet. These samples had higher threading dislocation density (1-5x10^9 cm^{-2}) compared to the growths on SiC (<5x10^8 cm^{-2}), so the radiative efficiency may have been slightly lower. On the other hand, the additional improvements in the p-superlattice led to similar overall IQE.

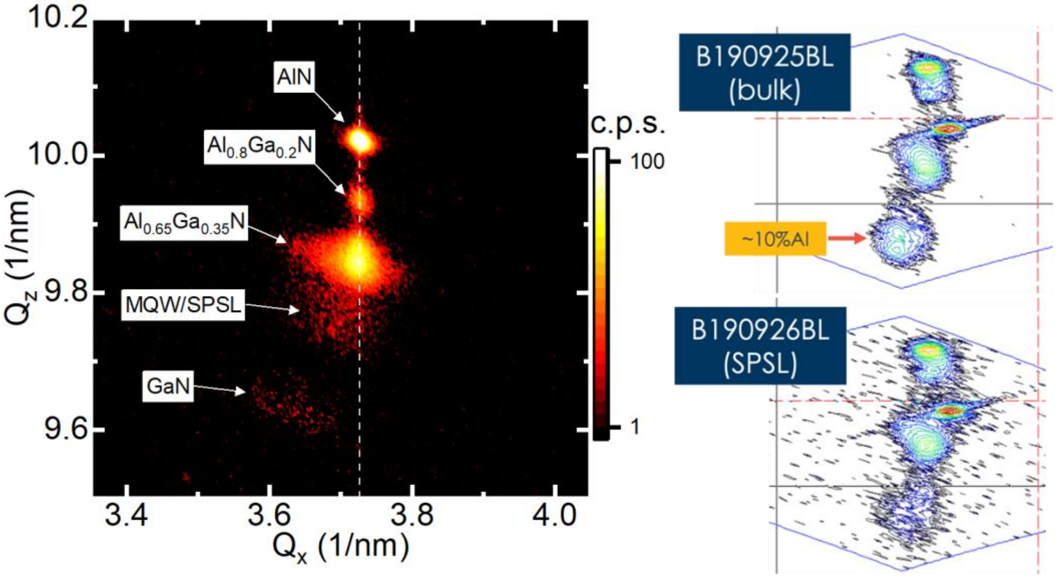

Figure 5.6: X-ray reciprocal space map of the LED structure shown in Figure 5.5, grown on a sapphire substrate (left). Epitaxial stacks grown on SiC had nearly identical reciprocal space maps (right), except that there was also a SiC (1 0 10) peak visible near the AlN peak. The AlGaN UID interlayer and n-type layer give strong reflections aligned vertically with the AlN peak, showing that they were fully coherent. The active region and superlattice multilayer structures gave low reflection intensity, but appeared to be partially relaxed. The GaN peak was weak because the film was very thin and did not fully cover the sample, and appeared to be fully relaxed. The superlattice gave a clearly visible peak in the vicinity of its average composition, but the intensity and sharpness of the peak were less than a comparable bulk layer.

Above the AlGaN:Mg layers, a p-GaN contact layer was grown under identical conditions for all samples. Based on calibrations performed on GaN/sapphire samples, the nominal thickness was around 10-20 nm, but various thicknesses and morphologies were observed for p-GaN layers grown above AlGaN, as shown in Figure 5.8 The observed p-GaN morphology differences may be related to the combination of high Mg doping [260] and strain due to varied underlying AlGaN average composition, i.e. lattice constant. Note that the p-GaN islands have a much greater height variation than the AlGaN morphologies shown in Figure 5.7 (the AlGaN is relatively flat compared to the p-GaN).

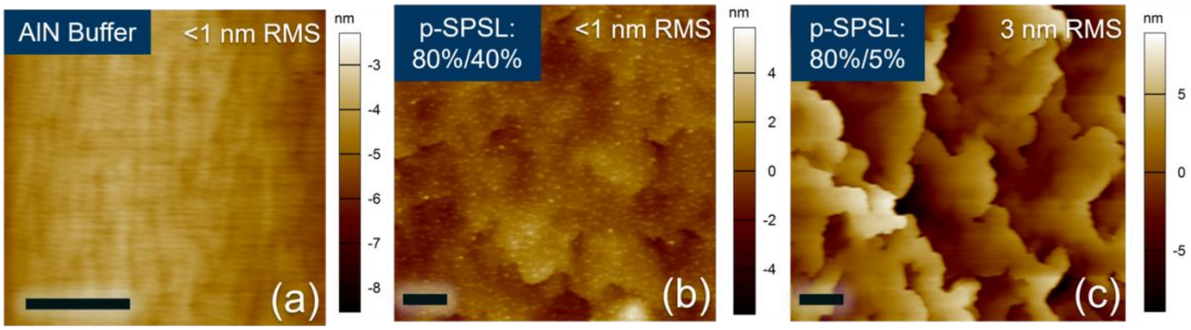

Figure 5.7: AFM images of underlying AlN (on sapphire) and p-superlattice films, showing the importance of strain. The superlattice with low composition contrast (b) showed atomically flat surface with <1 nm RMS roughness. On the other hand, the sample with high contrast (c) showed a step-terrace structure with large step heights, and an RMS roughness of 3 nm.

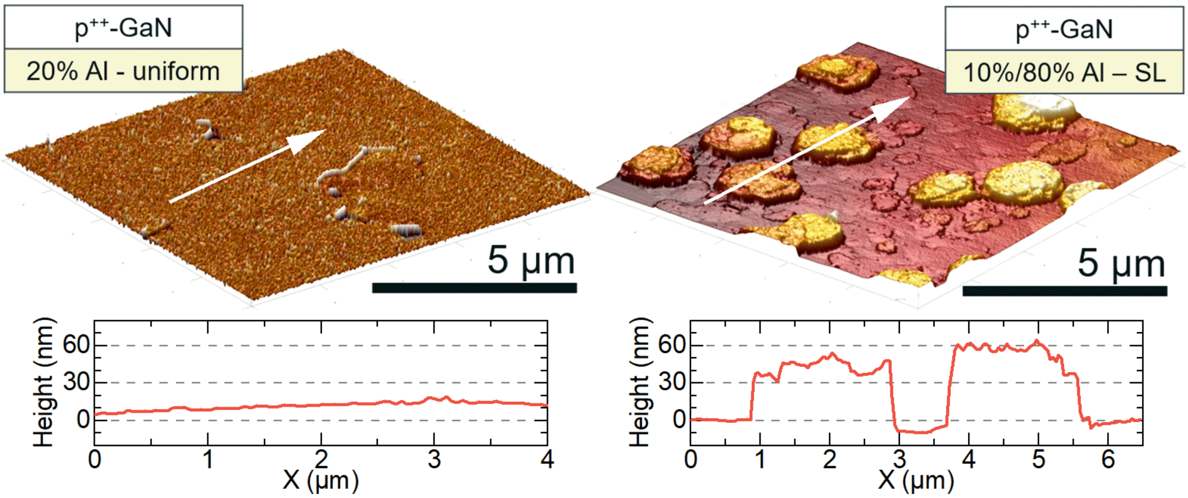

Figure 5.8: AFM images of p-GaN planar and 3D island layers on LED surfaces. Morphology of p-GaN grown on a 20% AlGaN uniform layer (left) representative of samples A and D is consistent with rough planar growth, whereas p-GaN grown on 10%/80% superlattice AlGaN (right) on sample C appears to form large Volmer-Weber islands. Line-scans along arrows show quantitative surface height data, indicating smooth surface (left) and island heights of 30 nm to 60 nm (right).

Lateral current spreading can be achieved in n-AlGaN but not p-GaN, let alone p-AlGaN, so current spreading layers must be placed on the p-side of the device. Transparent current spreading layers such as ITO are used in visible LEDs, but no established UV-transparent current spreading layers exist. Most UV LEDs therefore have opaque (and somewhat reflective) metal current spreading layers covering the entire device area. These metal contacts cannot make low-resistance ohmic contacts directly to p-AlGaN, so p-GaN contact layers are used, improving the VE with significant reduction in LEE.

5.2.3 Results

The first five UV LED devices are summarized in Figure 5.9 and Table 5-1, all with nominally identical UID AlGaN, n-AlGaN, and active-region structures, and differing only in the AlGaN:Mg layer(s). The first device (A) contained an $Al_{0.2}Ga_{0.8}N$:Mg (20% composition) layer of uniform composition, and provided emission power and voltage metrics to be used as a reference for analysis of subsequent devices. Peak IQE*IE=6% and WPE = 1.4%, and operational (measured at 20 A/cm^2) efficiencies of: IQE*IE = 3.9%, WPE = 0.7% were measured. The performance of this device was fairly typical of devices grown on that reactor with that epitaxial structure, as initially published by SaifAddin et al. [31], [261]. As discussed above, simply increasing the AlGaN:Mg composition to 45% (device E) did not yield any light output.

Table 5-1: UV-B LED data with uniform (U) and superlattice (SL) hole injection layers. IQE*IE (equal to EQE/LEE) assumes LEE=33% for TFFC devices with roughening (40% with encaps.).

ID:	p-AlGaN	Voltage^a	IQE*IE^a	EQE^a	WPE^a
A	20% (U), 35 nm	8.3 V	3.9%	1.3%	0.7%
B	10%/30% (SL), 35 nm	9.6 V	3.6%	1.2%	0.5%
C	10%/80% (SL), 35 nm	10.5 V	8.1%	2.7% (3.2%^{b})	1.1% (1.3%^{b})
D	10%/80% (SL), 17 nm + 20% (U), 17 nm	7.8 V	4.8%	1.6%	0.8%
E	45% (U), 35 nm	>15 V	<0.3%	<0.1%	<0.1%

^{a} Measured at 20 A/cm^2. ^{b} Efficiency after encapsulation with UV-grade fluororesin

A device with a superlattice comprising 10% and 80% layers (C) had the highest performance. In stark contrast to device E which had the same average composition of 45%, device C exhibited enhanced light output power and efficiency. A peak EQE of 4.8% (IQE = 14.4%, WPE = 2.8%) was measured at ~1 A/cm^2 after encapsulation, which enhanced the LEE by roughly 20%. At 20 A/cm^2, the EQE (IQE, WPE) drooped to 3.2% (9.6%, 1.3%), while the voltage reached 10.5 V. The full details of the subsequent experiments including pulsed and high power measurements can be found in Ref. [32], but the main takeaway was that high superlattice contrast was needed for good hole injection. In the first round of experiments, the composition of the low-Al layer was held constant at 10%, while only two p-high compositions were compared. Thus, there were some limitations in the interpretation of the data, as average Al composition and contrast were correlated.

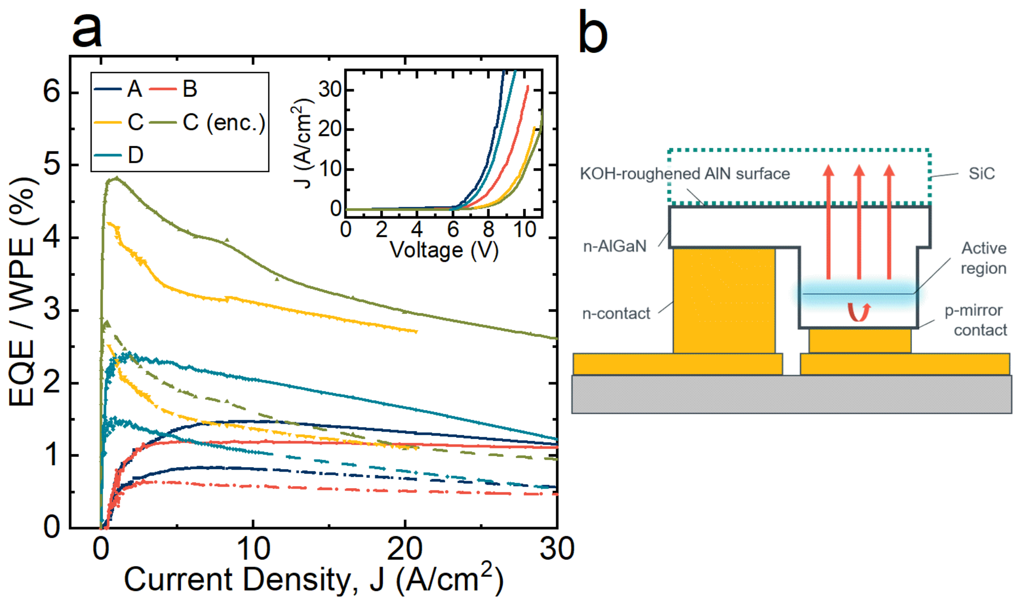

Figure 5.9: (a) EQE (solid) and WPE (dashed) for devices A-D. Devices with high-contrast p-superlattices (C, D) have EQE characteristics which peak at higher values, and peak at lower current densities, than the reference samples (A, B). Device C data for bare die (C) and encapsulated (C, enc.) structures. Current-voltage data (inset) shows increased voltage for all samples without a uniform 20% contact layer (B, C), and comparatively low voltage performance for both samples with a contact layer (A, D). (b) Schematic of thin film flip chip device architecture: emission through nitrogen-polar side after substrate removal, backside roughening.

The second round of experiments on sapphire substrates was performed about 18 months after the first round, due to a number of factors including long lab shutdowns caused by the COVID-19 pandemic, and difficulties in bringing equipment back up. We also switched to commercial sapphire substrates at this time, so a few month months of work at the end of 2020 and beginning of 2021 were focused on bringing up high quality AlN on these. Nonetheless, within less than 6 months of rebooting the reactors post-COVID shutdown and transferring to sapphire, we had LEDs emitting UV light with fairly high power. Even more encouragingly—we found that the p-superlattice conditions developed on SiC and discussed above worked perfectly on the sapphire epi. The next logical step was to continue where we had left off with a more thorough optimization of the p-superlattice.

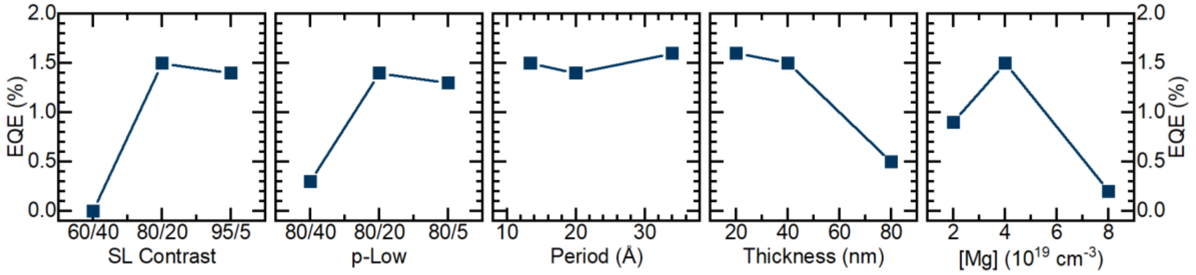

Figure 5.10: Summary of EQE trends for various parameters of p-SL grown on sapphire substrates.

A brief summary of the EQE trends is plotted in Figure 5.10, and more details for all samples are shown in Table 5-2. The strongest effects were found to be the compositional contrast of the superlattice, and the concentration of magnesium dopants. Superlattice period was found to have little effect on LED efficiency, in good agreement with simulations which showed that the hole concentration was nearly identical in all three cases. Full details of this study, in which Y. Yao was the primary investigator, can be found in Ref. [259] (accepted manuscript).

Table 5-2: Summary of experiments carried out on sapphire substrates. IQE*IE (equal to EQE/LEE) calculated assuming LEE=18%. * Extrapolated from lower currents

Comment	**ID**	**p-high**	**p-low**	**Period**	**Total thickness**	**[Mg], cm^{-3}**	**EQE @ 10A/cm^2**	**IQE*IE @ 10 A/cm^2**
Optimized device	1	80%	20%	13.4 Å	40 nm	4x10^{19}	1.5%	8.3%
SL Contrast	2	**95%**	**5%**				1.4%	7.8%
	3	**60%**	**40%**				<0.01%	
p-Low composition	4	80%	**5%**	**20 Å**			1.3%	7.2%
	5	80%	**40%**				0.3%	1.7%
Period thickness		80%	20%				1.4%	7.8%
				34 Å			1.6%	8.9%
Total thickness				20 Å	**20 nm**		1.6%	8.9%
					80 nm		0.5%*	2.8%
Mg doping					40 nm	**8x10^{19}**	0.2%	1.1%
						2x10^{19}	0.9%*	5%

The most important result of this work was that the LED efficiency gains from superlattice composition and period optimization could be almost fully explained in terms of hole concentration, as Y. Yao computed using 1-dimensional Poisson calculations. The structures with the highest computed hole concentration (high Mg doping, high SL contrast) gave the highest experimentally measured EQE, attributed to increased IE. When comparing structures with similar hole concentration (such as in the period series), only small efficiency differences were observed. Finally, structures in which structural degradation was expected (very high Mg concentration, thickness over 50 nm) gave lower EQE. Using the optimized p-SPSL platform, a high efficiency UVC LED was demonstrated with 5.5 mW output at 100 A/cm^2, corresponding to an estimated IQE of nearly 10%, as summarized in Table 5-2.

5.2.4 Discussion

The aims of this experiment were 1) to study the difference between uniform AlGaN:Mg layers and superlattice layers, and then 2) to confirm that the reason the superlattices boost EQE is due to the polarization enhancement effect. As expected, uniform layers show a very strong negative correlation between electrical performance and Al composition, making transparent GUV LEDs with uniform AlGaN:Mg layers impractical. Superlattice layers, in contrast, showed a much weaker negative correlation—voltage performance diminished only slightly with increased average Al content, while optoelectronic performance was markedly enhanced.

Because there are numerous benefits of superlattices on AlGaN:Mg performance—including polarization, valence band engineering, electron blocking, transparency, and Poole-Frenkel enhancement [27], [195], [258], [262]–[264]—we could not initially explain the poor performance of sample B in comparison to sample A (see Table 5-1) based simply on LIV experiments. The second round of experiments in which we more fully explored the parameter space and used computational methods helped us to conclude with some confidence that the 2D polarization enhancement effect described above explained the increased EQE observed in these LEDS.

Combining the results of both studies, we observed that a) the composition contrast is the single most important variable in optimization of the superlattice, as this is what determines the equilibrium hole concentration, and b) the average composition of the superlattice has a weaker but non-negligible effect, with higher average composition giving higher EQE, but also slightly higher voltage.

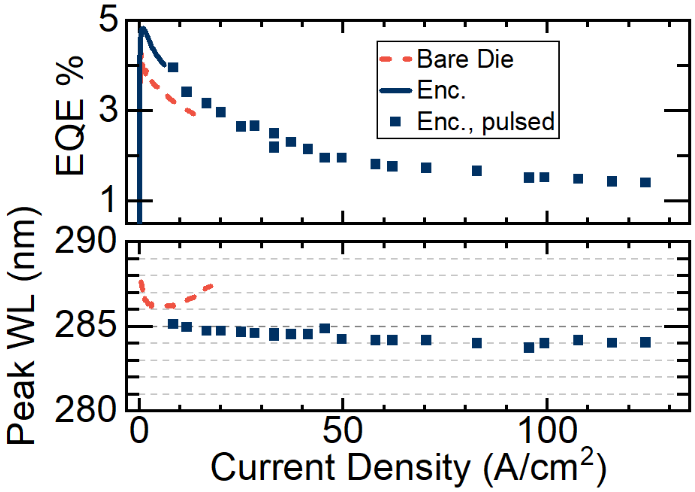

Figure 5.11. EQE droop and peak wavelength shift versus current density for the optimized device (C), tested as bare die (dashed), with encapsulation (solid), and with encapsulation under pulsed operation (squares). Pulsed measurements appear to eliminate heating effects (redshift is eliminated), but do not significantly reduce droop, suggesting that efficiency droop is not primarily due to device heating.

As shown in Figure 5.11, device C exhibited efficiency droop behavior, which had not been observed in our previous work. This may be because the devices in this work have lower dislocation density, improving IQE at very low carrier concentrations (where IQE increases rapidly with current density due to charged defect saturation [265]).

Simultaneously, emission wavelength under continuous current injection redshifted at increased current densities, indicating device heating [266], [267]. To isolate the effect of heating, continuous measurements were compared with pulsed measurements (duty cycles of 5%, 1%, and 0.1%). Pulsed current injection eliminated the redshift in the EL, without significantly affecting droop, so heating is not the primary mechanism behind the observed droop. In other words, this is true efficiency droop, not thermal droop.

Both devices with enhanced hole injection via the high-contrast superlattice (C and D) show peak efficiency at much lower current densities than the reference samples, which is consistent with an Auger-related droop mechanism because improved hole injection increases hole concentration within the active region at a given current density. An increased hole concentration would lead to enhanced EL emission at low current densities, but also to enhanced Auger recombination at high current densities, in agreement with the observed trends. (The devices in Ref. [259] had nearly identical wavelength shift and droop characteristics, so our interpretation of those results is similar with respect to Auger and droop.)

5.3 3D polarization enhanced AlGaN Experiments

We performed some preliminary experiments to confirm the efficacy of the 3D polarization enhancement method, using linearly compositionally graded AlGaN layers (Y. Yao performed the growths for these experiments, and I did the processing and testing). These preliminary experiments showed that graded structures had similar performance to superlattices, so we proceeded with further superlattice optimization and did not pursue graded layers further at the time. Future work will include more thorough optimization of device design and growth conditions for graded AlGaN layers, which have many benefits.

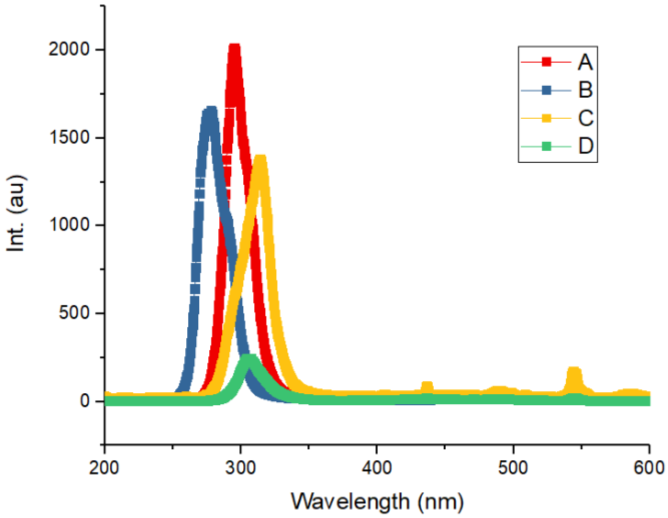

Device	***x***	***y***	***t***	**WL (nm)**	**Power**	**Est. *p***
A	0.8	0.2	60nm	273	1.2mW	5×10^{18} cm^{-3}
B	0.8	0.2	40nm	295	1.2mW	7.5×10^{18} cm^{-3}
C	0.8	0.2	20nm	315	1.1mW	1.5×10^{19} cm^{-3}
D	0.8	0.5	40nm	304	0.1mW	3.8×10^{18} cm^{-3}

Figure 5.12: Data and table for 3D polarization enhanced graded p-AlGaN UV LEDs.

Figure 5.12 shows spectra along with power data for four investigated graded p-AlGaN UV LEDs. Samples A-C had compositional grading from 80% Al to 20% Al over thicknesses of 60 nm, 40 nm, and 20 nm, and sample D had a compositional grading from 80% to 50% Al over 40 nm. Samples A-C showed high emission power of >1 mW at 50 mA, typical of devices grown on sapphire before the SPSL optimizations discussed above. Sample D, with a much lower compositional difference, had much lower light output power. However, clear trends were not observed in power vs. hole concentration, so more work will be needed to fully understand the ideal structures for 3D polarization enhanced hole injection structures for our UV LEDs. Interestingly, the wavelength appeared to redshift with increasing hole concentration, perhaps related to electric fields in the active region. (The 304 nm peak in the low-power sample may not be quantum well emission, as I will explain in the next chapter, so it is not too surprising that this extremely inefficient device does not follow the same wavelength trend as the highly efficient devices.)

6 Active regions

Seek simplicity, but distrust it.

-Alfred North Whitehead

6.1 Active region: theory

The active region of an LED is located between the n- and p-type carrier injection layers and comprises a series of alternating high- and low-bandgap layers, called barriers and wells, respectively. In nitride LEDs, there is often also an additional barrier layer with still wider bandgap on the p-side of the active region, which forms an electron blocking layer (EBL).

The active region must be designed such that both electron and hole concentrations are as high as possible, giving the highest possible radiative recombination rate $\mathrm{B}pn$. This is usually expressed as $\mathrm{B}n^2$ because the active region is assumed to be charge neutral and dopant-free, requiring that $p=n$. For a smoothly varying Fermi level, the carrier concentration changes abruptly at alloy heterointerfaces; the carrier concentration can be orders of magnitude greater in a narrower-bandgap well adjacent to a wider-bandgap barrier. Thus, the recombination rate is much greater in the well than in the adjacent barrier. This is referred to as carrier confinement and is already present in this purely classical picture, before we even consider quantum mechanical confinement effects. The effects of quantum confinement increase the bandgap slightly, as shown in Figure 6.1—for the most extreme possible case of an AlN/GaN MQB/MQW system, the bandgap is increased by at most 200 meV. In UV LEDs with alloy wells and barriers, a blueshift up to 10 nm by quantum confinement could occur.

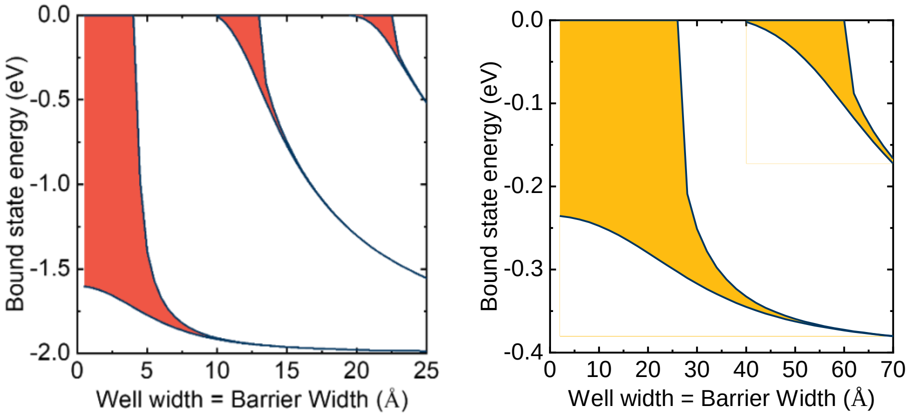

Figure 6.1: Calculated confined conduction bands for AlN/GaN superlattices (left) and AlGaAs/GaAs, assuming CB discontinuities of 2 eV and 0.4 eV, respectively. The heavier hole electron mass in the III-N case creates narrower bands, with significant tunneling occurring only below 5 A (as opposed to 20-30 A for the arsenide case). See Ref. [255].

Fundamental radiative lifetimes decrease with increasing bandgap, so that ultrawide bandgap AlGaN active regions have, in principle, a very high theoretical radiative recombination rate (see Figure 6.2) [3], [5][24]. In addition, the rather low mobility of holes in AlGaN increases the effective nonradiative recombination lifetime. These effects combine to give AlGaN a very high expected IQE, perhaps even exceeding that of InGaN.

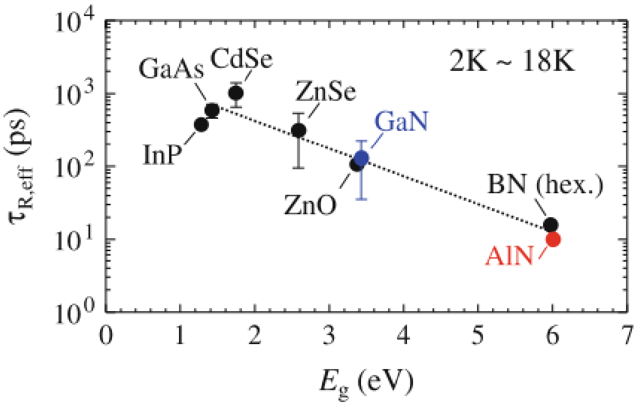

Figure 6.2: Low-temperature effective radiative lifetimes (measured by time-resolved photoluminescence) for fundamental optical transitions in a selection of compound semiconductors as a function of band gap. Shorter radiative lifetime is an indicator of potential for high radiative efficiency. Reproduced under Fair Use from [3].

---

[24] The proportionality of the spontaneous emission rate to the third power of the emission frequency was first calculated by Einstein, and predates the Schrödinger equation.

6.1.1 Strain effects – piezoelectric polarization

In nitride LEDs, polarization sheet charges at hetero-interfaces set up electric fields which spatially separate the electron and hole distributions, increasing the recombination lifetime [268], [269]. As explained by Kioupakis *et al.*, this reduces *all* recombination rates (not just the radiative rate), increasing the carrier concentration for a given current injection level. In turn, this enhances nonradiative Auger recombination processes, increases carrier overshoot, and increases device driving voltage. Furthermore, the potential difference created by polarization fields causes a significant redshift of emission photon energy, on the order of 100 meV/nm or more (e.g., a 3 nm thick well might give a redshift on the order of 300 meV, from 275 nm to 295 nm). Notice that the polarization-related redshift is much stronger than the quantum-confinement blueshift in wells more than 1-2 nm wide. There is some interest in reducing the magnitude of the polarization fields in the quantum wells.

Some degree of polarization discontinuity at the well/barrier interface is inevitable. The band offset is a device design constraint, so *the spontaneous polarization difference cannot be freely varied*. High-quality wells are always coherently strained to the barriers, so that some degree of piezoelectric polarization difference is always present. The question, then, is whether the strain state of the *cladding* layers (e.g., the n-type AlGaN current spreading layer) can be tuned to minimize the well/barrier polarization mismatch. In this section we will use the term *cladding* to denote the n-AlGaN or barrier layers, i.e. *the layers to which the wells and barriers are coherently strained*. We assume barrier compositions equal to the cladding composition here, but the analysis can readily be extended to barriers with compositions that do not match the n-AlGaN, or devices such as laser diodes in which the cladding layer is distinct from the current spreading and barrier layers, etc...

The *polarization difference* between the barrier and well determines the magnitude of the electric field in the quantum wells [268], [269]. Figure 6.3 shows the dependence of the piezoelectric- and total polarization values for $Al_{0.45}Ga_{0.55}N$ wells strained epitaxially to $Al_{0.65}Ga_{0.35}N$ cladding layers. The strain-dependence is given in terms of a relaxation percentage *of the cladding layer*, with 0% relaxation referring to fully coherently stressed layer, and 100% relaxation referring to a layer with lattice parameters matching those of a bulk, unstressed layer (assuming an equibiaxially stressed film with strains $\varepsilon_{xx} = \varepsilon_{yy}$ and $\varepsilon_{zz} = -\frac{2C_{13}}{C_{33}}\varepsilon_{xx}$). The cladding layer is thick enough that it may be partially or fully relaxed by the inclination of existing threading dislocations—that is, relaxation of the thick cladding layer does not imply the generation of new dislocations, although it is possible that new dislocations could form under non-ideal growth conditions (not relevant for high-WPE UV LED devices).

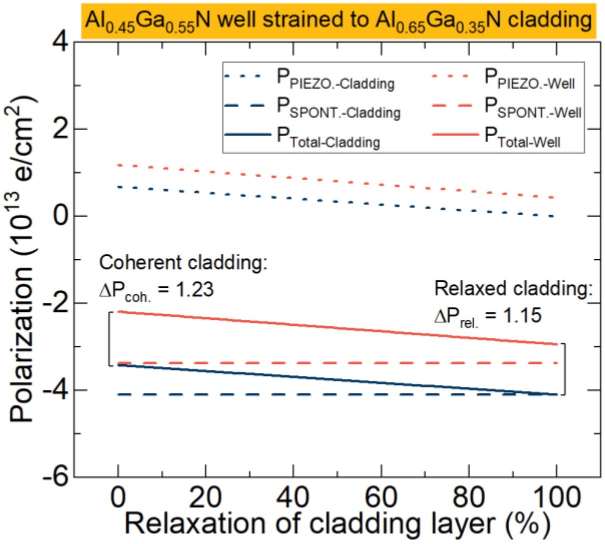

Figure 6.3: A *x* = 0.45 quantum well coherently strained to a *x* = 0.65 cladding layer: the effect of the relaxation of the cladding layer is shown. The well/barrier polarization discontinuity, ΔP, is 6.5% smaller in the relaxed case than in the coherently strained case. This difference is unlikely to be experimentally measurable in terms of device WPE.

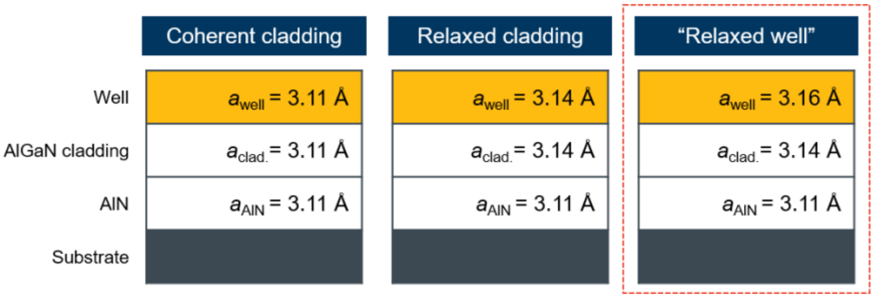

Figure 6.4: Schematic diagram shows the approximate lattice parameters, *a*, for each layer within the epitaxial stacks in each scenario. The "relaxed well" scenario is unlikely to occur in high-quality, high-WPE epitaxial material.

The polarization difference between barrier and well at UV-C relevant compositions is dominated by the large spontaneous contribution, and only weakly affected by the cladding's strain state, because the *strain difference* between the layers is almost entirely determined by the alloy composition offset. This strain difference does not depend strongly on the strain state of the underlying cladding.

So, if the strain difference is not measurably affected by the absolute strain state, the next question is whether the polarization difference is. Here, the case for absolute strain dependence is a bit stronger because the piezoelectric coefficients are not constant with composition. The product of a linearly varying composition and a linearly varying piezoelectric coefficient gives a very slightly quadratic polarization. As a result, the polarization charge is very slightly different in the coherent barrier case and fully relaxed case, as shown in Figure 6.3. This difference is unlikely to be measurable in real devices. The scenarios of coherent cladding, fully relaxed cladding, and "relaxed well" are illustrated in Figure 6.4, although relaxed wells are unlikely to be present in high-WPE devices because the only way for such thin layers to become relaxed would be by catastrophic extended defect generation.

6.1.2 Strain effects – valence band ordering

The valence band maximum at the Γ-point in nitride semiconductors is predominantly nitrogen-p-like, comprising combinations of p_x-, p_y-, and p_z-like orbitals. Due to strong anisotropy along the *c*-axis ($\hat{\boldsymbol{z}}$ direction) in wurtzite crystals, the energy of the p_z-like wavefunctions, $|Z\rangle$, shifts by an amount called the crystal-field splitting energy [270] with respect to the nearly degenerate $|X \pm iY\rangle$ bands. These bands are called: crystal-field split off valence band (CH), heavy-hole (HH), and light-hole (LH), respectively. The conduction band minimum at the Γ-point is predominantly cation-s-like and nondegenerate.

In GaN, the crystal-field splitting energy is *positive* and the CH band is *below* the HH and LH bands; in AlN this splitting is *negative*, such that the CH band lies *above* the HH and LH bands. The physics of this CH band is of great importance for UV LEDs, because recombination occurs primarily with holes from the topmost valence band. The properties of the valence sub-bands in wurtzite AlGaN alloys were described in detail over 20 years ago [271], [272], including the effects of strain and quantum confinement. The details of the implications of these calculations are worked through in Ref. [55], so I'll just recall the important parts here.

When radiative recombination involves holes with $|Z\rangle$ character, (from the CH band), the emitted wave is predominantly in-plane (it propagates toward the mesa sidewall, rather than vertically out of a *c*-plane device). This recombination is highly likely to become trapped in a guided mode within the semiconductor, as discussed in Chapter 8, and is therefore considered a detrimental light emission mode for *c*-plane LED devices. Recombination with $|X \pm iY\rangle$ holes (LH or HH) results in strong emission in all directions. These electric field directions ($\boldsymbol{E} \parallel \boldsymbol{c}$ from CH and $\boldsymbol{E} \perp \boldsymbol{c}$ from LH/HH) are sometimes referred to as transverse magnetic and transverse electric (TM and TE) polarizations, respectively, as summarized in Figure 6.5. In short, recombination involving CH holes is undesirable for UV LEDs, and recombination with the LH and HH holes is preferable. The band-crossing composition where the crystal field splitting crosses zero, and above which the detrimental in-plane emission becomes dominant, is therefore an important materials property.

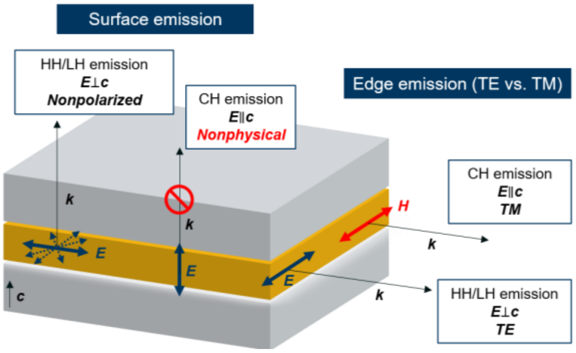

Figure 6.5: HH/LH emission yields $\boldsymbol{E}\perp\boldsymbol{c}$, giving strong emission in all directions. CH emission is optically polarized with $\boldsymbol{E}\parallel\boldsymbol{c}$ giving strong emission only in the in-plane (edge emitting) direction. For the HH/LH, surface emitting case, the electric field may be in any in-plane direction, as indicated by the additional dotted arrows. TE/TM nomenclature here refers to waveguide modes (i.e. edge emission); surface emission is nonpolarized in *c*-plane devices.

In unstrained bulk $Al_xGa_{1-x}N$, the band crossing occurs below $x = 0.1$, so that detrimental in-plane emission dominates over nearly the entire alloy range. The crossing point moves out significantly to $x = 0.65$ for $Al_xGa_{1-x}N$ coherently strained to AlN. Because the effective mass (along $\boldsymbol{c}$) of the CH band is much lighter than the other two bands, it is very strongly influenced by quantum confinement [273]. Combining both strain and quantum confinement effects, the crossover composition increases further to $x = 0.67$.

Recent reports have shown that UV LEDs with wavelengths corresponding to nearly the entire composition range can have HH/LH dominated emission. Ref. [274] compiles LH/HH emission results all the way down to 222 nm, and CH emission as high as 300 nm, depending on strain and confinement.

In conclusion: in 265 nm – 280 nm UV LEDs, in-plane emission can be prevented with well-designed active regions, however it may become a significant challenge for far UV-C devices.

6.2 Active region optimization

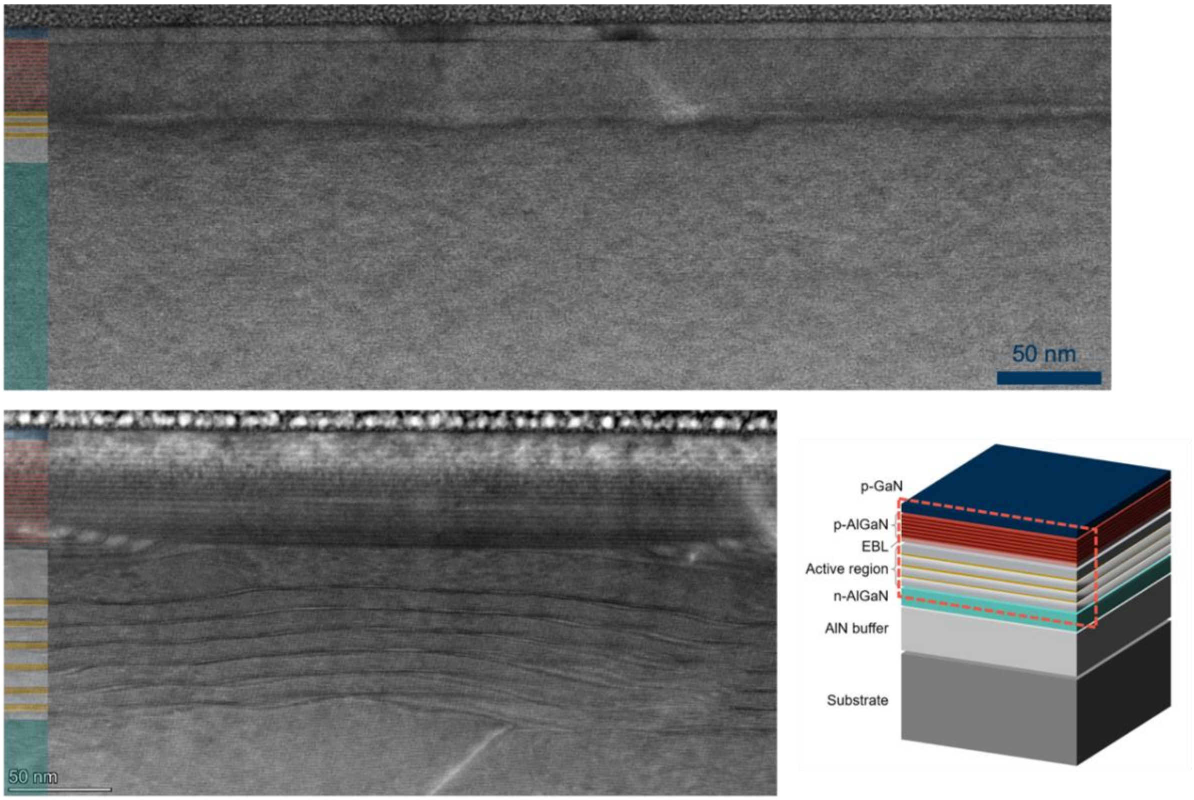

Figure 6.6: TEM comparison of active regions on SiC [32] (top) and sapphire [196], [259] (bottom). Schematic structure shown on bottom right, indicating region of interest. Nominal growth structure shown schematically using colored rectangles on the left of each image—it is notable that the expected MQW structure is not clearly visible in the upper image (on SiC), and is visible but has an unexpected undulating or “wavy” morphology in the lower image (on sapphire).

As discussed above, the point of the active region is to maximize the concentration of both electrons and holes, in the same place. The ingredients for this are 1) quasi-Fermi levels close to the respective bands i.e. good carrier injection, and 2) well-defined quantum well/barrier structures. Our early UV LED growth conditions were a bit unpredictable, drifting suddenly and giving different light output power, emitting at different wavelengths, or giving different IV characteristics from run to run. We found that LED performance became more reliable with a simplified active region consisting of our low V/III n-AlGaN growth condition sans disilane injection. These devices gave IQE of 8-9% as discussed in Chapter 5, but also gave some strange trends.

6.2.1 Structure of active regions: TEM and SIMS

The microstructure of this simplified active region is shown in Figure 6.6. There is very weak contrast between the well and barriers, suggesting that the interface quality is poor. The entire "multiquantum well" active region appears as one or two slightly darker stripe(s) in the sample on SiC. This lack of contrast could be due to interface roughness (since the TEM image shows a projection along the thickness of the foil), or uniform intermixing. The sample on SiC had nominal well and barrier compositions around 40% and 60% respectively, while the sample on sapphire had slightly higher contrast of 35% and 65-70%. This may be the reason for the slightly improved contrast in the TEM image of the sample on sapphire.

Also visible are micron-scale undulations in the active region morphology, in good agreement with what we know about the AFM of our low V/III n-AlGaN growth condition (see Chapter 4), showing that the MQW active region grows conformally above the undulating n-AlGaN. In contrast, the p-superlattice (grown under much higher V/III ratios over 2,000, and under a pulsed growth mode, both of which are known to favor surface smoothing) planarizes the surface so that the top of the superlattice is atomically flat (again consistent with AFM) on both SiC and sapphire.

We tried many times to improve LED performance by smoothening the MQW active region. Increasing the growth temperature, reducing the growth rate, increasing the V/III ratio, and introducing a lightly doped n^- smoothing layer before the active region all smoothened the morphology expected (AFM not shown), but universally led to reduced LED output. At this time, it is unclear whether the slightly undulating surface morphology of the MQW is beneficial, or whether there is something else about the current growth conditions that is highly favorable, and the morphology is merely coincidental. Exploring this further is a matter of “future work,” but it is likely that there is a way to smooth the active region and improve LED output power; it must be done carefully without drastic changes to the growth conditions of the MQWs themselves, which appear to be quite sensitive.

Returning to the discussion of MQW abruptness, the more clearly visible MQW features in the sample grown on sapphire may be related to another subtle difference in the growth conditions. As mentioned, the conditions *during* the deposition such as growth rate, V/III, temperature, etc. were all similar. However, the sample grown on sapphire included a new development we found to improve LED power: *growth pauses*. We found that by introducing pauses of 20-60 seconds after the growth of each well and barrier, LED power was significantly better than without a pause (I will go into more detail in Section 6.2.4), and the emission wavelength was on target at 285 nm, indicative of emission from the active region (whereas the wavelength without pauses was 322 nm, indicative of p-superlattice emission).

These pauses produced thin regions of relatively lower [Ga] (i.e. higher [Al]) at the heterointerfaces (shown in Figure 6.7 and Figure 6.8), forming thin barrier layers that enhance carrier confinement and perhaps also smooth the surface. Based on the difference in emission wavelength, it could be the case that the pauses improve IE, causing electrons to recombine in the active region rather than overshooting into the p-superlattice. We have observed in the past that impurities like O and H pile up at growth pauses in some cases (data not shown), so perhaps there is some impurity gettering effect as well.

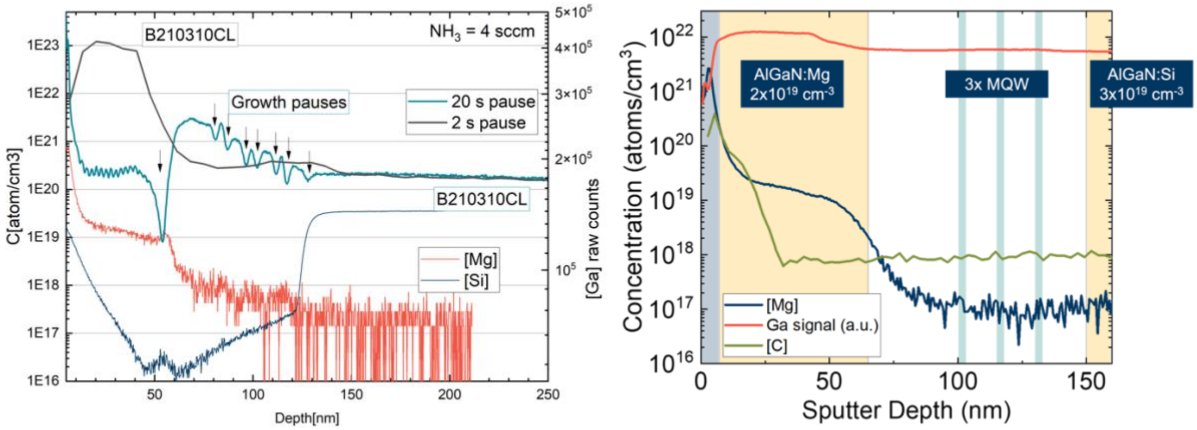

Figure 6.7: SIMS data for UV LEDs from March 2021 (left) and June 2020 (right).

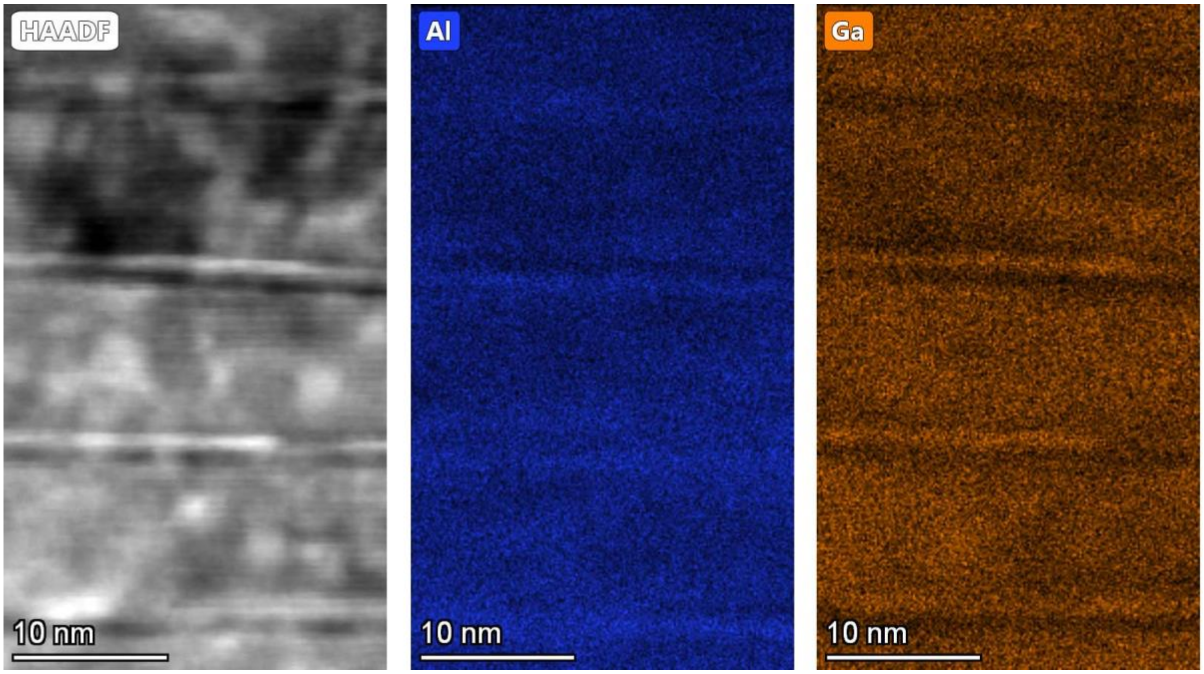

Figure 6.8: EDX elemental maps of UV LED active regions grown on sapphire, as shown in Figure 6.6 on sapphire. Above and below each Ga-rich quantum well (4 QWs shown here), are two thin Al-rich regions. The EDX signal for Al is not as clear as for Ga due to the lower atomic number of Al.

Also shown in Figure 6.7 is the Ga signal for another LED grown with only 2s pauses in the active region, on an otherwise identical structure. This structure gave much lower light output power, and did not have any evidence of thin Al-rich barriers at each heterointerface. The Mg concentration in the active region is higher than intended, remaining close to 10^{18} cm^{-3} throughout most of the active region, potentially causing reduced LED efficiency through nonradiative recombination, or radiative recombination at undesired luminescent Mg defect lines. This was later improved to below 10^{17} cm^{-3} by baking the MOCVD reactor under H_2 between growths, reducing background Mg. The [C] level of 10^{18} cm^{-3} was fairly typical for LEDs grown at this time—work aimed at reducing this value by e.g. increasing growth temperature or V/III ratio led to lower power, and was not pursued further (but this is also something that should be improved in future devices). Oxygen levels (not shown) were in the range of 10^{17} cm^{-3} in all devices we reported.

6.2.2 Wavelength control

Almost every time we looked at the active region before Spring of 2021, the MQW composition and thickness had weak effects on emission wavelength (see Table 6-1 for an example of the type of trends we often observed). Instead, the strongest trends in wavelength often came from changing the composition of the barriers! This could be attributed to a strong effect of electric fields in the quantum wells, alloy intermixing and poor interface abruptness, quantum confinement, or some other factor. Recalling the discussion in Section 4.1.2, it is notable that in the barrier composition series shown in Table 6-1, the emission wavelength is uniformly about 0.5-0.8 eV below the band-edge of the barrier AlGaN in all three cases. The emission wavelength of around 310±5 nm was found in almost all samples with barriers (and spacers) with 65% Al composition. Removing the quantum wells completely (leaving just an undoped 65% Al spacer region between the p- and n-sides) resulted in 306 nm emission of 0.5 mW at 60 mA (quicktest), nearly identical to samples with QWs at that time.

These trends, in combination with the structural data discussed above, could be interpreted as indicating that the emission from our devices in the early days was dominated by emission from other areas (not the QWs). This could include the QBs, n-type AlGaN, spacer layers, or p-side of the device. As mentioned above, though, we found significant evidence that the emission from the p-side of the device was around 330-340 nm, consistent with emission from the p-AlGaN. This conclusion was based on the fact that this emission was strongest in samples with weak hole injection (i.e. high electron overshoot) such as: low-contrast superlattices, samples with low Mg concentration, 3D polarization doped structures with weak composition gradients, samples with strongly n-type quantum barriers (discussed below), and samples in which the p-side undoped spacer was removed (so that the MQW was directly adjacent to the thin EBL and p-SPSL).

Table 6-1: Dependence of emission power and wavelength with well composition, barrier composition, and well thickness. Dependence on well thickness and composition is negligible, and the strongest trends come from barrier composition differences. Expected wavelength shown in parentheses refers to the band-edge wavelength of the well composition.

Well composition	Power @ 60mA	Measured (*expected*) Wavelength (nm)
45%	1.0 mW	306 (*277*)
40%	1.0 mW	308 (*285*)
35%	2.0 mW	313 (*295*)
Barrier composition		
65%	0.2 mW	314 (*295*)
73%	0.01 mW	290 (*295*)
81%	0.07 mW	277 (*295*)
Well thickness (nm)		
4	0.2 mW	314
2.5	0.3 mW	306
1.5	0.5 mW	302

The SIMS data in Figure 6.7 showed an unexpectedly high [Mg] in the active region, such that $N_A > N_D$ throughout the QWs. In other words, the *metallurgical* junction (i.e. where $N_A = N_D$, in contradistinction to the *p-n* junction where $p=n$) was located completely to the n-side of the active region, rather than roughly *in* the active region, where we expected it to be. We performed a few experiments to place the metallurgical junction more squarely in the MQW active region, with great success. First, simply removing the n-side spacer so that the first QW was grown directly on the n-AlGaN greatly increased LED power. This device had an emission wavelength of 289 nm and an emission power of 2.1 mW at 60 mA. At the time, this was our brightest LED to date.

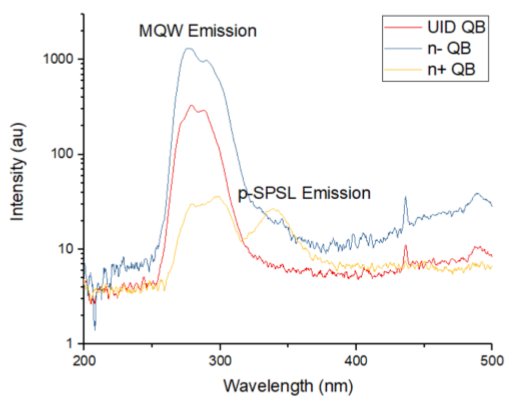

[Si] in QB	Power @ 20 mA
Undoped	0.3 mW
n^-	1.2 mW
n^+	<0.01 mW

Figure 6.9: Quantum barrier doping series, showing that output power is maximized when barrier doping is on the order of mid-10^{17} cm^{-3} (n$^-$). Undoped wells give quantum well emission with reduced power, whereas strongly doped wells give greatly reduced output power and a long-wavelength peak indicative of emission from the p-superlattice.

Second, lightly doping ([Si] ≈ mid-10^{17} cm^{-3}) the QBs was found to increase power even more. In contrast, strongly doping them around 10^{18} cm^{-3} or greater reduced power almost to zero, and produced an emission peak in the 320-330 nm range, attributed to emission from the p-superlattice, as shown in Figure 6.9.

After implementing the above changes (placing the first MQW directly adjacent to the n-type AlGaN, and lightly doping the QBs), device power improved. More importantly, returning to our QW experiments under these new conditions gave us much stronger control over the wavelength of the light emission. As shown in Figure 6.10, we now saw strong trends with QW thickness and composition, with thinner and more Al-rich wells both giving blue-shifted emission. Notably, samples with very short emission wavelengths began to emit a second peak of unknown origin at a longer wavelength, perhaps related to the defect emission peak discussed in Chapter 4.

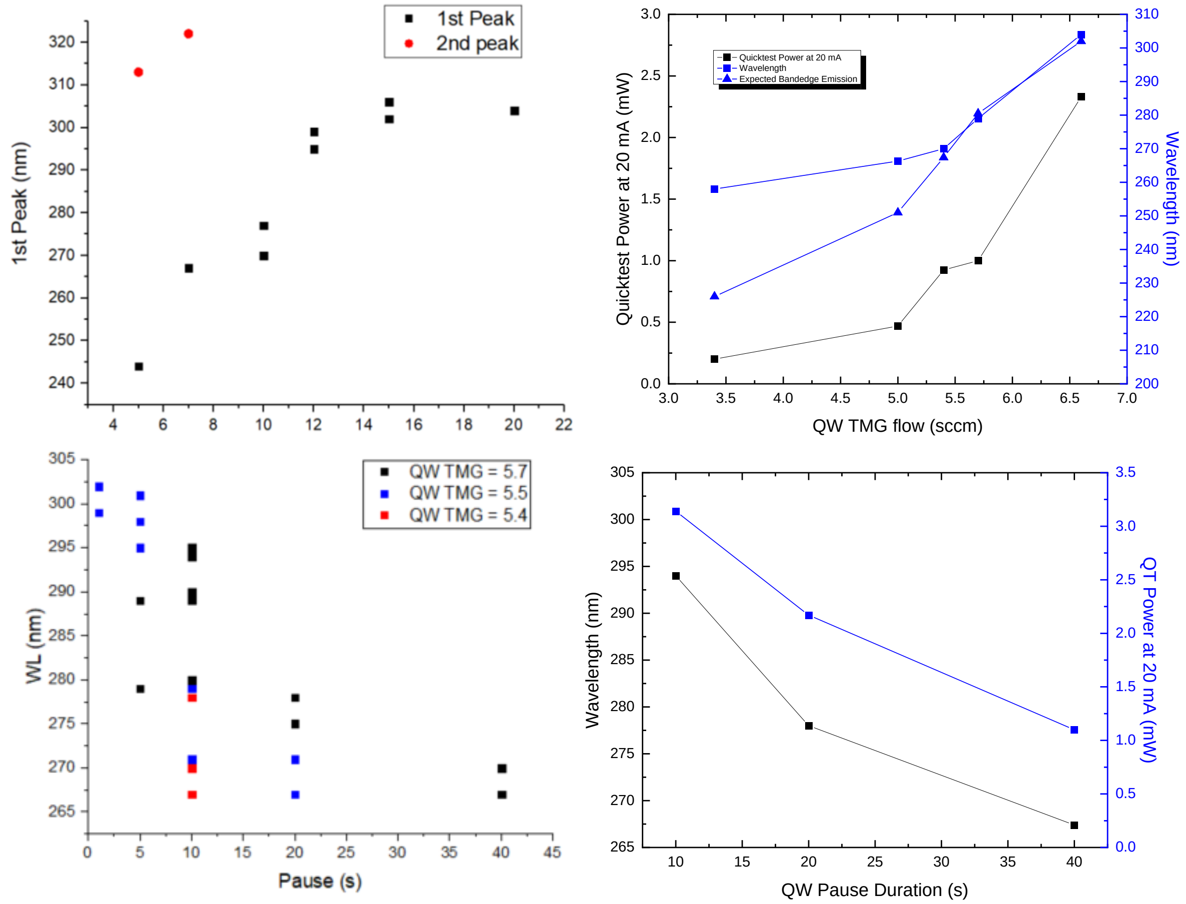

Figure 6.10: Effect of MQW thickness, TMG, and pause time on LED wavelength and output power. Good wavelength control was achieved in these samples, with improved active region structures.

We observed a blue shift with increased growth pause duration, suggesting the pauses were likely bringing about some desorption of material. A few possible explanations: 1) desorption of AlGaN when no metalorganic precursors were supplied (the pauses took place under very low NH_3 flow), giving a QW thinning effect, 2) selective desorption of Ga out of a thin surface layer, producing Al-rich QWs, or 3) desorption of surface-riding precursors like TMG (giving decreased Ga incorporation). Regarding the increased EQE of devices with pauses, explanations could also include desorption of TMI (perhaps gettering impurities), or desorption of surface-riding impurity species like unintentional Mg (always present in

MOCVD due to the memory effect), C, or O. However, pause durations longer than 20 s are detrimental, so a simple impurity-desorption explanation is probably insufficient.

6.2.3 Temperature dependent electroluminescence

As discussed above, some samples displayed multiple emission peaks. For typical GUV devices, there were three commonly observed peaks (although not always in the same samples). Samples understood to have significant electron overshoot had strong emission at roughly 330 nm, attributed to p-superlattice emission with some confidence. This peak was easily eliminated with improved active region design, and did not appear in the high EQE samples discussed in the latter half of this Chapter. Next, there was a quantum well peak, attributed with confidence to band-edge emission from the MQW due to its clear dependence on QW thickness and composition as discussed above. Finally, there was a third peak which did not appear to depend on MQW properties, but instead shifted significantly with changes to the quantum barriers and spacer layers, as shown in Table 6-1. To investigate the two emission peaks separately, a sample was grown with a QW emission target of 315 nm, so that it would emit at both 315 nm (wavelength-controllable MQW emission) and 285 nm (unattributed peak, perhaps related to barrier or spacer layers). (M. Wang performed much of the growth and experimental measurements for this section; details will be in a future publication).

The electroluminescence spectra were compared at different temperatures using a cryostat. LEDs were tested under pulsed operation with a 1% duty cycle to prevent self-heating effects. Spectra were collected using a fiber-coupled Ocean Optics Flame UV-Vis spectrometer at 25 K increments, and at various drive currents. These devices were approximately 0.1 mm^2 in area, so that 1 mA $\approx$ 1 A/cm^2. Representative spectra at 5 K and 350 K are shown in Figure 6.11.

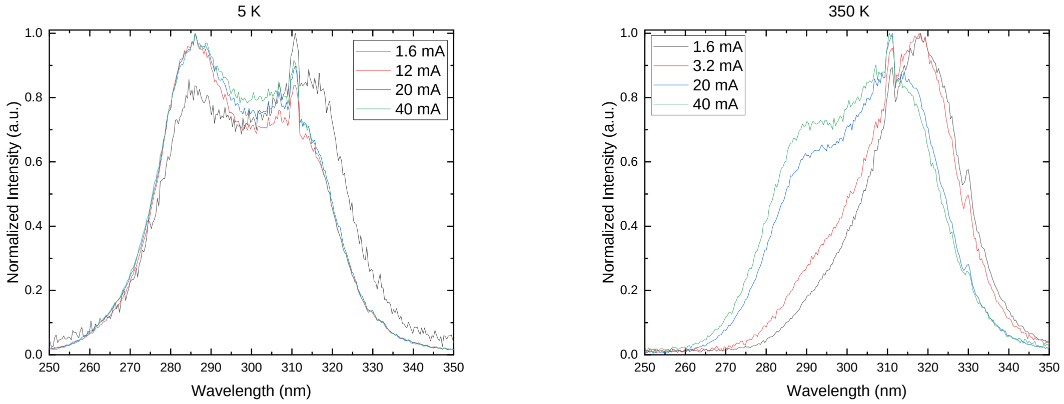

Figure 6.11: LED spectra at 5 K and 350 K, showing two peaks. The long wavelength peak around 315 nm corresponds to quantum well emission. The short wavelength peak around 285 nm is of unknown origin, but is attributed to defect-related luminescence from outside the QW, perhaps in the quantum barrier or spacer layers. At low temperatures, both peaks are strongly emitting. At high temperatures, the quantum well emission dominates at low currents, but the short wavelength peak returns at high currents.

At low temperatures, both peaks are strong, potentially resulting from poor hole injection efficiency at low temperatures (p-superlattice hole injection layers are expected to show non-negligible temperature dependent acceptor ionization, unlike 3D polarization enhanced graded layers). Low hole concentration in the p-SL leads to low hole concentration in the QWs, so that the radiative rate in the QWs does not greatly outweigh that in the barrier or spacer regions. At high T and low J, where IE is likely to be highest (low electron overshoot at low voltage), the short wavelength peak is nearly invisible. As J is increased, a weak short wavelength peak returns, perhaps related to high carrier concentration outside the QWs.

More work is needed to fully explore the emission wavelengths observed in this study and discussed in Chapter 4. For now, we tentatively attribute the short-wavelength peak to defect emission from the spacer or barrier layers. This is based on our consistent observation of a strongly luminescent defect peak in our n-AlGaN layers grown under identical conditions to the barrier and spacer layers, and based on the conjecture that the short wavelength peak appears in the temperature dependent EL data whenever IE is lowest (i.e. when hole concentration in the QW is lowest for a given current). With additional active region optimization, we were able to develop devices in which the unknown peak's intensity was greatly reduced or eliminated.

6.2.4 High power UV LEDs

Placing the MQW immediately above the n-AlGaN (without a spacer), introducing 10-20 s pauses after each well and barrier, and lightly doping the quantum barriers resulted in LEDs with EQE above 3%, as shown in Figure 6.12. These LEDs showed strong effect of MQW thickness on both efficiency and wavelength, however there was still significant variation across each particular sample, as shown in Figure 6.13.

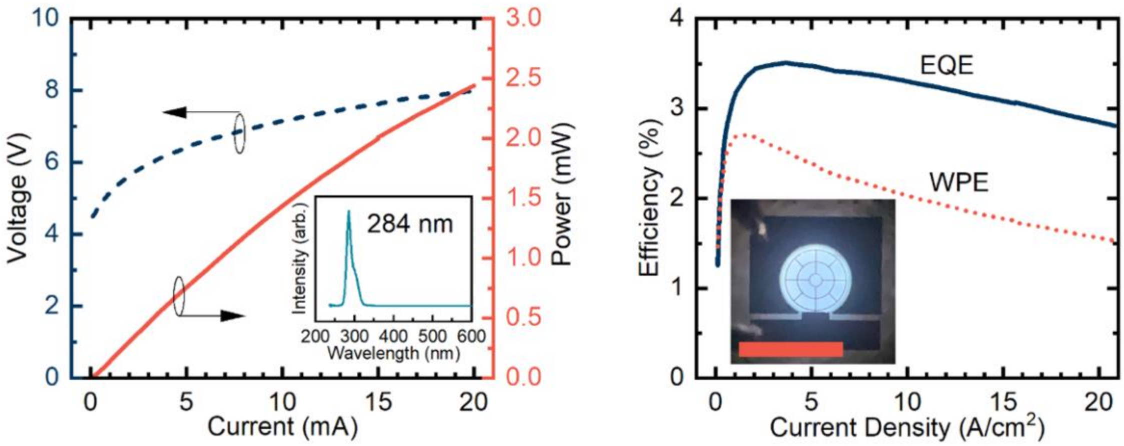

(a)

(b)

Figure 6.12: Improved 284 nm UV LED (**a**) Voltage and output power versus current, inset: spectrum showing sharp peak at 284 nm, and no observable UV-A or visible parasitic emission. Operating voltage is below 8V, providing a voltage efficiency of 54% at 20 A/cm^2. (**b**) External quantum efficiency (EQE) and wall plug efficiency (WPE) of the UV LED versus current density, inset: microscope image of operating UV LED showing uniform emission pattern with 500 μm scale bar.

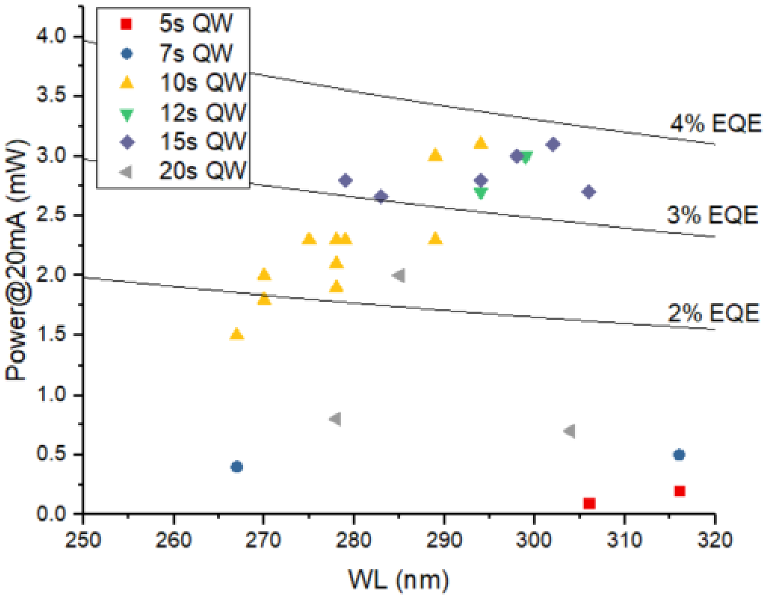

Figure 6.13: Effect of QW pause duration on LED power and wavelength after significant optimization of MQW placement, composition, pause duration, and barrier doping.

The next set of experiments involved further optimization of the quantum barrier doping, focusing particularly on exploring *which* barriers should be doped or undoped. M. Wang was the primary grower in these experiments, leading our efforts in active region optimization beginning in the second half of 2021. We found that doping only some number of barriers, followed by subsequent MQW growth with undoped barriers, gave massive increases in output power. This is attributed to further fine tuning of the effective p-n junction, i.e. placing the region of maximum recombination (in which n*p is highest) entirely within the MQW active region. For instance, in 6x MQW samples, we found that doping only the first two barriers increased peak EQE to 5.5%, drooping to about 4% at 20 A/cm^2. Then, increasing the number of MQW periods with doped barriers to 8 (while keeping 4 undoped barriers) further increased peak EQE to 7.7%. After full device processing and integrating sphere testing, final values of EQE = 10.6% and WPE = 7.7% were achieved for 285 nm emission. Further details and full analysis of these devices will be published by Wang *et al.*.

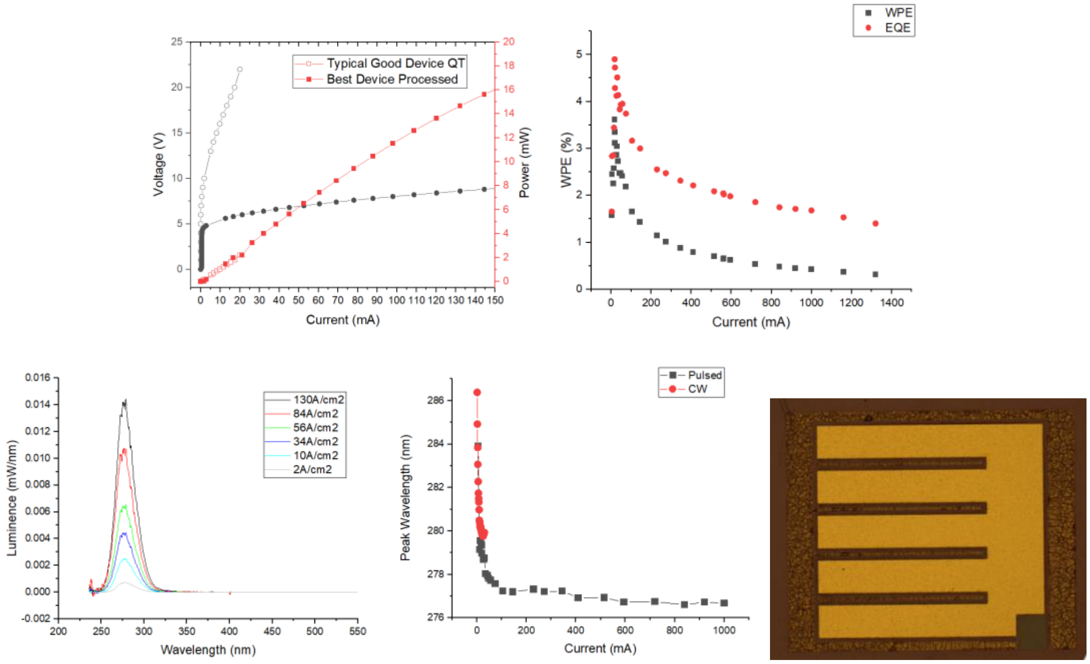

Figure 6.14: High power LED data for a 1 mm^2 device. **Top left**: LIV curves showing quicktest (open symbols) and fully processed integrating sphere testing (filled symbols). Power was similar for both, indicating that LEE for the large devices was similar to that for on-wafer testing. Device processing with annealed ohmic contacts greatly improved device voltage, which remained below 10 V even for currents as high as 150 mA. **Top right**: EQE and WPE data for the power data shown on the left, as well as for high power measurements taken under pulsed conditions. Devices were operated at currents as high as 1 A without degradation or failure. **Bottom left**: spectra showing single-peak operation with no measurable parasitic side-peaks. **Bottom center**: Peak wavelength data showing strong blue shift at higher current injection associated with electric fields in the active region—no evidence of thermal redshifting due to the pulsed measurement condition. **Bottom right**: microscope image of the device, with each side measuring about 1200 μm.

Perhaps even more notable was the improved uniformity and reliability these changes provided to our devices. With active regions optimized according to the above methods, we began to routinely achieve devices with EQE in the range of 3-6%, in which nearly the entire epitaxial area (10x10 mm^2 wafer pieces) emitted strongly. One such sample with a peak EQE of 5% was processed into a large area (1 mm^2) LED in order to investigate device characteristics under high total current and high power operation. Data for this device (collected by Y. Yao) are summarized in Figure 6.14.

7 LED fabrication and testing

A process cannot be understood by stopping it. Understanding must move with the flow of the process, must join it and flow with it.

-The First Law of Mentat

Figure 7.1 shows three common LED architectures: bulk flip chip, thin film flip chip, and transparent p-contact. The first two are called flip-chip because the epiwafer is bonded ("flipped") onto a submount wafer (the submount is not shown in Figure 7.1), and light is emitted from the bottom of the device. The flip-chip architecture is needed for GUV LEDs because there is no transparent p-side current spreading layer available, and therefore the p-contact must cover the entire device mesa. Light emitted in the active region is partially reflected by the metal p-contact.

In a the thin-film flip-chip architecture, the growth substrate is removed after flip-chip bonding, leaving only the epitaxial layers behind [275]. The N-face AlN (bottom side in Fig. 7) of the thin-film flip chip device can be roughened using a dilute KOH solution, enhancing light extraction efficiency [185], [276]. In future devices, a transparent p-contact architecture could be used for enhanced topside emission. The transparent p-side architecture has very high light extraction efficiency and is ubiquitous in commercially available blue LEDs (using ITO).

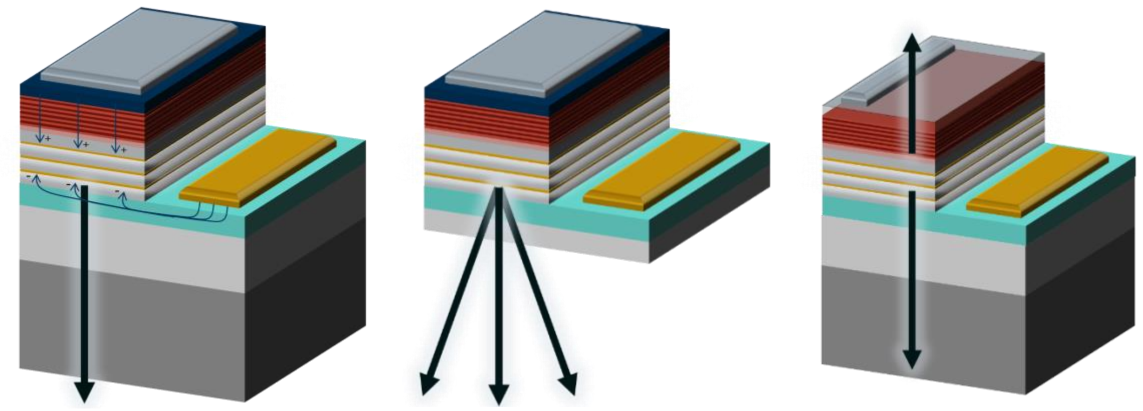

Figure 7.1: Three UV LED architectures: conventional flip chip (left), thin film flip chip (center), and transparent p-contact (right). Blue arrows indicate the lateral and vertical current flow needed for hole and electron injection into the active region. The n-ohmic (yelllow) and p-ohmic (gray) contacts inject carriers into the device. Substrate removal improves light extraction significantly, for both TE and TM emission modes, and can be combined with backside surface roughening to achieve LEE up to 40% (even with p-GaN). In the transparent p-contact device (right), the p-side ohmic covers only a small portion of the device mesa, so that light may be emitted from the top or bottom of the device. Transparent p-side devices are not yet widely available but early results using n-AlGaN tunnel junction contacts show the potential of this architecture.

As discussed in the previous chapters, high quality AlN and AlGaN-based device layers can be grown on SiC substrates. The UV-C optical absorption of the SiC substrate presents both a challenge and an opportunity for LED fabrication. As discussed by Dr. SaifAddin in his PhD dissertation and publications [31], [185], [261], [277], SiC is much more practical to remove than sapphire, because it contains Si and can be etched using an ICP dry etch method much like the Bosch etch used in the silicon industry. Furthermore, the use of SF_6 is a natural choice for SiC substrate removal etching because the fluorine forms an inert Al-F layer as soon as it reaches the underlying AlN layer, creating a hard mask and protecting the AlN from further etching. So, the SF_6 ICP is both highly effective in removing SiC, and highly selective against AlN etching.

But why go through the trouble of removing the substrate in the first place? Sapphire is transparent, so isn't the light extraction efficiency higher anyway? As it turns out, this is not the case for slightly counterintuitive reasons discussed in Chapter 8. The bottom line is, a thin-film flip chip architecture with backside substrate roughening is by far the highest light-extraction structure for UV LEDs, as it is the most effective structure for extracting guided modes before they interact too strongly with the highly absorbing semiconductor layers.

7.1 Quickfab processing

On the other hand, growth of LEDs on SiC presents a challenge for short-cycle device characterization. UV LEDs on sapphire can be tested using the "quicktest" method immediately after MOCVD growth. In this method, indium dots are deposited on the epitaxial material using a foil mask, and an n-contact is scribed onto a corner of the wafer. Then, light emission power can be measured through the bottom of the sapphire wafer, providing quick and quantitative measurements of LED output power. One option for quicktest on SiC is to place the radiometric detector *above* the sample surface, but this is difficult in practice when making room for electrical probes, and it is especially difficult to ensure the detector is placed at the exact same location and angle each time. Therefore, devices grown on SiC must be processed and packaged, then tested in an integrating sphere before quantitative measurements of output power can be made. The full TFFC process took around a month, so a quicker process was needed.

To facilitate a shorter cycle between epitaxy growth and device results, we developed a "quickfab" process which provided some of the quantitative results of the full process (with much lower LEE), while only taking about a week from epitaxy growth to data collection in the integrating sphere. Just as in the full LED process, mesa etch was performed using reactive ion etching with $SiCl_4/Cl_2$ chemistry [278] and metallization using electron-beam evaporation. The V (15 nm)/Al (80 nm)/Ni (20 nm)/Au (300 nm) n-contact was annealed under flowing N_2

for 30 s at 900 °C [277]. For reference, the reflective p-mirror contact in downward emitting structures comprised Ni (1 nm)/Al (100 nm)/Ni (100 nm)/Au (800 nm).

This quickfab process made use of a thin p-contact, as shown in Figure 7.2. This contact is semi-transparent because the metals are less than 10 nm thick. Early iterations of the process made use of 2 nm Ni/3 nm Au, which provided adequate current spreading and good voltage performance with LEE around 3-4%. The problem with these Ni/Au contacts was that they were not robust during operation. Above around 13 V or 100 mA, these contacts failed rapidly as shown in Figure 7.2. The morphological change in certain areas of the contact (separated by thick multilayer stack electrodes as shown in the schematic) corresponded to stepwise reductions in LED power and increases in voltage, suggesting that the effective LED active area was decreasing as each successive region of thin metal failed.

This problem was solved by changing from Ni/Au to Ni/Pt. The platinum contacts proved more robust against high power operation, and had the added benefit that Pt is itself a fairly good ohmic contact material to p-GaN so that the voltage performance may have improved slightly.

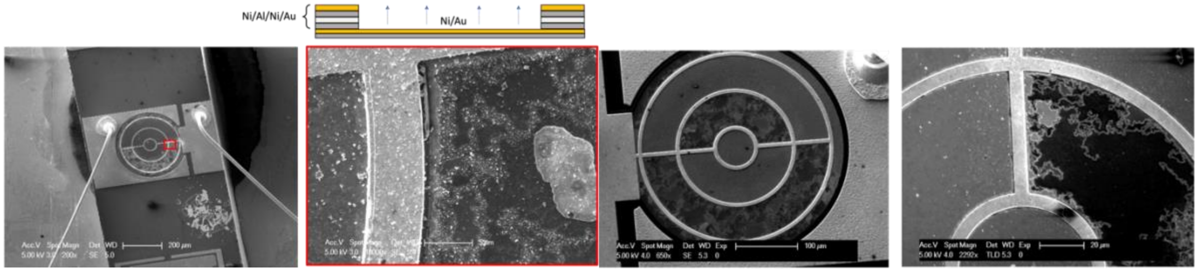

Figure 7.2: SEM images of Ni/Au thin-metal used in QF process, after device operation. Samples with thin Ni/Au contacts failed catastrophically during devices testing, with corresponding stepwise increases in voltage and decreases in power. SEM inspection showed failure of individual regions of thin contacts. This issue was resolved by replacing Ni/Au with Ni/Pt.

7.2 Flip chip

The flip-chip bonding process used to achieve high-LEE UV LEDs based on SiC substrates has been described previously [31], [185], [261], [277]. One key aspect of this process was the Au-Au thermocompression wafer bond, in which both the n- and p- metal contacts were aligned and bonded to a patterned submount with metal contacts for wirebonding. In initial experiments, the yield of this bond process was below 50%, resulting in delamination of devices from the submount wafer during ICP etching.

Focused ion beam analysis using SEM, shown in Figure 7.3, indicated that a thin region of low-Z material appeared to be sandwiched between the metals. This material appears as a dark region in the SEM image, and is most noticeable by its effect on the contour of lighter-colored Ga material deposited during the FIB process, which appears as a light gray ribbon on the lower left portion of Figure 7.3. The dark material (above the ribbon in the image, and thinly sandwiched between the Au metals which have been falsely colored yellow) is presumed to be some organic residue such as photoresist residue or solvent residue not fully removed during sample cleaning. A low power oxygen plasma clean or “ash” was implemented to improve the Au surface before bonding, which signifincantly improved device yield to over 80%.

The second limiting factor in the flip-chip process was the substrate removal. This comprised a three-step process: 1) mechanical thinning using a polishing tool, 2) fast, high-power ICP etch to rapidly etch SiC at 30 nm/s (~10.8 μm/hr) as shown in Figure 7.4, and 3) a slower but highly selective ICP etch.

Figure 7.3: FIB analysis of failed UV LED flip chip device. Dark residue can be seen sandwiched between the falsely yellow colored Au pads. Semiconductor mesa is shown in green.

While the ICP etch rate was found to be highly uniform and repeatable (even over the course of several years, and with good agreement across 6H and 4H SiC from various suppliers), the mechanical thinning step introduced a significant degree of nonuniformity in the wafer thickness, shown schematically in Figure 7.4. Additionally, the original polishing system had unreliable rotation rate and loading, and polishing rates varied from one sample to another. Furthermore, there was no way to monitor the polishing rate during operation, so samples had to be unloaded and measured manually with a gauge repeatedly during thinning.

These issues in polishing/lapping resulted in challenges during ICP etching. Because the total thickness variation was large, polishing had to be stopped with 80-100 μm of SiC remaining. As a result, long ICP etch durations were needed. While the ICP etch is indeed highly selective against AlN, the ICP conditions attacked the Au metal used for bonding near the edge of the wafer. If a wafer was left in the ICP for too long after the substrate had been fully removed, the edge of the wafer began to deliminate, as shown in Figure 7.4.

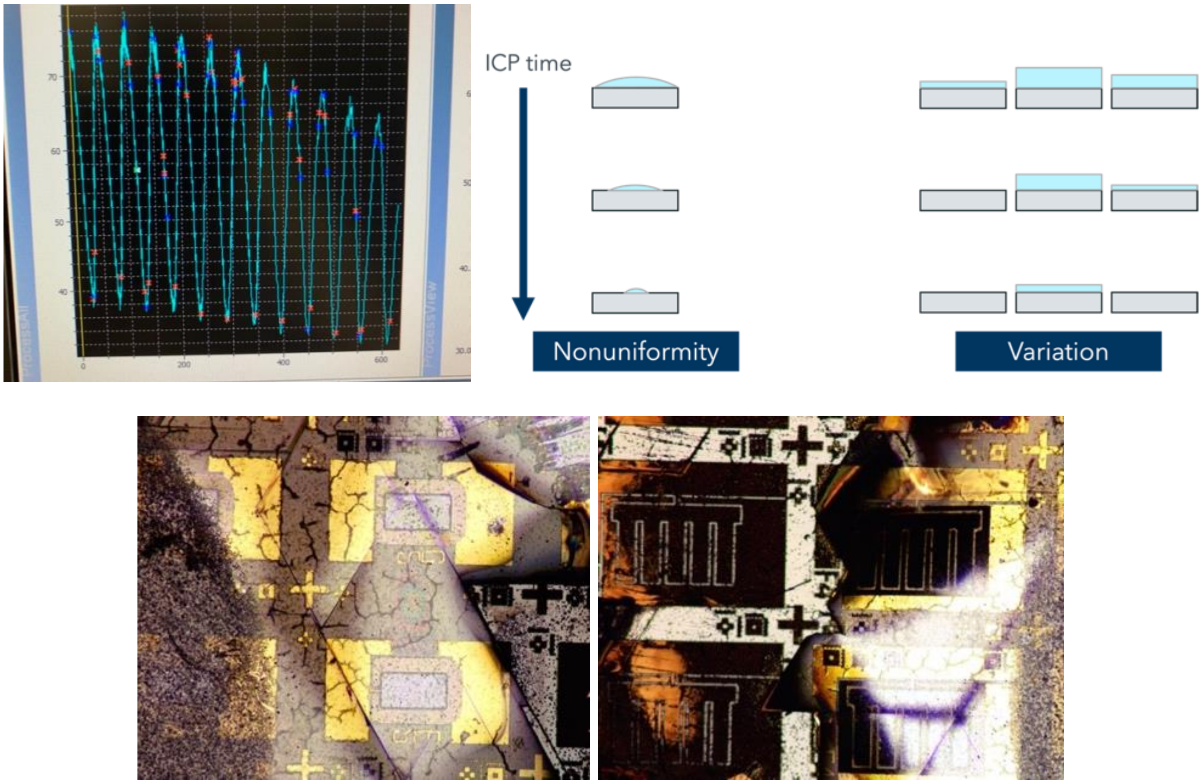

Figure 7.4: Polishing for substrate removal. **Top left**: in-situ laser monitoring of ICP etching of SiC substrate (x-axis is minutes, y-axis is reflectivity), showing an etch rate of about 180 nm/min. **Top right**: schematic image showing the issues of nonuniformity and variation across wafers caused by the insufficient precision of the polishing tool used in early experiments. **Bottom**: two microscope images showing intact AlN devices with some SiC remaining on the left hand side of the image, and the edge of a wafer where the Au metal has been attacked by the ICP etch and the AlGaN film has fully delaminated.

Etching of small amounts of metal from debris within the chamber or from unintentionally exposed device regions resulted in sputtering of this metal onto the wafer surface. These small metal particles act as etch barriers and lead to the formation of narrow pillars, or grassing. This is shown in Figure 7.5. Therefore we found there was a strong need to improve the polishing process, both in terms of wafer uniformity (i.e. doming) and variation between wafers. Y. Yao led an effort to transfer our polishing process to a new tool located in the CNSI TEM prep area which was better suited for the precise alignments needed for uniform and reliable polishing rates.

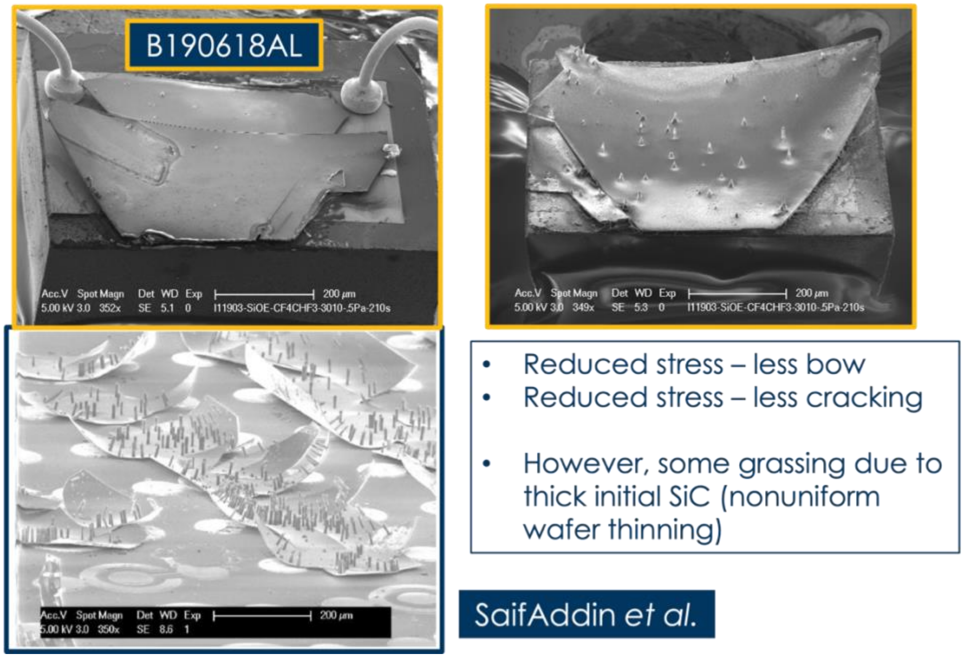

- Reduced stress – less bow
- Reduced stress – less cracking

- However, some grassing due to thick initial SiC (nonuniform wafer thinning)

SaifAddin *et al.*

Figure 7.5: SEM images of TFFC devices. Top left: optimized device with low stress and no grassing after improvements discussed in this section. Top right: low-stress device with grassing caused by long duration ICP etching. Bottom left: typical appearance of high stress devices with grassing, before optimizations discussed in this section and in Chapter 3.

Figure 7.5 also shows an added benefit of the low-stress AlN we produced by the methods described in Chapter 3. Whereas previous generations of devices were grown on material with large tensile stress gradients that showed significant cracking and bowing after substrate removal, devices grown on low-stress AlN templates showed almost no observable bowing after substrate removal. These samples remained planar after substrate removal and showed only minimal chipping after wafer dicing. To expose the underlying metal contact pads, the films were physically scraped using tweezers to remove the excess thin film. The devices were remarkably robust during this process, remaining fully bonded in the regions where the Au-Au bond was located, and requiring some force to break off the excess AlN. In an industrial setting, this process could be readily replaced with a backside lithography step to remove the excess AlN in a faster and more repeatable way. Overall, we estimated that reduced bowing and cracking improved overall wafer yields by a factor of two.

The data from this new process after full optimization are shown in Figure 7.6. Firstly, the polishing rate reduced slightly over the course of a single polishing run, so that a new piece of polishing paper was needed every 1-2 runs. Fortunately, this polisher had an integrated micro-thickness gauge, so that the polishing rate could be tracked in-situ, and the sample could simply be polished until the desired thickness was reached and then removed. The sample thickness variation was measured using the Nanofabrication facility's KLA Tencor P7 profilometer which is capable of measuring large steps of several hundred microns.

We introduced a number of improvements to the polishing process, such as replacing the lapping paper after every one or two runs, depending on which specific paper type was used. Additionally, careful alignment of the wafer before lapping was possible on the new tool so that the doming effect was greatly reduced, decreasing the total thickness variation edge-to-center from 23 μm to 7 μm.

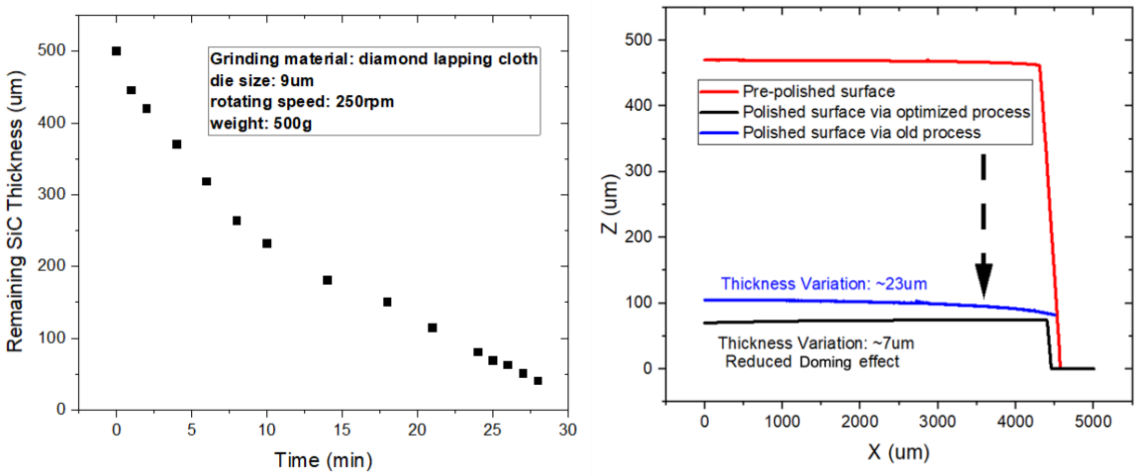

Figure 7.6: Data for improved polishing process. The polishing rate measured in-situ (right) slowed slightly so that a new polishing cloth was used after 1-2 samples were processed. The doming effect in the new system with improved wafer alignment was reduced by a factor of 3, decreasing the total thickness variation edge-to-center from 23 μm to 7 μm.

Firstly, the rotation axes and translation axis of the polisher itself needed to be aligned. Fortunately, we were one of the only groups using the tool, so this calibration was not necessary for every processing run, as the calibration was found the remain quite stable. Next, samples were mounted on parallel fixture by heating the fixture to 150 C on a hot plate and using CrystalBond wax, ensuring no wax got on top of the sample. Then, the polishing platen and cloth were installed, and the platen was pressed against the cloth for a few minutes to remove bubbles. Finally, the parallel polishing plate and sample were installed. The parameters used were 250 RPM for the disk, 4 RPM for the fixture, with disk and fixture rotating in opposite directions. Arm traversal and 500 g loading were used, and polishing was stopped with 60 μm of SiC left. Then samples were unloaded by heating to remove most wax and solvent cleaned.

7.3 Vertical packaging

Once the decision was made to switch to sapphire substrates, processing was greatly simplified. It was no longer necessary to perform a full flip-chip process with substrate removal to achieve LEE over 10%. However, the total achievable LEE from these sapphire substrates was lower than the previous TFFC devices on SiC, as will be discussed in the next chapter.

One way that LEE of devices on sapphire might be improved is with the implementation of a vertical configuration. This has been demonstrated in blue LEDs as I will discuss in the next chapter but has not been demonstrated in UV LEDs. We developed a simple process for vertically mounting UV LEDs grown on sapphire on TO-style headers, as shown in Figure 7.7. One major advantage of this method was that samples were not bonded to a separate submount wafer. There are limited options for UV-transparent bonding materials so such a process is likely to reduce LEE, although it may improve thermal performance if a thermally conductive submount could be found.

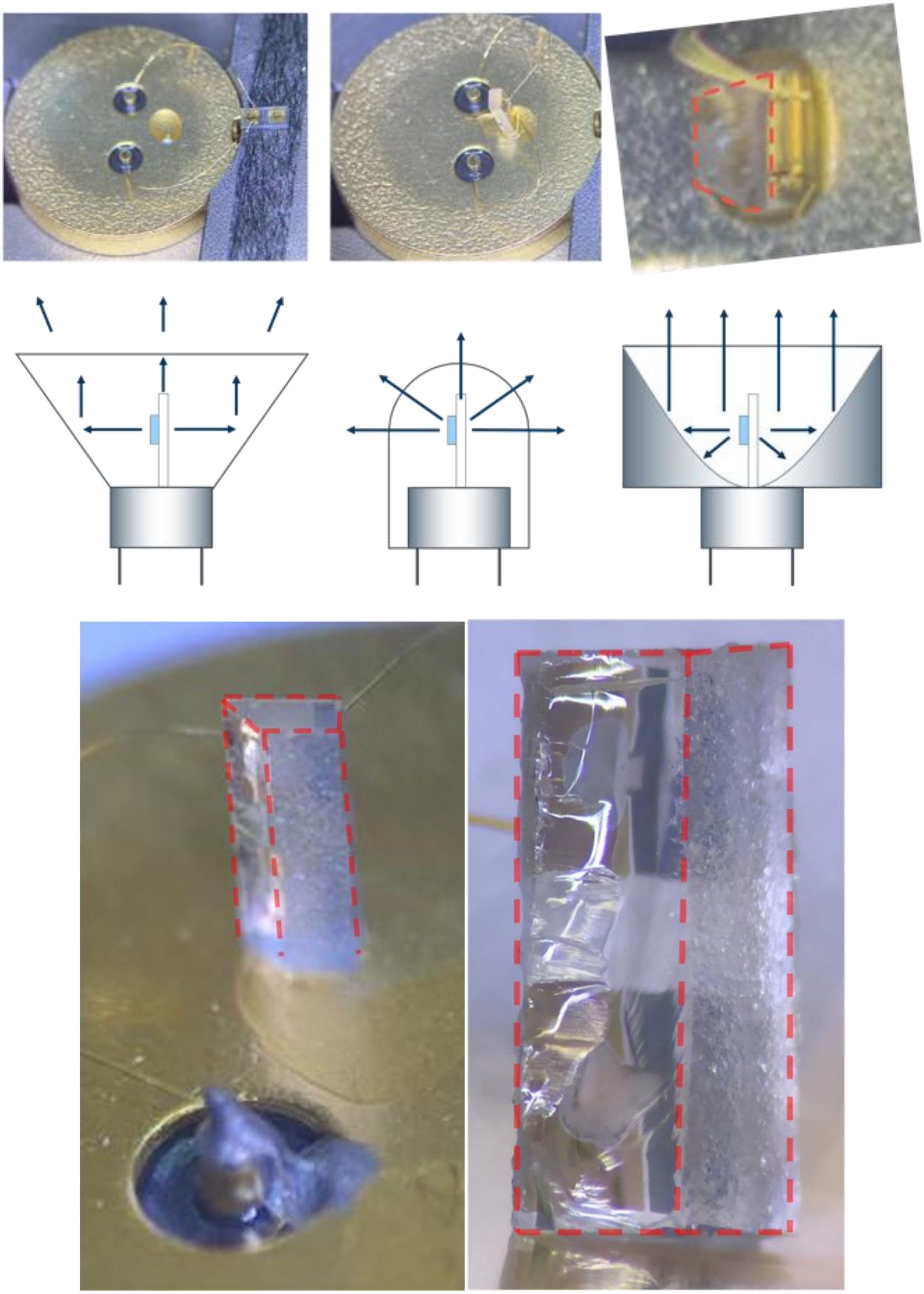

Figure 7.7: Images and schematics of vertical UV LED on sapphire mounting scheme, and potential high LEE versions of the design. Dotted lines indicate the (unintentional) chip shaping caused by sapphire chipping during dicing, which may have increased LEE.

UV LED processed wafers were diced into 1x2 mm^2 rectangles so that one device could be operated, while the extra millimeter of die length served to separate the operating device from the optically absorbing header and adhesive. Device die were first attached to the wire bonding sample holder plate using double-sided tape. Then, they were wire bonded to the n- and p-side posts on an Au-coated header as normal. Next, samples were manually placed onto the header using UV-transparent CYTOP resin adhesive, and heated to 150 C for 30 minutes. The LEE of this structure will be discussed presently.

8 UV LED device architectures and LEE

For every complex problem there is an answer that is clear, simple, and wrong.

-H. L. Mencken

8.1 Introduction

Light extraction efficiency in conventional blue LEDs is quite high. As shown in the pie chart representation of EQE breakdown in Figure 8.1, the best commercially available blue LEDs have EQE around 72%, meaning 72% of injected electron hole pairs (ehps) are converted in photons that are efficiently extracted from the device. A further 13% of ehps are converted into photons that are absorbed within the device. In other words, the product IQE*IE of the device is 85% = 72% (emitted photons, dark yellow) + 13% (absorbed photons, light yellow).

In contrast, commercially available UV-C LEDs often have EQE around 4%. As shown in Figure 8.1, plenty of light is actually produced inside the device (shown by the large total yellow area), but most of it is optically absorbed, since LEE is around 10%. Additionally, injection efficiency may be less than unity in UV LEDs due to the poor p-type AlGaN used for hole injection. Therefore electron overshoot may be non-negligible.

The best reported UV LED (in WPE terms [35]) achieved greatly improved IQE*IE, represented by the large total yellow region in the pie chart. We estimate their IQE*IE was around 80%, almost as high as that of modern blue LEDs due to greatly improved active region and p-AlGaN developments similar to those discussed in Chapters 5 and 6. However, their LEE remained very low, resulting optical loss and less than 20% EQE.

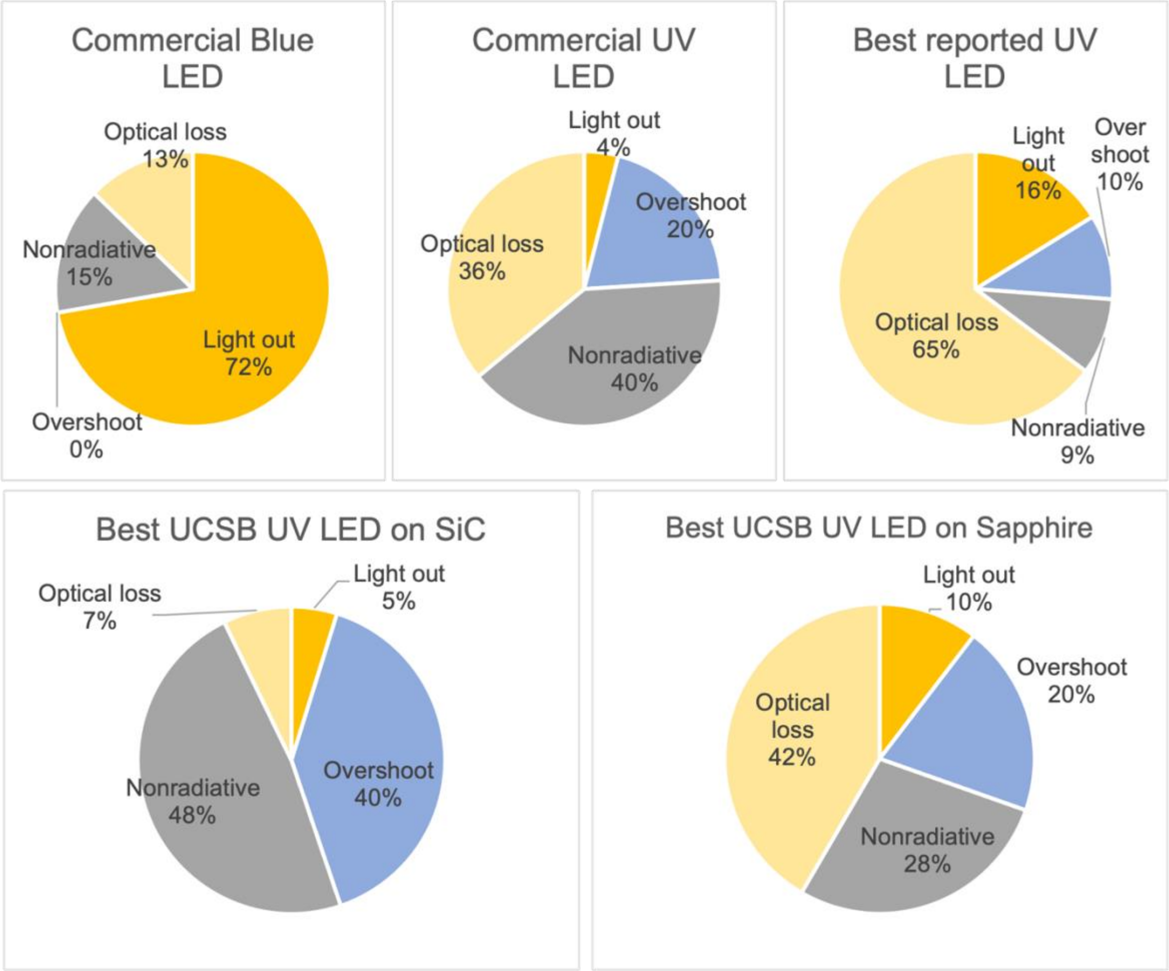

Figure 8.1: Pie chart representation of EQE in selected LEDs. The best commercially available blue LEDs now have EQE above 70% under high current operating conditions. The yellow regions of the pie charts denote the IQE*IE, with the lighter yellow representing light that is absorbed in the structure. Nonradiative recombination is shown in gray, and electron overshoot (representative of low injection efficiency) is shown in blue. The yellow portions (light out and light absorbed) can be estimated with confidence as they result from calculations based on LEE and EQE. However, the breakdown between nonradiative recombination (gray) and overshoot (blue) is based on conjecture regarding the radiative and injection contributions to EQE.

Our best reported UV LEDs on SiC [32] and sapphire (manuscript accepted) are shown in Figure 8.1 as well. On SiC, we made improvements to our p-superlattice, improving our estimated injection efficiency to 60% (i.e. 40% overshoot). While the overall IQE*IE was still rather low, our LEE of 40% (best reported for a p-GaN containing deep UV LED) enabled us to achieve nearly 5% EQE. Moving to sapphire and making further improvements to our p-AlGaN and active region greatly increased our injection and radiative efficiencies, leading to an estimated IQE of over 50%. However, the sapphire bulk vertical package had lower LEE than the optimized TFFC process we were able to achieve on SiC.

8.2 Motivation: should we expect high IQE in AlGaN LEDs?

Recall that the radiative rate for spontaneous emission in any two-state system is proportional to the third power of the radiation frequency; that is, the fundamental radiative rate (the "B coefficient") in ultrawide-bandgap AlGaN could be significantly higher than InGaN. Furthermore, the well-known insensitivity of InGaN to threading dislocation densities, mostly due to the very short hole diffusion lengths in this material, is likely to extend to AlGaN as well, in which hole diffusion lengths are *even shorter*; that is, the defect-related nonradiative recombination rate (the "A coefficient") may be lower for AlGaN than it is for InGaN for a given defect density. To wit: almost all world-record EQE and WPE results for GUV LEDs are grown on sapphire substrates with TDD in the $5x10^8$-$5x10^9$ cm^{-2} range, as are several recent GUV laser diode results [279].

And, because current state-of-the-art deep-UV LEDs are all-alloy structures with active regions around 50%, alloy disorder-related benefits such as carrier localization and percolation-enhanced transport are also likely to be present. Finally, while the importance of Auger recombination in AlGaN remains an open question, it may be less pronounced in ultrawide bandgap AlGaN devices than it is in InGaN. Thus, the overall conclusion in light of the recent developments is that AlGaN devices are likely to have excellent IQE*IE. [5], [280]

The most important outstanding bottleneck in improving GUV LED WPE is therefore considered to be LEE. In the deep-UV, almost all common materials used in blue-LED technologies have poor optical performance. The most common material for metal-coated package components, silver, is highly reflective in the visible range, but becomes absorbing below ~320 nm. The only materials with reflectivity above 75% in the UV-C are aluminum and PTFE; Al does not form a good electrical contact to n- or p-type $Al_xGa_{1-x}N$ (x>50%), and both materials are challenging for coating parts such as SMD and TO-style headers compared to Ag or Au. Organic resins and silicones used for blue LEDs have UV-absorption as well as lifetime and reliability issues, limiting the achievable LEE-enhancements for packaged devices which therefore usually rely on quartz encapsulation. The standard transparent conducting oxide, ITO, used as a current spreading layer in blue LEDs, is non-transparent in the UV, and therefore metal current spreading layers are used.

If the metal current spreading layer thickness is below about 20 nm, it is considered semi-transparent and provides an inefficient but reliable and low-cost light extraction architecture for quick epitaxy feedback and device design toward future fully transparent structures. This architecture only provides LEE in the range of 5-10%, but is easy to model using ray-tracing methods and is well-studied in the analogous (fully-transparent) case of the ITO-coated blue LED. For the purposes of this report, this will be referred to as the "conventional" device design. More common in the UV is to cover the thin, semi-transparent metallic p-ohmic contact with a highly reflective Al layer which reflects the emitted radiation downward toward the substrate (see Figure 8.2). This light can then be extracted through the bottom of the wafer (on-wafer testing) or in a packaged device via a flip-chip architecture. This is referred to as a Ni/Al based reflective p-contact.

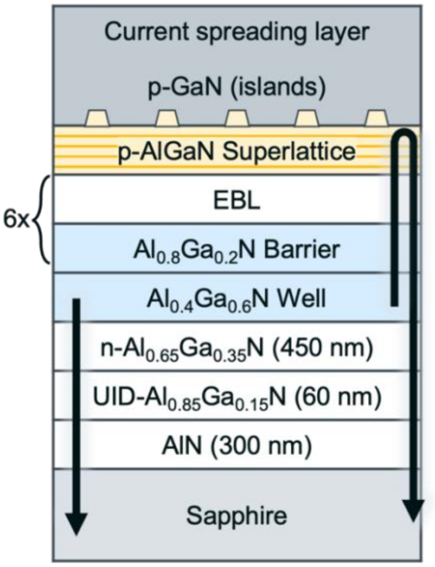

Figure 8.2: Schematic depiction of the reflective-contact UV LED architecture used for the devices discussed in this section, based on devices similar to those shown in Chapter 5, before the improvements of Chapter 6.

The highest LEE architecture for UV (and blue) LEDs is the thin-film flip-chip structure with backside roughening [31], [32], [281]. This architecture relies on a substrate removal technology, which allows the epitaxial LED structure to be bonded to a separate carrier wafer and then separated from the growth wafer, exposing the pristine semiconductor backside. The backside can then be roughened using low-cost means such as colloidal lithography or AlN KOH chemical roughening, providing massive LEE benefits as discussed below. Substrates such as Si or SiC can be removed rather easily using mature technologies borrowed from the conventional semiconductor industry, as we have previously reported [31], [32], [185]. However, sapphire substrates are more chemically inert and cannot be removed using dry- or wet etching.

In some cases, sapphire and AlN interfaces can be separated using laser liftoff or other novel methods [282]–[285], but this approach has not yet been widely adopted in UV LEDs. For this reason, sapphire-based UV LEDs usually employ a bulk flip-chip structure, in which the transparent sapphire substrate remains in place after flip-chip bonding. This method allows significant LEE improvement relative to the conventional method with semi-transparent metal, but is limited by its inability to efficiently extract guided modes which are totally internally reflected at the AlN/sapphire interface. The major benefits of the flip-chip geometry are in this case largely due to the ability to form large area, low-profile metal connections to the n- and p-pads for good thermal and electrical performance.

One packaging method that has become immensely commercially successful in "filament style" white LEDs is the vertical configuration, in which the LED is suspended vertically so as to efficiently emit from nearly all sides of the die and limit the opaque bonding area to a small region located far from the light emission region. In visible LEDs this geometry has enabled high LEE and novel device designs; applied to the UV, this method could be compatible with many epitaxial structures including current reflector-based designs as well as future fully-transparent designs with both top- and bottom-side emission. If a fully transparent UV LED can be realized, the vertical configuration is expected to give comparable LEE to the TFFC design. Furthermore, the positioning of the light emitting region away from the optically absorbing mechanical components and bonding materials fundamentally reduces loss due to absorption and scattering at those materials, and could be combined with optics (e.g. a parabolic Al mirror) to produce precisely controlled, directional or omnidirectional emission characteristics (in the UV, encapsulant materials have low refractive index and high absorption, so reflective optics are expected to be more important than refractive optics). A summary of the UV LED packaging schemes is given in Figure 8.3.

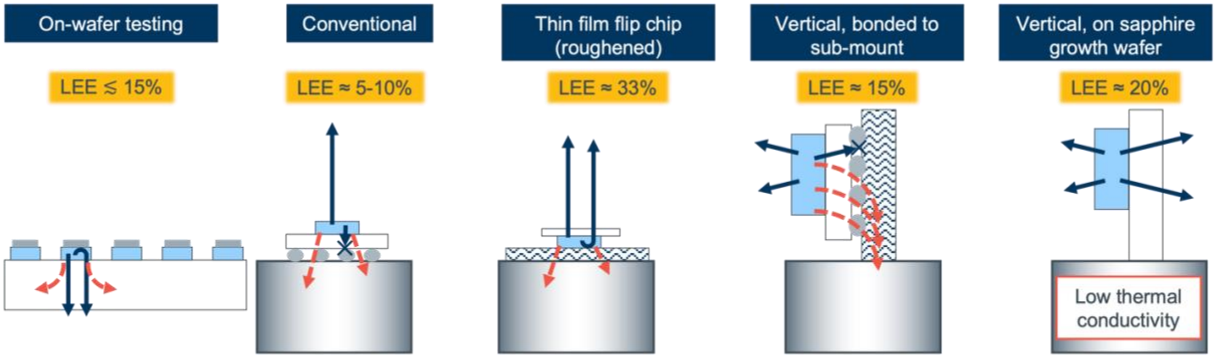

Figure 8.3: Schematic comparison of UV LED packaging configurations. TFFC with roughening (LEE=33%) and encapsulation (40%) gives the highest efficiency. Vertical packaging gives higher LEE than on-wafer testing or conventional mounting, achieving LEE similar to TFFC without roughening, while also enabling potential novel device designs such as filament-style LED packages.

To date, there have been no demonstrations of vertically packaged GUV LEDs, most likely because the materials used for vertical mounting, wafer bonding, and packaging are not UV-compatible. In this chapter, we discuss a novel, simplified method for vertical mounting of sapphire-based UV LEDs making use of the growth substrate wafer as the vertical mounting support wafer, rather than bonding to another wafer. Combined with chip-shaping, this method provides LEE greater than conventional and bulk flip chip architectures, and may approach similar LEE to TFFC designs with future optimization.

8.3 Theory and Background

8.3.1 Methods for LEE calculation

The most widely applicable method for LEE calculations in visible LEDs is the Fresnel ray-tracing method. This method is best for modeling large structures (much larger than the light’s wavelength), so it is most powerful for comparing different LED packaging architectures for a given epitaxial and fabrication structure. For blue LEDs, in which most elements are highly transparent or reflecting, and in which optical properties (*n* & *k*) are well known, excellent agreement has been reached between computational and empirical results. For UV LEDs, which contain highly absorbing p-GaN and non-reflective metallic components, the quantitative outcomes of modeled LEE calculations are sensitively dependent on the selected optical properties of these materials which are less precisely known[25]. AlGaN-based active regions sometimes produce recombination involving holes from multiple valence bands, resulting in a mixture of isotropic and sidewall-directed emission (sometimes called TE and TM, respectively). The details of TE/TM emission ratio depend on the quantum well thickness, strain state, and wavelength of the emitted light (see Chapter 6), and strongly affect the overall device LEE. In addition, optical properties of the p-GaN contact layer and metal contacts depend on the details of the growth and fabrication methods, and lead to non-negligible variation in reported LEE even for nominally identical LED architectures.

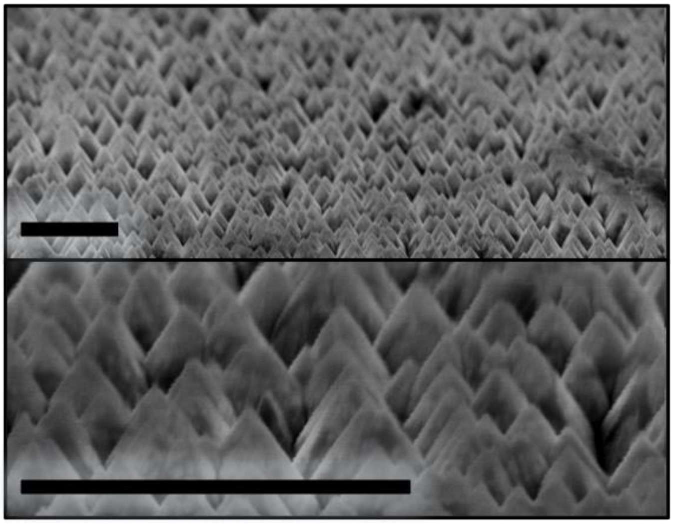

Figure 8.4: Scanning electron micrographs of KOH-roughened AlN N-face as described elsewhere [31], [185], [261]. Scale bars 1 µm. LEE is maximized when the length scale of the nano-roughened features approximately matches the wavelength of the emitted light.

Wave-optical effects including diffraction, scattering from sub-wavelength structures, gand cavity effects are best modeled using finite-difference time-domain (FDTD) simulations

---

[25] Reports of precise wavelength-dependent UV-C optical properties of AlN are few and far between, and they are even less commonly reported for AlGaN. Optical properties in the vicinity of the band gap are very strongly dispersive, and depend sensitively on defect content, doping, and alloy composition. Detailed reports of these optical properties are not widely available in the literature.

which solve for the electric field profiles in small volumes numerically. While ray-tracing underestimates the LEE of the roughened TFFC structure shown in Figure 8.4 by about a factor of ½, FDTD calculations are able to correctly model the optical properties of the nano-roughened AlN interface [276], [286]. On the other hand, FDTD simulations can only handle small volumes with simplified geometries, and therefore cannot model entire LED packages.

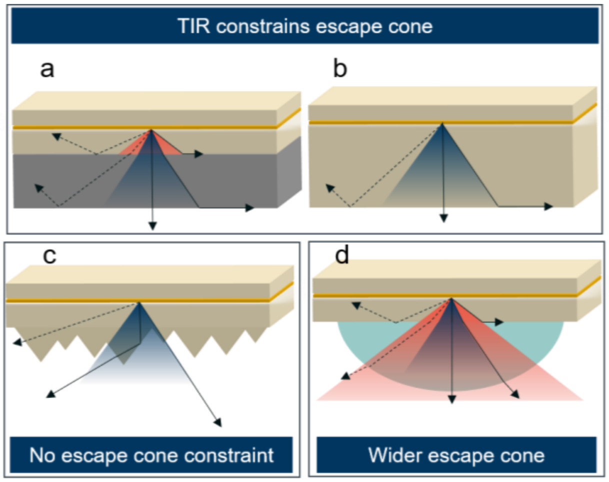

Figure 8.5: The escape cone of high-refractive-index materials such as sapphire and AlN is limited by Snell's law. a) In the case of AlN on sapphire, or AlN with flat encapsulation, the escape cone (blue) is limited. There is a second, wider cone (red) which is determined by TIR at the AlN/sapphire interface, but this light is not efficiently extracted. b) For AlN without sapphire or encapsulation, the LEE is the same as case (a). c) For an AlN device with backside roughening, the light propagation direction is randomized at the rough surface, and the emission is not constrained by TIR (light rays outside the blue escape cone are also extracted). This also applies to PSS. d) With hemispherical encapsulation, the size of the escape cone is increased, because the encapsulant/air interface is not parallel with the other interfaces. For simplicity, encapsulation with the same refractive index as sapphire is considered. In this example, the wide (red) escape cone determined by the AlN/encapsulant interface is the relevant escape cone. This also applies to a sapphire wafer with backside roughening.

Computationally even simpler than the FDTD model is the analytical approach, in which the Fresnel equations, cavity effects, and geometric considerations are written down and solved explicitly for certain simplified geometries such as parallelepiped-shaped chips or 1-D layer stacks. This method provides a reasonable first-order approximation of LEE from simple planar structures such as bulk flip-chip or on-wafer configurations without patterning or roughening, giving remarkably good agreement with ray-tracing in these end cases [287]. When neglecting absorption and scattering, the analytical approach is valuable in that it provides best-case upper limits on LEE from various emission modes, guiding future device designs and informing which device types are most interesting to pursue in experimental or computational efforts. Analytical modelling can also be modified to include complex effects such as current crowding, optical emission, roughening, and non-rectangular geometries, and is an excellent complement to ray- and wave-optical methods [287], [288].

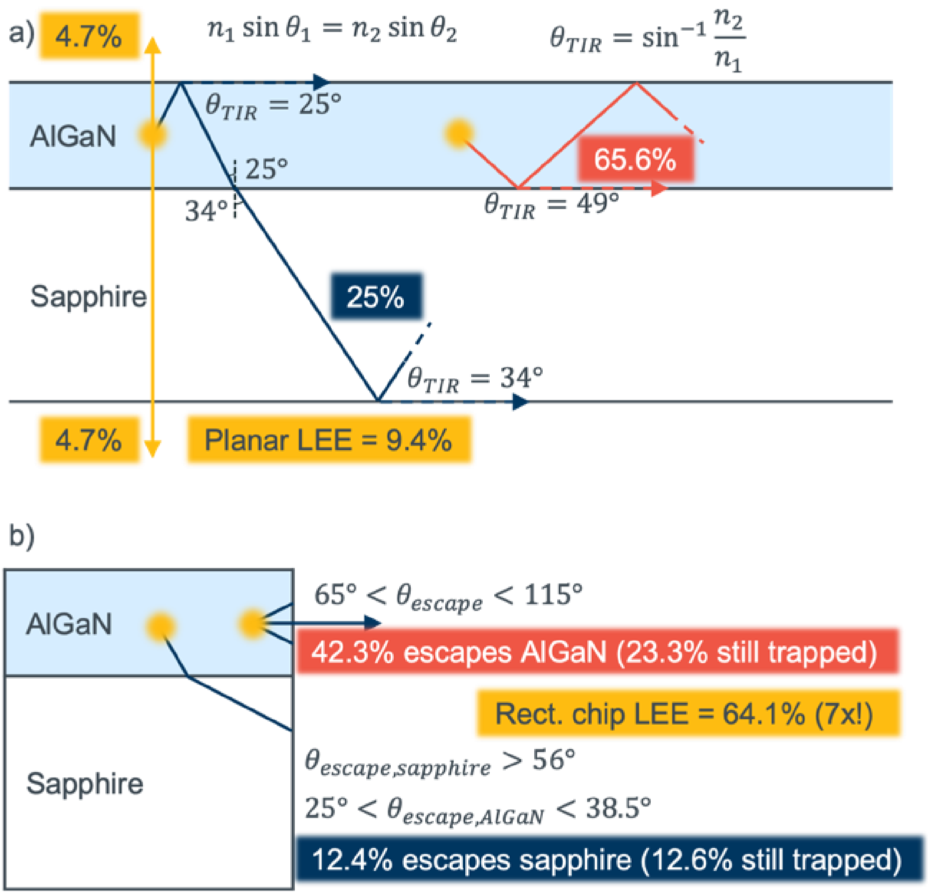

Figure 8.6: Diagram representing some results of an analytical description of a simplified UV LED device. Neglecting absorption, the modal breakdown of isotropically emitted light comprises about 10% into the escape cone (yellow), 25% trapped in a mode which is split between the sapphire and semiconductor (blue), and 66% into a mode which is fully trapped inside the semiconductor (red). In a small chip where sidewall emission is considered, an additional 12.4% of the blue mode and 42.3% of the red mode may in principle be extracted (in practice much of this is likely to be absorbed, but in a future fully transparent device it may be extracted.

Figure 8.6(a) summarizes some key findings of analytical modelling of a simplified AlGaN/sapphire-based UV emitting multilayer structure. Firstly, neglecting absorption in n-AlGaN, AlN, and sapphire, a lower limit of around 4.7% LEE can be achieved in a downward emission geometry (e.g., on-wafer or bulk flip chip). This suggests that reports of on-wafer LEE below 4% are likely to be underestimating LEE, unless sidewall-directed TM emission is dominant (which may be the case in far-UV-C emitters but is unlikely in high-quality 260-290 nm emitting device structures). If a portion of the upward emission is captured, the LEE may increase toward 8-10% (this may be reasonable for In-dot quick-test measurements, as In has a UV-reflectivity above 70%). If the sapphire backside is roughened, a portion of the sapphire-guided mode (shown in blue, Figure 8.6) may be out-coupled, increasing LEE up to 15% if wide-acceptance-angle optics are employed. Finally, despite the simplicity of the analytical model, it makes clear that *nearly two thirds* of the emitted light (assuming isotropic emission) remains trapped within the semiconductor films, where it is inevitably absorbed (this mode is actually further divided into an AlGaN mode and an AlN mode, but that division is not shown here for simplicity). The outcoupling of this guided or trapped mode (represented in red) is *the most important requirement* for achieving high-LEE in UV-C LEDs, and is the reason why the thin-film flip-chip structure with backside roughening is by far the highest LEE geometry. Patterned sapphire substrates achieve a similar effect in principle, however they require several passes for efficient extraction (as confirmed by both ray- and wave-optical calculations [287], [289]), whereas a roughened free-surface achieves significant extraction after only a small number of passes.

The most important point here is the following: the detrimental effect of absorbing p-GaN and low-reflectivity p-contacts is not their reduction in emission of the vertical (yellow) mode, which is a small reduction to a small component of total LEE. Instead, the detriment of absorbing layers is due to their effect on *guided modes*, which interact very strongly with these layers. Therefore, structures which weakly outcouple guided modes (lenses, PSS, chip-shaping) will give much smaller improvements than structures which very efficiently outcouple guided modes (TFFC with roughening). An illustrative end-case is that in which the p-mirror reflectivity is set to zero—in this case, the LEE enhancement of, e.g., a sapphire lens, is zero. This principle is the reason why (performance and lifetime issues aside) encapsulation is unlikely to give major LEE benefits in current UV LEDs, and why *fully transparent* p-GaN free epitaxial structures must be developed.

In a small chip, emission from the sidewalls of both the semiconductor mesa and the chip face may be considered (see Figure 8.6(b)). These emission contributions are typically ignored in planar devices because they are mostly lost to absorptive packaging materials, but they may be more efficiently emitted from a vertically mounted device. Neglecting absorption, an upper bound of over 60% LEE is calculated when emission of guided modes from chip sidewalls is considered—notably, the emission of the sapphire mode (blue) is a rather small contribution, whereas most of the improvement comes from the emission of the semiconductor-guided trapped mode (red), again suggesting the benefit will be great only if transparent epitaxial structures are used. Even greater enhancement is expected for a device with chip-shaping, in which the sidewalls are at non-right-angles, allowing nearly full extraction of all guided modes [288], as shown in Figure 7.7. In summary, the LEE enhancement of a vertical device is expected to be modest when highly absorbing semiconductor layers are used, and much greater when fully-transparent semiconductor layers are implemented.

Computational models can be made arbitrarily complex to account for all sorts of subtle effects, but the end-resulting LEE value is only as accurate as the optical properties inserted into the model. On the other hand, experimental measurements of EQE provide excellent data for relative comparisons of LEE for different architectures, but include the fundamental limitation that the measured EQE value requires an assumption of IQE*IE before it can be converted to LEE, so absolute LEE measurements cannot be made purely empirically either. Considering the limitations of each of these methods (ray tracing, FDTD, analytical, and empirical), it becomes clear that a combination of all of these methods is the most reliable approach for arriving at confident evaluations of the LEE of the most common LED architectures [288]. We tabulate the LEE values of our previous work as well as a selection of milestone results from the literature as determined using this combination of techniques in **Error! Reference source not found.**.

8.3.2 What limits UV LED LEE?

The LEE of all reported UV LEDs is much lower than the current state of the art blue devices. The most obvious reason for this is the use of thick p-GaN and non-reflective metallic contacts, but other common arguments include concerns over TM emission, and guided modes.

8.3.2.1 TM emission is not found to be a major limitation for conventional GUV devices.

Fortunately, a closer analysis of the TE/TM emission question shows that sidewall-directed TM emission is not actually favored in most state of the art GUV LEDs. Firstly, high-quality GUV LED active regions are always fully coherently strained to the underlying AlGaN buffer (which may itself be fully or partially strained to the AlN template), and this compressive strain is known to suppress TM emission (see Chapter 6). Long *et al.* demonstrated that the higher the Al-content of the template and barriers, the more TE emission was favored, and thus the higher the UV LED LEE [290]. There are also many other reports of TE emission throughout the GUV region, in good agreement with the ***k.p*** theory [55], [271], [272]. Even recent reports of laser diodes with thick quantum wells show strongly TE polarized emission, further supporting the result that TM emission is not favored in conventional, high-quality GUV-wavelength devices [18], [195]. The small amount of TM emission which may be produced can be extracted efficiently using angled sidewalls, substrate patterning, or roughening [288], [289].

8.3.2.2 Absorbing p-GaN is the greatest concern, but the dependence of LEE on p-GaN thickness is not straightforward.

At 280 nm, GaN has an absorption coefficient of over 100,000 cm^{-1} [281], [288], [291]. This would yield vertical single-pass losses of only 18% at 20 nm of thickness, 40% at 50 nm, and 63% at 100 nm. In other words, over one third of the light could be expected to transmit through a 100 nm thick layer of p-GaN. However, this consideration misses an important aspect of LEE modeling caused by guided modes (rays propagating non-vertically), which interact strongly with the absorbing p-GaN. As was recently reported, [35], reducing the p-GaN thickness of a GUV LED from 700 nm to 50 nm (while also eliminating an absorbing ITO layer and replacing it with Rh) did not give the ~4x LEE enhancement an analytical approach would predict, giving only a 2x enhancement instead.

Computational [292] and experimental [293] evidence shows that only about 20-50 nm of p-GaN is needed to limit LEE to below 10%, because the effective interaction length for a guided mode is many times greater than the true thickness. Above about 50 nm there is almost *no benefit* to reducing the p-GaN thickness, as the guided mode is fully absorbed anyway. Below 20 nm, there is great benefit to reducing p-GaN thickness *only* in roughened/patterned samples with guided mode extraction (in which the light can be successfully outcoupled before interacting with a great volume of p-GaN), with only a very weak dependence on p-GaN thickness for planar samples (in which guided modes strongly interact with the p-GaN regardless of the real thickness). A device on PSS with 700 nm of p-GaN [35] therefore has similar LEE to one with <200 nm of p-GaN [26].

In summary: the p-GaN absorption issue is of great importance because guided modes cause light to interact with a much greater “effective” interaction thickness of p-GaN than the real thickness physically present on the device. The LEE does not simply decrease monotonically with increasing p-GaN thickness. For samples with some guided mode extraction (PSS, roughened TFFC), p-GaN must be less than 50 nm thick for strong thickness dependence to be measured. For samples without good guided mode extraction, any amount of p-GaN will cause complete absorption of guided modes, and you might as well use hundreds of nanometers of it, as recently demonstrated [35]. p-GaN free TFFC structures are expected to achieve LEE up to 80% [292].

8.3.2.3 Mirror reflectivity has similar importance to p-GaN thickness.

Along with p-GaN thickness, the most commonly investigated LEE enhancement strategy is p-ohmic mirror reflectivity. Just as with p-GaN thickness, the importance of the p-mirror reflectivity is magnified in planar structures, and is less important in TFFC or patterned structures [13]. Lobo-Ploch *et al.* demonstrated the importance of mirror reflectivity by comparing a conventional Pd mirror (R<50%) to a patterned contact with small Pd pixels blanketed by reflective Al (R>90%), showing a 2x LEE enhancement with this innovation. Instead of patterning small pixels, a similar effect can be achieved using a thin p-ohmic metal such as Pd, Ni, or Pt, (R~40%) which allows reasonable ohmic contact formation over a large area while also transmitting a fraction of incident light through to the Al mirror deposited above. Significant mirror reflectivity can be achieved with this approach, as shown in Figure 8.7. Both the pixel approach and the thin-metal approach introduce tradeoffs between voltage and light-extraction performance, but the thin-metal approach is simpler from a processing perspective and eliminates the current crowding effect.

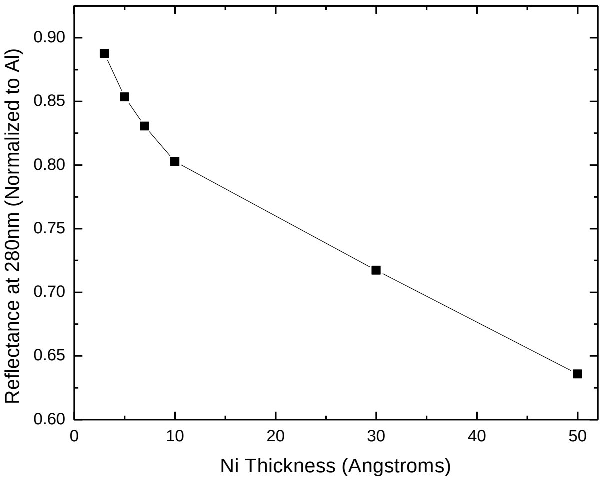

Figure 8.7: Reflectance of a Ni/Al reflector deposited on sapphire. Ni as thin as 0.5 nm is sufficient to improve device voltage significantly while maintaining reflectivity above 80%. Nano-pixel patterning with thick Ni, Pd, Pt, or other ohmic metal is unlikely to outperform thin Ni, and thin Ni has the added benefit of eliminating current crowding effects. Data collected by M. Wang.

Maeda *et al.* have recently compared a standard Ni contact to a reflective Rh (R>60%, with decent ohmic contact performance to p-AlGaN) and a semi-reflective Ni/Mg multilayer contact, achieving up to 17% LEE by eliminating the p-GaN layer [294]. Takano *et al.* [26] achieved record EQE>20% by removing the absorptive p-GaN and using a Rh-mirror contact (R=68%), which increased LEE from 3% to 27% (LEE was further increased to 34% and 43% by introducing a patterned sapphire substrate (PSS) and hemispherical encapsulation, respectively). Matsukura *et al.* [35] improved on this approach with a thin p-GaN and Rh mirror, giving slightly lower EQE but higher WPE—although their LEE is estimated to be only

20%, their device had much better voltage efficiency and IQE attributed to the presence of 50 nm of p-GaN and improved epitaxial quality, respectively. Notably, the reflectivity of an indium contact (such as is commonly used for quick on wafer testing or "quicktest") has an expected reflectivity of nearly 90%, so that the LEE of on-wafer In-based quicktest is actually quite similar if not slightly higher than the equivalent processed device. However, In has poor mechanical and thermal characteristics, so it cannot be used as a reliable contact for high current density operation and is difficult to lithographically pattern reliably.

8.3.2.4 UV-compatible encapsulation materials are expensive and unreliable, and do not provide significant LEE increases even in principle if p-GaN is present.

One of the most reliable methods for LEE enhancement in *blue* LEDs is using silicone encapsulation. Silicone is not transparent in the UV and degrades quickly under UV illumination, however other fluorine-based resins [295] have been demonstrated in a small number of reports to provide modest LEE enhancement in the UV. With further optimization and development such materials may become common in the future, but current materials are orders of magnitude more expensive than silicone, and have lower optical quality and lifetime; most commercial GUV LEDs use quartz packaging [296] with no underfilling or hemispherical resin encapsulant.

Furthermore, the refractive index of commercially available UV-transparent fluororesins is around 1.4, similar to silicone in the visible range, compared to 1.6 for glass, and 1.8 for sapphire. The smaller the refractive index of the encapsulant material, the lesser the LEE enhancement. Ichikawa et al [13] calculate that an encapsulant with n = 1.43 gives only 1.2x LEE increase, whereas n = 1.8 gives 1.6x (in good agreement with ray-tracing and analytical predictions [287]), predicting one of the highest LEE values of 24% with hemispherical sapphire packaging.

8.3.2.5 Other recently observed considerations for LEE in UV LEDs

The effect of the p-AlGaN thickness has been generally assumed to be dominated by the effect of optical losses in the p-AlGaN, and therefore the p-AlGaN is often kept below 100 nm in thickness (also reducing driving voltage). However, it has been proposed [297] and recently experimentally confirmed [35] that the most important effect of p-AlGaN thickness may actually be related to the optical cavity effect, which can only be simulated using wave-optical approaches. The dependence of LEE on p-AlGaN thickness has been observed to be oscillatory—there exist optimal p-AlGaN thicknesses which minimize the interaction of guided modes with the p-GaN. This occurs when the thickness of the optical cavity formed by the active region and p-type cladding layers is such that there is no electric field antinode within the p-GaN, and therefore is most pronounced when the p-GaN is thinner than ~100 nm (the wavelength of UV-C light in AlGaN). This effect is likely to be especially important for limiting modal loss in UV laser diodes.

Photonic crystals—ordered wavelength-scale structures which are predicted by wave-optics to give improved LEE compared to disordered or larger-scale structures—have long been hoped to improve performance of UV LEDs. Thus far there is no experimental evidence of photonic crystals providing higher LEE than TFFC, chip-shaping, or patterned sapphire (not even in blue LEDs) [8], [298]–[300]. Photonic crystal technologies have been studied in the visible and provide improved directionality, and slightly improved LEE in specialized low-profile geometries where bulky packaging is undesirable. The highest reported LEE enhancement factors for PhC structures are up to 2x, but PhC devices still remain below 15%

in total LEE [8], [301]–[303], in agreement with FDTD calculations [303]. There are only two reports of over 2x enhancement: Inoue *et al.* [301] reported a 3x enhancement with the combination of both roughening and PhC patterning, with PhC alone giving only 2x, and Shin *et al.* [299] reported 2.5x enhancement in irradiance in a *particular direction*, but did not report data that can be considered strong evidence of an increase in *total* LEE.

8.3.2.6 Summary of this section

A selection of reports of high LEE GUV LEDs representative of the literature is listed in **Error! Reference source not found.**. We have previously shown that the highest LEE achievable for p-GaN-containing UV LEDs is via the TFFC geometry (LEE=15%) with backside roughening (LEE=33%). A further improvement is possible with resin encapsulation (LEE=40%) [31], [32], [185], and we predict a small further increase to LEE=50% with hemispherical encapsulant shaping [26]. These values are close to the expected practical upper bound for LEE from p-GaN containing devices [304], and are the only reports of LEE similar to that achieved in p-GaN-free transparent UV devices.

Table 8-1: Summary of reported light extraction efficiency values from selected publications for various GUV LED architectures.. The highest reported LEE values are 40% for a p-GaN containing structure, using the TFFC architecture with backside roughening and encapsulation; and 43% for a p-GaN free structure in a bulk flip-chip architecture with PSS. 38% LEE was achieved using bonding to a quartz lens. Photonic crystal structures have not achieved LEE over 12%. Tabulated LEDs have the following conventional structures unless stated otherwise: Ni-based p-contact, p-GaN contact layer at least 20 nm thick, flat (SSP) sapphire substrate. Using the convention EQE=IQE*IE*LEE (note that some references use a different convention, [EQE=IQE*LEE] wherein IQE=RE*IE).

Architecture	**EQE**	**LEE**	**LEE enhancement**	**IQE*IE**	**Details**	**Reference**
Conventional package (thin metal)	0.5% (SiC)	3%		17%	Int. Sphere testing	[32]
	1.4% (sapphire)	5-10%*		15-30%		This work
	2.3%(TJ, no thin metal)	9%	1.8x	26%		[305]
On-wafer testing	3%	15%		18-20%	284 nm device (not shown)	This work
	1.37%			9%	275 nm device	
	7.5%			50-55%		In prep.
		5-15%			On-wafer LEE depends strongly on measurement details, wafer type, and optical polarization.	Various reports, e.g. [13], [24], [26], [294], [305], [306]
Vertical packaging	3.2%	16-18%*	2x (vs. conventional)	17-19%	284 nm device: thin Ni/Pt	This work
	3.5%	18-20%	2.3x (vs. conventional)		Ni/Al mirror p-contact	
	3.9%	20-22%	2.6x (vs. conventional)		Ni/Al mirror, with encapsulation	
	1.6%	16-18%		9%	275 nm device	
	10% (unpub.)	18-20%		50-55%	After active region opt.(Ni/Al mirror)	In prep.
Vertical packaging, simulation		35%*			Analytical (1D Fresnel, no abs.)	This work
Thin-film flip chip	1%	16%		6%	Smooth surface	[185]
	2%	33%	2x (vs. smooth)	6%	Roughened	
	4%	33%	2x (vs. smooth)	12%	Roughened	[32]
	4.8%	40%	2.5x (vs. smooth)	12%	Roughened and encapsulated	
TFFC, simulation		~13%			Ray tracing, w/ roughening	[276]
		30%			Wave optics, w/ roughening	[286]
		30%			FDTD, 20 nm GaN, w/ roughening	[292]
		80%			FDTD, no GaN, w/ roughening	
Bulk flip chip	3%	7.5%		40%**	Ni/Au p-contact, no p-GaN	[294]
	4.5%	11%	1.5x		Rh mirror contact, no p-GaN	

Architecture	EQE	LEE	LEE enhancement	IQE*IE	Details	Reference
Bulk flip chip	6.7%	17%	2.3x		Ni/Mg mirror contact, no p-GaN	
	4.3%	9%		48%	Ni-based mirror	[26]
	12.7%	27%	3x		Remove p-GaN, Rh mirror	
	16.1%	34%	3.8x		PSS substrate	
	20.3%	43%	4.7x		PSS+Encapsulation	
	7%	<10%*		>70%	700 nm p-GaN	[35]
	15%	~20%	>2x		50 nm p-GaN, opt. p-AlGaN thick.	
	4%	15%		27%	FSS	[13]
	10%	38%	2.5x		Sapphire Lens, expt.	
			1.6x***		Mesa sidewall angle optimization	
			2.8x***		" plus roughening	
	13%	>17%****		<76%	p-AlN hole gas contact	[6]
Bulk FC, simulation		24%	1.6x		FSS with sapphire lens	[13]
		5%			FDTD wave optics	[297]
		15%	3x		Small GaN islands	
		20%	4x		Optimized p-AlGaN cavity thickness	
		7-10%			FDTD, regardless of GaN thickness	[292]
Photonic Crystal structures		4-5%			Flat AlN substrate	[301], [307]
		8%	2x		PhC structure	[301]
		12%	3x		PhC+roughness	[301]
			1.43x		Nanocolumns	[302]
	2.4%	4%		60%	Flat AlN	[8]
	4.5%	7.5%	1.9x		Nano-patterned AlN	
			1.7x		Nano-patterned AlN, confirmed by FDTD	[303]
			2.5x***		Nanocolumns	[299]
Transparent Conventional		>80%			Based on blue LED literature (PSS)	[308], [309]
Transparent Vertical		75%			Int. Sphere testing and analytical modeling (PSS)	

*Estimated based on modeled structures in which precise absorption values are unknown. **From temperature dependent photoluminescence intensity comparisons, which only provide an approximate upper limit on radiative efficiency, and neglect injection efficiency. ***Reports relative increase in irradiance (measured by a wand photodetector), not increase in radiant flux (as would be measured in a below-wafer or integrating sphere setup). Therefore not strictly a report LEE enhancement, as directionality effects are not ruled out.**** Estimates LEE=17% assuming unity injection efficiency, so that 17% is taken as a lower bound.

8.4 Vertical Packaging Methods

The epitaxial growth structure is shown schematically in Figure 8.2, and details of the growth conditions and methods have been described elsewhere [32], [196], [259] and in Chapters 3-6. The p-type GaN contact layer comprised a nominally 20 nm thick layer, with an island morphology giving nonuniform surface coverage expected to improve LEE. Devices were fabricated as described in Chapter 7. The LEDs were first tested on-wafer, then packaged into conventional and vertical geometries (see Figure 8.3).

LED wafers were diced into 1x2 mm^2 pieces, then attached to gold-coated copper TO-style headers. Gold plating (R~35%) provides slightly improved LEE compared to the silver plating (R~25%) commonly used for blue LEDs. Further improvement would be expected with aluminum-coated headers (R>90%) [310]. Samples were then wire bonded to the header posts using Au wire. In the case of the vertical mounting method, samples were first wire bonded, then adhered to the header in a vertical configuration because they could not be wire bonded once placed vertically. UV-transparent fluororesin (CYTOP) was used as an adhesive to fix the devices to the headers to reduce optical absorption. Next, devices were baked in a vacuum oven at 200 °C for several hours to evaporate the resin solvent (while the resin itself is UV-transparent, the solvent is not). On high-power samples, resin was first partially evaporated to about 50% (by wt.) to increase viscosity, then used to encapsulate the light emitting region and further baked at 200 °C to fully evaporate the rest of the solvent. I'd like to note that it is not clear whether 100% of the solvent was removed, and that some air bubbles remained in the encapsulant, which may have caused some losses. Further optimization of the encapsulation process is likely to improve LEE.

Header-mounted UV LEDs were tested using an ISP-75 integrating sphere and spectroradiometer recently calibrated by the manufacturer. Calibrations were confirmed with testing of multiple commercially available UV-C LEDs. On-wafer testing was carried out using a radiometrically calibrated photodiode located below the wafer, while separately capturing spectral data using a fiber-coupled spectrometer (Ocean Optics). Pulsed testing was carried out using the integrating sphere and spectroradiometer, along with a voltage pulse generator (Texas Instruments) and oscilloscope (Tektronix), with a 10 kHz frequency and a 1% duty cycle.

Optical properties of thin films were measured using spectroscopic ellipsometry (J. A. Woollam Co., M-2000DI). Data were analyzed using the Woollam WVASE software package and models for transparent (Cauchy) and absorbing (Lorentz) materials were fitted using nonlinear least-squares to determine optical properties (*n* & *k*). The CYTOP resin was found to have negligible absorption in the UV-C, with a refractive index of 1.37 at 280 nm.

8.5 Results and Discussion

In this work, two UV LED devices were investigated, emitting at 275 nm and 284 nm. Both samples were first tested on-wafer, then packaged for further testing.

The first LED sample emitting at 275 nm was used to compare the vertical packaging configuration to on-wafer testing of processed devices. The sample was processed using the thin-metal p-contact method described above, then tested on-wafer (without dicing). We estimate the LEE of this on-wafer setup to be 15% (on the high end of the typically reported values of 5-15%, see **Error! Reference source not found.**) due to the wide acceptance angle of the detector and roughened sapphire backside.

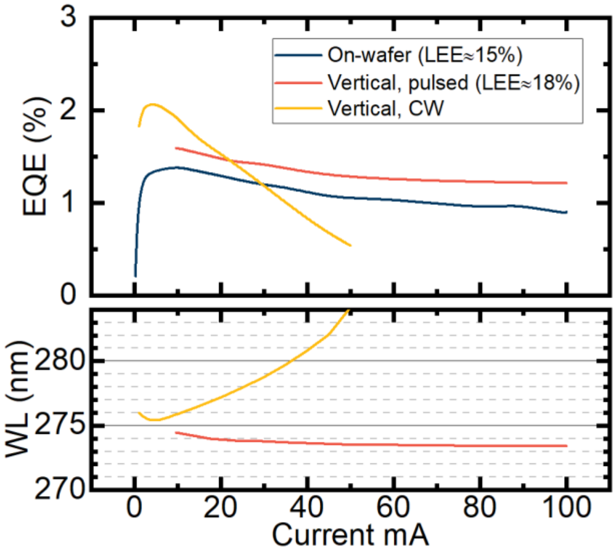

Figure 8.8: EQE and wavelength shift for on-wafer and vertical testing of the same UV-C LED device.

Next, the exact same devices were diced and vertically packaged. The data for the on-wafer and vertical devices are shown in Figure 8.8. Data collected under continuous current injection from the packaged devices showed two key differences: first, there was an anomalous increase in peak EQE which cannot be attributed to LEE increase alone, and second, there was a strong thermal droop (accompanied by the typical thermal redshift [266], [267]). In order to confirm that the increased droop was due to heating, pulsed testing was carried out showing a fairly uniformly increased LEE = 18% with no significant change in the shape of the EQE curve nor the peak wavelength. On the other hand, the anomalous EQE increase at very low current densities (below 10 A/cm^2) cannot be easily explained in terms of IQE or LEE considerations. One possible speculative explanation could be that this increase is due to slight heating causing the hole concentration in the p-AlGaN to increase, improving IE. This would be in good agreement with the temperature dependent EL data shown in Section 6.2.3, in which we observed that EQE was strongly temperature dependent at low J, but only weakly temperature dependent at higher J. In devices with low IE, a small IE increase could have strong effects at low J. Another possible explanation could be that the integrating sphere is more sensitive at very low power levels, however we do not have any data to confirm this directly.

These results suggest that future improvements to the thermal performance of the vertical package may increase efficiency. For instance, other implementations of vertical packaging for blue LEDs have shown that ZnO provides better thermal performance than sapphire. Unfortunately, there are few UV-transparent, low-cost, high-thermal-conductivity materials available. To avoid significant heating, vertical UV LED devices are preferably operated at low current density, for example using large device areas or several devices connected in series or parallel, such as in a filament-style geometry.

In that first set of devices, the objective was to compare vertical packaging with on-wafer measurements and identify the LEE benefits and thermal drawbacks of the method, keeping all aspects of growth and fabrication identical. In the second set of devices, 284 nm emitting LEDs from a particular wafer were co-processed to ensure the epitaxial quality and processing were identical, with half the devices having Ni/Al reflective p-mirror contacts, and the other half having thin-metal Ni/Pt p-contacts. Then, devices were packaged into either the vertical or conventional geometry, using identical cleaning, wire bonding, headers, and adhesive materials. The results for these devices are shown in Figure 8.9.

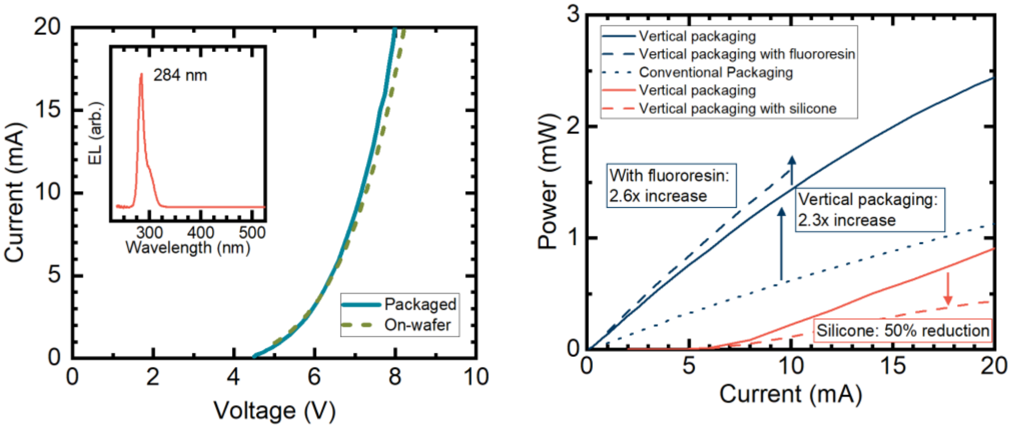

Figure 8.9: LED data for vertically packaged devices. The wavelength and IV-relationships are shown on the left, and the LI relationships are shown on the right. Vertical packaging increased LEE by 2.3x relative to conventional packaging with thin-metal, increasing to 2.6x with fluororesin encapsulation. No changes were observed to the IV relation before and after dicing and packaging. As a control, a low-EQE sample from the edge of the device was coated in silicone resin (used for blue LEDs) and a 50% reduction in LEE was observed, as expected.

Firstly, the current-voltage (IV) and spectrum data were observed for the packaged devices, with negligible difference between the conventional and vertical packaging. Thin-metal contacts gave identical voltage performance compared to mirror-based p-contact devices. Notably, the voltage performance was similar after dicing and packaging to on-wafer tests, with a slight voltage reduction for the fully packaged devices attributed to device heating (the data shown in Figure 8.9 are from the same exact LED before and after packaging). All LEDs showed spectra similar to that shown in Figure 8.9 (inset) with a dominant peak near 284 nm and a weak shoulder around 300 nm attributed to parasitic recombination pathways [311]–[313]. LED power showed some variability across the wafer, with devices from near the edge of the wafer showing slightly less than half the power of central devices.

Figure 8.9 shows the power versus current (LI) relation for a typical 284 nm device as well as a less efficient device from the edge of the LED wafer, indicating variation across the wafer. The first 284 nm device emitted slightly over 1 mW at 20 mA in the conventional packaging scheme, with an estimated LEE in the range of 5-10% (see **Error! Reference**

source not found.). With vertical packaging, the output power increased by a factor of 2.3, to nearly 2.5 mW at 20 mA, while also showing slightly increased droop attributed to device heating (note that in this device the EQE enhancement is nearly uniform, unlike in Figure 8.8 where the EQE enhancement of the CW device peaked at 5 mA and then quickly dropped to a much lower value by the time 10 mA was reached, see also Figure 8.10).

As expected, the output power was significantly higher in the vertical geometry, because the conventional geometry relies primarily on topside emission (through the semitransparent contact) with limited reflection from the bottom of the wafer (which is adhered to the Au header), whereas the vertical package efficiently emits light from many directions including the bottom side (directly or after reflection from the mirror contact) as well as the lateral sides of the die. Finally, a slight additional LEE enhancement was achieved with resin encapsulation, providing a total improvement factor of 2.6 for an estimated LEE around 20%. The second (low-EQE) device was used to confirm the expected poor performance of conventional silicone encapsulant. This device, packaged in a vertical geometry, emitted just below 1 mA at 20 mA before encapsulation; emission power then dropped to half that value after encapsulation with silicone.

Figure 8.10 shows the data for the high-EQE 284 nm device as well as a similarly efficient device from the same wafer with thin metal p-contact, in terms of EQE versus current density. The 2.3x and 2.6x enhancements due to vertical packaging and vertical packaging with encapsulation, respectively, can be seen to increase the peak EQE of the device from 1.4% to 3.5% and 3.9%, respectively. The thin-metal device is also shown in Figure 8.10, in which a 2x enhancement in LEE to 16-18% is observed (slightly lower than the vertical configuration with mirror contact). This pair of experiments validates the flexibility of the vertical packaging method for a variety of device types including both topside and bottom side emission. For example, future devices may be p-GaN free, comprising either a highly reflective mirror contact or a fully transparent structure with both top- and bottom side emission. The vertically packaged UV LED is the only device structure capable of implementing a truly fully transparent structure with no mirrors or absorbing components, for omni-directional emission.

Neglecting p-GaN absorption, ray-tracing simulations show that encapsulation with $n = 1.37$ could provide roughly 2x LEE enhancement on a flat wafer with no chip shaping. The enhancement factor drops significantly to 1.2x for a device with chip-shaping, and 1.15x for a device with chip-shaping and roughening [287]. In other words, encapsulation appears to have a sort of LEE ceiling, providing great benefit for low LEE structures, but providing lesser benefit for structures with more advanced symmetry-breaking features such as roughening and chip shaping. The vertically packaged device does not break the symmetry requirements for TIR as completely as non-rectangular chip shaping, but it is more efficient at outcoupling guided modes than the conventional structure, and therefore it is reasonable that the enhancement factor from encapsulation was only 11%.

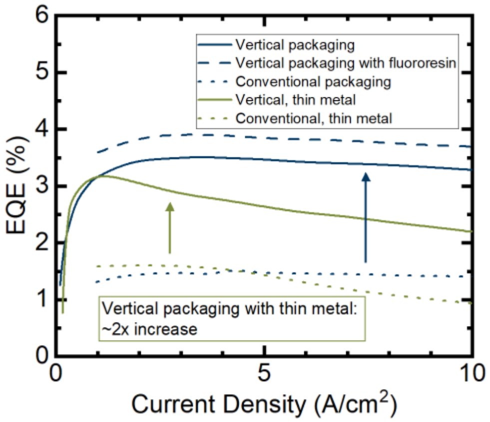

Figure 8.10: EQE comparison of thin metal and mirror contact p-side contact metallization.

8.6 Conclusions

In this chapter, we discussed the applicability of the vertical packaging configuration for UV-C and UV-B LEDs, emitting in both one-directional and omni-directional patterns. This packaging method has proven successful in blue LEDs, enabling innovations such as filament-style LEDs and high-LEE packaging configurations. In the deep-UV, where no reliable high-index encapsulant resins have yet been widely adopted, reflective optics (such as Al mirrors) are likely to be more important than refractive optics (lenses), so vertical devices in which the light emission region can be placed at, say, the focus of a parabolic mirror, rather than lying flat on a surface, may be favorable. Furthermore, the packaging process is significantly simpler, faster, and less costly than the flip-chip process with SiC removal.

Most importantly, we show that the vertical packaging configuration enables high LEE of approximately 20%, similar to flip-chip structures, without the need for patterned sapphire or surface roughening. Other high LEE structures such as roughened TFFC (LEE=40%), quartz hemispherical lens bonding (LEE=38%), and removal of p-GaN with very high voltage penalty (LEE=43%), provide excellent EQE but have some drawbacks including process complexity and cost. On the other hand, conventional and bulk flip-chip devices have LEE below 10%. Future work will include improved thermal management as well as encapsulation and advanced mirror packaging.

9 Conclusions and Future Work

The word 'finished' is artificial.

-Wayne Shorter

Go out on a limb every once in a while. Remember, that is where the fruit is.

-Bob Ross

In the past decade, there have been a number of breakthroughs in GUV LED technologies, and devices with WPE over 20% are now within reach. Commercial applications of currently available LEDs with WPE below 5% are already widespread due to the advantages of LEDs for portable, low-power applications. In the next few years, it is expected that current GUV LED technologies will continue to displace Hg lamps for certain applications. Within the next decade, it is likely that GUV LEDs will replace Hg lamps in almost all UVGI applications, just as visible LEDs are now replacing conventional lamps for illumination.

9.1 Next generation UV LED technologies

There has been great progress in AlN heteroepitaxial material quality since the first reports of high-temperature annealing in 2016 by Miyake *et al.* [163], with dislocation densities on the order of 10^9 cm^{-2} or lower now widely reported and commercially available [147], [164], [167], [168], [314], [315]. We have demonstrated high quality UV LEDs grown on commercially available AlN/sapphire wafers, and have also demonstrated high epitaxial quality AlN/SiC using direct MOCVD growth without the need for lateral overgrowth or slow growth rates. We predict that AlN on foreign substrates with TDD comparable to GaN will be commercially available within the next one or two years.

There is currently a bottleneck in LEE because the p-GaN layers needed for reasonable voltage and hole injection are optically absorbing. Even as VE and IQE become quite high in state-of-the-art LEDs, high WPE will not be possible until major breakthroughs are made in LEE. As discussed in Chapter 8, photonic crystals and encapsulation have been investigated significantly, but it is not likely that they will be enough to achieve LEE over 50%.

Bolb, Inc. demonstrated a novel p-AlN hole gas contact, reducing the needed p-GaN thickness, and improving LEE. However, this device still relies on a metal mirror contact, and therefore LEE is limited to below 50%. One possible improvement to the mirror-based device could be replacing with Ni/Al based thin-metal mirrors with an ITO based mirror. It could be the case that with proper optimization a thin ITO layer could outperform the thin Ni layers currently use in Ni/Al based mirror contact devices. Ref. [316] reports that, while a pure Al mirror is over 90% reflective in the UV-C, a multilayer of 5 nm ITO coated in Al is around 80% reflective, greatly outperforming thin metal contacts based on Mo/Al or Ni/Al (both of which have R~75%).

The ultimate high LEE device of the future is most likely to be a tunnel junction device, in which n-AlGaN is used as an electrical contact *and* transparent current spreading layer, enabling topside emission or the implementation of highly reflective dielectric mirrors such as MgF_2/Al (R>95%) or a dielectric distributed Bragg reflector. Tunnel junctions have been widely proven in visible devices, but their commercial implementation has been limited due to the excellent properties and low cost of transparent conductive oxide current spreading layers such as ITO. Because ITO is not transparent in the UV, tunnel junctions are the only currently proposed fully transparent solution. For a p-GaN free, fully transparent tunnel injected structure with either a roughened thin-film or PSS-based architecture, LEE up to 85-90% is predicted, similar to current blue LED state-of-the-art.

As discussed in Chapters 4 and 5, the electron- and hole-supply layers in UV LEDs have improved very significantly in the last 5-10 years. Voltage efficiency in commercial devices is around 80-90%. We have observed that improved p-AlGaN structures give marked improvements in device EQE, even without making any changes to the active region, suggesting that IE cannot be assumed to be unity in current UV LEDs. Thus, we predict that improvements to both IE and IQE are needed to achieve high EQE UV devices. In summary, current state-of-the-art devices have IQE*IE around 60%, VE of at least 80%, and LEE of at most 10%, leading to overall WPE around $60\%\times80\%\times10\%\approx5\%$. If the LEE bottleneck can be broken with fully transparent GaN-free devices, LEE could improve to over 75%, leading to overall WPE of over 30%. Furthermore, if IQE, IE, and VE can be increased to 80-90%, WPE well over 50% is feasible.

One outstanding question not covered in this dissertation is the question of Mg-doped AlGaN's activation mechanism. While Mg-doped GaN must be thermally annealed in order to be made p-type [317], [318], AlGaN:Mg appears to be p-type as grown[26]. For example, the two most recent reports of MOCVD-grown tunnel junction UV-C LEDs [245], [305] grow n-AlGaN above the p-type structure without any type of patterning to enable hydrogen escape (hydrogen does not diffuse through n-type III-nitride materials, only p-type). Our own preliminary work suggests our p-SPSL layers are p-type as grown, as indicated by strong LED

---

[26] Of course, 3D polarization enhanced (graded) structures are p-type as grown regardless, since they do not rely on the presence of activated Mg acceptors, but that is a separate topic.

emission[27]. Annealing our UV-LED samples at high temperatures for more than about 2 minutes reduces emission power greatly and destroys the diode characteristic IV relationship. If annealing only reduced power with no change to IV relation, that would suggest that the active region may be degraded by those annealing conditions perhaps by Al/Ga intermixing (unlikely at temperatures below 1000 °C) or motion of some mobile point defect such as H or vacancies (perhaps not unlikely at such temperatures). Since annealing both reduces power and destroys diode characteristic, this suggests that it is degrading the p-AlGaN itself, not just the active region (it very well could be destroying both). Future work is needed to understand this strange behavior in our UV LEDs.

One possible explanation is the large polarization fields in the material, which may interact with hydrogen which moves as a charged particle through the material. Another explanation could be that hydrogen behaves differently in ultrawide bandgap AlGaN compared to GaN, or that the unusual growth conditions (higher temperatures, lower reactor pressures) prevent H incorporation in the first place. Jadhav *et al.* recently reported that H concentrations in as-grown p-AlGaN were an order of magnitude lower than Mg concentrations [319], and that p-AlGaN was more conductive without activation annealing than with annealing (below 10 V). This is in stark contrast to p-GaN, which is very resistive as grown, with [H] equal to [Mg] before activation annealing. Only with activation is [H] in GaN:Mg reduced, and p-type conduction enabled. These findings, along with our preliminary results, suggest that p-type AlGaN may behave quite differently than expected based on our understand of p-type GaN.

---

[27] Every emitted photon represents at least one injected hole, and therefore LED emission power is the most practical way to measure the hole concentration in the p-SPSL. Transport (Hall, CTLM, etc.) measurements of highly resistive p-AlGaN are difficult, and are made more complex when polarization-enhanced multilayers and anisotropic transport through heterostructures are considered.

In any case, the two takeaways from these preliminary observations are 1) AlGaN based tunnel junctions may benefit from this behavior, as no complex patterning or multistep growths are needed to ensure p-AlGaN activation, and 2) it may be prudent to implement a temperature budget below around 700 °C for UV-C LED processing to avoid degradation (one major UV-C LED manufacturer has disclosed that they are working on reducing the temperature of their n-contact anneal from >900 °C to below 700 °C, although they have not explained why).

9.2 Beyond UV-C LEDs

In light of recent excitement over potential safety advantages of far UV-C for UVGI applications, research interest in UV LEDs with wavelengths below 230 nm has increased. The details of this research area are beyond the scope of my work, but it is well understood that all of the challenges discussed in this dissertation are even more significant with increasing Al content and shorter wavelengths. For example, Si *DX* center formation becomes dominant at high Al content, AlN bulk substrate absorptivity increases, and quantum confinement is harder to achieve. At very short wavelengths, sidewall emission may become dominant in *c*-plane devices. At the time of this writing, there are no reports of WPE > 1% below 245 nm, nor of WPE > 0.01% in the far UV-C. Far UV-C devices with WPE > 1% are unlikely to reach the market within the next several years.

As there are no mature semiconductor materials with bandgaps wider than that of AlN, it may be the case that novel device structures will be needed to achieve good hole injection in far UV-C LEDs. One potential such device could make use of the type-II band alignment predicted for BAlN/AlGaN heterojunctions, which may have excellent electron blocking characteristics, as proposed by Sun *et al.* [320]. Reports of BAlN growth by MOCVD are rare, but it appears that it is feasible to grow single crystal films on AlN or AlGaN templates [321]. BAlN has a smaller in-plane lattice constant than AlGaN or AlN, which presents growth challenges, but it should be possible to grow films thinner than 10-20 nm for devices (coherent SPSLs may be feasible). In addition, the smaller in-plane lattice constant makes BAlN easier to characterize by x-ray compared to an AlN reference peak compared to, say, ScAlN (another novel and interesting wurtzite material) which has lattice constants similar to AlGaN and therefore is almost impossible to distinguish by x-ray alone. (Very thin films of, say, ScAlN on GaN, are almost indistinguishable from AlGaN on GaN by x-ray diffraction, SIMS, any many other methods, and some small amount of Ga incorporation is highly likely).

Another interesting question is the area of UV-B. There have been some comments to the effect that there exists a “UV-B gap” analogous to the green gap in visible LEDs, but I do not think there is any proof that this is a valid analogy. In the case of the green gap, we know quite well the reasons for reduced efficiency at those wavelengths: strong polarization fields, strain, compositional pulling, low-quality epitaxy at low growth temperatures, blue shifting due to electric fields…the list goes on. It may be the case that there are fundamental reasons why UV-B LEDs are less efficient, but there is no concrete evidence of this, in my opinion. If one looks at a plot of EQE versus wavelength in the UV, one will find that almost every single one if the top-EQE UV-B results in the graph are from publications before 2010, with only 1-2 research groups working on this area recently. UV LEDs are comparatively less studied than visible LEDs, and the vast majority of the UV resources have been devoted to UV-C devices. This is also why UV LED efficiency peaks at 270-280 nm, just short enough to be considered “UV-C”, rather than at 265 nm where disinfection efficacy and commercial demand are highest.

It appears that relaxed AlGaN can be grown quite well on AlN, due to the benefits of tensile strain gradients created by dislocation inclination. The compositional pulling effect is much weaker than in InGaN, and films can be grown at temperatures high enough to ensure good material quality. Plus, the materials science and electrical characteristics of low-Al content alloys have been thoroughly studied in the context of HEMTs. Therefore, I expect that UV-B LEDs and laser diodes will improve greatly within the next few years, if there is commercial interest, and will be more efficient than their UV-C counterparts in the medium to long term.

9.3 Closing remarks

The only light source at any wavelength that can compete with vapor lamps on cost/W terms is the semiconductor LED. Because there is very little difference between the tools and precursors needed for UV and blue LEDs, there is no reason that UV LEDs should not approach similar production costs to visible LEDs as production technologies mature.

UV LEDs are already competitive on system-scale WPE and cost in applications where portability, directionality, low power consumption, or durability are needed. The wavelength tunability of UV LEDs is enabling disinfection research with more precise and flexible wavelength control than has been possible in the past, and novel applications are likely to follow.

With the commercialization of the latest technologies, UV-C LEDs will reach 10-15% WPE, and costs are likely to fall rapidly as market share and production volume increase, and as maturing fabrication technologies improve device yield and reliability. If production costs become similar to white LEDs, then UV-C LED cost per watt will be below US$ 10. This could occur within the next five years. As we have discussed, there are no fundamental physical limitations preventing further WPE improvements to 20% or 30%, which are expected to occur within the next ten years, bringing UV-C LEDs nearly to parity with Hg lamps on both efficiency and cost.

So it is not a matter of if, but when UV-C LEDs will replace Hg lamps. AlN material quality has increased greatly, so AlN bulk substrates are not needed, and inexpensive AlN/sapphire is now widely available on the market. Highly conductive n-type AlGaN with Al content up to 70% is now quite well understood, and voltage efficiencies above 90% are not uncommon, especially in commercial devices which benefit from mature GaN-like processing technologies. Using polarization enhancement, p-type AlGaN is no longer a major hurdle to UV-C LED efficiency, as proven by recent demonstrations of UV-C laser diodes and improved LEDs.

The final bottleneck remains light extraction efficiency. A transparent p-GaN free structure is needed to solve this problem (as detailed in Chapter 8), and is likely the only route to high WPE comparable to blue LEDs. Future work focused on eliminating the p-GaN using either a novel p-AlN contact or, better yet, a transparent tunnel junction, will be the key. If p-GaN free transparent tunnel junctions are successfully implemented, UV-C LEDs with WPE over 50% are within our reach.

10 References

[1] Y. Taniyasu, M. Kasu, and T. Makimoto, “An aluminium nitride light-emitting diode with a wavelength of 210 nanometres.,” *Nature*, vol. 441, no. 7091, pp. 325–328, 2006, doi: 10.1038/nature04760.

[2] H. Hirayama, N. Maeda, S. Fujikawa, S. Toyoda, and N. Kamata, “Recent progress and future prospects of AlGaN-based high-efficiency deep-ultraviolet light- emitting diodes,” *Jpn. J. Appl. Phys.*, vol. 53, no. 10, p. 100209, 2014.

[3] T. Onuma, K. Hazu, A. Uedono, T. Sota, and S. F. Chichibu, “Identification of extremely radiative nature of AlN by time-resolved photoluminescence,” *Appl. Phys. Lett*, vol. 96, p. 61906, 2010, doi: 10.1063/1.3284653.

[4] H. Amano *et al.*, “The 2020 UV emitter roadmap,” *J. Phys. D. Appl. Phys.*, vol. 53, no. 50, 2020, doi: 10.1088/1361-6463/aba64c.

[5] S. Islam *et al.*, “Enhancing Wall-Plug Efficiency for Deep-UV Light-Emitting Diodes: From Crystal Growth to Devices,” in *Light-Emitting Diodes: Materials, Processes, Devices and Applications*, J. Li and G. Q. Zhang, Eds. Springer, 2019, pp. 337–395.

[6] J. Zhang, Y. Gao, L. Zhou, Y.-U. Gil, and K.-M. Kim, “Transparent deep ultraviolet light-emitting diodes with a p-type AlN ohmic contact layer,” *Proc. SPIE 10940, Light. Devices, Mater. Appl.*, vol. 1094002, p. 1, Mar. 2019, doi: 10.1117/12.2506918.

[7] Y. Zhang *et al.*, “Tunnel-injected sub 290 nm ultra-violet light emitting diodes with 2.8% external quantum efficiency,” *Appl. Phys. Lett.*, vol. 112, no. 7, p. 071107, 2018, doi: 10.1063/1.5017045.

[8] S. I. Inoue, N. Tamari, and M. Taniguchi, “150 mW deep-ultraviolet light-emitting diodes with large-area AlN nanophotonic light-extraction structure emitting at 265 nm,” *Appl. Phys. Lett.*, vol. 110, no. 14, p. 141106, 2017, doi: 10.1063/1.4978855.

[9] T. Kinoshita *et al.*, “Performance and reliability of deep-ultraviolet light-emitting diodes fabricated on AlN substrates prepared by hydride vapor phase epitaxy,” *Appl. Phys. Express*, vol. 6, no. 9, 2013, doi: 10.7567/APEX.6.092103.

[10] T. Kinoshita *et al.*, “Deep-ultraviolet light-emitting diodes fabricated on aln substrates prepared by hydride vapor phase epitaxy,” *Appl. Phys. Express*, vol. 5, no. 12, 2012, doi: 10.1143/APEX.5.122101.

[11] D. Liu *et al.*, “229 nm UV LEDs on aluminum nitride single crystal substrates using p-type silicon for increased hole injection,” *Appl. Phys. Lett.*, vol. 112, no. 8, p. 081101, 2018, doi: 10.1063/1.5011180.

[12] A. Fujioka *et al.*, “High-output-power 255/280/310 nm deep ultraviolet light-emitting diodes and their lifetime characteristics,” *Semicond. Sci. Technol.*, vol. 29, no. 8, p. 084005, 2014, doi: 10.1088/0268-1242/29/8/084005.

[13] M. Ichikawa *et al.*, “High-output-power deep ultraviolet light-emitting diode assembly using direct bonding,” *Appl. Phys. Express*, vol. 9, no. 7, pp. 1–5, 2016, doi: 10.7567/APEX.9.072101.

[14] R. Choi, “Current status and future works of high-power deep UV LEDs (Conference Presentation),” 2017, doi: https://doi.org/10.1117/12.2250000.

[15] M. Shatalov *et al.*, “278 nm deep ultraviolet LEDs with 11% external quantum efficiency,” *Device Res. Conf. - Conf. Dig. DRC*, pp. 255–256, 2012, doi: 10.1109/DRC.2012.6257013.

[16] M. Shatalov *et al.*, “Large chip high power deep ultraviolet light-emitting diodes,” *Appl. Phys. Express*, vol. 3, no. 6, pp. 3–6, 2010, doi: 10.1143/APEX.3.062101.

[17] V. Adivarahan *et al.*, “High-efficiency 269 nm emission deep ultraviolet light-emitting diodes,” *Appl. Phys. Lett.*, vol. 84, no. 23, pp. 4762–4764, 2004, doi: 10.1063/1.1756202.

[18] Z. Zhang *et al.*, “A 271.8 nm deep-ultraviolet laser diode for room temperature operation,” *Appl. Phys. Express*, vol. 12, no. 12, p. 124003, 2019, doi: 10.7567/1882-0786/ab50e0.

[19] C. Pernot *et al.*, “Improved efficiency of 255-280 nm AlGaN-based light-emitting diodes,” *Appl. Phys. Express*, vol. 3, no. 6, pp. 2–4, 2010, doi: 10.1143/APEX.3.061004.

[20] Y. Nagasawa, A. Hirano, Y. Nagasawa, and A. Hirano, “A Review of AlGaN-Based Deep-Ultraviolet Light-Emitting Diodes on Sapphire,” *Appl. Sci.*, vol. 8, no. 8, p. 1264, Jul. 2018, doi: 10.3390/app8081264.

[21] M. Kaneda *et al.*, “Uneven AlGaN multiple quantum well for deep-ultraviolet LEDs grown on macrosteps and impact on electroluminescence spectral output,” *Jpn. J. Appl. Phys.*, vol. 56, no. 6, pp. 0–9, 2017, doi: 10.7567/JJAP.56.061002.

[22] N. Susilo *et al.*, “Improved performance of UVC-LEDs by combination of high-temperature annealing and epitaxially laterally overgrown AlN/sapphire,” *Photonics Res.*, vol. 8, no. 4, p. 589, 2020, doi: 10.1364/prj.385275.

[23] N. Lobo-Ploch *et al.*, “Milliwatt power 233 nm AlGaN-based deep UV-LEDs on sapphire substrates,” *Appl. Phys. Lett.*, vol. 117, no. 11, 2020, doi: 10.1063/5.0015263.

[24] N. Susilo *et al.*, “AlGaN-based deep UV LEDs grown on sputtered and high temperature annealed AlN/sapphire,” *Appl. Phys. Lett.*, vol. 112, no. 4, 2018, doi: 10.1063/1.5010265.

[25] F. Mehnke, L. Sulmoni, M. Guttmann, T. Wernicke, and M. Kneissl, “Influence of light absorption on the performance characteristics of UV LEDs with emission between 239 and 217 nm,” *Appl. Phys. Express*, vol. 12, no. 1, 2019, doi: 10.7567/1882-0786/aaf788.

[26] T. Takano, T. Mino, J. Sakai, N. Noguchi, K. Tsubaki, and H. Hirayama, “Deep-ultraviolet light-emitting diodes with external quantum efficiency higher than 20% at 275 nm achieved by improving light-extraction efficiency,” *Appl. Phys. Express*, vol. 10, no. 3, 2017, doi: 10.7567/APEX.10.031002.

[27] H. Hirayama, Y. Tsukada, T. Maeda, and N. Kamata, “Marked enhancement in the efficiency of deep-ultraviolet AlGaN light-emitting diodes by using a multiquantum-barrier electron blocking layer,” *Appl. Phys. Express*, vol. 3, no. 3, 2010, doi: 10.1143/APEX.3.031002.

[28] H. Hirayama, N. Noguchi, and N. Kamata, “222nm deep-ultraviolet AlGaN quantum well light-emitting diode with vertical emission properties,” *Appl. Phys. Express*, vol. 3, no. 3, 2010, doi: 10.1143/APEX.3.032102.

[29] J. R. Grandusky *et al.*, “270nm pseudomorphic ultraviolet light-emitting diodes with over 60mW continuous wave output power,” *Appl. Phys. Express*, vol. 6, no. 3, 2013, doi: 10.7567/APEX.6.032101.

[30] T. Mino, H. Hirayama, T. Takano, N. Noguchi, and K. Tsubaki, “Highly-uniform 260 nm-band AlGaN-based deep-ultraviolet light-emitting diodes developed by 2-inch x 3 MOVPE system,” *Phys. Status Solidi Curr. Top. Solid State Phys.*, vol. 9, no. 3–4, pp. 749–752, 2012, doi: 10.1002/pssc.201100358.

[31] B. K. Saifaddin *et al.*, “AlGaN Deep-Ultraviolet Light-Emitting Diodes Grown on SiC

Substrates," *ACS Photonics*, vol. 7, no. 3, pp. 554–561, Mar. 2020, doi: 10.1021/acsphotonics.9b00600.

[32] C. J. Zollner *et al.*, "Superlattice hole injection layers for UV LEDs grown on SiC," *Opt. Mater. Express*, vol. 10, no. 9, pp. 2171–2180, 2020, doi: 10.1364/OME.398146.

[33] S. Hwang *et al.*, "A hybrid micro-pixel based deep ultraviolet light-emitting diode lamp," *Appl. Phys. Express*, vol. 4, no. 1, pp. 8–11, 2011, doi: 10.1143/APEX.4.012102.

[34] V. Adivarahan, Q. Fareed, M. Islam, T. Katona, B. Krishnan, and A. Khan, "Robust 290 nm emission light emitting diodes over pulsed laterally overgrown AlN," *Japanese J. Appl. Physics, Part 2 Lett.*, vol. 46, no. 36–40, 2007, doi: 10.1143/JJAP.46.L877.

[35] Y. Matsukura *et al.*, "Improving light output power of AlGaN-based deep-ultraviolet light-emitting diodes by optimizing the optical thickness of p-layers," *Appl. Phys. Express*, vol. in press, 2021, doi: https://doi.org/10.35848/1882-0786/ac154c Manuscript.

[36] J. R. Grandusky, S. R. Gibb, M. C. Mendrick, C. Moe, M. Wraback, and L. J. Schowalter, "High output power from 260nm pseudomorphic ultraviolet light-emitting diodes with improved thermal performance," *Appl. Phys. Express*, vol. 4, no. 8, 2011, doi: 10.1143/APEX.4.082101.

[37] J. R. Grandusky, S. R. Gibb, M. Mendrick, and L. J. Schowalter, "Reliability and performance of pseudomorphic ultraviolet light emitting diodes on bulk aluminum nitride substrates," *Phys. Status Solidi Curr. Top. Solid State Phys.*, vol. 8, no. 5, pp. 1528–1533, 2011, doi: 10.1002/pssc.201000892.

[38] J. R. Grandusky, S. R. Gibb, M. C. Mendrick, and L. J. Schowalter, "Properties of mid-ultraviolet light emitting diodes fabricated from pseudomorphic layers on bulk aluminum nitride substrates," *Appl. Phys. Express*, vol. 3, no. 7, pp. 1–4, 2010, doi: 10.1143/APEX.3.072103.

[39] A. Yoshikawa *et al.*, "Improve efficiency and long lifetime UVC LEDs with wavelengths between 230 and 237 nm," *Appl. Phys. Express*, vol. 13, no. 2, p. 022001, Jan. 2020, doi: 10.35848/1882-0786/AB65FB.

[40] C. G. Moe, S. Sugiyama, J. Kasai, J. R. Grandusky, and L. J. Schowalter, "AlGaN Light-Emitting Diodes on AlN Substrates Emitting at 230 nm," *Phys. Status Solidi Appl. Mater. Sci.*, vol. 215, no. 10, pp. 1–5, 2018, doi: 10.1002/pssa.201700660.

[41] D. Liu *et al.*, "226 nm AlGaN/AlN UV LEDs using p-type Si for hole injection and UV reflection," *Appl. Phys. Lett*, vol. 113, p. 11111, 2018, doi: 10.1063/1.5038044.

[42] WHO, "2.1 billion people lack safe drinking water at home, more than twice as many lack safe sanitation," *Press Release: World Health Organization*, 2017. https://www.who.int/news/item/12-07-2017-2-1-billion-people-lack-safe-drinking-water-at-home-more-than-twice-as-many-lack-safe-sanitation.

[43] P. Gwimbi, M. George, and M. Ramphalile, "Bacterial contamination of drinking water sources in rural villages of Mohale Basin, Lesotho: Exposures through neighbourhood sanitation and hygiene practices," *Environ. Health Prev. Med.*, vol. 24, no. 1, pp. 1–7, 2019, doi: 10.1186/s12199-019-0790-z.

[44] M. A. Montgomery and M. Elimelech, "Water and Sanitation in Developing Countries: Including Health in the Equation," *Am. Chem. Soc.*, 2007, doi: 10.1021/es072435t.

[45] T. O. E. Programme, "IMPROVING WATER MANAGEMENT : RECENT OECD EXPERIENCE," 2003.

[46] M. Pritchard, T. Mkandawire, A. Edmondson, J. G. O. Neill, and G. Kululanga,

“Potential of using plant extracts for purification of shallow well water in Malawi,” *Phys. Chem. Earth*, vol. 34, no. 13–16, pp. 799–805, 2009, doi: 10.1016/j.pce.2009.07.001.

[47] B. C. Alkire *et al.*, “Global access to surgical care: A modelling study,” *Lancet Glob. Heal.*, vol. 3, no. 6, pp. e316–e323, 2015, doi: 10.1016/S2214-109X(15)70115-4.

[48] C. C. Miller, “UVC Documentary Standard Development in the IES/TPC,” 2020.

[49] M. T. Mamahlodi, “Potential benefits and harms of the use of UV radiation in transmission of tuberculosis in South African health facilities,” *J. Public Health Africa*, vol. 10, pp. 31–34, 2019, doi: 10.4081/jphia.2019.

[50] K. Song, M. Mohseni, and F. Taghipour, “Application of ultraviolet light-emitting diodes (UV-LEDs) for water disinfection: A review,” *Water Res.*, vol. 94, pp. 341–349, 2016, doi: 10.1016/j.watres.2016.03.003.

[51] C. Prasse, U. Von Gunten, and D. L. Sedlak, “Chlorination of Phenols Revisited: Unexpected Formation of α,β-Unsaturated C4-Dicarbonyl Ring Cleavage Products,” *Environ. Sci. Technol.*, vol. 54, no. 2, pp. 826–834, 2020, doi: 10.1021/acs.est.9b04926.

[52] W. Chu, C. Fang, Y. Deng, and Z. Xu, “Intensified Disinfection Amid COVID-19 Pandemic Poses Potential Risks to Water Quality and Safety,” *Environ. Sci. Technol.*, pp. 4–6, 2020, doi: 10.1021/acs.est.0c04394.

[53] R. J. Fischer *et al.*, “Effectiveness of N95 respirator decontamination and reuse against SARS-CoV-2 Virus,” *Emerg. Infect. Dis.*, vol. 26, no. 9, pp. 2253–2255, 2020, doi: 10.3201/eid2609.201524.

[54] Section, “Special Section on Ultraviolet Technologies for Public Health,” *J. Res. Natl. Inst. Stand. Technol.*, vol. 126, 2021.

[55] C. J. Zollner, S. P. DenBaars, J. Speck, and S. Nakamura, “Germicidal ultraviolet LEDs: a review of applications and semiconductor technologies,” *Semicond. Sci. Technol.*, 2021, doi: 10.1088/1361-6641/ac27e7.

[56] W. Kowalski, *Ultraviolet Germicidal Irradiation Handbook*. Berlin Heidelberg: Springer Verlag, 2009.

[57] M. O. Ryan, C. N. Haas, P. L. Gurian, C. P. Gerba, B. M. Panzl, and J. B. Rose, “Application of quantitative microbial risk assessment for selection of microbial reduction targets for hard surface disinfectants,” *Am. J. Infect. Control*, vol. 42, no. 11, pp. 1165–1172, 2014, doi: 10.1016/j.ajic.2014.07.024.

[58] R. L. Miller and P. G. W. Plagemann, “Effect of Ultraviolet Light on Mengovirus: Formation of Uracil Dimers, Instability and Degradation of Capsid, and Covalent Linkage of Protein to Viral RNA,” *J. Virol.*, vol. 13, no. 3, pp. 729–739, 1974, doi: 10.1128/jvi.13.3.729-739.1974.

[59] M. Correia, M. T. Neves-Petersen, P. B. Jeppesen, S. Gregersen, and S. B. Petersen, “UV-Light Exposure of Insulin: Pharmaceutical Implications upon Covalent Insulin Dityrosine Dimerization and Disulphide Bond Photolysis,” *PLoS One*, vol. 7, no. 12, 2012, doi: 10.1371/journal.pone.0050733.

[60] M. T. Neves-Petersen *et al.*, “High probability of disrupting a disulphide bridge mediated by an endogenous excited tryptophan residue,” *Protein Sci.*, vol. 11, no. 3, pp. 588–600, 2009, doi: 10.1110/ps.06002.

[61] Y. Aoyagi *et al.*, “Inactivation of Bacterial Viruses in Water Using Deep Ultraviolet Semiconductor Light-Emitting Diode,” *J. Environ. Eng.*, vol. 137, no. 12, pp. 1215–1218, Dec. 2011, doi: 10.1061/(ASCE)EE.1943-7870.0000442.

[62] C. Bowker, A. Sain, M. Shatalov, and J. Ducoste, "Microbial UV fluence-response assessment using a novel UV-LED collimated beam system," *Water Res.*, vol. 45, no. 5, pp. 2011–2019, 2011, doi: 10.1016/j.watres.2010.12.005.

[63] M. Clauß, "Higher effectiveness of photoinactivation of bacterial spores, UV resistant vegetative bacteria and mold spores with 222 nm compared to 254 nm wavelength," *Acta Hydrochim. Hydrobiol.*, vol. 34, no. 6, pp. 525–532, 2006, doi: 10.1002/aheh.200600650.

[64] D. Wang, T. Oppenländer, M. G. El-Din, and J. R. Bolton, "Comparison of the disinfection effects of vacuum-UV (VUV) and UV light on bacillus subtilis spores in aqueous suspensions at 172, 222 and 254 nm," *Photochem. Photobiol.*, vol. 86, no. 1, pp. 176–181, 2010, doi: 10.1111/j.1751-1097.2009.00640.x.

[65] H. Woo *et al.*, "Efficacy of Inactivation of Human Enteroviruses by Dual-Wavelength Germicidal Ultraviolet (UV-C) Light emitting diodes (LEDs)," *Water*, vol. 6, no. Cdc, p. 1131, 2019.

[66] C. Chatterley and K. Linden, "Demonstration and evaluation of germicidal UV-LEDs for point-of-use water disinfection," *J. Water Health*, vol. 8, no. 3, pp. 479–486, Sep. 2010, doi: 10.2166/wh.2010.124.

[67] R. M. Jenny, O. D. Simmons, M. Shatalov, and J. J. Ducoste, "Modeling a continuous flow ultraviolet Light Emitting Diode reactor using computational fluid dynamics," *Chem. Eng. Sci.*, vol. 116, pp. 524–535, Sep. 2014, doi: 10.1016/j.ces.2014.05.020.

[68] K. Oguma, R. Kita, H. Sakai, M. Murakami, and S. Takizawa, "Application of UV light emitting diodes to batch and flow-through water disinfection systems," *Desalination*, vol. 328, pp. 24–30, Nov. 2013, doi: 10.1016/j.desal.2013.08.014.

[69] K. Oguma, S. Rattanakul, and J. R. Bolton, "Application of UV Light–Emitting Diodes to Adenovirus in Water," *J. Environ. Eng.*, vol. 142, no. 3, p. 04015082, Mar. 2016, doi: 10.1061/(ASCE)EE.1943-7870.0001061.

[70] H. Mamane-Gravetz, K. G. Linden, A. Cabaj, and R. Sommer, "Spectral sensitivity of Bacillus subtilis spores and MS2 coliphage for validation testing of ultraviolet reactors for water disinfection," *Environ. Sci. Technol.*, vol. 39, no. 20, pp. 7845–7852, Oct. 2005, doi: 10.1021/es048446t.

[71] K. G. Pennell, Z. Naunovic, and E. R. Blatchley, "Sequential Inactivation of *Bacillus Subtilis* Spores with Ultraviolet Radiation and Iodine," *J. Environ. Eng.*, vol. 134, no. 7, pp. 513–520, Jul. 2008, doi: 10.1061/(ASCE)0733-9372(2008)134:7(513).

[72] K. A. Sholtes, K. Lowe, G. W. Walters, M. D. Sobsey, K. G. Linden, and L. M. Casanova, "Comparison of ultraviolet light-emitting diodes and low-pressure mercury-arc lamps for disinfection of water," *Environ. Technol.*, vol. 37, no. 17, pp. 2183–2188, Sep. 2016, doi: 10.1080/09593330.2016.1144798.

[73] M. Clauß, R. Mannesmann, and A. Kolch, "Photoreactivation of Escherichia coli and Yersinia enterolytica after irradiation with a 222 nm excimer lamp compared to a 254 nm low-pressure mercury lamp," *Acta Hydrochim. Hydrobiol.*, vol. 33, no. 6, pp. 579–584, 2005, doi: 10.1002/aheh.200400600.

[74] Y. Gerchman, H. Mamane, N. Friedman, and M. Mandelboim, "UV-LED disinfection of Coronavirus: Wavelength effect," *J. Photochem. Photobiol. B Biol.*, vol. 212, no. September, 2020, doi: 10.1016/j.jphotobiol.2020.112044.

[75] A. H. Malayeri, M. Mohseni, B. Cairns, and B. J. R., "Fluence (UV Dose) Required to Achieve Incremental Log Inactivation of Bacteria, Protozoa, Viruses and Algae," 2020.

[Online]. Available: http://uvsalesinfo.com/Documents/NavLink/UV_Destruction_Chart_uid7102009502412.pdf.

[76] S. E. Beck *et al.*, “Evaluating UV-C LED disinfection performance and investigating potential dual-wavelength synergy,” *Water Res.*, vol. 109, pp. 207–216, 2017, doi: 10.1016/j.watres.2016.11.024.

[77] H. Yamada, “Performance test for virus inactivation efficacy by UV irradiation,” *Test Rep.*, 2019.

[78] L. Y. Kuritzky, C. Weisbuch, and J. S. Speck, “Prospects for 100% wall-plug efficient III-nitride LEDs,” *Opt. Express*, vol. 26, no. 13, p. 16600, 2018, doi: 10.1364/oe.26.016600.

[79] M. Kneissl *et al.*, “Advances in group III-nitride-based deep UV light-emitting diode technology,” *Semicond. Sci. Technol.*, vol. 26, no. 1, p. 014036, 2011, doi: 10.1088/0268-1242/26/1/014036.

[80] M. A. Khan, M. Shatalov, H. P. Maruska, H. M. Wang, and E. Kuokstis, “III-nitride UV devices,” *Japanese J. Appl. Physics, Part 1 Regul. Pap. Short Notes Rev. Pap.*, vol. 44, no. 10, pp. 7191–7206, 2005, doi: 10.1143/JJAP.44.7191.

[81] Z. Bryan, I. Bryan, J. Xie, S. Mita, Z. Sitar, and R. Collazo, “High internal quantum efficiency in AlGaN multiple quantum wells grown on bulk AlN substrates,” *Appl. Phys. Lett.*, vol. 106, no. 14, pp. 1–5, 2015, doi: 10.1063/1.4917540.

[82] R. L. Schwoebel and E. J. Shipsey, “Step motion on crystal surfaces,” *J. Appl. Phys.*, vol. 37, no. 10, pp. 3682–3686, 1966, doi: 10.1063/1.1707904.

[83] X. . Wu *et al.*, “Dislocation generation in GaN heteroepitaxy,” *J. Cryst. Growth*, vol. 189–190, pp. 231–243, 1998, doi: 10.1016/S0022-0248(98)00240-1.

[84] S. Nakamura, “GaN Growth Using GaN Buffer Layer,” *Jpn. J. Appl. Phys.*, vol. 30, no. 10A, pp. 1705–1707, 1991.

[85] B. Heying *et al.*, “Role of threading dislocation structure on the x-ray diffraction peak widths in epitaxial GaN films,” *Appl. Phys. Lett.*, vol. 643, no. 1996, p. 643, 1995, doi: 10.1063/1.116495.

[86] A. Khan, K. Balakrishnan, and T. Katona, “Ultraviolet light-emitting diodes based on group three nitrides,” *Nat. Photonics*, vol. 2, no. 2, pp. 77–84, 2008, doi: 10.1038/nphoton.2007.293.

[87] K. Balakrishnan, A. Bandoh, M. Iwaya, S. Kamiyama, H. Amano, and I. Akasaki, “Influence of high temperature in the growth of low dislocation content AlN bridge layers on patterned 6H-SiC substrates by metalorganic vapor phase epitaxy,” *Japanese J. Appl. Physics, Part 2 Lett.*, vol. 46, no. 12–16, pp. L307–L310, 2007, doi: 10.1143/JJAP.46.L307.

[88] S. Yamada, J. Kato, S. Tanaka, and I. S. Avramescu, “Nucleation and growth kinetics of AlN films on atomically smooth 6H – SiC (0001) surfaces,” *Appl. Phys. Lett*, vol. 78, no. 3612, 2001, doi: 10.1063/1.1377309.

[89] K. Balakrishnan *et al.*, “Critical aspects of high temperature MOCVD growth of AlN epilayers on 6H-SiC substrates,” *Phys. Status Solidi Curr. Top. Solid State Phys.*, vol. 3, no. 6, pp. 1392–1395, 2006, doi: 10.1002/pssc.200565387.

[90] F. Brunner, H. Protzmann, M. Heuken, A. Knauer, M. Weyers, and M. Kneissl, “High-temperature growth of AlN in a production scale 11x2’’ MOVPE reactor,” *Phys. Status Solidi Curr. Top. Solid State Phys.*, vol. 5, no. 6, pp. 1799–1801, 2008, doi:

10.1002/pssc.200778658.

[91] A. S. Almogbel *et al.*, “Growth of highly-conductive Al-rich AlGaN:Si with low group III vacancy concentration,” *Manuscr. Submitt.*, 2021.

[92] Z. Chen *et al.*, “Pulsed lateral epitaxial overgrowth of aluminum nitride on sapphire substrates,” *Appl. Phys. Lett.*, vol. 89, no. 8, pp. 2–5, 2006, doi: 10.1063/1.2245436.

[93] M. Shatalov, “Deep UV LEDs with record external quantum efficiency,” *Semicond. Today*, vol. 7, no. 7, pp. 92–93, 2012.

[94] T. Wang, J. Bai, P. J. Parbrook, and A. G. Cullis, “Air-bridged lateral growth of an Al0.98Ga0.02N layer by introduction of porosity in an AlN buffer,” *Appl. Phys. Lett.*, vol. 87, no. 15, pp. 1–3, 2005, doi: 10.1063/1.2089182.

[95] H. Okumura, T. Kimoto, and J. Suda, “Enhancement of initial layer-by-layer growth and reduction of threading dislocation density by optimized Ga pre-irradiation in molecular-beam epitaxy of 2H-AlN on 6H-SiC (0001),” *Phys. Status Solidi Curr. Top. Solid State Phys.*, vol. 7, no. 7–8, pp. 2094–2096, 2010, doi: 10.1002/pssc.200983579.

[96] Kusse and Westwig, *Mathematical Physics*, 2nd ed. Wiley-VCH, 2005.

[97] H. M. Foronda *et al.*, “Low threading dislocation density aluminum nitride on silicon carbide through the use of reduced temperature interlayers,” *J. Cryst. Growth*, vol. 483, pp. 134–139, 2018, doi: 10.1016/J.JCRYSGRO.2017.11.027.

[98] A. Mogilatenko, S. Walde, S. Hagedorn, C. Netzel, C.-Y. Huang, and M. Weyers, “Impact of Si doping on dislocation behavior in MOVPE-grown AlN on high-temperature annealed AlN buffer layers Impact of Si doping on dislocation behavior in MOVPE-grown AlN on high-temperature annealed AlN buffer layers,” vol. 045702, no. September 2021, 2022, doi: 10.1063/5.0073076.

[99] J. B. Casady and R. W. Johnson, “Status of silicon carbide (SiC) as a wide-bandgap semiconductor for high-temperature applications: A review,” *Solid. State. Electron.*, vol. 39, no. 10, pp. 1409–1422, 1996, doi: 10.1109/9780470544884.ch69.

[100] A. Suzuki, M. Ikeda, N. Nagao, H. Matsunami, and T. Tanaka, “Liquid-phase epitaxial growth of 6H-SiC by the dipping technique for preparation of blue-light-emitting diodes,” *J. Appl. Phys.*, vol. 47, no. 10, pp. 4546–4550, 1976, doi: 10.1063/1.322428.

[101] V. A. Dmitriev, Y. V. Morozenko, B. V. Tzarenkov, and V. E. Chelnokov, “Silicon carbide blue and violet light-emitting diodes,” *Displays*, vol. 13, no. 2, pp. 97–106, 1992, doi: 10.1016/0141-9382(92)90104-Y.

[102] J. A. Edmond, “BLUE LIGHT EMITTING DIODE FORMED IN SLICON CARBDE,” 4,918,497, 1990.

[103] S. Keller *et al.*, “Influence of the substrate misorientation on the properties of N-polar GaN films grown by metal organic chemical vapor deposition,” *J. Appl. Phys.*, vol. 102, no. 8, p. 083546, Oct. 2007, doi: 10.1063/1.2801406.

[104] J. Lemettinen *et al.*, “MOVPE growth of nitrogen- and aluminum-polar AlN on 4H-SiC,” *J. Cryst. Growth*, vol. 487, pp. 50–56, 2018, doi: 10.1016/j.jcrysgro.2018.02.020.

[105] F. Ponce, C. Van de Walle, and J. Northrup, “Atomic arrangement at the AlN/SiC interface,” *Phys. Rev. B - Condens. Matter Mater. Phys.*, vol. 53, no. 11, pp. 7473–7478, 1996, doi: 10.1103/PhysRevB.53.7473.

[106] F. A. Ponce, B. S. Krusor, J. S. Major, W. E. Plano, and D. F. Welch, “Microstructure of GaN epitaxy on SiC using AlN buffer layers,” *Appl. Phys. Lett.*, vol. 67, no. 410, p. 410, 1995, doi: 10.1063/1.114645.

[107] C. Hallin *et al.*, “In situ substrate preparation for high-quality SiC chemical vapour

deposition," *J. Cryst. Growth*, vol. 181, no. 3, pp. 241–253, 1997, doi: 10.1016/S0022-0248(97)00247-9.

[108] J. Bernhardt, J. Schardt, U. Starke, and K. Heinz, "Epitaxially ideal oxide – semiconductor interfaces : Silicate adlayers on hexagonal (0001) and (000) SiC surfaces," *Appl. Phys. Lett.*, vol. 74, no. 1084, 1999, doi: 10.1063/1.123489.

[109] S. Nakamura, T. Kimoto, H. Matsunami, S. Tanaka, and N. Teraguchi, "Formation of periodic steps with a unit-cell height on 6H – SiC (0001) surface by HCl etching Formation of periodic steps with a unit-cell height on 6H – SiC „ 0001 … surface by HCl etching," vol. 3412, no. 0001, pp. 8–11, 2000, doi: 10.1063/1.126663.

[110] S. Yamada *et al.*, "Nucleation and growth kinetics of AlN films on atomically smooth 6H-SiC (0001) surfaces," *Appl. Phys. Lett.*, vol. 78, no. 23, pp. 3612–3614, 2001, doi: 10.1063/1.1377309.

[111] Z. Y. Xie, J. H. Edgar, B. K. Burkland, J. T. George, and J. Chaudhuri, "DPBs-free and polytype controlled growth of SiC via surface etching on on-axis 6H-SiC(0 0 0 1)," *J. Cryst. Growth*, vol. 224, no. 3–4, pp. 235–243, 2001, doi: 10.1016/S0022-0248(01)01024-7.

[112] N. Onojima, J. Suda, and H. Matsunami, "Molecular-beam epitaxial growth of insulating AlN on surface-controlled 6H-SiC substrate by HCl gas etching," *Appl. Phys. Lett.*, vol. 80, no. 1, pp. 76–78, 2002, doi: 10.1063/1.1428620.

[113] H. Okumura, T. Kimoto, and J. Suda, "Formation mechanism of threading-dislocation array in AlN layers grown on 6H-SiC (0001) substrates with 3-bilayer-high surface steps," *Appl. Phys. Lett.*, vol. 105, no. 7, pp. 1–5, 2014, doi: 10.1063/1.4892807.

[114] S. Tanaka, R. S. Kern, and R. F. Davis, "Initial stage of aluminum nitride film growth on 6H-silicon carbide by plasma-assisted, gas-source molecular beam epitaxy," *Appl. Phys. Lett.*, vol. 66, no. 37, 1995, doi: 10.1063/1.114173.

[115] Y. N. Picard *et al.*, "Threading dislocation behavior in AlN nucleation layers for GaN growth on 4H-SiC," *Appl. Phys. Lett.*, vol. 91, no. 1, 2007, doi: 10.1063/1.2754638.

[116] Y. N. Picard, J. D. Caldwell, M. E. Twigg, C. R. Eddy, and M. A. Mastro, "The Influence of Substrate Atomic Step Morphology on Threading Dislocation Distributions in III-Nitride Films," pp. 3–4, 2007.

[117] H. Nakagawa, S. Tanaka, and I. Suemune, "Self-ordering of nanofacets on vicinal sic surfaces," *Phys. Rev. Lett.*, vol. 91, no. 22, pp. 2–5, 2003, doi: 10.1103/PhysRevLett.91.226107.

[118] J. Suda, K. Miura, M. Honaga, Y. Nishi, N. Onojima, and H. Matsunami, "Effects of 6H-SiC surface reconstruction on lattice relaxation of AlN buffer layers in molecular-beam epitaxial growth of GaN," *Appl. Phys. Lett.*, vol. 81, no. 27, pp. 5141–5143, 2002, doi: 10.1063/1.1533855.

[119] H. Okumura, T. Kimoto, and J. Suda, "Reduction of threading dislocation density in 2H-AlN grown on 6H-SiC(0001) by minimizing unintentional active-nitrogen exposure before growth," *Appl. Phys. Express*, vol. 4, no. 2, pp. 2–5, 2011, doi: 10.1143/APEX.4.025502.

[120] H. Okumura, T. Kimoto, and J. Suda, "Over-700-nm Critical Thickness of AlN Grown on 6H-SiC(0001) by Molecular Beam Epitaxy," *Appl. Phys. Express*, vol. 5, no. 10, p. 105502, Oct. 2012, doi: 10.1143/APEX.5.105502.

[121] H. Okumura, M. Horita, T. Kimoto, and J. Suda, "Impact of surface step heights of 6H-SiC (0 0 0 1) vicinal substrates in heteroepitaxial growth of 2H-AlN," *Appl. Surf. Sci.*,

vol. 254, pp. 7858–7860, 2008, doi: 10.1016/j.apsusc.2008.02.165.

[122] C. G. Moe, Y. Wu, S. Keller, J. S. Speck, S. P. DenBaars, and D. Emerson, "Crystal quality and growth evolution of aluminum nitride on silicon carbide," *Phys. Status Solidi*, vol. 203, no. 7, pp. 1708–1711, 2006, doi: 10.1002/pssa.200565388.

[123] C. J. Zollner *et al.*, "Reduced dislocation density and residual tension in AlN grown on SiC by metalorganic chemical vapor deposition," *Appl. Phys. Lett.*, vol. 115, no. 16, p. 161101, Oct. 2019, doi: 10.1063/1.5123623.

[124] B. Heying, E. J. Tarsa, C. R. Elsass, P. Fini, S. P. DenBaars, and J. S. Speck, "Dislocation mediated surface morphology of GaN," *J. Appl. Phys.*, vol. 85, no. 9, pp. 6470–6476, 1999, doi: 10.1063/1.370150.

[125] R. M. Farrell *et al.*, "Origin of pyramidal hillocks on GaN thin films grown on free-standing m-plane GaN substrates," *Appl. Phys. Lett.*, vol. 96, no. 23, pp. 1–3, 2010, doi: 10.1063/1.3447926.

[126] A. S. Almogbel *et al.*, "Growth of highly conductive Al-rich AlGaN : Si with low group-III vacancy concentration," *AIP Adv.*, vol. 11, no. 095119, pp. 1–8, 2021, doi: 10.1063/5.0066652.

[127] P. Reddy *et al.*, "Charge neutrality levels, barrier heights, and band offsets at polar AlGaN," *Appl. Phys. Lett.*, vol. 107, no. 9, 2015, doi: 10.1063/1.4930026.

[128] A. E. Romanov *et al.*, "Cracking of III-nitride layers with strain gradients," *Appl. Phys. Lett.*, vol. 89, no. 16, 2006, doi: 10.1063/1.2352043.

[129] J. Han *et al.*, "Control and elimination of cracking of AlGaN using low-temperature AlGaN interlayers," *Appl. Phys. Lett.*, vol. 78, no. 1, pp. 67–69, 2001, doi: 10.1063/1.1336812.

[130] P. Cantu *et al.*, "Si doping effect on strain reduction in compressively strained Al0.49Ga0.51N thin films," *Appl. Phys. Lett.*, vol. 83, no. 4, pp. 674–676, Jul. 2003, doi: 10.1063/1.1595133.

[131] A. E. Romanov and J. S. Speck, "Stress relaxation in mismatched layers due to threading dislocation inclination," *Appl. Phys. Lett.*, vol. 83, no. 13, pp. 2569–2571, 2003, doi: 10.1063/1.1613360.

[132] T. Böttcher *et al.*, "The role of high-temperature island coalescence in the development of stresses in GaN films," *Appl. Phys. Lett.*, vol. 78, no. 14, pp. 1976–1978, 2001, doi: 10.1063/1.1359780.

[133] K. Kinosita, K. Maki, K. Nakamizo, and K. Takeuchi, "Stress in Vacuum Deposited Films of Silver," *Jpn. J. Appl. Phys.*, vol. 6, no. 1, pp. 42–53, 1967, doi: 10.1143/jjap.6.42.

[134] W. D. Nix and B. M. Clemens, "Crystallite coalescence: A mechanism for intrinsic tensile stresses in thin films," *J. Mater. Res.*, vol. 14, no. 8, pp. 3467–3473, 1999, doi: 10.1557/JMR.1999.0468.

[135] I. C. Manning, X. Weng, J. D. Acord, M. A. Fanton, D. W. Snyder, and J. M. Redwing, "Tensile stress generation and dislocation reduction in Si-doped AlxGa1-xN films," *J. Appl. Phys.*, vol. 106, p. 023506, 2009, doi: 10.1063/1.3160331.

[136] P. Cantu *et al.*, "Role of inclined threading dislocations in stress relaxation in mismatched layers," *J. Appl. Phys.*, vol. 97, p. 103534, 2005, doi: 10.1063/1.1897486.

[137] M. Hawkridge, D. Cherns, and T. Myers, "Lateral migration of dislocations in oxygen-doped GaN grown by molecular beam epitaxy," *Appl. Phys. Lett.*, vol. 89, no. 25, pp. 87–90, 2006, doi: 10.1063/1.2420790.

[138] S. K. Mathis, A. E. Romanov, L. F. Chen, G. E. Beltz, W. Pompe, and J. S. Speck, “Modeling of threading dislocation reduction in growing GaN layers,” *J. Cryst. Growth*, vol. 231, no. 3, pp. 371–390, 2001, doi: 10.1016/S0022-0248(01)01468-3.

[139] H. M. Foronda, A. E. Romanov, E. C. Young, C. A. Roberston, G. E. Beltz, and J. S. Speck, “Curvature and bow of bulk GaN substrates,” *J. Appl. Phys.*, vol. 120, no. 3, 2016, doi: 10.1063/1.4959073.

[140] J. D. Acord, I. C. Manning, X. Weng, D. W. Snyder, and J. M. Redwing, “In situ measurement of stress generation arising from dislocation inclination in AlxGa1-xN:Si thin films,” *Appl. Phys. Lett.*, vol. 93, no. 11, pp. 1–4, 2008, doi: 10.1063/1.2986448.

[141] Y. Taniyasu, M. Kasu, and T. Makimoto, “Threading dislocations in heteroepitaxial AlN layer grown by MOVPE on SiC (0 0 0 1) substrate,” *J. Cryst. Growth*, vol. 298, no. SPEC. ISS, pp. 310–315, 2007, doi: 10.1016/j.jcrysgro.2006.10.032.

[142] H. Okumura, “Formation Mechanism of Extended Defects in AlN Grown on SiC {0001} and Their Reduction by Initial Growth Control,” Kyoto University, 2012.

[143] Z. Li and R. C. Bradt, “Thermal expansion of the hexagonal (4 *H*) polytype of SiC,” *J. Appl. Phys.*, vol. 60, no. 2, pp. 612–614, Jul. 1986, doi: 10.1063/1.337456.

[144] W. M. Yim and R. J. Paff, “Thermal expansion of AlN, sapphire, and silicon,” *J. Appl. Phys.*, vol. 45, no. 3, pp. 1456–1457, Mar. 1974, doi: 10.1063/1.1663432.

[145] J. Y. Tsao, *Materials Fundamentals of Molecular Beam Epitaxy*. San Diego: Academic Press, Inc., 1993.

[146] Z. Chen *et al.*, “High quality AlN grown on SiC by metal organic chemical vapor deposition,” *Appl. Phys. Lett.*, vol. 93, no. 19, pp. 1–4, 2008, doi: 10.1063/1.2988323.

[147] M. Nemoz, R. Dagher, S. Matta, A. Michon, P. Vennéguès, and J. Brault, “Dislocation densities reduction in MBE-grown AlN thin films by high-temperature annealing,” *J. Cryst. Growth*, vol. 461, no. December 2016, pp. 10–15, 2017, doi: 10.1016/j.jcrysgro.2016.12.089.

[148] R. Yoshizawa, H. Miyake, and K. Hiramatsu, “Effect of thermal annealing on AlN films grown on sputtered AlN templates by metalorganic vapor phase epitaxy,” *Jpn. J. Appl. Phys.*, vol. 57, no. 1, pp. 1–4, 2018, doi: 10.7567/JJAP.57.01AD05.

[149] M. Nazari and M. W. Holtz, “Near-ultraviolet Raman and micro-Raman analysis of electronic materials,” *Appl. Phys. Rev.*, vol. 5, no. 4, p. 041303, Dec. 2018, doi: 10.1063/1.5054660.

[150] T. Prokofyeva *et al.*, “Vibrational properties of AlN grown on (111)-oriented silicon,” *Phys. Rev. B*, vol. 63, no. 12, p. 125313, 2001, doi: 10.1103/PhysRevB.63.125313.

[151] G. Bauer, A. Krost, and J. Woitok, “High Resolution X-Ray Diffraction,” in *Optical Characterization of Semiconductor Materials*, 1st ed., G. Bauer and W. Richter, Eds. Springer, 1996, pp. 287–390.

[152] L. B. Freund and S. Suresh, *Thin Film Materials: Stress, Defect Formation, and Surface Evolution*. Cambridge: Cambridge University Press, 2003.

[153] G. L. Harris, “Young’s Modulus of SiC,” in *Properties of Silicon Carbide*, EMIS Datareview Series, 1995, p. 8.

[154] M. Dudley, X. Huang, and W. M. Vetter, “Contribution of x-ray topography and high-resolution diffraction to the study of defects in SiC,” *J. Phys. D. Appl. Phys.*, vol. 36, no. 10A, pp. A30–A36, May 2003, doi: 10.1088/0022-3727/36/10A/307.

[155] R. S. Okojie, T. Holzheu, X. Huang, and M. Dudley, “X-ray diffraction measurement of doping induced lattice mismatch in *n* -type 4H-SiC epilayers grown on *p* -type

substrates," *Appl. Phys. Lett.*, vol. 83, no. 10, pp. 1971–1973, Sep. 2003, doi: 10.1063/1.1606497.

[156] J. Ruska, L. J. Gauckler, J. Lorenz, and H. U. Rexer, "The quantitative calculation of SiC polytypes from measurements of X-ray diffraction peak intensities," *J. Mater. Sci.*, vol. 14, no. 8, pp. 2013–2017, 1979, doi: 10.1007/BF00551044.

[157] P. R. Bevington and D. K. Robinson, *Data Reduction and Error Analysis for the Physical Sciences*, 3rd ed. New York: McGraw-Hill, 2003.

[158] R. Kaplan and T. M. Parrill, "REDUCTION OF SiC SURFACE OXIDES BY A Ga MOLECULAR BEAM : LEED and Electron Spectroscopy Studies," *Surf. Sci.*, vol. 165, pp. 45–52, 1986.

[159] C. Önneby and C. G. Pantano, "Silicon oxycarbide formation on SiC surfaces and at the SiC/SiO2 interface," *J. Vac. Sci. Technol. A Vacuum, Surfaces, Film.*, vol. 15, no. 3, pp. 1597–1602, May 1997, doi: 10.1116/1.580951.

[160] J. S. Speck and S. J. Rosner, "The Role of Threading Dislocations in the Physical Properties of GaN and its Alloys," *Phys. B*, vol. 273–274, pp. 24–32, 1999, doi: 10.4028/www.scientific.net/MSF.353-356.769.

[161] M. Shatalov *et al.*, "AlGaN Deep Ultraviolet Light-Emitting Diodes with External Quantum Efficiency above 10 %," *Appl. Phys. Express*, vol. 082101, no. 2021, pp. 1–12, 2012, doi: http://dx.doi.org/10.1143/APEX.5.082101.

[162] S. Chen *et al.*, "Defect Reduction in AlN Epilayers Grown by MOCVD via Intermediate-Temperature Interlayers," *J. Electron. Mater.*, vol. 44, no. 1, pp. 217–221, 2015, doi: 10.1007/s11664-014-3462-1.

[163] H. Miyake *et al.*, "Annealing of an AlN buffer layer in N2-CO for growth of a high-quality AlN film on sapphire," *Appl. Phys. Express*, vol. 9, no. 2, 2016, doi: 10.7567/APEX.9.025501.

[164] M. X. Wang *et al.*, "Crystal quality evolution of AlN films via high-temperature annealing under ambient N2 conditions," *CrystEngComm*, vol. 20, no. 41, pp. 6613–6617, 2018, doi: 10.1039/C8CE00967H.

[165] K. Uesugi, Y. Hayashi, K. Shojiki, and H. Miyake, "Reduction of threading dislocation density and suppression of cracking in sputter-deposited AlN templates annealed at high temperatures," *Appl. Phys. Express*, vol. 12, no. 6, p. 065501, Jun. 2019, doi: 10.7567/1882-0786/ab1ab8.

[166] B. Tang *et al.*, "Growth of high-quality AlN films on sapphire substrate by introducing voids through growth-mode modification," *Appl. Surf. Sci.*, vol. 518, no. March, p. 146218, 2020, doi: 10.1016/j.apsusc.2020.146218.

[167] F. Brunner, L. Cancellara, S. Hagedorn, M. Albrecht, and M. Weyers, "High-temperature annealing of AlN films grown on 4H–SiC," *AIP Adv.*, vol. 10, no. 12, p. 125303, 2020, doi: 10.1063/5.0027330.

[168] D. Wang, K. Uesugi, S. Xiao, K. Norimatsu, and H. Miyake, "Low dislocation density AlN on sapphire prepared by double sputtering and annealing," *Appl. Phys. Express*, vol. 13, no. 9, 2020, doi: 10.35848/1882-0786/ababec.

[169] J. Ruschel *et al.*, "Reliability of UVC LEDs fabricated on AlN / sapphire templates with different threading dislocation densities," *Appl. Phys. Lett*, vol. 117, no. 241104, p. 241104, 2020, doi: 10.1063/5.0027769.

[170] S. Hagedorn *et al.*, "Stabilization of sputtered AlN/sapphire templates during high temperature annealing," *J. Cryst. Growth*, vol. 512, pp. 142–146, Apr. 2019, doi:

10.1016/J.JCRYSGRO.2019.02.024.

[171] H. Long *et al.*, “High quality 10.6 μ m AlN grown on pyramidal patterned sapphire substrate by MOCVD,” *Appl. Phys. Lett.*, vol. 114, no. 4, p. 042101, Jan. 2019, doi: 10.1063/1.5074177.

[172] M. Kim *et al.*, “AlGaN-Based Deep Ultraviolet Light-Emitting Diodes Fabricated on Patterned Sapphire Substrates,” *Appl. Phys. Express*, vol. 4, no. 9, pp. 4–6, Aug. 2011, doi: 10.1143/APEX.4.092102.

[173] L. Zhang *et al.*, “High-quality AlN epitaxy on nano-patterned sapphire substrates prepared by nano-imprint lithography,” *Sci. Rep.*, vol. 6, no. April, pp. 1–8, 2016, doi: 10.1038/srep35934.

[174] C. He *et al.*, “High-Quality AlN Film Grown on Sputtered AlN/Sapphire via Growth-Mode Modification,” *Cryst. Growth Des.*, p. acs.cgd.8b01045, 2018, doi: 10.1021/acs.cgd.8b01045.

[175] D. Wang, K. Uesugi, S. Xiao, K. Norimatsu, and H. Miyake, “High-quality AlN/sapphire templates prepared by thermal cycle annealing for high-performance ultraviolet light-emitting diodes,” *Appl. Phys. Express*, vol. 14, no. 3, pp. 12–17, 2021, doi: 10.35848/1882-0786/abe522.

[176] J. Wang *et al.*, “Control of dislocations in heteroepitaxial AlN films by extrinsic supersaturated vacancies introduced through thermal desorption of heteroatoms,” *Appl. Phys. Lett.*, vol. 118, no. 16, p. 162103, 2021, doi: 10.1063/5.0045552.

[177] M. Imura *et al.*, “Microstructure of epitaxial lateral overgrown AlN on trench-patterned AlN template by high-temperature metal-organic vapor phase epitaxy,” *Appl. Phys. Lett.*, vol. 89, no. 22, pp. 2005–2007, 2006, doi: 10.1063/1.2364460.

[178] R. Jain *et al.*, “Migration enhanced lateral epitaxial overgrowth of AlN and AlGaN for high reliability deep ultraviolet light emitting diodes,” *Appl. Phys. Lett.*, vol. 93, no. 5, pp. 2006–2009, Aug. 2008, doi: 10.1063/1.2969402.

[179] M. Imura *et al.*, “Impact of high-temperature growth by metal-organic vapor phase epitaxy on microstructure of AlN on 6H-SiC substrates,” *J. Cryst. Growth*, vol. 310, no. 7–9, pp. 2308–2313, 2008, doi: 10.1016/j.jcrysgro.2007.11.206.

[180] H. Hirayama, T. Yatabe, N. Noguchi, T. Ohashi, and N. Kamata, “226-273 nm AlGaN deep-ultraviolet light-emitting diodes fabricated on multilayer AlN buffers on sapphire,” *Phys. Status Solidi Curr. Top. Solid State Phys.*, vol. 5, no. 9, pp. 2969–2971, 2008, doi: 10.1002/pssc.200779303.

[181] S. Y. Karpov and Y. N. Makarov, “Dislocation effect on light emission efficiency in gallium nitride,” *Appl. Phys. Lett.*, vol. 81, no. 25, pp. 4721–4723, 2003, doi: 10.1063/1.1527225.

[182] S. Ichikawa, M. Funato, and Y. Kawakami, “Dominant Nonradiative Recombination Paths and Their Activation Processes in Al x Ga 1−x N-related Materials,” *Phys. Rev. Appl.*, vol. 10, p. 64027, 2018, doi: 10.1103/PhysRevApplied.10.064027.

[183] S. Washiyama, Y. Guan, S. Mita, R. Collazo, and Z. Sitar, “Recovery kinetics in high temperature annealed AlN heteroepitaxial films,” *J. Appl. Phys.*, vol. 127, no. 11, Mar. 2020, doi: 10.1063/5.0002891.

[184] K. Uesugi *et al.*, “Fabrication of AlN templates on SiC substrates by sputtering-deposition and high-temperature annealing,” *J. Cryst. Growth*, vol. 510, pp. 13–17, Mar. 2019, doi: 10.1016/J.JCRYSGRO.2019.01.011.

[185] B. K. Saifaddin *et al.*, “Impact of roughening density on the light extraction efficiency

of thin-film flip-chip ultraviolet LEDs grown on SiC," *Opt. Express*, vol. 27, no. 16, p. A1074, Aug. 2019, doi: 10.1364/OE.27.0A1074.

[186] A. Mogilatenko, A. Knauer, U. Zeimer, C. Hartmann, H. Oppermann, and M. Weyers, "Silicon induced defect reduction in AlN template layers for epitaxial lateral overgrowth," *J. Cryst. Growth*, vol. 462, no. August 2016, pp. 18–23, 2017, doi: 10.1016/j.jcrysgro.2016.12.099.

[187] A. Knauer *et al.*, "MOVPE growth for UV-LEDs," *Proc. SPIE*, vol. 7231, no. February 2009, p. 72310G, 2009, doi: 10.1117/12.816927.

[188] M. A. Reshchikov and H. Morkọ, "Luminescence properties of defects in GaN," *J. Appl. Phys.*, vol. 97, no. 6, 2005, doi: 10.1063/1.1868059.

[189] T. Koppe, H. Hofsäss, and U. Vetter, "Overview of band-edge and defect related luminescence in aluminum nitride," *Journal of Luminescence*. 2016, doi: 10.1016/j.jlumin.2016.05.055.

[190] J. S. Harris *et al.*, "On compensation in Si-doped AlN," *Appl. Phys. Lett.*, vol. 112, no. 15, p. 152101, Apr. 2018, doi: 10.1063/1.5022794.

[191] I. Bryan *et al.*, "Doping and compensation in Al-rich AlGaN grown on single crystal AlN and sapphire by MOCVD," *Appl. Phys. Lett.*, vol. 112, no. 6, 2018, doi: 10.1063/1.5011984.

[192] C. G. Van De Walle and J. Neugebauer, "First-principles calculations for defects and impurities: Applications to III-nitrides," *J. Appl. Phys.*, vol. 95, no. 8, pp. 3851–3879, 2004, doi: 10.1063/1.1682673.

[193] F. Mehnke *et al.*, "Electronic properties of Si-doped Alx Ga 1 - X N with aluminum mole fractions above 80%," *J. Appl. Phys.*, vol. 120, no. 14, 2016, doi: 10.1063/1.4964442.

[194] X. Guo and E. F. Schubert, "Current crowding and optical saturation effects in GaInN/GaN light-emitting diodes grown on insulating substrates," *Appl. Phys. Lett.*, vol. 78, no. 21, pp. 3337–3339, 2001, doi: 10.1063/1.1372359.

[195] K. Sato *et al.*, "Room-temperature operation of AlGaN ultraviolet-B laser diode at 298 nm on lattice-relaxed Al0.6Ga0.4N/AlN/sapphire," *Appl. Phys. Express*, vol. 13, no. 3, p. 031004, Feb. 2020, doi: 10.35848/1882-0786/AB7711.

[196] C. J. Zollner *et al.*, "Highly Conductive n-Al0.65Ga0.35N Grown by MOCVD Using Low V/III Ratio," *Crystals*, vol. 11, no. 1006, pp. 1–12, 2021.

[197] H. M. Foronda *et al.*, "Electrical properties of (11-22) Si:AlGaN layers at high Al contents grown by metal-organic vapor phase epitaxy," *Appl. Phys. Lett.*, vol. 117, no. 22, p. 221101, 2020, doi: 10.1063/5.0031468.

[198] R. France, T. Xu, P. Chen, R. Chandrasekaran, and T. D. Moustakas, "Vanadium-based Ohmic contacts to n-AlGaN in the entire alloy composition," *Appl. Phys. Lett*, vol. 90, p. 062115, 2007, doi: 10.1063/1.2458399.

[199] N. Nagata, T. Senga, M. Iwaya, T. Takeuchi, S. Kamiyama, and I. Akasaki, "Reduction of contact resistance in V-based electrode for high AlN molar fraction n-type AlGaN by using thin SiNx intermediate layer," *Phys. Status Solidi Curr. Top. Solid State Phys.*, vol. 14, no. 8, 2017, doi: 10.1002/pssc.201600243.

[200] H. K. Cho *et al.*, "Low resistance n-contact for UVC LEDs by a two-step plasma etching process," *Semicond. Sci. Technol.*, vol. 35, no. 9, 2020, doi: 10.1088/1361-6641/ab9ea7.

[201] L. Sulmoni, F. Mehnke, A. Mogilatenko, M. Guttmann, T. Wernicke, and M. Kneissl, "Electrical properties and microstructure formation of V/Al-based n-contacts on high

Al mole fraction n-AlGaN layers,” *Photonics Res.*, vol. 8, no. 8, p. 1381, 2020, doi: 10.1364/prj.391075.

[202] J. H. Wang, S. E. Mohney, S. H. Wang, U. Chowdhury, and R. D. Dupuis, “Vanadium-based ohmic contacts to n-type Al0.6Ga0.4N,” *J. Electron. Mater.*, vol. 33, no. 5, pp. 418–421, 2004, doi: 10.1007/s11664-004-0194-7.

[203] K. Mori *et al.*, “Low-ohmic-contact-resistance V-based electrode for n-type AlGaN with high AlN molar fraction,” *Jpn. J. Appl. Phys.*, vol. 55, no. 05FL03, 2016.

[204] J. Yun *et al.*, “Low-resistance ohmic contacts to digital alloys of n-AlGaN/AlN,” *IEEE Electron Device Lett.*, vol. 27, no. 1, pp. 22–24, 2006, doi: 10.1109/LED.2005.861255.

[205] S. Bharadwaj *et al.*, “Bandgap narrowing and Mott transition in Si-doped Al0.7Ga0.3N,” *Appl. Phys. Lett.*, vol. 114, no. 11, pp. 0–5, 2019, doi: 10.1063/1.5086052.

[206] F. Mehnke *et al.*, “Highly conductive n-AlxGa1-xN layers with aluminum mole fractions above 80%,” *Appl. Phys. Lett.*, vol. 103, no. 21, pp. 1–4, 2013, doi: 10.1063/1.4833247.

[207] Y. Taniyasu, M. Kasu, and T. Makimoto, “Electrical conduction properties of n-type Si-doped AlN with high electron mobility (>100cm2V−1s−1),” *Appl. Phys. Lett.*, vol. 85, no. 20, pp. 4672–4674, 2004, doi: 10.1063/1.1824181.

[208] S. Washiyama *et al.*, “The role of chemical potential in compensation control in Si:AlGaN,” *J. Appl. Phys.*, vol. 127, no. 10, 2020, doi: 10.1063/1.5132953.

[209] R. Collazo *et al.*, “Progress on n-type doping of AlGaN alloys on AlN single crystal substrates for UV optoelectronic applications,” *Phys. Status Solidi Curr. Top. Solid State Phys.*, vol. 8, no. 7–8, pp. 2031–2033, 2011, doi: 10.1002/pssc.201000964.

[210] M. L. Nakarmi, K. H. Kim, K. Zhu, J. Y. Lin, and H. X. Jiang, “Transport properties of highly conductive n-type Al-rich AlxGa1−xN(x⩾0.7),” *Appl. Phys. Lett.*, vol. 85, no. 17, pp. 3769–3771, 2004, doi: 10.1063/1.1809272.

[211] A. Kakanakova-Georgieva, D. Nilsson, X. T. Trinh, U. Forsberg, N. T. Son, and E. Janzén, “The complex impact of silicon and oxygen on the n-type conductivity of high-Al-content AlGaN,” *Appl. Phys. Lett.*, vol. 102, no. 13, 2013, doi: 10.1063/1.4800978.

[212] A. Uedono *et al.*, “Native cation vacancies in Si-doped AlGaN studied by monoenergetic positron beams,” *J. Appl. Phys.*, vol. 111, no. 1, pp. 1–6, 2012, doi: 10.1063/1.3675270.

[213] A. M. Armstrong, M. W. Moseley, A. A. Allerman, M. H. Crawford, and J. J. Wierer, “Growth temperature dependence of Si doping efficiency and compensating deep level defect incorporation in Al0.7Ga0.3N,” *J. Appl. Phys.*, vol. 117, no. 18, pp. 0–5, 2015, doi: 10.1063/1.4920926.

[214] K. Zhu, M. L. Nakarmi, K. H. Kim, J. Y. Lin, and H. X. Jiang, “Silicon doping dependence of highly conductive n-type Al0.7Ga0.3N,” *Appl. Phys. Lett.*, vol. 85, no. 20, pp. 4669–4671, 2004, doi: 10.1063/1.1825055.

[215] S. F. Chichibu *et al.*, “Impacts of Si-doping and resultant cation vacancy formation on the luminescence dynamics for the near-band-edge emission of Al0.6Ga0.4N films grown on AlN templates by metalorganic vapor phase epitaxy,” *J. Appl. Phys.*, vol. 113, no. 21, pp. 0–6, 2013, doi: 10.1063/1.4807906.

[216] F. Tuomisto and I. Makkonen, “Defect identification in semiconductors with positron annihilation: Experiment and theory,” *Rev. Mod. Phys.*, vol. 85, no. 4, pp. 1583–1631, Nov. 2013, doi: 10.1103/RevModPhys.85.1583.

[217] R. Krause-Rehberg and H. S. Leipner, *Positron annihilation in semiconductors : defect studies*. Springer, 1999.

[218] K. Uesugi, K. Shojiki, Y. Tezen, Y. Hayashi, and H. Miyake, “Suppression of dislocation-induced spiral hillocks in MOVPE-grown AlGaN on face-to-face annealed sputter-deposited AlN template,” *Appl. Phys. Lett.*, vol. 116, no. 6, 2020, doi: 10.1063/1.5141825.

[219] I. Bryan *et al.*, “The role of surface kinetics on composition and quality of AlGaN,” *J. Cryst. Growth*, vol. 451, pp. 65–71, 2016, doi: 10.1016/j.jcrysgro.2016.06.055.

[220] J. Yang, Y. H. Zhang, D. G. Zhao, P. Chen, Z. S. Liu, and F. Liang, “Realization low resistivity of high AlN mole fraction Si-doped AlGaN by suppressing the formation native vacancies,” *J. Cryst. Growth*, vol. 570, no. July, p. 126245, 2021, doi: 10.1016/j.jcrysgro.2021.126245.

[221] J. Slotte, F. Tuomisto, K. Saarinen, C. G. Moe, S. Keller, and S. P. DenBaars, “Influence of silicon doping on vacancies and optical properties of AlxGa1−xN thin films,” *Appl. Phys. Lett.*, vol. 90, no. 15, p. 151908, Apr. 2007, doi: 10.1063/1.2721132.

[222] J. Makinen *et al.*, “Observation of a Vacancy at the DX Center in Si- and Sn-Doped AlGaAs,” *Phys. Rev. Lett.*, vol. 71, no. 19, pp. 3154–3157, 1993.

[223] X. T. Trinh, D. Nilsson, I. G. Ivanov, E. Janzén, A. Kakanakova-Georgieva, and N. T. Son, “Stable and metastable Si negative-U centers in AlGaN and AlN,” *Appl. Phys. Lett.*, vol. 105, no. 16, 2014, doi: 10.1063/1.4900409.

[224] S. Washiyama *et al.*, “A thermodynamic supersaturation model for the growth of aluminum gallium nitride by metalorganic chemical vapor deposition,” *J. Appl. Phys.*, vol. 124, no. 11, 2018, doi: 10.1063/1.5045058.

[225] B. Liu *et al.*, “Correlation between electrical properties and growth dynamics for Si-doped Al-rich AlGaN grown by metal-organic chemical vapor deposition,” *Superlattices Microstruct.*, 2022, doi: 10.1016/j.spmi.2021.107141.

[226] Z. Bryan *et al.*, “Fermi level control of compensating point defects during metalorganic chemical vapor deposition growth of Si-doped AlGaN,” *Appl. Phys. Lett.*, vol. 105, no. 22, 2014, doi: 10.1063/1.4903058.

[227] L. B. Rowland, K. Doverspike, and D. K. Gaskill, “Silicon doping of GaN using disilane,” *Appl. Phys. Lett.*, vol. 1495, no. January 1995, p. 1495, 1995, doi: 10.1063/1.113666.

[228] M. W. Fay *et al.*, “Structural and electrical characterization of AuTiAlTi/AlGaN/GaN ohmic contacts,” *J. Appl. Phys.*, vol. 92, no. 1, pp. 94–100, 2002, doi: 10.1063/1.1481960.

[229] K. O. Schweitz, P. K. Wang, S. E. Mohney, and D. Gotthold, “V/Al/Pt/Au Ohmic contact to n-AlGaN/GaN heterostructures,” *Appl. Phys. Lett.*, vol. 80, no. 11, pp. 1954–1956, 2002, doi: 10.1063/1.1459768.

[230] P. Patsalas *et al.*, “Conductive nitrides: Growth principles, optical and electronic properties, and their perspectives in photonics and plasmonics,” *Mater. Sci. Eng. R Reports*, vol. 123, pp. 1–55, 2018, doi: 10.1016/j.mser.2017.11.001.

[231] D. K. Schroder, *SEMICONDUCTOR MATERIAL AND DEVICE CHARACTERIZATION*. Hoboken, NJ: John Wiley & Sons, Inc., 2006.

[232] J. L. Lyons, A. Janotti, and C. G. Van De Walle, “Effects of hole localization on limiting p-type conductivity in oxide and nitride semiconductors,” *J. Appl. Phys.*, vol. 115, no. 1, 2014, doi: 10.1063/1.4838075.

[233] Y.-H. Liang and E. Towe, "Progress in efficient doping of high aluminum-containing group III-nitrides," *Appl. Phys. Rev.*, vol. 5, no. 1, p. 011107, Mar. 2018, doi: 10.1063/1.5009349.

[234] H.-H. Chen, J. S. Speck, C. Weisbuch, and Y.-R. Wu, "Three dimensional simulation on the transport and quantum efficiency of UVC- LEDs with random alloy fluctuations," *Appl. Phys. Lett*, vol. 113, p. 153504, 2018, doi: 10.1063/1.5051081.

[235] Z. Kabilova, C. Kurdak, and R. L. Peterson, "Observation of impurity band conduction and variable range hopping in heavily doped (010) β-Ga2O3," *Semicond. Sci. Technol.*, vol. 34, p. 03LT02, 2019, doi: 10.1088/1361-6641/ab0150.

[236] R. J. Molnar, T. Lei, and T. D. Moustakas, "Electron transport mechanism in gallium nitride," *Appl. Phys. Lett.*, vol. 62, no. 72, p. 1832, 1993, doi: 10.1063/1.108823.

[237] T. Kinoshita, T. Obata, H. Yanagi, and S. Inoue, "High p-type conduction in high-Al content Mg-doped AlGaN," *Appl. Phys. Lett.*, vol. 102, no. 012105, 2013, doi: 10.1063/1.4773594.

[238] N. H. Tran, B. H. Le, S. Zhao, and Z. Mi, "On the mechanism of highly efficient p-type conduction of Mg-doped ultra-wide-bandgap AlN nanostructures," *Appl. Phys. Lett.*, vol. 110, no. 3, p. 032102, 2017, doi: 10.1063/1.4973999.

[239] D. Ji, B. Ercan, and S. Chowdhury, "Experimental Determination of Velocity-Field Characteristic of Holes in GaN," *IEEE Electron Device Lett.*, vol. 41, no. 1, pp. 23–25, 2020, doi: 10.1109/LED.2019.2953873.

[240] N. F. Mott and R. W. Gurney, *Electronic Processes in Ionic Crystals*, 1st ed. Oxford University Press, 1940.

[241] M. H. Crawford, "Materials Challenges of AlGaN-Based UV Optoelectronic Devices," *Semicond. Semimetals*, vol. 96, pp. 3–44, Jan. 2017, doi: 10.1016/BS.SEMSEM.2016.11.001.

[242] J. Neugebauer and C. G. Van De Walle, "Chemical trends for acceptor impurities in GaN," *J. Appl. Phys.*, vol. 85, no. 5, pp. 3003–3005, 1999, doi: 10.1063/1.369619.

[243] A. Chakraborty *et al.*, "Electrical and structural characterization of Mg-doped p-type Al0.69Ga0.31N films on SiC substrate," *J. Appl. Phys.*, vol. 101, no. 5, p. 053717, 2007, doi: 10.1063/1.2710303.

[244] Y. Wu, C. G. Moe, S. Keller, S. P. Denbaars, and J. S. Speck, "Vertical defects in heavily Mg-doped Al0.69Ga0.31N," *Phys. Status Solidi Appl. Mater. Sci.*, vol. 204, no. 10, pp. 3423–3428, 2007, doi: 10.1002/pssa.200723195.

[245] K. Nagata *et al.*, "Reduction in operating voltage of AlGaN homojunction tunnel junction deep-UV light-emitting diodes by controlling impurity concentrations," *Appl. Phys. Express*, vol. 14, no. 084001, 2021, doi: https://doi.org/10.35848/1882-0786/ac0fb6.

[246] E. C. H. Kyle, S. W. Kaun, E. C. Young, and J. S. Speck, "Increased p-type conductivity through use of an indium surfactant in the growth of Mg-doped GaN," *Appl. Phys. Lett.*, vol. 106, no. 22, p. 222103, Jun. 2015, doi: 10.1063/1.4922216.

[247] Y. Chen *et al.*, "High hole concentration in p-type AlGaN by indium-surfactant-assisted Mg-delta doping," *Appl. Phys. Lett.*, vol. 106, no. 16, 2015, doi: 10.1063/1.4919005.

[248] U. K. Mishra and J. Singh, *Semiconductor Device Physics and Design*. Springer, 2008.

[249] S. Li *et al.*, "Polarization induced hole doping in graded AlxGa 1-xN (x = 0.7 ~ 1) layer grown by molecular beam epitaxy," *Appl. Phys. Lett.*, vol. 102, no. 6, pp. 7–10, 2013, doi: 10.1063/1.4792685.

[250] J. Simon, V. Protasenko, C. Lian, H. G. Xing, and D. Jena, "Polarization-Induced Hole Doping in Semiconductor Heterostructures," *Science (80-.).*, vol. 327, no. 5961, pp. 60–64, 2010, doi: 10.1126/science.1183226.

[251] Z. Zhang *et al.*, "Space charge profile study of AlGaN-based p-type distributed polarization doped claddings without impurity doping for UV-C laser diodes," *Appl. Phys. Lett.*, vol. 117, no. 15, 2020, doi: 10.1063/5.0027789.

[252] E. F. Schubert, W. Grieshaber, and I. D. Goepfert, "Enhancement of deep acceptor activation in semiconductors by superlattice doping," *Appl. Phys. Lett*, vol. 69, no. 3737, p. 4, 1996, doi: 10.1063/1.117206.

[253] K. Ebata, J. Nishinaka, Y. Taniyasu, and K. Kumakura, "High hole concentration in Mg-doped AlN/AlGaN superlattices with high Al content," *Jpn. J. Appl. Phys.*, vol. 57, no. 4, pp. 2–5, 2018, doi: 10.7567/JJAP.57.04FH09.

[254] A. A. Allerman, M. H. Crawford, M. A. Miller, and S. R. Lee, "Growth and characterization of Mg-doped AlGaN-AlN short-period superlattices for deep-UV optoelectronic devices," *J. Cryst. Growth*, vol. 312, no. 6, pp. 756–761, 2010, doi: 10.1016/j.jcrysgro.2009.12.047.

[255] C. Weisbuch, "Fundamental Properties of III-V Semiconductor Two-Dimensional Quantized Structures: The Basis for Optical and Electronic Applications," in *Semiconductors and Semimetals*, vol. 24, R. Dingle, Ed. Bell Telephone Laboratories, Incorporated, 1987.

[256] A. Agarwal, C. Gupta, A. Alhassan, T. Mates, S. Keller, and U. Mishra, "Abrupt GaN/p-GaN:Mg junctions grown via metalorganic chemical vapor deposition," *Appl. Phys. Express*, vol. 10, no. 11, pp. 12–15, Nov. 2017, doi: 10.7567/APEX.10.111002.

[257] T. Zheng *et al.*, "High Mg effective incorporation in Al-rich AlxGa1-xN by periodic repetition of ultimate V/III ratio conditions," *Nanoscale Res. Lett.*, vol. 9, no. 1, pp. 1–7, 2014, doi: 10.1186/1556-276X-9-40.

[258] T. C. Zheng *et al.*, "Improved p -type conductivity in Al- rich AlGaN using multidimensional Mg-doped superlattices," *Nat. Sci. Reports*, vol. 6, no. 21897, pp. 1–10, 2016, doi: 10.1038/srep21897.

[259] Y. Yao *et al.*, "Polarization-enhanced p-AlGaN superlattice optimization for GUV LED," *Manuscr. Submitt.*, 2022.

[260] M. Akiba, H. Hirayama, Y. Tomita, Y. Tsukada, N. Maeda, and N. Kamata, "Growth of flat p-GaN contact layer by pulse flow method for high light-extraction AlGaN deep-UV LEDs with Al-based electrode," *Phys. Status Solidi Curr. Top. Solid State Phys.*, vol. 9, no. 3–4, pp. 806–809, 2012, doi: 10.1002/pssc.201100370.

[261] B. K. Saifaddin *et al.*, "Fabrication technology for high light-extraction ultraviolet thin-film flip-chip (UV TFFC) LEDs grown on SiC," *Semicond. Sci. Technol.*, vol. 34, no. 035007, Dec. 2019, doi: 10.1088/1361-6641/aaf58f.

[262] P. Kozodoy *et al.*, "Polarization-enhanced Mg doping of AlGaN/GaN superlattices," *Appl. Phys. Lett.*, vol. 75, no. 16, p. 2444, 1999, doi: 10.1063/1.125042.

[263] J. Zhang, Y. Gao, L. Zhou, and Y. Gil, "Surface hole gas enabled transparent deep ultraviolet light-emitting diode," *Semicond. Sci. Technol.*, vol. 33, pp. 1–6, 2018, doi: 10.1088/1361-6641/aac7c1.

[264] L. Li *et al.*, "On the Hole Injection for III-Nitride Based Deep Ultraviolet Light-Emitting Diodes," *Materials (Basel).*, vol. 10, no. 10, p. 1221, Oct. 2017, doi: 10.3390/ma10101221.

[265] A. David, N. G. Young, C. Lund, and M. D. Craven, “Review—The Physics of Recombinations in III-Nitride Emitters,” *ECS J. Solid State Sci. Technol.*, vol. 9, no. 1, p. 016021, Jan. 2020, doi: 10.1149/2.0372001jss.

[266] Y. P. Varshni, “Temperature dependence of the energy gap in semiconductors,” *Physica*, vol. 34, no. 1, pp. 149–154, Jan. 1967, doi: 10.1016/0031-8914(67)90062-6.

[267] J. Cho, C. Sone, Y. Park, and E. Yoon, “Measuring the junction temperature of III-nitride light emitting diodes using electro-luminescence shift,” *Phys. Status Solidi Appl. Mater. Sci.*, vol. 202, no. 9, pp. 1869–1873, 2005, doi: 10.1002/pssa.200520041.

[268] E. Kioupakis, Q. Yan, and C. G. Van De Walle, “Interplay of polarization fields and Auger recombination in the efficiency droop of nitride light-emitting diodes,” *Appl. Phys. Lett.*, vol. 101, no. 23, pp. 1–5, 2012, doi: 10.1063/1.4769374.

[269] P. Lefebvre *et al.*, “Quantum-confined Stark effect and recombination dynamics of spatially indirect excitons in MBE-grown GaN-AlGaN quantum wells,” *MRS Internet J. Nitride Semicond. Res.*, vol. 4S1, p. G3.69, 1999.

[270] Y. M. Sirenko *et al.*, “Hole scattering and optical transitions in wide-band-gap nitrides: Wurtzite and zinc-blende structures,” *Phys. Rev. B - Condens. Matter Mater. Phys.*, vol. 55, no. 7, pp. 4360–4375, 1997, doi: 10.1103/PhysRevB.55.4360.

[271] M. Suzuki, T. Uenoyama, and A. Yanase, “First-principles calculations of effective-mass parameters of AlN and GaN,” *Phys. Rev. B*, vol. 52, no. 11, pp. 8132–8139, 1995, doi: 10.1103/PhysRevB.52.8132.

[272] S. Chuang and C. Chang, “K·p method for strained wurtzite semiconductors,” *Phys. Rev. B - Condens. Matter Mater. Phys.*, vol. 54, no. 4, pp. 2491–2504, 1996, doi: 10.1103/PhysRevB.54.2491.

[273] A. Atsushi Yamaguchi, “Valence band engineering for remarkable enhancement of surface emission in AlGaN deep-ultraviolet light emitting diodes,” *Phys. Status Solidi Curr. Top. Solid State Phys.*, vol. 5, no. 6, pp. 2364–2366, 2008, doi: 10.1002/pssc.200778740.

[274] C. Liu, “Polarization Engineering for Deep-Ultraviolet Light-Emitting Diodes,” Rochester Institute of Technology, 2020.

[275] O. B. Shchekin *et al.*, “High performance thin-film flip-chip InGaN-GaN light-emitting diodes,” *Appl. Phys. Lett.*, vol. 89, no. 7, pp. 2004–2007, 2006, doi: 10.1063/1.2337007.

[276] T.-Y. Seong, J. Han, H. Amano, and H. Morkoc, *III-Nitride Based Light Emitting Diodes and Applications*, vol. 126. Springer, 2013.

[277] B. Saifaddin *et al.*, “Developments in AlGaN and UV-C LEDs grown on SiC,” *Proc. SPIE*, vol. 10554, p. 1E, 2018, doi: 10.1117/12.2317660.

[278] D. Selvanathan, L. Zhou, V. Kumar, and I. Adesida, “Low resistance Ti/Al/Mo/Au Ohmic contacts for AlGaN/GaN heterostructure field effect transistors,” *Phys. Status Solidi Appl. Res.*, vol. 194, no. 2 SPEC., pp. 583–586, Dec. 2002, doi: 10.1002/1521-396X(200212)194:2<583::AID-PSSA583>3.0.CO;2-3.

[279] M. Iwaya *et al.*, “Recent development of UV-B laser diodes,” *Jpn. J. Appl. Phys.*, vol. in press, 2021, [Online]. Available: https://doi.org/10.35848/1347-4065/ac3be8.

[280] L. Zhang *et al.*, “Deep ultraviolet light-emitting diodes with improved performance via nanoporous AlGaN template,” *Opt. Express*, vol. 27, no. 4, p. 4917, 2019, doi: 10.1364/oe.27.004917.

[281] Y. J. Sung *et al.*, “Enhancing the light extraction of AlGaN-based vertical type deep-ultraviolet light-emitting-diodes with an internal reflector,” *Appl. Phys. Express*, vol.

12, no. 12, p. 122011, Dec. 2019, doi: 10.7567/1882-0786/ab52b6.

[282] M. A. Bergmann *et al.*, “Electrochemical etching of AlGaN for the realization of thin-film devices,” *Appl. Phys. Lett.*, vol. 115, no. 18, p. 182103, Oct. 2019, doi: 10.1063/1.5120397.

[283] M. A. Bergmann, J. Enslin, F. Hjort, T. Wernicke, M. Kneissl, and Å. Haglund, “Thin-film flip-chip UVB LEDs realized by electrochemical etching,” *Appl. Phys. Lett.*, vol. 116, no. 12, p. 121101, Mar. 2020, doi: 10.1063/1.5143297.

[284] F. Hjort *et al.*, “A 310 nm Optically Pumped AlGaN Vertical-Cavity Surface-Emitting Laser,” *ACS Photonics*, 2020, doi: 10.1021/acsphotonics.0c01382.

[285] J. R. Grandusky, L. J. Schowalter, and C. Moe, “ALUMINUM NITRIDE SUBSTRATE REMOVAL FOR ULTRAVIOLET LIGHT - EMITTING DEVICES,” US 10,756,234 B2, 2020.

[286] A. David, “Surface-roughened light-emitting diodes: An accurate model,” *IEEE/OSA J. Disp. Technol.*, vol. 9, no. 5, pp. 301–316, 2013, doi: 10.1109/JDT.2013.2240373.

[287] C. L. Keraly, L. Kuritzky, M. Cochet, and C. Weisbuch, “Light Extraction Efficiency Part A. Ray Tracing for Light Extraction Efficiency (LEE) Modeling in Nitride LEDs,” in *III-Nitride Based Light Emitting Diodes and Applications*, vol. 126, T. Y. Seong, J. Han, H. Amano, and H. Morkoç, Eds. Dordrecht: Springer, 2013, pp. 231–269.

[288] J. W. Lee *et al.*, “An elegant route to overcome fundamentally-limited light extraction in AlGaN deep-ultraviolet light-emitting diodes: Preferential outcoupling of strong in-plane emission,” *Sci. Rep.*, vol. 6, no. August 2015, pp. 1–9, 2016, doi: 10.1038/srep22537.

[289] H. Wan, S. Zhou, S. Lan, and C. Gui, “Light Extraction Efficiency Optimization of AlGaN-Based Deep-Ultraviolet Light-Emitting Diodes,” *ECS J. Solid State Sci. Technol.*, vol. 9, no. 4, p. 046002, Apr. 2020, doi: 10.1149/2162-8777/AB85C0.

[290] H. Long *et al.*, “Internal strain induced significant enhancement of deep ultraviolet light extraction efficiency for AlGaN multiple quantum wells grown by MOCVD,” *Opt. Express*, vol. 26, no. 2, pp. 680–686, 2018, doi: 10.1364/OE.26.000680.

[291] J. F. Muth *et al.*, “Absorption coefficient, energy gap, exciton binding energy, and recombination lifetime of GaN obtained from transmission measurements,” *Appl. Phys. Lett.*, vol. 71, no. 18, pp. 2572–2574, 1997, doi: 10.1063/1.120191.

[292] H.-Y. Y. Ryu *et al.*, “Investigation of Light Extraction Efficiency in AlGaN Deep-Ultraviolet Light-Emitting Diodes,” *Appl. Phys. Express*, vol. 6, no. 062101, 2013, doi: 10.7567/APEX.6.062101.

[293] N. Susilo *et al.*, “Effect of the GaN:Mg Contact Layer on the Light-Output and Current-Voltage Characteristic of UVB LEDs,” *Phys. status solidi*, vol. 215, no. 10, p. 1700643, May 2018, doi: 10.1002/pssa.201700643.

[294] N. Maeda, J. Yun, M. Jo, and H. Hirayama, “Enhancing the light-extraction efficiency of AlGaN deep-ultraviolet light-emitting diodes using highly reflective Ni/Mg and Rh as p-type electrodes,” *Jpn. J. Appl. Phys.*, vol. 57, no. 4, pp. 2–6, 2018, doi: 10.7567/JJAP.57.04FH08.

[295] K. Yamada *et al.*, “Development of underfilling and encapsulation for deep-ultraviolet LEDs,” *Appl. Phys. Express*, vol. 8, no. 1, 2015, doi: 10.7567/APEX.8.012101.

[296] J. Qiu, Y. Peng, X. Min, X. Wang, and M. Chen, “Enhanced Light Extraction of DUV LEDs by Using a Quartz Lens with Three-Dimensional Structure,” *IEEE Photonics Technol. Lett.*, vol. PP, no. c, pp. 1–1, 2021, doi: 10.1109/lpt.2021.3123574.

[297] Y. Zheng *et al.*, “Effects of Meshed p-type Contact Structure on the Light Extraction Effect for Deep Ultraviolet Flip-Chip Light-Emitting Diodes,” *Nanoscale Res. Lett.*, vol. 14, no. 1, p. 149, Dec. 2019, doi: 10.1186/s11671-019-2984-0.

[298] Y. Kashima *et al.*, “High external quantum efficiency (10%) AlGaN-based deep-ultraviolet light-emitting diodes achieved by using highly reflective photonic crystal on p-AlGaN contact layer,” *Appl. Phys. Express*, vol. 11, no. 1, pp. 1–5, 2018, doi: 10.7567/APEX.11.012101.

[299] W. Shin, A. Pandey, X. Liu, Y. Sun, and Z. Mi, “Photonic crystal tunnel junction deep ultraviolet light emitting diodes with enhanced light extraction efficiency,” *Opt. Express*, vol. 27, no. 26, p. 38413, 2019, doi: 10.1364/oe.380739.

[300] M. S. Alias *et al.*, “Review of nanophotonics approaches using nanostructures and nanofabrication for III-nitrides ultraviolet-photonic devices,” *J. Nanophotonics*, vol. 12, no. 04, p. 1, Jul. 2018, doi: 10.1117/1.JNP.12.043508.

[301] S. I. Inoue, T. Naoki, T. Kinoshita, T. Obata, and H. Yanagi, “Light extraction enhancement of 265 nm deep-ultraviolet light-emitting diodes with over 90 mW output power via an AlN hybrid nanostructure,” *Appl. Phys. Lett.*, vol. 106, no. 13, 2015, doi: 10.1063/1.4915255.

[302] Y. Zhang *et al.*, “Enhanced Light Extraction in Tunnel Junction Enabled Top Emitting UV LEDs Yuewei Zhang,” *Appl. Phys. Express*, vol. 9, p. 052102, 2016.

[303] D. Lee *et al.*, “Improved performance of AlGaN-based deep ultraviolet light-emitting diodes with nano-patterned AlN/sapphire substrates,” *Appl. Phys. Lett.*, vol. 110, no. 19, 2017, doi: 10.1063/1.4983283.

[304] M. Kneissl, J. Rass, C. Dreyer, and F. Mildner, “III-Nitride Ultraviolet Emitters Chapter 1,” *Springer Ser. Mater. Sci.*, vol. 227, pp. 415–434, 2016, doi: 10.1007/978-3-319-24100-5.

[305] C. Kuhn *et al.*, “MOVPE-grown AlGaN-based tunnel heterojunctions enabling fully transparent UVC LEDs,” *Photonics Res.*, vol. 7, no. 5, p. B7, 2019, doi: 10.1364/prj.7.0000b7.

[306] M. Guttmann *et al.*, “Optical light polarization and light extraction efficiency of AlGaN-based LEDs emitting between 264 and 220 nm,” *Jpn. J. Appl. Phys.*, vol. 58, no. SC, 2019, doi: 10.7567/1347-4065/ab0d09.

[307] R. Ishii, A. Yoshikawa, K. Nagase, M. Funato, and Y. Kawakami, “Temperature-dependent electroluminescence study on 265-nm AlGaN-based deep-ultraviolet light-emitting diodes grown on AlN substrates,” *AIP Adv.*, vol. 10, no. 12, 2020, doi: 10.1063/5.0024179.

[308] M. S. Wong *et al.*, “Demonstration of high wall-plug efficiency III-nitride micro-light-emitting diodes with MOCVD-grown tunnel junction contacts using chemical treatments,” *Appl. Phys. Express*, vol. 14, no. 8, 2021, doi: 10.35848/1882-0786/ac1230.

[309] C. C. Pan *et al.*, “Vertical stand transparent light-emitting diode architecture for high-efficiency and high-power light-emitting diodes,” *Jpn. J. Appl. Phys.*, vol. 49, no. 8 PART 1, pp. 0–3, 2010, doi: 10.1143/JJAP.49.080210.

[310] E. D. Palik, *Handbook of Optical Constants of Solids*. Orlando: Academic Press, Inc., 1985.

[311] T. Kolbe *et al.*, “Improved injection efficiency in 290 nm light emitting diodes with Al(Ga)N electron blocking heterostructure,” *Appl. Phys. Lett.*, vol. 103, no. 3, 2013, doi:

10.1063/1.4813859.

[312] T. Kolbe *et al.*, "Effect of electron blocking layer doping and composition on the performance of 310 nm light emitting diodes," *Materials (Basel).*, vol. 10, no. 12, pp. 1–8, 2017, doi: 10.3390/ma10121396.

[313] F. Mehnke *et al.*, "Efficient charge carrier injection into sub-250 nm AlGaN multiple quantum well light emitting diodes," *Appl. Phys. Lett.*, vol. 105, no. 5, pp. 1–5, 2014, doi: 10.1063/1.4892883.

[314] J. Ben *et al.*, "Defect evolution in AlN templates on PVD-AlN/sapphire substrates by thermal annealing," *CrystEngComm*, vol. 20, no. 32, pp. 4623–4629, 2018, doi: 10.1039/C8CE00770E.

[315] C.-Y. Y. Huang *et al.*, "High-quality and highly-transparent AlN template on annealed sputter-deposited AlN buffer layer for deep ultra-violet light-emitting diodes," *AIP Adv.*, vol. 7, no. 5, p. 055110, 2017, doi: 10.1063/1.4983708.

[316] H. K. Cho *et al.*, "Enhanced Wall Plug Efficiency of AlGaN-Based Deep-UV LEDs Using Mo/Al as p-Contact," *IEEE Photonics Technol. Lett.*, vol. 32, no. 14, pp. 891–894, 2020, doi: 10.1109/LPT.2020.3003164.

[317] S. Nakamura, N. Iwasa, M. Senoh, and T. Mukai, "Hole Compensation Mechanism of P-Type GaN Films," *Jpn. J. Appl. Phys.*, vol. 31, no. 5A, pp. 1258–1266, 1992, [Online]. Available: http://iopscience.iop.org/article/10.1143/JJAP.31.1258/meta.

[318] S. Nakamura, T. Mukai, M. Senoh, and N. Iwasa, "Thermal Annealing Effects on P-Type Mg-Doped GaN Films," *Jpn. J. Appl. Phys.*, vol. 31, pp. 139–142, 1992, [Online]. Available: http://iopscience.iop.org/article/10.1143/JJAP.31.L139/meta.

[319] A. Jadhav *et al.*, "On Electrical Analysis of Al-rich p-AlGaN films for III-nitride UV light emitters," *Semicond. Sci. Technol. Submitt.*, pp. 0–21, 2021.

[320] H. Sun *et al.*, "Band alignment of B0.14Al0.86N/Al0.7Ga0.3N heterojunction," *Appl. Phys. Lett.*, vol. 111, no. 12, pp. 0–5, 2017, doi: 10.1063/1.4999249.

[321] X. Li, S. Wang, H. Liu, F. A. Ponce, T. Detchprohm, and R. D. Dupuis, "100-nm thick single-phase wurtzite BAlN films with boron contents over 10%," *Phys. Status Solidi Basic Res.*, vol. 254, no. 8, pp. 1–5, 2017, doi: 10.1002/pssb.201600699.

[322] D. K. Bowen and B. K. Tanner, *High Resolution X-ray Diffractometry and Topography*. Bristol, PA: Taylor and Francis Ltd., 1998.

[323] T. Mukai, M. Yamada, and S. Nakamura, "Characteristics of InGaN-Based UV/Blue/Green/Amber/Red Light-Emitting Diodes," *Jpn. J. Appl. Phys*, vol. 1, no. 7A, pp. 3976–3981, 1999.

[324] P. M. Mooney, "Deep donor levels (DX centers) in III-V semiconductors," *J. Appl. Phys.*, vol. 67, no. R1, 1990, doi: 10.1063/1.345628.

[325] P. M. Mooney, T. N. Theis, and S. L. Wright, "Effect of local alloy disorder on emission kinetics of deep donors (DX centers) in Al x Ga 1−x As of low Al content," *Appl. Phys. Lett*, vol. 53, p. 2546, 1988, doi: 10.1063/1.100203.

[326] A. A. Istratov and O. F. Vyvenko, "DX-like center generated by uniaxial strains of screw dislocations in CdS," *J. Appl. Phys.*, vol. 80, no. 4400, 1996, doi: 10.1063/1.363400.

[327] T. Baba, M. Mizuta, T. Fujisawa, J. Yoshino, and H. Kukimoto, "The Local-Environment-Dependent DX Centers: Evidence for the Single Energy Level with a Specified Configuration," *Jpn. J. Appl. Phys.*, vol. 28, no. 6, pp. 891–894, 1989.

[328] E. Calleja *et al.*, "Effects of the local environment on the properties of DX centers in Si-doped GaAs and dilute AlxGa1−xAs alloys," *Appl. Phys. Lett.*, vol. 56, no. 934, 1990,

doi: 10.1063/1.102630.

[329] P. N. Murgatroyd, “Theory of space-charge-limited current enhanced by Frenkel effect,” *J. Phys. D. Appl. Phys.*, vol. 3, no. 2, pp. 151–156, 1970, doi: 10.1088/0022-3727/3/2/308.